# Modélisation non infiniment rapide de la combustion des solides dans le contexte de la sécurité incendie

van Minh Le

# THESE

Pour l'obtention du Grade de

DOCTEUR DE L'UNIVERSITE DE POITIERS

(Faculté des Sciences Fondamentales et Appliquées)
(Diplôme National - Arrêté du 25 mai 2016)

Ecole Doctorale :

Sciences et Ingénierie en Matériaux, Mécanique, Energétique

Secteur de Recherche : Energétique, Thermique, Combustion

Présentée par :

Van-Minh LE

**********

MODELING OF FINITE RATE CHEMISTRY EFFECTS IN THE COMBUSTION OF SOLID FUELS RELEVANT TO FIRE SAFETY PROBLEMS

**********

Directeurs de Thèse : Thomas ROGAUME, Franck RICHARD, Jocelyn LUCHE

**********

Soutenue le 20 Décembre 2019

Devant la Commission d'Examen

**********

## JURY

| | |
|---|---|
| Rapporteurs : | |
| PORTERIE Bernard | Professeur, Université Aix-Marseille |
| BEJI Tarek | Professeur, Université de Gent |
| | |
| Examinateurs : | |
| CUENOT Bénédicte | Dr HDR, CERFACS |
| TROUVE Arnaud | Professeur, Université du Maryland |
| RICHARD Franck | Maitre de Conférences, Université de Poitiers |
| BOULET Pascal | Professeur, Université de Lorraine |
| LUCHE Jocelyn | Maitre de Conférences, Université de Poitiers |
| ROGAUME Thomas | Professeur, Université de Poitiers |

# Acknowledgements

This project is financially supported at Université de Poitiers by the French Government program “Investissements d’Avenir” (LABEX INTERACTIFS, reference ANR-11-LABEX-0017-01). Special thanks the University of Poitiers for this financial support as well as the “Institut des Risques Industriels, Assurantiels et Financiers” for its technical and financial support via the platform “Incendie” Hestia.

It is also supported by a collaboration with the University of Maryland (UMD). The separate but related project at UMD is financially supported by the U.S. National Science Foundation (NSF, CBET Program, Award #1604907) and by FM Global. The project is also supported by supercomputing resources made available by UMD (http://www.it.umd.edu/hpcc) and by NSF (XSEDE Program, Grant #TG-CTS140046). Dr. James White contributed to this work while a PhD student at UMD and is now employed at FM Global.

I am grateful to everyone who has helped me in my struggle to achieve my dream of becoming a Ph. D. First and foremost, I would like to thank my advisors, Dr. Thomas Rogaume and Dr. Arnaud Trouvé for giving me the invaluable opportunity to work on challenging and extremely interesting projects over the past three years. Thanks for indoctrinating me into the ways of science, combustion and numerical simulations, for their steadfast support, limitless patience, and encouragement that they have given to me, and for their commitment to excellence in research.

I would like to thank my co-advisors, Dr. Franck Richard and Dr. Jocelyn Luche, for the support they provided to me to carry out this work, their enthusiasm, advices, and encouragement.

I would like to thank Dr. Bernard Porterie and Dr. Tarek Beji for accepting to be reviewers of this thesis and for their remarks which greatly helped me improve the quality of this manuscript. Thanks also to Dr. Bénédicte Cuenot for accepting to be part of the jury and Dr. Pascal Boulet for accepting our invitation to the thesis defense session.

I would like to thank Jocelyne, Marie Cannelle, Nadia, Christine for their support and help with complicated administrative paperwork.

I would like to thank my fellow colleagues for valuable discussions on technical issues and for helping me greatly to improve my programming skills: Alexis, Salman, Rui and Mohamed. Thanks to my fellow graduate students and my friend for the joy they brought to me working with them and for the friendships we developed: Cong, Alexis, Minerve, Salman, Rafi, Talia, Shiyun, Rui, Mohamed, Yiren, Fabien, Simon, Benji, Phuong Anh, Quang, Tram, Xiaowen, Pièrre, Julien, Jérémy, Tarik, Anars, Hussain, Olivier, Marc, Souffiane, Nguyen, Tung Hoang, Dat, Bach, Nhung, Tran Anh, Duc, Huan, Thuy, Thanh, etc.

Finally, I would like to thank most sincerely my beloved wife & family for their unlimited encouragement, support and love along this journey. I dedicate this work to them.

Minh

# Table of contents

# Symbols and Abbreviations

## Latin letters

| | Unit | Description |
|---|---|---|
| $a_k$ | [-] | Coefficient in the grey radiation model of species $k$ |
| $c_p$ | [J.kg$^{-1}$.K$^{-1}$] | Specific heat capacity |
| $C_v$ | [0] | Constant model in Algebraic model 1 |
| $C_{Diff}$ | [-] | Constant in the EDC combustion model |
| $C_{EDC}$ | [-] | Constant in the EDC combustion model |
| $C_e$ | [-] | Constant in turbulence model |
| $C_k$ | [-] | Constant in turbulence model |
| $C_\varepsilon$ | [-] | Constant in turbulence model |
| $D_k$ | [m$^2$.s$^{-1}$] | Diffusion coefficient of species $k$ |
| $D$ | [m$^2$.s$^{-1}$] | Mean diffusion coefficient for all species |
| $F_{rad}^l$ | [-] | Local radiative heat loss fraction |
| $g$ | [m.s$^{-2}$] | Gravity |
| $h$ | [J.kg$^{-1}$] | Total enthalpy (sensible plus formation) |
| $h_F$ | [J.kg$^{-1}$] | Total enthalpy of fuel side |
| $h_O$ | [J.kg$^{-1}$] | Total enthalpy of oxidizer side |
| $h_{ad}$ | [J.kg$^{-1}$] | Total enthalpy at the adiabatic conditions |
| $I$ | [W.m$^{-2}$.sr$^{-1}$] | Radiation intensity |
| $I_b$ | [W.m$^{-2}$.sr$^{-1}$] | Local black body radiation intensity |
| $I_j$ | [W.m$^{-2}$.sr$^{-1}$] | Radiation intensity of a fictitious gas $j$ in the WSGG model |
| $k_{sgs}$ | [m$^2$.s$^{-2}$] | Sub-grid scale turbulent kinetic energy |
| $L$ | [m] | Characteristic length |
| $MW$ | [kg. mol$^{-1}$] | Gas molecular weight |
| $N_\Omega$ | [-] | Number of solid angles |

| | | |
|---|---|---|
| $Pr$ | [-] | Prandtl number associated with molecular mixing |
| $Pr_{sgs}$ | [-] | Prandtl number associated with sub-grid scale turbulent mixing |
| $p$ | [kg.m$^{-1}$.s$^{-2}$] | Total pressure |
| $p_{rgh}$ | [kg.m$^{-1}$.s$^{-2}$] | Total pressure without the hydrostatic pressure |
| $\dot{q}''$ | [W.m$^{-2}$] | Radiative flux |
| $r_s$ | [-] | Stoichiometric oxygen-to-fuel mass ratio |
| $R$ | [J.kg$^{-1}$.K$^{-1}$] | Specific gas constant |
| $R_u$ | [J.kmol$^{-1}$.K$^{-1}$] | Universal gas constant |
| $S_{ij}$ | [s$^{-1}$] | Strain rate tensor |
| $t$ | [s] | Time |
| $T$ | [K] | Gas temperature |
| $u_j$ | [m.s$^{-1}$] | Velocity in $j$ direction |
| $x_k$ | [-] | Mole fraction of species $k$ |
| $Y_k$ | [-] | Mass fraction of species $k$ |
| $Z$ | [-] | Mixture fraction |
| $Z_{st}$ | [-] | Stoichiometric scalar dissipation rate |
| $Z_v$ | [-] | Sub-grid scale variance of mixture fraction |

## Greek letters

| | **Unit** | **Description** |
|---|---|---|
| $\upsilon$ | [m$^2$/s] | Molecular viscosity |
| $\sigma$ | [W.m$^{-2}$.K$^{-4}$] | Stefan-Boltzmann constant |
| $\rho$ | [kg/m$^3$] | Gas mass density |
| $\kappa L$ | [-] | Optical thickness |
| $\kappa$ | [m$^{-1}$] | Gas Planck mean absorption coefficient |
| $\varepsilon$ | [s$^{-1}$] | Strain rate |
| X | [s$^{-1}$] | General denotation for the flame stretch |

| | | |
|---|---|---|
| H | [J.kg$^{-1}$] | General denotation for the heat loss parameter in the flamelet combustion model |
| $\Delta\Omega$ | [sr] | Elementary solid angle |
| $-\nabla.\dot{q}''$ | [W.m$^{-3}$] | Volumetric radiation heat loss |
| $\Delta h$ | [J.kg$^{-1}$] | Enthalpy deficit |
| $\Delta h_{st}$ | [J.kg$^{-1}$] | Stoichiometric enthalpy deficit |
| $\Delta$ | [m] | Filter width |
| $\chi_{st}$ | [s$^{-1}$] | Stoichiometric scalar dissipation rate |
| $\chi_{st,Eff}$ | [s$^{-1}$] | Effective stoichiometric scalar dissipation rate |
| $\chi_{rad}^{l}$ | [-] | Local radiative heat loss fraction |
| $\chi_{rad}^{g}$ | [-] | Global radiative heat loss fraction |
| $\chi_{max}$ | [s$^{-1}$] | Maximum scalar dissipation rate |
| $\chi_{ext}^{low}$ | [s$^{-1}$] | Low extinction limit caused the radiation heat loss |
| $\chi_{ext}^{high}$ | [s$^{-1}$] | High extinction limit caused by the aerodynamic strain rate |
| $\upsilon_{sgs}$ | [m$^2$/s] | Sub-grid scale viscosity |
| $\tau_{sgs}$ | [s] | Turbulent mixing time scale |
| $\tau_{reaction\ zone}$ | [s] | Characteristic time scale for diffusion across the inner chemically active layer |
| $\tau_{diffusion\ zone}$ | [s] | Characteristic time scale for diffusion across the outer diffusive layer |
| $\tau_{chemistry}$ | [s] | Characteristic time scale for chemistry |
| $\tau_{EDC}$ | [s] | EDC mixing time scale |
| $\tau_{\chi_{st},Eff}$ | [s] | Characteristic time scale for the time variations of the effective flame stretch |
| $\varepsilon_{sgs}$ | [m$^2$.s$^{-3}$] | Sub-grid eddy dissipation rate |
| $\delta_{ij}$ | [-] | Kronecker symbol |
| $\dot{\omega}_k'''$ | [kg.m$^{-3}$.s$^{-1}$] | Volumetric production rate of species $k$ |
| $\dot{\omega}_T'''$ | [kg.K.m$^{-3}$.s$^{-1}$] | Heat release rate |
| $\dot{\omega}_{h_s}'''$ | [W.m$^{-3}$] | Volumetric heat release rate |

## Abbreviations and acronyms

| | |
|---|---|
| CFD | Computational Fluid Dynamics |
| CFL | Courant-Friedrichs-Lewy |
| DNS | Direct Numerical Simulation |
| EBU | Eddy Break-Up |
| EDC | Eddy Dissipation Concept |
| FPE | Fire Protection Engineering |
| HRR | Heat Release Rate |
| LBN | Turbulent Line Burner |
| LES | Large Eddy Simulation |
| LUT | Look-Up Table |
| MPI | Message Passing Interface |
| PDF | Probability Density Function |
| PGRF | Prescribed Global Radiant Fraction |
| PIMPLE | Pressure Implicit Method for Pressure-Linked Equations |
| PISO | Pressure Implicit with Splitting of Operator |
| PLRF | Prescribed Local Radiant Fraction |
| RANS | Reynolds Averaged Navier-Stokes |
| RHS | Right Hand Side |
| SGS | Sub-Grid Scale |
| SIMPLE | Semi-Implicit Method for Pressure-Linked Equations |
| SLFV1 | Steady Laminar Flamelet Version 1 |
| SLFV2 | Steady Laminar Flamelet Version 2 |
| SNB | Statistical Narrow Bands |
| TRE | Radiative Transfer Equation |
| TRI | Turbulence-Radiation Interactions |
| ULFV1 | Unsteady Laminar Flamelet Version 1 |
| ULFV2 | Unsteady Laminar Flamelet Version 2 |
| UMD | University of Maryland, College Park |

| | |
|---|---|
| UCSD | University of California San Diego |
| WSGG | Weighted-Sum-of-Grey-Gases |
| FFT | Fast Fourier Transform |

# List of Figures

# List of Tables

# Chapter I Introduction

## I.1 Prologue

Fires have played an important role in the development and evolution of human society. Fires have been used in rituals, in agriculture for clearing land, for cooking foods, for signaling, producing heat and light, propulsion objective, smelting, forging, etc. Beside the positive effects of fire including stimulating growth and maintaining various ecological systems in our society, destructions of fires have been dramatic, *e.g.*, conflagrations that threaten human life, animal life, health, and/or property for recent centuries. To prevent and reduce losses, understanding of the science of fire is essential, so that we become better able to quantify and predict fire behavior and apply our knowledge to fire safety in general.

One of main tool in fire research nowadays is Computational Fluid Dynamics (CFD) modeling, which has emerged over the past two decades as a powerful tool for both research- and engineering-level projects in the area of fire safety [1][2][3][4]. CFD is classified into three categories. First, Reynolds Averaged Navier-Stokes (RANS) equations are statistically-averaged equations of motion for fluid flow, *i.e.*, conservation equation of mass, momentum and energy. In the momentum equation, the Reynold stress is calculated using a turbulence closure model. Second, Large Eddy Simulation (LES) is a method in which the smallest scales of the flow are removed through a filtering operation and their effect are closed by sub-grid scale models. The method allows the largest and most important scales of the turbulence to be resolved, while hugely reducing the computational cost incurred by the smallest (sub-grid) scales. For high-fidelity LES simulations, the grid must be guaranteed to resolve at least 80% of the turbulent kinetic energy [5]. The requirement of computational cost in LES is greater than in RANS, but far cheaper than in Direct Numerical Simulation (DNS), which resolves the entire range of turbulent length scales. In DNS, no turbulence model is required, but it is extremely computationally expensive. The computational cost is proportional to $Re^{9/4}$ where $Re$ is a characteristic Reynolds number of the flow. Plus, it is very difficult to deal with complex geometries or flow configurations. Due to the nature of fires, *i.e.*, flow has a possible range from a few centimeters up to several meters and are strongly in transient phases, hence LES is the dominant method in fire simulations.

## I.2 Computational Fluid Dynamic (CFD) applied to fire problems

Two solvers represent the state-of-the-art of fire modeling based on the LES approach: FDS developed by the National Institute of Standards and Technology, USA (https://pages.nist.gov/fds-smv/), and FireFOAM developed by FM Global, USA (https://github.com/fireFoam-dev/fireFoam-dev).

### I.2.1 Fire Dynamic Simulator (FDS)

Fire Dynamics Simulator (FDS) [6], is a computational fluid dynamics (CFD) model of fire-driven fluid flow. FDS solves numerically a form of the Navier-Stokes equations appropriate for low-speed (Ma < 0.3), thermally-driven flow with a concentration on smoke and heat transport from fire.

FDS is a free open-souce software, which is developed by the National Institute of Standards and Technology (NIST) of the United States Department of Commerce, in cooperation with VTT Technical Research Centre of Finland. Smokeview is the companion visualization tool that can be used to display the output of FDS. Up to now, about half of the applications of the model have been designed for smoke handling systems and sprinkler/detector activation studies. The other half features residential and industrial fire reconstructions. Throughout its development, FDS's goal is to solve practical fire problems in fire protection engineering, while at the same time provide a tool to study fundamental fire dynamics and combustion.

### I.2.2 FireFOAM

FireFOAM [7] is a CFD model developed by FM Global in the United States for fire safety applications and based on a general-purpose library called OpenFOAM [8]. FireFOAM is a free open-souce software. We chose to use FireFOAM in the present project. Numerical developments will be realized in a simplified context, but our long-term objective is to provide a basis for the development and validation of engineering-level models used in real-world fire applications, which need to handle a wide range of interacting physical phenomena and complex geometry in industrial or real scenarios. Therefore, the requirements for a CFD code, which is capable of modeling large-scale industrial fire growth and suppression, far exceed the level of a typical in-house research code. The CFD package of choice should be capable of

massive parallelization and handling unstructured computational meshes. Moreover, given extension of new models and code implementation, an open-source platform, which can allow collaborative model development, is a preferred choice.

The object-oriented code structure of OpenFOAM [8] enables multiple alternative sub-models to co-exist. Unstructured mesh codes, such as OpenFOAM, have complex addressing rules when compared to the structured mesh codes, hence, cannot take advantage of an FFT (Fast Fourier Transform)-based direct linear solver. As a result, the code may be slower in a single processor mode than those designed for a Cartesian grid, such as FDS [6]. However, the capability of massive parallelization and flexibility of local mesh refinement alleviate effectively the speed issue. FireFOAM [7][9] uses the OpenFOAM platform and is designed to simulate industrial fire growth and suppression. It integrates the main gas phase CFD solver with numerous sub-models in a form of object libraries including diffusion-controlled combustion, turbulence [9], pyrolysis [11][12], surface water film [13][14], Lagrangian droplet transport [15][16], radiation, soot [16], wall boundary layer [17], etc.

## I.3 Numerical modeling challenges

### I.3.1 Combustion modeling

Because the fuel sources are typically poorly characterized, combustion models used in simulations of fires generally rely on a global combustion equation and do not include finite rate chemistry. These models therefore rely on crude treatments to describe important phenomena like flame extinction/re-ignition, which are complex phenomena and depend on a wide range of factor evolving in time such as temperature, oxygen mole concentration as well as flame residence time. Extinction/re-ignition are fundamental fire phenomena, which the fire community is highly interested in. Studies on the phenomena are essential to deal with the issue of fire suppression. Developing a simple model to capture ignition and extinction is itself a challenging task. Moreover, using the Large Eddy Simulation (LES) approach in modeling fire extinction, which is the preferred approach adopted in fire modeling such as in Fire Dynamics Simulator (FDS) or FireFOAM, makes the task even more difficult. The reason is that sub-grid scale thermo-chemical quantities such as temperature and flame stretch are

unresolved in LES simulations and require additional closures. During the past decades, researchers have tried to address the issue of flame extinction modeling in the context of LES:

- Hu *et al.* [18] have derived combustion modeling capabilities used in computational fluid dynamics solvers to deal with under-ventilated compartment fires. More specifically, they described two models and implemented these models into FDS: diffusion flame extinction due to air vitiation; and the emission of carbon monoxide (CO) and unburnt hydrocarbon (HC) mass in a compartment fire.
- A similar model based on the concept of a limiting flame temperature was also implemented in FDS V2 [19]. In brief, the model examines a grid cell and determines if combustion of the fuel in that cell as a stoichiometric mixture would raise the temperature of that mixture in excess of the limiting flame temperature. As initially developed in FDS V2, this model examines only fuel and oxygen concentrations and assumes the gas is air with a constant specific heat.
- To improve the previous extinction model in FDS, Vaari *et al.* [20] have proposed an improved flame extinction criterion for gaseous suppressants under the lumped species model with transport-limited combustion (infinitely fast chemistry).
- Snegirev *et al.* [21] have formulated a simplified approach to capture the major flame extinction mechanisms and calibrated their model against the measurement data for critical strain rates of laminar diffusion counter-flow flames with fuel and (or) oxidizer streams diluted by nitrogen. The model is based on the perfectly stirred reactor concept, thereby assuming rapid reactant mixing in the reaction zone, where reactants are delivered in stoichiometric proportions.
- Vilfayeau *et al.* [22] improved these extinction model by deriving a new unified extinction model in FireFOAM, which is capable to capture all different kind of extinction mechanisms (*i.e.*, aerodynamic, thermal and dilution quenching). The new model includes a flame extinction model based on the concept of a critical flame Damköhler number and a flame re-ignition model based on the concept of a critical gas temperature.

Despite the recent progress, these combustion models above still rely on a global combustion equation and do not include, or only include in a much-simplified manner finite

rate chemistry information. Moreover, a shift towards new ambitious objectives aimed at simulating important phenomena like ignition, extinction, the formation of soot or the emission of toxic species is increasing. Hence, there is an unmet need to incorporate combustion chemistry into CFD fire models.

### I.3.2 Radiation modeling

Thermal radiation is known to play an important role in heat transfer mechanism for large-scale fires. Because of the wavelength dependence, modeling radiation heat transfer in a flame is a challenging task [1][2][3][4]. Generally, radiation models are based on solving the radiative transfer equation (RTE). The numerical integration of the RTE is difficult and the associated computational cost can easily dominate the overall cost in a CFD solver. A typical simplification aimed at controlling cost and avoiding complexity is to assume a linear relationship between radiative power and heat release rate using a coefficient of proportionality called the global radiative loss fraction (or global radiant fraction (GRF) or prescribed global radiative heat loss fraction (PGRF)). The global radiative loss fraction is an empirical parameter that provides a convenient solution to the problem of representing changes in radiant emissions when considering different fuels but that fails to represent changes in radiant emissions in response to evolving fire conditions. Moreover, there is no guarantee that the model is locally accurate. In addition, experimental data for the global radiative loss fraction that depends on fuel type and combustion conditions [23] are often unknown. There is therefore an unmet need to bring more fundamental descriptions of radiation to CFD fire models.

## I.4 Objectives of the study

As discussed in section I.3, CFD modeling applied to fire safety problems has made remarkable progress over the past two decades, but modeling capabilities still remain limited by a number of simplifying assumptions of variable and often unknown accuracy. Combustion models used in simulations of fires generally rely on a global combustion equation and do not include finite rate chemistry. These models therefore rely on crude treatments to describe important phenomena like flame extinction. In addition, radiation models used in simulations of fires generally rely on the assumption of a linear relationship between radiative power and

heat release rate using a coefficient of proportionality or the global radiant fraction (GRF). These models must rely on the empirical calibration of GRF with fuel type and fire conditions.

The general objective of this research project is to develop models that account for combustion chemistry and that calculate (rather than prescribe) radiant emissions. A number of studies with the similar objectives can already be found in the fire modeling literature. For example, recent studies using a flamelet model with detailed chemistry to simulate combustion in a Large Eddy Simulation (LES) framework can be found in [24][25]. Similar studies using a perfectly stirred reactor model with single-step chemistry can be found in [21][26]. Furthermore, examples of recent LES studies using a full RTE framework to calculate radiant emissions (*i.e.*, without a prescribed GRF) combined with a grey model can be found in [27]. Similar studies using a non-grey model based on a Weighted-Sum-of-Grey-Gases (WSGG) formulation can be found in in [24][25][28]. Additional studies using a non-grey model based on mid-to-high fidelity spectral formulations like the Statistical Narrow Band Correlated-k method or the Full Spectrum Correlated-k model can be found in [29][30]. Note that due to their high computational cost, these more advanced formulations are typically applied to benchmark tests in a decoupled post-processing mode rather than applied to CFD in a fully-coupled flow-flame-radiation simulation mode.

In this context, the present study will explore the potential of the flamelet modeling approach for coupled flow-flame-radiation simulations of fire configurations. The proposed modeling framework uses the LES approach and is based on a laminar flamelet model and a careful treatment of the coupling between combustion and radiation that differentiates between non-local (*i.e.*, non-flamelet) and local (*i.e.*, flamelet) effects. The model also includes a description of sub-grid scale turbulence-radiation interactions (TRI). This modeling approach is tested against measurements performed in an experiment previously studied at the University of Maryland (UMD) and corresponding to a buoyancy-driven, turbulent line flame with a controlled air-nitrogen co-flow [23][31][32]. The UMD turbulent line burner is representative of the flame conditions found in fires, including conditions featuring flame extinction phenomena when the oxygen strength of the co-flow is reduced to sub-critical levels. The burner uses methane as the fuel and a controlled fuel flow rate. Note that the UMD turbulent line burner is one of the target experiments selected by a recent initiative of the International

Association for Fire Safety Science (IAFSS) called the IAFSS Working Group on Measurement and Computation of Fire Phenomena (MaCFP) [33]. In the MaCFP effort, the experiments are used to describe changes in the flame structure as co-flow conditions approach the oxygen extinction limit. Regarding the specific objectives of our project, the use of methane in the UMD experiment offers several benefits:

- Methane is a well-studied fuel, which allows using state-of-the-art combustion models
- Methane is a weakly sooting fuel, which allows neglecting soot and focusing on gas radiation.

The LES software adopted in the present project is FireFOAM, a fire modeling solver developed by FM Global [7].

## I.5 Outline of the thesis

In Chapter I, a brief introduction on fire, principals CFD methods and two solvers representing the state-of-the-art of fire modeling based on the LES approach are first presented. Then, limitations of the current combustion and radiation models in fire applications and how these restrictions motivate our research project are introduced. At the end, specific objectives solving these limitations are planned.

In Chapter II, the numerical solver is presented briefly. The general governing equations for flows are next introduced, followed by an introduction of the adopted turbulence model, of the baseline combustion model as well as radiation models.

Preliminary studies on the laminar, planar, strained counterflow diffusion flame considered as flamelet in the flamelet combustion model are presented in Chapter III. The basic concepts, notations and governing equations in both physical space and mixture fraction space, which are important to understand how such flows are solved for in combustion codes, are introduced. Next, the chapter investigates the sensitivity of the laminar flamelet solutions to modeling choices in radiation model, chemical kinetic mechanism as well as stoichiometric scalar dissipation rate under the steady state assumption to select baseline modeling choices for the subsequent LES simulations. Finally, interesting and important physical phenomenon related to unsteady effects are presented for both constant and time-dependent $\chi_{st}$ cases.

Chapter IV introduces exclusively the flamelet combustion model, which differs in choices made for the flamelet library generation, flamelet parametrization, the Probability Density Function (PDF) formulation as well as parameter variables used for the turbulent Look-Up Table (LUT). Four different methods for producing the laminar flamelet library are proposed. Then, the relation between the local thermochemical quantities and LES-filtered ones is provided using the presumed PDF approach. The assumption of statistically independent parameters in the joint PDF is made. The scalar dissipation rate PDF $\tilde{p}(\mathrm{X})$, the heat loss parameter PDF $\tilde{p}(\mathrm{H})$ are assumed to be a Dirac delta function. The $\beta$-PDF or the top-hat PDF is adopted for the PDF of mixture fraction $\tilde{p}(Z)$. The turbulent LUT that is parametrized by $(\tilde{Z}, \widetilde{Z_v}, \tilde{\mathrm{X}}, \tilde{\mathrm{H}})$ is pre-tabulated. Finally, the chapter provides various modeling options for $\tilde{Z}$, $\widetilde{Z_v}$, $\tilde{\mathrm{X}}$, and $\tilde{\mathrm{H}}$ in the LES-solver.

In Chapter V, the purpose is to present the flamelet combustion model and radiation model for large eddy simulations (LES) of well-controlled laboratory-scale turbulent fires. The development of the combustion model consists of studying the different libraries of flamelet solutions produced using different methods (SLFV1, SLFV2, ULFV1, ULFV2) and studying the different models of the turbulent flame LUT parameters such as the sub-grid scale variance of mixture fraction, the scalar dissipation rate as well as a heat loss parameter. The radiation model features a description of non-local phenomena through the Radiative Transfer Equation (RTE). Different treatments of coupled combustion and radiation effects at flamelet scale are considered:

- A treatment in which local radiation phenomena are neglected inside the flamelet solver.
- A treatment in which these phenomena are included inside the flamelet solver and also sub-grid scale turbulence-radiation interactions (TRI) are included in the RTE solver.

This chapter also presents a study on the sensitivity of the number of outer loops in the PIMPLE algorithm. It is evaluated in simulations of a statistically, two-dimensional, plane, buoyancy-driven, turbulent, diffusion methane-air flame experimentally characterized by measurements of local temperatures and global flame emissive power. The best models and best choices of parameters are determined and going to be used in simulations in Chapter VI.

Results presented in Chapter VI are the continuation of the study in Chapter V and aim to support the development and validation of models used to simulate the response of fires to the activation of suppression systems by gaseous agents. The modeling framework features the flamelet combustion model and the grey radiation model with TRI. The experimental configuration is the turbulent line fire with a controlled co-flow. The co-flow is an air-nitrogen mixture with variable oxygen dilution conditions, in which the conditions leading to full flame extinction is not considered in this study. The description of flame extinction and re-ignition events requires an additional laminar flamelet library parameter typically chosen as a reaction progress variable. This extension of the model will be considered in future work. Numerical results are obtained and evaluated against experimental measurements characterized by local temperatures, local oxygen mole-fraction, global flame emissive power as well as combustion efficiency.

Finally, conclusion and direction for future work are addressed.

# Chapter II Numerical modeling

In this chapter, the numerical solver, the general governing equations for flows are introduced, followed by an introduction of the adopted turbulence model, of the baseline combustion model as well as radiation models.

## II.1 Numerical solver

Numerical simulations in this study are performed using a modified version of FireFOAM [7], a fire modeling solver developed by FM Global and based on an open-source, general-purpose and free CFD software package called OpenFOAM [8]. OpenFOAM is an object-oriented, C++-based, second order accurate, finite-volume solver with implicit time integration. The solver features advanced meshing capabilities (structured/unstructured polyhedral mesh) and a massively parallel computing capability using MPI protocols.

The developed version of FireFOAM is a large eddy simulation (LES) fire dynamics solver that uses a Favre-filtered compressible flow formulation and brings a choice between several modeling options for the treatment of combustion, turbulence and thermal radiation.

## II.2 Governing equations

To obtain the mass density $\rho$ and flow velocity $u$, the developed version of FireFOAM solves transport equation of mass and momentum, written as below:

Mass:

$$\frac{\partial \bar{\rho}}{\partial t} + \frac{\partial (\bar{\rho} \tilde{u}_j)}{\partial x_j} = 0 \qquad \text{(II-1)}$$

Momentum:

$$\frac{\partial(\bar{\rho}\tilde{u}_j)}{\partial t} + \frac{\partial(\bar{\rho}\tilde{u}_i\tilde{u}_j)}{\partial x_j} = \left(\bar{\rho}(\upsilon + \upsilon_{sgs})\left(\frac{\partial\tilde{u}_i}{\partial x_j} + \frac{\partial\tilde{u}_j}{\partial x_i} - \frac{2}{3}\frac{\partial\tilde{u}_k}{\partial x_k}\delta_{ij}\right)\right) - \frac{\partial\bar{p}_{rgh}}{\partial x_i} - (g_i \cdot h_i)\frac{\partial\bar{\rho}}{\partial x_i} \quad \text{(II-2)}$$

State relation:

$$\bar{p} = \bar{\rho}R\tilde{T} \quad \text{(II-3)}$$

where $\tilde{}$ and $\bar{}$ are respectively the Favre and Reynolds filtering operator, $t$ is time, $\upsilon$ is the molecular viscosity, $\upsilon_{sgs}$ is the sub-grid scale viscosity, $p$ is the pressure, $g$ is the gravity, $T$ is the gas temperature, $\bar{p}_{rgh}$ is the pressure without the hydrostatic pressure and calculated as: $\bar{p}_{rgh} = \bar{p} - \bar{\rho}(g_i \cdot h_i)$ with $h_i$ is the position vector. The specific gas constant $R$ is related to the universal gas constant $R_u$(81315 $J/(kmol.K)$) and the gas molecular weight $MW$ by $R = R_u/MW$.

To obtain the mass fraction of species and temperature, FireFOAM provides different combustion modelling options: The Eddy Dissipation Concept (EDC) model and the flamelet combustion models, which has different methods, hence different equations to solve. Details of the EDC model and the flamelet combustion modelling are given in section II.4 and Chapter IV, respectively.

The algorithm used in FireFOAM is PIMPLE, which is a combination of PISO (Pressure Implicit with Splitting of Operator) and SIMPLE (Semi-Implicit Method for Pressure-Linked Equations). All these algorithms are iterative, but PISO and PIMPLE are both used for transient cases, whereas SIMPLE is used for steady state cases. The PIMPLE algorithm is understood as a SIMPLE algorithm for every time step, where outer correctors are the iterations, and once converged will move on to the next time step until the simulation is complete. Better stability is gained from PIMPLE over PISO for this reason. If the number of outer corrector loop is set to be one, PIMPLE will become PISO. Additional information about the iterative procedure of these algorithms and discretization scheme can be found in [34][35].

## II.3 Turbulence model

In LES, not all the scales of the flow are resolved, only the large scales are resolved by the grid and the sub-grid scales, which are the most computationally expensive to resolve, and reconstructed by the turbulence model. The effect of the sub-grid scales on the resolved-scale are through the sub-grid viscosity $\upsilon_{sgs}$, which plays an important role providing the unresolved transport of mass, momentum, energy, species and some other scalar variables, etc. In addition, the turbulence model provides the mixing time scale used in the EDC combustion model. Therefore, the choice of turbulence model is critical. Each turbulence model has its own limitations and has been designed for certain kind of applications. Based on the suggestion by Ref. [34], we adopt the constant coefficient one-equation eddy viscosity model.

The model is based on solving a transport equation for the sub-grid scale turbulent kinetic energy $k_{sgs}$ [36], written as follows:

$$\frac{\partial(\bar{\rho}k_{sgs})}{\partial t}+\frac{\partial(\bar{\rho}\tilde{u}_j k_{sgs})}{\partial x_j}=\left(\bar{\rho}\left(\upsilon+\upsilon_{sgs}\right)\frac{\partial k_{sgs}}{\partial x_j}\right)+P-\varepsilon_{sgs} \tag{II-4}$$

where $\varepsilon_{sgs}$ is the sub-grid eddy dissipation rate and calculated as $\varepsilon_{sgs}= C_e {k_{sgs}}^{3/2}/\Delta$, $C_e$ is a model constant (generally chosen as $C_e = 1.048$), and $\Delta$ is the filter width, which is proportional to the grid cell size and defined as $\Delta= (\Delta_x\Delta_y\Delta_z)^{1/3}$. The source term $P$ is given by:

$$P=-\frac{2}{3}\bar{\rho}\left(k_{sgs}+\upsilon_{sgs}\frac{\partial\tilde{u}_k}{\partial x_k}\right)\frac{\partial\tilde{u}_j}{\partial x_i}+2\bar{\rho}\upsilon_{sgs}\tilde{S}_{ij}\tilde{S}_{ij} \tag{II-5}$$

where the first term corresponds to the variation of turbulent kinetic energy due to thermal expansion and the second term due to strain rate. The strain rate tensor has been defined here in tensor notation as:

$$\tilde{S}_{ij}=\frac{1}{2}\left(\frac{\partial\tilde{u}_i}{\partial x_j}+\frac{\partial\tilde{u}_j}{\partial x_i}\right) \tag{II-6}$$

Then, the sub-grid scale kinematic viscosity $\upsilon_{sgs}$ is calculated as:

$$\upsilon_{sgs}=C_k {k_{sgs}}^{1/2}\Delta \tag{II-7}$$

where $C_k$ is a constant model (chosen as $C_k = 0.094$). Finally, the turbulent mixing time scale $\tau_{sgs}$, which is used in the EDC combustion model, is given by:

$$\tau_{sgs} = \frac{k_{sgs}}{\upsilon_{sgs}} = \frac{1}{C_k}\frac{\Delta}{{k_{sgs}}^{1/2}} \tag{II-8}$$

## II.4 EDC combustion model

When the EDC combustion model is used, in addition to the mass and momentum conservation equations (See Eqs. (II-1), (II-2)), FireFOAM also solves transport equations for sensible enthalpy and species, written as follows:

Sensible enthalpy:

$$\frac{\partial(\bar{\rho}\tilde{h}_s)}{\partial t} + \frac{\partial(\bar{\rho}\tilde{u}_j\tilde{h}_s)}{\partial x_j} = \frac{\partial}{\partial x_i}\left(\bar{\rho}(\frac{\nu}{Pr} + \frac{\nu_{sgs}}{Pr_{sgs}})\frac{\partial\tilde{h}_s}{\partial x_j}\right) + \overline{\dot{\omega}_{h_s}^{'''}} - \overline{\nabla.\dot{q}''} \tag{II-9}$$

Species Mass Fraction:

$$\frac{\partial(\bar{\rho}\tilde{Y}_k)}{\partial t} + \frac{\partial(\bar{\rho}\tilde{u}_j\tilde{Y}_k)}{\partial x_j} = \frac{\partial}{\partial x_i}\left(\bar{\rho}(\frac{\nu}{Pr} + \frac{\nu_{sgs}}{Pr_{sgs}})\frac{\partial\tilde{Y}_k}{\partial x_j}\right) + \overline{\dot{\omega}_k^{'''}} \tag{II-10}$$

where $Pr$ and $Pr_{sgs}$ denote the Prandtl numbers associated with molecular mixing and sub-grid scale turbulent mixing, respectively (we use $Pr_{sgs} = 0.5$), $(-\overline{\nabla.\dot{q}''})$ is the radiation power density (with $q''$ is the radiative heat flux), which is obtained through radiation models introduced in section II.5; $\tilde{h}_s$ is the LES-filtered sensible enthalpy and $\tilde{Y}_k$ is the LES-filtered mass fraction of species $k$. The filtered chemical source terms, $\overline{\dot{\omega}_k^{'''}}$, and the volumetric heat release rate (HRR), $\overline{\dot{\omega}_{h_s}^{'''}}$, require closure modeling. In this study, an Eddy Dissipation Concept (EDC) model is adopted to estimate these source terms.

The EDC model proposed in [37] for non-premixed turbulent combustion is an extended version of the Eddy Break-Up (EBU) model introduced in [37][38] for premixed turbulent combustion. EDC applies to turbulent flames corresponding to high Damhköler number and high Reynold number conditions, *i.e.*, conditions for which chemistry is fast and for which the rate of combustion is controlled by the rate of turbulent mixing between fuel and air. The fuel mass reaction rate per unit volume may be written as:

$$\overline{\dot{\omega}_{h_s}'''} = \frac{\bar{\rho}}{\tau_{EDC}} min\left(\tilde{Y}_F, \frac{\tilde{Y}_{O2}}{r_s}\right) \quad \text{(II-11)}$$

where $\bar{\rho}$ is the LES-filtered mass density, $\tilde{Y}_F$ and $\tilde{Y}_{O2}$ the LES-filtered mass fractions of fuel and oxygen, $r_s$ the stoichiometric oxygen-to-fuel mass ratio. In the fully developed turbulent flow region, the EDC mixing time scale is taken from the turbulence model (see Eq. (II-8)): $\tau_{EDC} = \tau_{sgs}/C_{EDC}$ with $C_{EDC} = 4$. However, this description assumes turbulent mixing and does not apply to regions where the flow is quasi-laminar, *i.e.*, the flame base region. In these regions, fuel-air mixing is controlled by molecular diffusion and we write: $\tau_{EDC} = C_{Diff}\Delta^2/\alpha$ where $\alpha$ is thermal diffusivity and the constant model $C_{Diff} = 4$. Finally, two formulas can be combined to form $\tau_{EDC}$:

$$\tau_{EDC} = min\left(\frac{\tau_{sgs}}{C_{EDC}}, \frac{C_{Diff}\Delta^2}{\alpha}\right) \quad \text{(II-12)}$$

Note that in Eq. (II-11), a global combustion equation has been assumed, $F + r_s\, O_2 \rightarrow (1 + r_s)\, P$ (where $F$, $O_2$ and $P$ denote fuel, oxygen and product, respectively), where the equation is written per unit mass of fuel.

The EDC model provides a cost-effective description of the location and intensity of combustion and heat release rate processes under a range of flow conditions. However, the model is also known to have several limitations. First and foremost, EDC assumes that the rate of combustion is entirely determined by the rate of fuel-air mixing and therefore does not represent flame extinction/ignition phenomena, which also depend on combustion chemistry. In addition, EDC has a domain of validity restricted to turbulent flames and does not correctly represent laminar combustion. In the following, we consider the flamelet modeling approach (see Chapter IV) that has the potential to overcome both of these limitations, *i.e.*, the flamelet modeling approach includes a description of finite rate chemical kinetics and is based on laminar flame calculations that apply to both the laminar combustion and turbulent flamelet combustion regimes.

## II.5 Radiation model

### II.5.1 Introduction

Thermal radiation is known to play an important role in heat transfer mechanism for large-scale fires. Because of the wavelength dependence, modeling radiation heat transfer in a flame is a challenging task. In the literature [39], a number of radiation models with various degrees of complexity are developed and can be categorized into two principal classes: grey and non-grey models, which assume that radiation does not and does vary with wavelength, respectively. Plus, grey gas models used in many combustion problems further simplify the radiation treatment by making an optically thin medium assumption, which neglects the self-absorption of the gas and utilizes the Planck mean absorption coefficient. Non-grey narrow-band and wide-band models taking into account the variation of radiative properties with wavelength are more complex and much more computationally expensive than the grey models but are more accurate. In the following, we present different treatments of radiative properties through the Radiative Transfer Equation (TRE): the prescribed global radiant fraction (PGRF) model, the grey model and the Weighted-Sum-of-Grey-Gases (WSGG) model.

### II.5.2 Prescribed Global Radiant Fraction model (PGRF)

The model assumes a non-absorbing grey medium/optically thin medium (*i.e.*, the optical thickness $\kappa L$ of the radiating gas is below 0.1, where $\kappa$ is the gas Planck mean absorption coefficient and $L$ a characteristic length), hence $\overline{\kappa I} = 0$ and the model uses a prescribed global radiative loss fraction (PGRF) $\chi_{rad}^{g}$. The RTE equation is in that case:

$$\nabla \bar{I}.\vec{s} = \frac{\chi_{rad}^{g}\,\overline{\dot{\omega}_{h_s}'''}}{4\pi} \qquad \text{(II-13)}$$

where $\bar{I}$ is the (LES-filtered) radiation intensity in the angular direction defined by the unit vector $\vec{s}$ and an elementary solid angle $\Delta\Omega = (4\pi/N_{\Omega})$, with $N_{\Omega}$ the number of angles used in the discretization of angular space; and $\overline{\dot{\omega}_{h_s}'''}$ is the (LES-filtered) combustion heat release rate per unit volume. The radiation power density that appears in Eq. (II-9) is obtained by integration of the right-hand side of Eq. (II-13) over angular space and with the present model, can be simply written as:

$$-\overline{\nabla.\dot{q}''} = \int_{4\pi}\left(\frac{\chi_{rad}^{g}\,\overline{\dot{\omega}_{h_s}'''}}{4\pi}\right) = \chi_{rad}^{g}\,\overline{\dot{\omega}_{h_s}'''} \tag{II-14}$$

where $\dot{q}''$ is the radiative heat flux. In the following, we call this baseline model PGRF and use $\chi_{rad}^{g} = 23\%$ (see [23]) and $N_\Omega = 64$.

The practical method of prescribing the global radiant fraction provides a convenient solution to the problem of simulating radiation effects: this solution guarantees that in an average sense, the flame emits a realistic amount of radiation energy. This solution, however, assumes that measurements of the global radiant fraction $\chi_{rad}^{g}$ are available (such measurements are in fact only available for a limited number of fuels) and that the values provided by these measurements do not depend strongly on fire conditions (values of $\chi_{rad}^{g}$ do in fact depend on ventilation conditions, see [23]). The grey model and the WSGG model presented in the next two sections have the ambition to overcome these limitations; both models rely on solving the RTE equation with full emission and absorption effects.

### II.5.3 Grey Model

The RTE equation for the grey model is:

$$\nabla\bar{I}.\vec{s} = \overline{\kappa I_b} - \bar{\kappa}\bar{I} \tag{II-15}$$

where $\kappa$ is the mean absorption coefficient and $I_b$ the local blackbody radiation intensity, $I_b = (\sigma T^4/\pi)$, with $\sigma$ the Stefan-Boltzmann constant ($\sigma = 5.669 \times 10^{-8}\, W/m^2K^4$) and $T$ the local gas temperature. $\kappa$ is obtained from the composition and temperature of the gas:

$$\kappa = p(x_{CO2}a_{CO2} + x_{H2O}a_{H2O}) \tag{II-16}$$

where $p$ is pressure, $x_{CO2}$ and $x_{H2O}$ the mole fractions of carbon dioxide and water vapor, and $a_{CO2}$ and $a_{H2O}$ the Planck mean absorption coefficients for carbon dioxide and water vapor. In this description, the coefficients $a_{CO2}$ and $a_{H2O}$ are treated as known functions of temperature, $a_{CO2}(T)$ and $a_{H2O}(T)$ (see Ref. [40]).

In the grey model, two different treatments are considered. The first one is to ignore sub-grid scale turbulence-radiation Interactions (TRI) and simply write: $\overline{\kappa I_b} = (\bar{\kappa} \times \sigma\tilde{T}^4/\pi)$, $\bar{\kappa}\bar{I} = (\bar{\kappa} \times \bar{I})$, and $\bar{\kappa} = p\big(\tilde{x}_{CO2}a_{CO2}(\tilde{T}) + \tilde{x}_{H2O}a_{H2O}(\tilde{T})\big)$ where $\tilde{T}$, $\tilde{x}_{CO2}$and $\tilde{x}_{H2O}$ are the LES-filtered values of the gas temperature and the mole fractions of carbon dioxide and water vapor,

respectively. The second one is to account for sub-grid scale TRI through a flamelet-based description of the emission term and mean absorption coefficient that appear in the RTE equation combined with an application of the flamelet-LES coupling expressions presented in Eqs. (IV-16) and (IV-17) (readers should read Chapter IV before considering two following equations):

$$\overline{\kappa I_b} = \bar{\rho} \times \left(\widetilde{\frac{\kappa I_b}{\rho}}\right) = \bar{\rho} \times \int_0^1 \left(\frac{\kappa I_b}{\rho}\right)^{fl} \left(Z, \widetilde{\chi_{st}}, \widetilde{\Delta h_{st}}\right) p_\beta\left(Z; \tilde{Z}, \widetilde{Z_v}\right) dZ \tag{II-17}$$

$$\bar{\kappa} = \bar{\rho} \times \left(\widetilde{\frac{\kappa}{\rho}}\right) = \bar{\rho} \times \int_0^1 \left(\frac{\kappa}{\rho}\right)^{fl} \left(Z, \widetilde{\chi_{st}}, \widetilde{\Delta h_{st}}\right) p_\beta\left(Z; \tilde{Z}, \widetilde{Z_v}\right) dZ \tag{II-18}$$

Finally, the radiation power density is obtained by integration of the right-hand side of Eq. (II-15) over angular space and with the present model:

$$-\overline{\nabla . \dot{q}'''} = \int_{4\pi} \left(\overline{\kappa I_b} - \overline{\kappa I}\right) \tag{II-19}$$

For the grey model, we use $N_\Omega = 64$.

### II.5.4 Weighted-Sum-of-Grey-Gases

We now proceed to a discussion of the WSGG model in which spectral variations of radiation properties are taken into account. We consider the WSGG model developed by Modest [41] and that corresponds to a generalization of the original WSGG model developed by Hottel and Sarofim [42] for any arbitrary solution method. This model is often referred to as the banded WSGG model. In that case, the RTE is solved for each grey gas:

$$\nabla \overline{I_j} . \vec{s} = \overline{\kappa_j a_j I_b} - \overline{\kappa_j I_j} \tag{II-20}$$

where the subscript $j$ denotes a fictitious grey gas representing a certain spectral region, $\kappa_j$ is the mean absorption coefficient of the fictitious gas in that region and $a_j$ is a weight coefficient. One of the main advantages of this formulation is the absence of a mean beam length (a mean beam length is required in the original version of WSGG in order to convert a total emissivity into a global absorption coefficient). In WSGG, the accuracy of the method depends on the calibration of the coefficients $\kappa_j$ and $a_j$. Commonly, they are calibrated with specific

optimization methods for different values of the $H_2O$-to-$CO_2$ mole ratio (taking values between 0.125 and 2) and using a high-resolution radiation model (*i.e.*, a Statistical Narrow Band model or a Line-by-Line model) as a reference solution. In the present study, $\kappa_j$ and $a_j$ are described using the model proposed in Ref. [43] with the assumption that the $H_2O$-to-$CO_2$ mole ratio is equal to 2 (the maximum value considered in Ref. [43]). This choice was guided by separate flamelet calculations using a detailed chemistry that revealed that relevant values of the $H_2O$-to-$CO_2$ mole ratio were typically above 2, *i.e.*, above this maximum value. In the following, we again choose to ignore SGS TRI, call this non-grey model *WSGG*, and use 4 fictitious grey gases and $N_\Omega = 64$. Note that the computational cost of the WSGG model is 4 times the cost of the grey model.

# Chapter III Laminar diffusion flames

In the flamelet modeling approach, the turbulent or laminar reaction zone is viewed as a collection of flame elements (called flamelets) that are similar to canonical laminar flames (see Figure 1) [44]. The usual choice for a canonical configuration corresponds to one-dimensional, laminar, planar, strained counterflow diffusion flames. Before considering the flamelet combustion models in the next chapter, to have some preliminary understanding, we first study an important part of that model, the laminar diffusion flames.

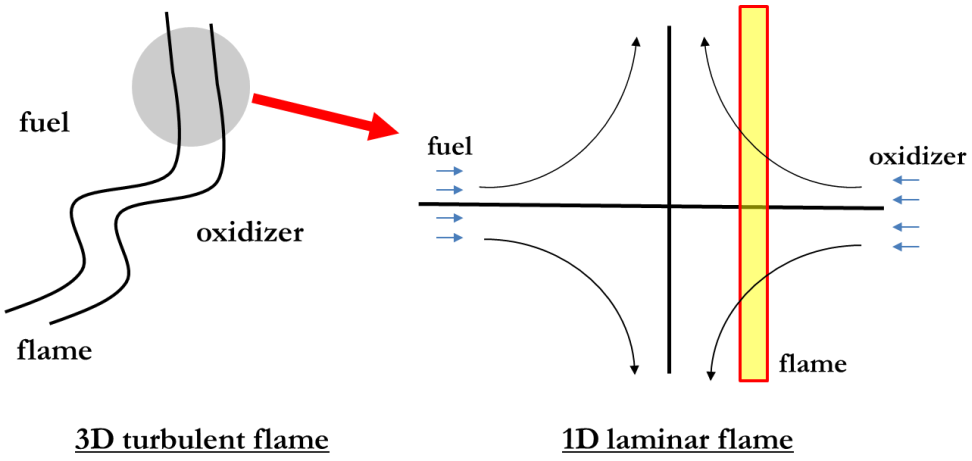


*Figure 1: Flamelet representation of a turbulent flame viewed as an ensemble of one-dimensional, laminar, planar, counterflow diffusion flames.*

## III.1 Laminar diffusion flame configuration

Figure 2 depicts the prototype of the strained, laminar diffusion flame configuration. Two boundary states (*i.e.*, the temperature, the species composition as well as the operating pressure) must now be considered: fuel side (which may be diluted in other gases) on the right and oxidizer (diluted or not) on the left side. Fuel and oxidizer diffuse towards the reaction zone where they burn and produce heat. Temperature reaches a maximum value in this zone and diffuses away from the flame front (orange line in Figure 2) towards the fuel and oxidizer streams.

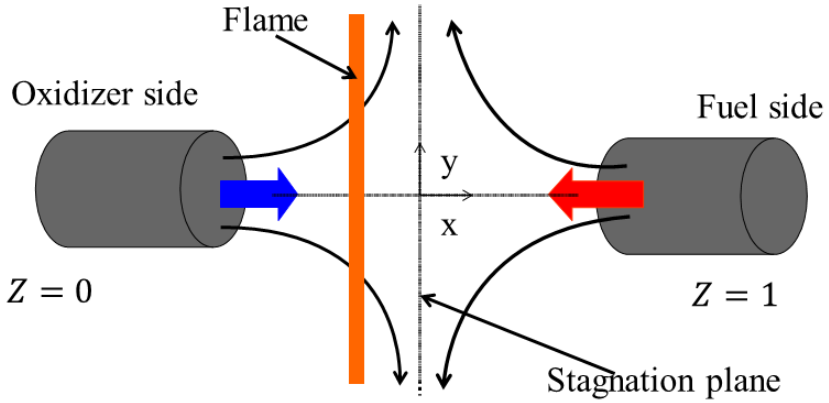


*Figure 2: Schematic view of a counterflow diffusion flame configuration*

Our laminar diffusion flame is strained flame, *i.e.*, the oxidizer and fuel streams are pushed toward each other at a given speed. At the place close to each side of the flame, the gas is either too lean or too rich to burn. The flame only appears in a limited region, where oxidizer and fuel are mixed adequately so that chemical reactions can take place. The most convenient location for the chemical reactions is at stoichiometric proportions.

A few main concepts related to diffusion fames are important to understand how such flows are solved for in combustion codes. Section III.2 presents these notions (mixture fraction, flame stretch, etc.) and governing equations in both physical space and mixture fraction space. Section III.3 and Section III.4 respectively consider the steady flamelet assumption and the unsteady flamelet assumption and interesting relevant physical phenomena. The chosen test case for these studies has a configuration corresponding to the laminar diffusion methane-air flame.

## III.2 Governing equations

Some derivations used in this section are based on assumptions made to analyze idealized diffusion flames. First, all the diffusion coefficients $D_k$ of chemical species $k$ are assumed to be equal $D$. Second, the heat capacities $c_{pk}$ of chemical species are equal to $c_p$.

The mass fraction $Y_k$ of each species is governed by the balance equation as follows:

$$\frac{\partial}{\partial t}(\rho Y_k) + \frac{\partial}{\partial x_i}(\rho u_i Y_k) = \frac{\partial}{\partial x_i}\left(\rho D \frac{\partial Y_k}{\partial x_i}\right) + \dot{\omega}_k''' \tag{III-1}$$

where $\dot{\omega}_k'''$ is species reaction rate. Suppose that the counter-flow diffusion flame has the reaction, which involves only fuel ($F$), oxidizer ($O$) and products ($P$), as follows:

$$\nu_F F + \nu_O O \rightleftharpoons \nu_P P \tag{III-2}$$

where $\nu_k$ is the molar stoichiometric coefficient of species $k$. Then, the conservation equations for fuel, oxidizer and temperature in physical space can be written as follows:

$$\frac{\partial}{\partial t}(\rho Y_F) + \frac{\partial}{\partial x_i}(\rho u_i Y_F) = \frac{\partial}{\partial x_i}\left(\rho D \frac{\partial Y_F}{\partial x_i}\right) + \dot{\omega}_F''' \tag{III-3}$$

$$\frac{\partial}{\partial t}(\rho Y_O) + \frac{\partial}{\partial x_i}(\rho u_i Y_O) = \frac{\partial}{\partial x_i}\left(\rho D \frac{\partial Y_O}{\partial x_i}\right) + s\dot{\omega}_F''' \tag{III-4}$$

$$\frac{\partial}{\partial t}(\rho T) + \frac{\partial}{\partial x_i}(\rho u_i T) = \frac{\partial}{\partial x_i}\left(\frac{\lambda}{c_p}\frac{\partial T}{\partial x_i}\right) - \frac{Q}{c_p}\dot{\omega}_F''' - \frac{1}{c_p}\nabla.\dot{q}'' \tag{III-5}$$

where $s$ is the stoichiometric ratio, $Q$ is the molar heat reaction and $\lambda$ is the thermal conductivity.

The mixture fraction, $Z$, measures the local fuel/oxidizer ratio and can be defined as follows:

$$Z = \frac{sY_F - Y_O + Y_O^0}{sY_F^0 + Y_O^0} \tag{III-6}$$

where the superscript $^0$ denotes the boundary condition. A necessary mathematical procedure reported in [45] combines both Eqs. (II-2), (II-3) and (II-5) into a balance equation without source terms for the conserved scalar $Z$, which has the boundary conditions: $Z = 1$ in the fuel stream and $Z = 0$ in the oxidizer stream (see Figure 2 and Table 1):

$$\frac{\partial}{\partial t}(\rho Z) + \frac{\partial}{\partial x_i}(\rho u_i Z) = \frac{\partial}{\partial x_i}\left(\rho D \frac{\partial Z}{\partial x_i}\right) \tag{III-7}$$

| Variable | Fuel side value | Oxidizer side value |
|---|---|---|
| Fuel mass fraction | $Y_F^0$ | 0 |
| Oxidizer mass fraction | 0 | $Y_O^0$ |
| Gas temperature | $T_F^0$ | $T_O^0$ |
| Mixture fraction $Z$ | 1 | 0 |

*Table 1: Boundary conditions for species mass fractions, gas temperature and the scalar mixture fraction $Z$.*

Based on the flamelet hypothesis, our multi-dimensional counter-flow diffusion flame locally has one-dimensional structure, which is depend on the mixture fraction $Z$. The species mass fraction balance equations (III-1) and the temperature equation (III-5) may be rewritten in the mixture fraction space $Z$ by adopting an appropriate space transformation and are called *the laminar flamelet equations*. Necessary intermediate mathematical derivations and assumptions for such transformation are described in [45][46] and are not presented here. In the following, the final conservation equations of species and energy in the mixture fraction space are written as:

$$\rho \frac{\partial Y_k}{\partial \tau} - \rho \frac{\chi}{2} \frac{\partial^2 Y_k}{\partial Z^2} = \dot{\omega}_k''' \tag{III-8}$$

$$\rho \frac{\partial T}{\partial \tau} - \rho \frac{\chi}{2}\left(\frac{\partial^2 T}{\partial Z^2} + \frac{1}{c_p}\frac{\partial c_p}{\partial Z}\frac{\partial T}{\partial Z}\right) = -\frac{1}{c_p}\sum_{k=1}^{n} h_k \dot{\omega}_k''' - \frac{1}{c_p}\nabla.\dot{q}'' \tag{III-9}$$

where $\tau$ is the time, $\rho$ is the density, $Y_k$ is the mass fraction of species $k$, $\dot{\omega}_k'''$is the chemical production rate of specie $k$, $c_p$ and $h_k$ are the heat capacity and the specific enthalpy of species $k$, respectively. The scalar dissipation rate $\chi$ is defined as $\chi(Z) = 2D(\nabla Z)^2$, with $D$ the molecular diffusivity of species mass or heat (as mentioned above, we adopt here the classical equi-diffusive assumption and consider that all molecular diffusion coefficients are equal). In the equations (III-8) and (III-9) reported above, the scalar dissipation rate $\chi$ must be modeled

across the flamelet. Several approaches are proposed [47][48][49], in which the most common is the expression by [47] and can be written as:

$$\chi = \chi_{st} \frac{\phi}{\phi_{st}} \frac{f(Z)}{f(Z_{st})} \tag{III-10}$$

with

$$\phi = \frac{3}{4} \frac{\left(\sqrt{\frac{\rho_\infty}{\rho}} + 1\right)^2}{2\sqrt{\frac{\rho_\infty}{\rho}} + 1} \tag{III-11}$$

where $Z_{st}$ is the stoichiometric mixture fraction; $\phi$ is a factor introduced in order to consider variable density effects [48]; the subscript $\infty$ means the oxidizer stream; and $f(Z) = \exp\left[-2[erfc^{-1}(2Z)]^2\right]$, where $erfc^{-1}$ is the inverse of the complementary error function. The radiative heat loss source $\nabla.\dot{q}''$ can be either prescribed or calculated through a more elaborate radiation model: either by the grey, or non-grey 25 bands WSGG [50], or SNB, which have just been added to FlameMaster [51] (a specialized software to solve the flamelet equations). Since WSGG and SNB are computationally very expensive and a few tests shown in section III.3.3 suggest that the flamelet solutions are not sensitive to the choice of radiation model, therefore, the grey model is mainly used. RTE for the grey model in 1-D physical space can be written as:

$$\nabla I.\vec{s} = \kappa I_b - \kappa I \tag{III-12}$$

The absorption coefficient, $\kappa$, is calculated based on the Planck mean absorption coefficients and more details on how to calculate $\kappa$ can be found in II.5.3. Here, RTE is solved using the discrete ordinates method with $S_8$-approximation [52]. Note that, before solving RTE, the temperature and mass fraction of $CO_2$ and $H_2O$ related to the calculation of $\kappa$ in $Z$-space are needed to transform to the physical space.

The laminar flamelets can be simulated by specialized software such as FlameMaster, libOpenSMOKE using detailed chemical kinetics as well as radiation model, etc. libOpenSMOKE [53][54] is a closed-source, steady flame solver solving flamelet equations without the radiative heat loss term. In contrast, FlameMaster is an open-source, well-

established laminar steady or unsteady flame solver with different radiation modeling treatments in both mixture fraction and physical space [51].

## III.3 Steady flamelet assumption

The structure of the laminar flamelet can be assumed to be steady, even though the flow itself (and especially the mixture fraction $Z$ field) depends on time. In this case, the steady solutions can be produced by solving the steady flamelet equations obtained by removing the temporal term in the Eqs. (III-8) and (III-9):

$$-\rho\frac{\chi}{2}\frac{\partial^2 Y_k}{\partial Z^2} = \dot{\omega}_k''' \tag{III-13}$$

$$-\rho\frac{\chi}{2}\left(\frac{\partial^2 T}{\partial Z^2} + \frac{1}{c_p}\frac{\partial c_p}{\partial Z}\frac{\partial T}{\partial Z}\right) = -\frac{1}{c_p}\sum_{k=1}^{n} h_k\dot{\omega}_k''' - \frac{1}{c_p}\nabla.\dot{q}'' \tag{III-14}$$

In the steady assumption context, we will investigate the sensitivity of the laminar flamelet solutions to modeling choices in radiation model, chemical kinetic mechanism as well as stoichiometric scalar dissipation rate.

Note that the steady approaches described here are applied to configurations without flame extinction, *i.e.*, to configurations in which the flame dynamics belong to the upper branch of the classical S-curve representing the flame response to stretch [55].

### III.3.1 Chemical kinetic mechanisms

There are some available chemical kinetic mechanisms that can be used in FlameMaster as well as libOpenSMOKE for producing flamelet solutions. We introduce here four detailed mechanisms:

- C1-C3 combustion chemistry [56] (we call it ***C1-C3***), which has more than a hundred of species and two thousands of reversible reactions and it is dedicated for the pyrolysis, partial oxidation and combustion of hydrocarbon fuels up to 3 C atoms

- A reduced chemical kinetic mechanism (28 species, 72 reversible reactions) developed for methane combustion chemistry and described in Ref. [57] (we call it ***CH4.72***).
- The San Diego mechanism version 2014-10-04 [58] (around 70 species, 235 reversible reactions) designed to hydrogen combustion in air and focus on conditions relevant to flames, high temperature ignition and detonations (we call it ***UCSD***).
- GRI-Mech v3.0 [59] is a popular, detailed chemical kinetic mechanism, which includes 53 species and 325 reversible reactions, is an optimized mechanism designed for natural gas combustion chemistry (we call it ***GRI v3.0***).

To evaluate these four mechanisms, flamelet simulations under adiabatic conditions are performed. Note that the flamelet solutions with C1-C3 are obtained in libOpenSMOKE since C1-C3 is the only mechanism available in that solver and the solutions with the other mechanisms are produced in FlameMaster.

Figure 3 shows a comparison of the peak temperature versus the stoichiometric scalar dissipation rate between the chemical kinetic mechanisms. Figure 4 gives a comparison of flamelet temperature profiles calculated between different chemical kinetic mechanisms at specific values of $\chi_{\mathrm{st}}$. We see that at high values of $\chi_{st}$, the result shows that the peak temperature as well as the flamelet temperature profiles (as seen in the left plot of Figure 4) are not sensitive to the selected mechanisms. The high extinction limits $\chi_{ext}^{high}$ (which is caused by the aerodynamic strain rate) predicted in FlameMaster (libOpenSMOKE does not have an algorithm to catch the limit) are close to each other between the mechanisms (33.89, 28.75, 30.15 [1/s] with CH4.72, UCSD and GRI v3.0 respectively). And at low values of $\chi_{st}$, the peak temperature and temperature profile (as demonstrated in the right plot of Figure 4) in CH4.72 differs from the predictions of other mechanisms. UCSD and GRI v3.0 agree very well in both peak temperature and temperature profile. For C1-C3, the peak temperature is a bit lower than that predicted by other mechanisms, but the temperature profiles agree well with those in UCSD and GRI v3.0.

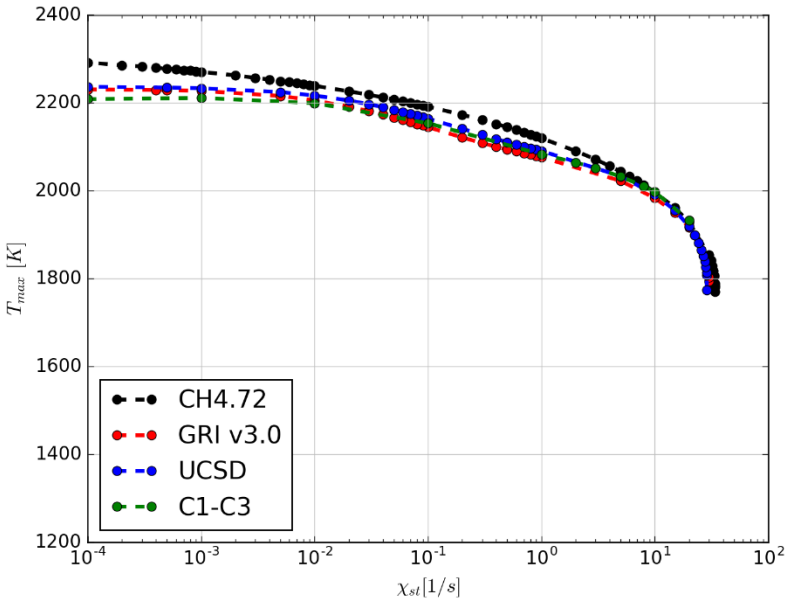


*Figure 3: Comparison of the peak temperature versus the stoichiometric scalar dissipation rate between the chemical kinetic mechanisms.*

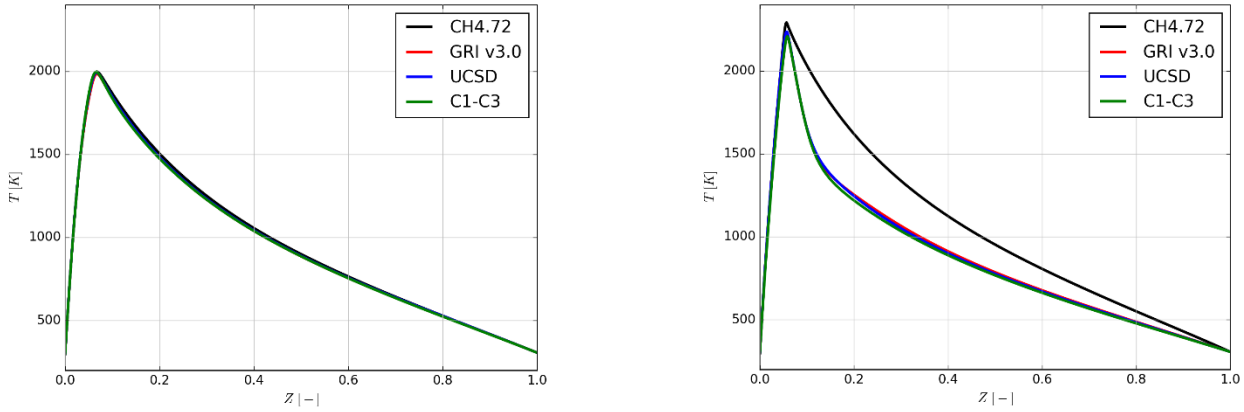


*Figure 4: Comparison of flamelet temperature profiles calculated for different chemical kinetic mechanisms at $\chi_{st} = 10\ s^{-1}$ (left plot) and at $\chi_{st} = 0.0001\ s^{-1}$ (right plot).*

In conclusion, we use C1-C3 in libOpenSMOKE since C1-C3 is the only choice. For FlameMaster, based on the results above, both GRI v3.0 and UCSD are very good choices. However, we decided to adopt GRI v3.0 in FlameMaster as the computational cost for calculations with GRI v3.0 is slightly cheaper than those calculated with UCSD.

### III.3.2 Scalar dissipation rate sensitivity

In the flamelet equations (III-8) (III-9), the scalar dissipation rate $\chi$ is modeled across the flamelet through Eq. (III-10) with the input parameter $\chi_{st}$, the scalar dissipation rate at the stoichiometric mixture fraction $Z_{st}$, which quantifies flame stretch. An example of modeled scalar dissipation rate profiles across the flamelet for different values of $\chi_{st}$ is displayed in Figure 5.

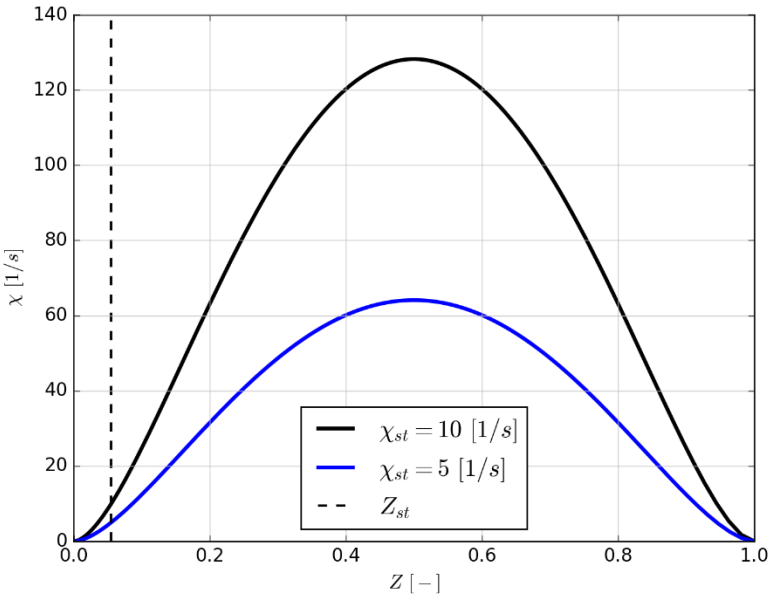


*Figure 5: Modeled scalar dissipation rate profiles across the flamelet for different values of $\chi_{st}$.*

Steady flamelet solutions are simulated using GRI v3.0 under adiabatic conditions for different values of $\chi_{st}$. Figure 6 shows how the flame stretch $\chi_{st}$ affects the mass fraction of the reactants. At high value of $\chi_{st}$, the flame is out of equilibrium where methane and oxygen can co-exist in the reaction zone (around the area $Z_{st} = 0.055$) (see Figure 6 (a)). When $\chi_{st}$ is decreased, the flame becomes close to equilibrium, where methane and oxygen do not overlap (see Figure 6 (b)). Figure 7 describes the gas temperature and volumetric heat release rate profiles across the flamelet. We observe that the peak temperature (the volumetric heat release rate) is higher (much lower) than the temperature (those) at high value of $\chi_{st}$.

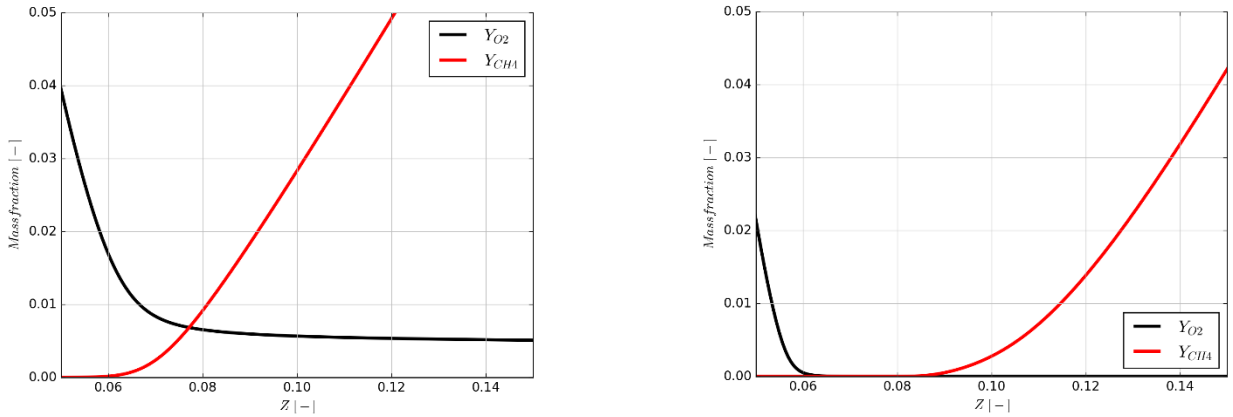


(a) (b)

*Figure 6: Mass fraction profiles of reactant species methane and oxygen at the reaction zone around* $Z_{st} = 0.055$ *for* $\chi_{st} = 10\ [1/s]$ *(a) and for* $\chi_{st} = 0.0001\ [1/s]$ *(b).*

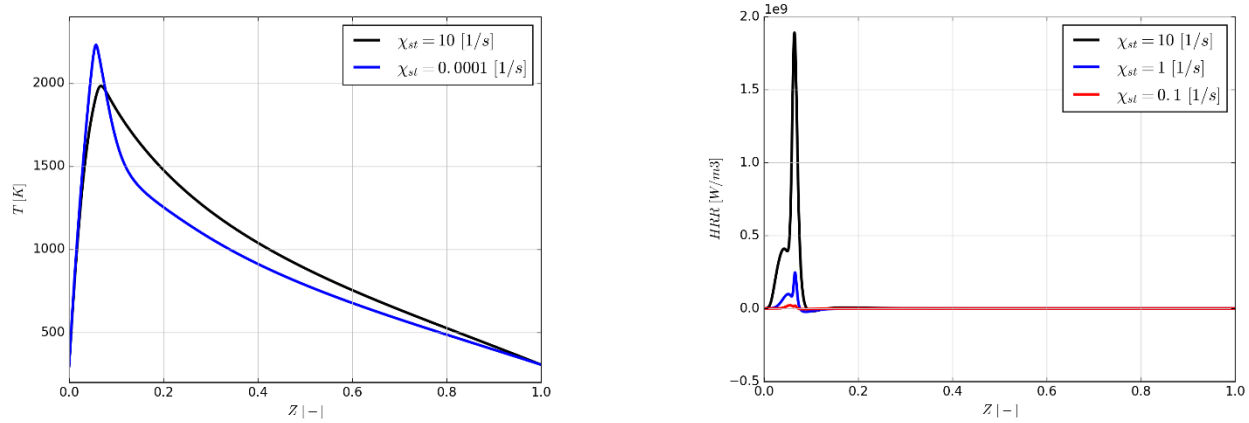


(a) (b)

*Figure 7: Temperature (a) and volumetric heat release rate (b) for different values of* $\chi_{st}$.

Figure 8 shows how the integrated heat release rate depends on the flame stretch $\chi_{st}$. Increasing $\chi_{st}$ promotes combustion because the straining velocity field brings more fuel and oxidizer to the reactive zone. Figure 8 (a) shows that the magnitude of integrated heat release rate increases like the square root of the stoichiometric scalar dissipation rate $\chi_{st}$. This evolution is stopped when $\chi_{st}$ reaches the high extinction limit $\chi_{ext}^{high} = 30.15$ [1/s], *i.e.*, chemistry becomes too slow to burn the incoming reactants and quenching occurs. Figure 8

(b) in the log-log plot bringing more access to the region of low value of $\chi_{st}$ shows that the magnitude of integrated heat release rate increases linearly as a function of the log of stoichiometric scalar dissipation rate $\chi_{st}$.

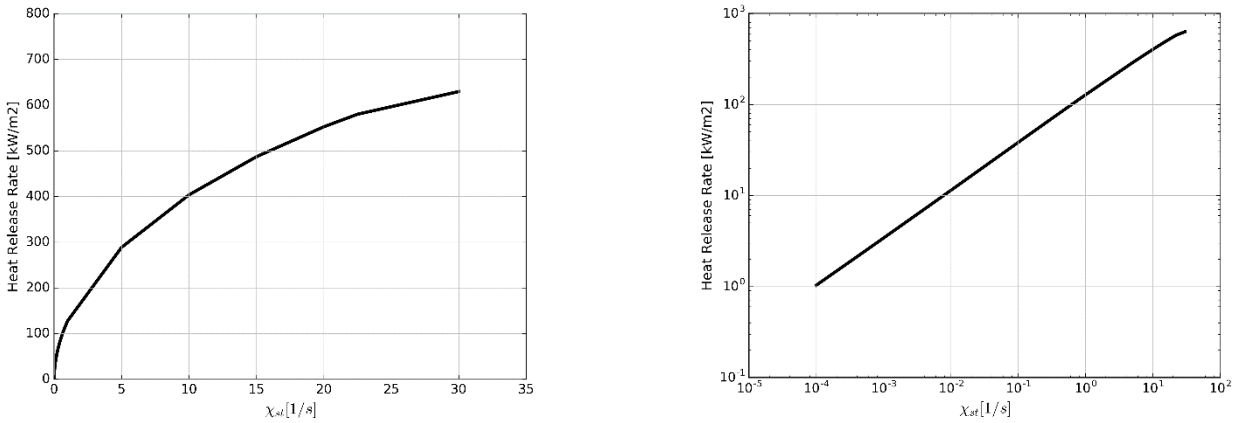


(a) (b)

*Figure 8: Integrated heat release rate across the flamelet as a function of $\chi_{st}$ in a linear plot (a) and log-log plot (b).*

### III.3.3 Radiation models

The baseline version of FlameMaster includes an optically thin flame radiation model. This version has been modified by Marchand *et al.* [63][64] through the introduction of a radiation module that solves the Radiative Transfer Equation (RTE) (in physical space) and that features three options for the treatment of radiation:

- A grey model [40].
- A banded Weighted-Sum-of-Grey-Gases (WSGG) model that accounts for spectral variations of radiation properties [41] (we use 25 fictitious grey gases; model coefficients are calibrated using the method proposed in Ref. [41]).
- A Statistical Narrow Band (SNB) model [62] (449 bands). The radiation module is coupled to the FlameMaster governing equations through the radiative power density source term that appears in the flame energy equation (III-14).

Figure 9 shows that at high values of $\chi_{st}$, radiation models have a limited impact on the peak temperature. This point is confirmed in Figure 10 (a) when the temperature profiles across

the flamelet for Grey, WSGG, SNB or even Adiabatic conditions look similar. When $\chi_{st}$ is decreased to lower values, radiation begins to play a bigger role leading to larger differences in the peak temperature (as seen in Figure 9) as well as the temperature profile (see Figure 10 (b)) between the cases. When comparing results obtained with the different radiation models, Figure 9 shows that the peak temperature with SNB is the most different from the other two models, specially at the locations of low value of $\chi_{st}$. Figure 11 presents variations of the radiation power density across the flamelet for different radiation models and shows that the performance in Grey is relatively similar to those in WSGG, but still predict a bit more heat loss and make the peak temperature lower. Hence, the low extinction limit $\chi_{ext}^{low}$ (which caused by the radiation heat loss) predicted in Grey (0.035 [1/s]) is higher than those in WSGG (0.026 [1/s]).

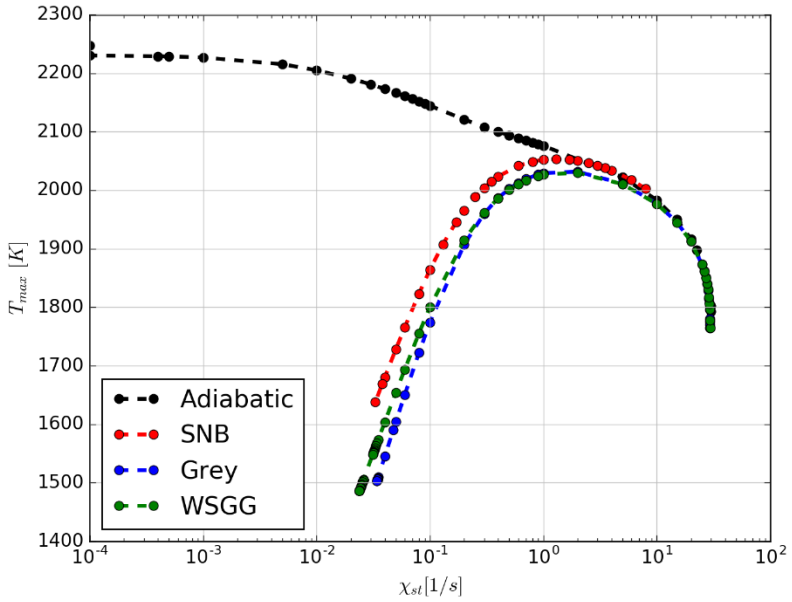


*Figure 9: Peak temperature as a function of stoichiometric scalar dissipation rate for different radiation models.*

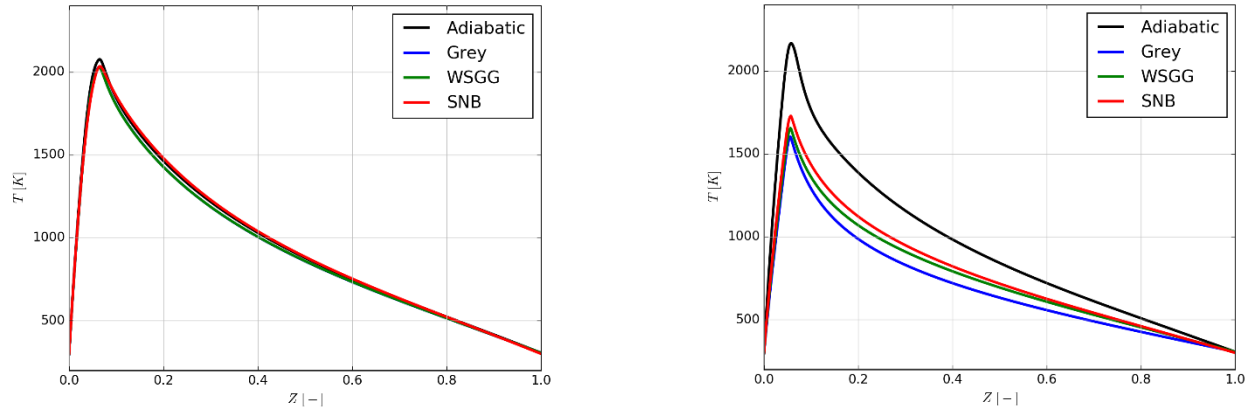


(a) (b)

*Figure 10: Comparison of steady flamelet temperature profiles for different radiation models at $\chi_{st} = 5$ [1/s] (a) and at $\chi_{st} = 0.05$ [1/s] (b).*

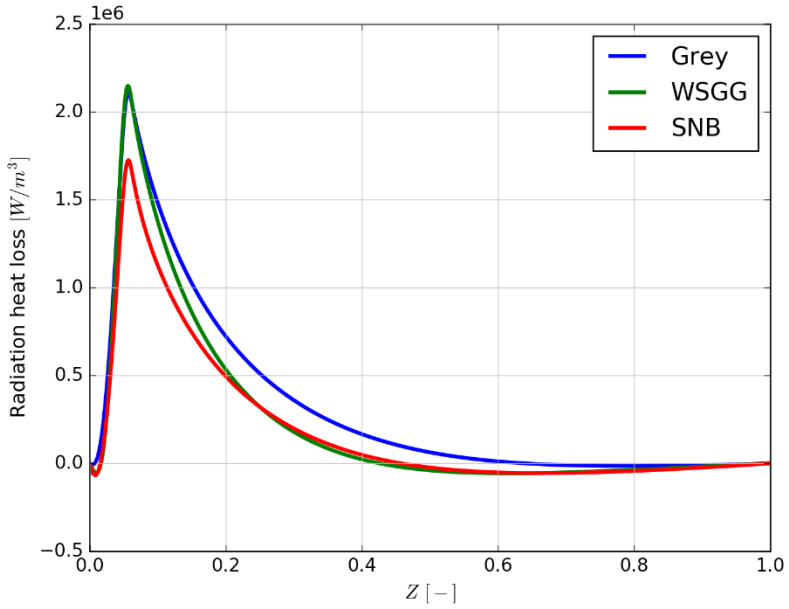


*Figure 11: Variations of the radiation power density across the flamelet characterized by $\chi_{st} = 0.1$ [1/s] for different radiation models.*

Theoretically, SNB is the best radiation model among the models proposed here, but it is computationally too expensive. Hence, it's unfeasible to use SNB in the flamelet calculations. In contrast, Grey and WSGG are computationally affordable and the performance between

these two models is similar. Therefore, we decided to use these two models in the non-adiabatic flamelet calculations in the following sections.

## III.4 Unsteady flamelet assumption

In the previous section, the sensitivity of the laminar flamelet solutions to modeling choices in radiation model, chemical kinetic mechanisms as well as stoichiometric scalar dissipation rate under the steady flamelets assumption has been described. In this section, interesting transient phenomena is studied. Unsteady flamelet solutions used to study these phenomena are produced by solving Eqs. (III-8) and (III-9).

### III.4.1 Constant $\chi_{st}$ over time case

In the literature, studying unsteady flamelets at a given value of $\chi_{st}$ over time basically has two methods. The first one computes the ignition or extinction process of the flamelets with an initial solution from the unstable branch in the S-shaped curve [63] and these simulations are performed without considering radiative heat losses. The second method computes with the initial solution located at the stable branch. Then, the process involves the decrease in the thermal state due to radiation heat losses [64]. The aim of our study in this section is to support the flamelet combustion modeling in Chapter IV, where radiation heat losses is considered as a very important part. Hence, we decided to study the second method. The GRI v3.0 chemical kinetic mechanism and the Grey radiation model are used to compute transient flamelets.

Steady adiabatic flamelets generated for different given values of $\chi_{st}$ ranging from $10^{-4}$ to 25 $s^{-1}$ (as demonstrated in Figure 12) are used as the initial solution for the unsteady flamelet calculations, which are finished when its solutions reach the Steady/Grey solution at a given $\chi_{st}$. The process is repeated for different given values of $\chi_{st}$ covering all the range. Figure 13 shows all unsteady flamelet solutions, which are denoted as black dots.

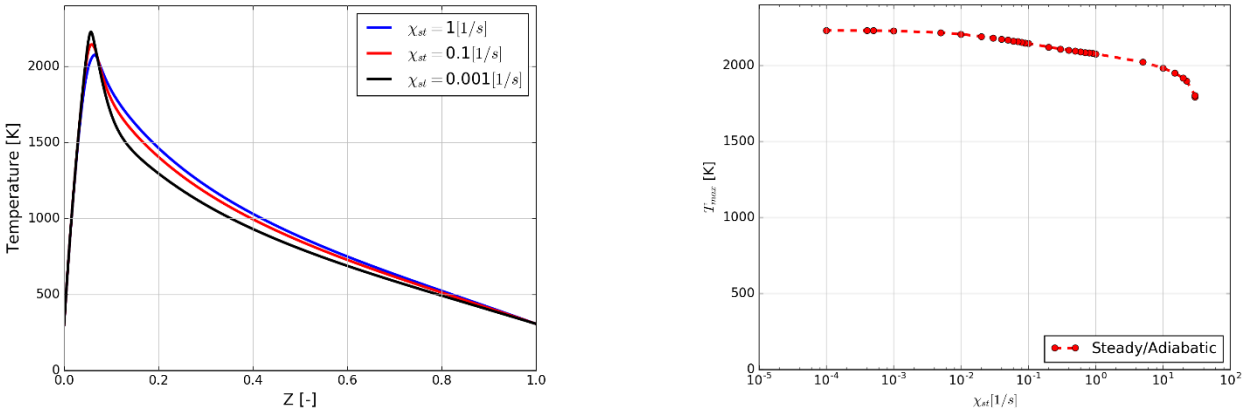


(a) (b)

*Figure 12: (a) Comparison of steady flamelet temperature profiles for different values of $\chi_{st}$; (b) The peak temperatures for different values of $\chi_{st}$ without heat losses.*

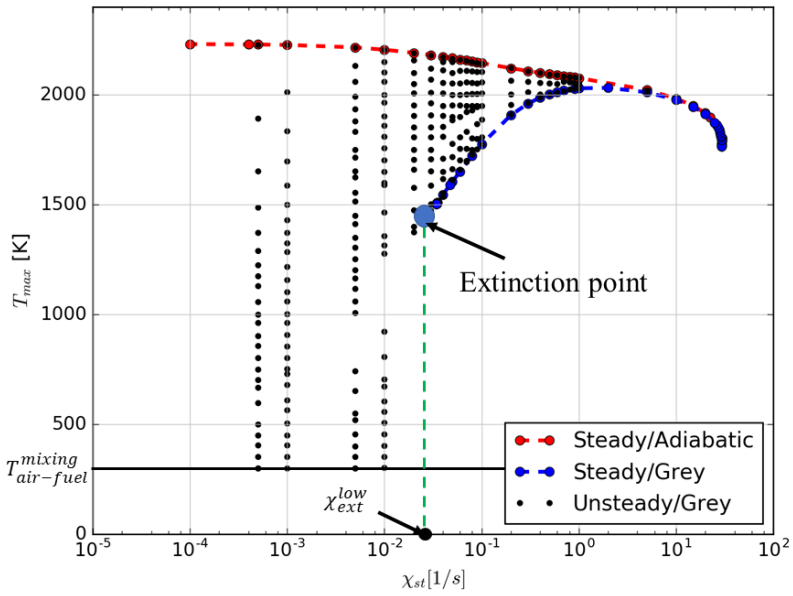


*Figure 13: Peak temperature as a function of stoichiometric scalar dissipation rate for all unsteady/grey solutions.*

The radiation heat losses affect insignificantly the gas temperature and can be ignored at the area of high values of flame stretch, but dominate and have a great impact on the temperature, even they can extinguish the flame at small values of flame stretch. Figure 13

confirms these points and the lower extinction limit $\chi_{ext}^{low}$ (denoted as the big blue dot and calculated using the steady/grey conditions), which indicates the extinction limit of the flame stretch $\chi_{st}$ due to radiation heat losses, is approximately 0.034 $s^{-1}$. When we let unsteady calculations long time enough, we have two possible cases as follows:

- for $\chi_{st} > \chi_{ext}^{low}$, unsteady/grey calculation will converge to the steady/grey solutions.
- for $\chi_{st} < \chi_{ext}^{low}$, unsteady/grey calculation will reach the extinction (or pure air-methane mixture).

Figure 14 depicts temperature profiles across the flamelet as an example of the two cases. In addition, when going from high to low values of flame stretch $\chi_{st}$, the flame response time to radiation of the unsteady calculation depends strongly on the flame stretch, *e.g.*, Figure 15 represents the peak temperature over time for the unsteady/grey calculation at a given value of $\chi_{st}$ and shows that to reach the steady/grey point (defined as the point where the maximum temperature no longer changes over time), the unsteady/grey at $\chi_{st} = 0.02\ \mathrm{s}^{-1}$ needs longer time than the case at $\chi_{st} = 0.2\ \mathrm{s}^{-1}$ (around 1.5 seconds versus 0.4 second).

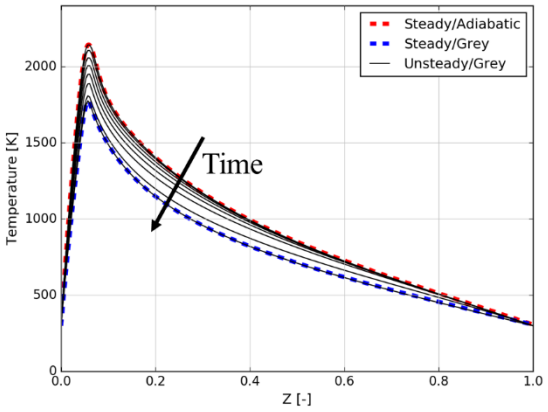


(a)

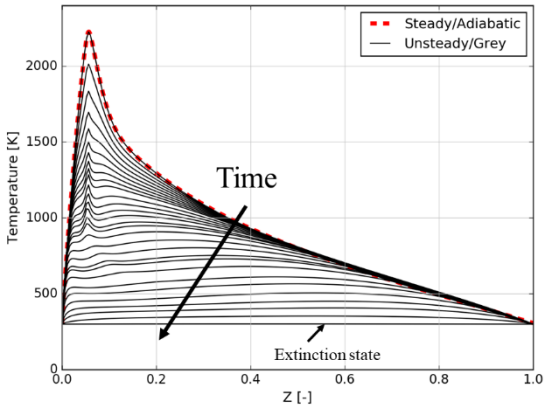


(b)

*Figure 14: (a) the unsteady/grey calculation at $\chi_{st} = 0.1\ s^{-1}$ when unsteady/grey calculation converges to the steady/grey solutions (a) and at $\chi_{st} = 0.001\ s^{-1}$ when unsteady/grey calculation reaches the extinction (b).*

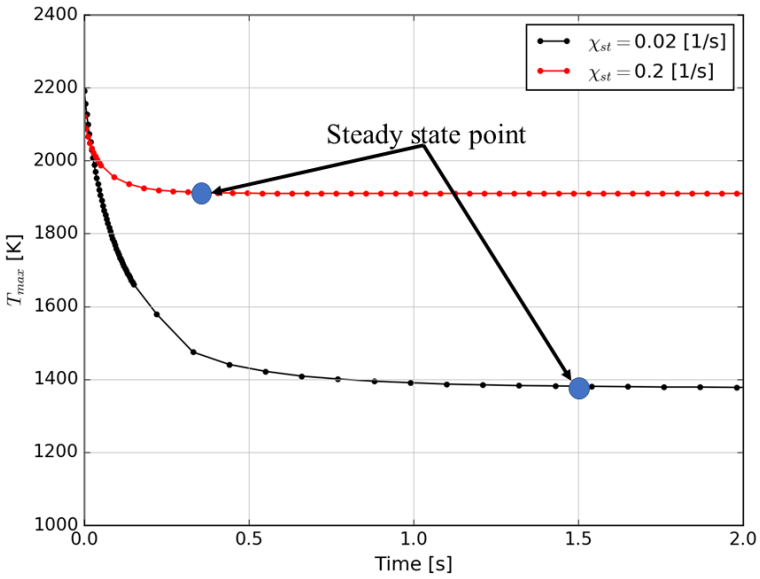


*Figure 15: Peak temperature over time for the unsteady/grey calculation at* $\chi_{st} = 0.02\ s^{-1}$ *and* $\chi_{st} = 0.2\ s^{-1}$.

### III.4.2 Time-dependent $\chi_{st}$ case

Cuenot *et al.* report in [65] that in the diffusion flame, when the stoichiometric flame stretch changes over time, $\chi_{st}(t)$, the flame needs time to adapt. The short or long time needed for the flame will determine whether the conditions are steady or unsteady. The paper also shows that the flame stretch really effecting on the flame is not the instantaneous flame stretch, $\chi_{st}(t)$, but instead, the effective one, $\chi_{st,Eff}(t)$. The effective flame stretch $\chi_{st,Eff}$ will be used as an input for the unsteady flamelet calculation as well as for time analysis, which will be described in detail below. Basically, the flamelet combustion has four different time scales to be considered: $\tau_{diffusion\ zone}$, $\tau_{reaction\ zone}$, $\tau_{chemistry}$ and $\tau_{\chi_{st},Eff}$; where $\tau_{diffusion\ zone}$ is a characteristic time scale for diffusion across the outer diffusive layer (it serves as characteristic time scale of changes in flame structure induced by thermal radiation) and calculated as:

$$\tau_{diffusion\ zone} = \frac{C_{d,1}}{\chi_{max}} = \frac{C_{d,2}}{\chi_{st}} \qquad \text{(III-15)}$$

where $C_{d,1}$, $C_{d,2}$ are constant models and $\chi_{max}$ is the maximum flame stretch. An example of the stoichiometric scalar dissipation rate $\chi_{st}$ and the maximum scalar dissipation rate $\chi_{max}$ is displayed in Figure 16; $\tau_{reaction\ zone}$ is a characteristic time scale for diffusion across the inner chemically active layer and calculated as follows:

$$\tau_{reaction\ zone} = C_r \frac{(Z_{st})^2}{\chi_{st}} \tag{III-16}$$

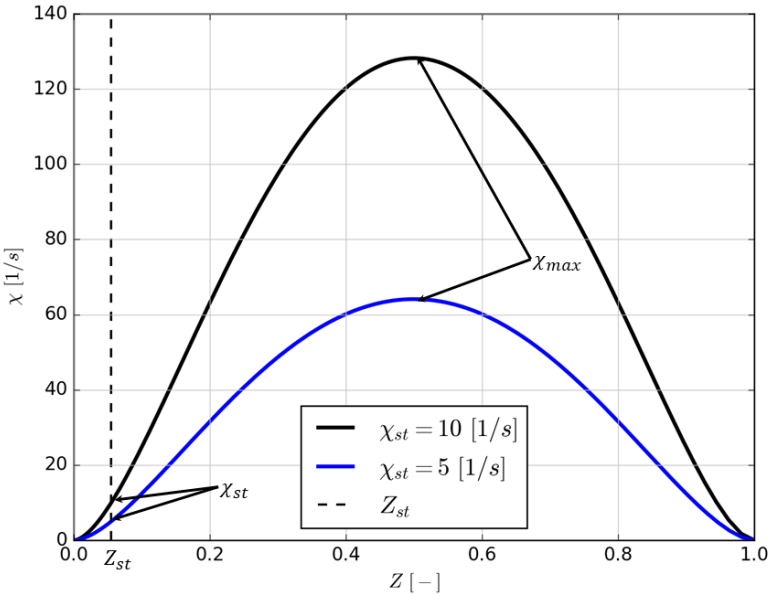


*Figure 16: Demonstration of the stoichiometric scalar dissipation rate $\chi_{st}$ and the maximum scalar dissipation rate $\chi_{max}$.*

where $C_r$ is a constant; $\tau_{chemistry}$ is a characteristic time scale for combustion chemistry and $\tau_{\chi_{st},Eff}$ is a characteristic time scale for the time variations of the effective flame stretch $\chi_{st,Eff}$:

$$\tau_{\chi_{st},Eff} = \frac{\chi_{st,Eff}}{\left|d\chi_{st,Eff}/dt\right|} \tag{III-17}$$

The effective flame stretch, $\chi_{st,Eff}$, can be calculated based on the following formula:

$$\chi_{st,Eff}(t) = \frac{C_\varepsilon \times \exp\left(2\int_0^t \frac{\chi_{st}(t)}{C_\varepsilon} dt\right)}{\frac{C_\varepsilon}{\chi_{st}(0)} + 2\int_0^t exp\left(2\int_0^{t'} \frac{\chi_{st}(t'')}{C_\varepsilon} dt''\right) dt'} \quad \text{(III-18)}$$

where the instantaneous flame stretch $\chi_{st}(t) = C_\varepsilon \times \varepsilon(t)$ with $\varepsilon(t)$ is the strain rate and $C_\varepsilon$ is a constant model and can be written as:

$$C_\varepsilon = \frac{exp(-2[erf^{-1}(1-2Z_{st})]^2)}{\pi} \quad \text{(III-19)}$$

where $erf^{-1}$ is the reversal error function. In the typical conditions (far from ignition/extinction), we have:

$$\tau_{chemistry} < \tau_{reaction\ zone} < \tau_{diffusion\ zone} \quad \text{(III-20)}$$

Figure 17 (a) gives a comparison of the stoichiometric scalar dissipation rate over time $\chi_{st}(t)$ for different mathematical formulas and the $\chi_{st}$ variations of UMD three-dimensional turbulent line burner (we call it ***the UMD LBN case***). The chosen flame stretch $\chi_{st}(t)$ in this study has a mathematical formula: $\chi_{st}(t) = 25\exp(-40t)$, which is shaped like the most the UMD LBN case. $\chi_{st,Eff}(t)$ is then calculated through the equation (III-18) and compared with the $\chi_{st}(t)$, the result is plotted in Figure 17 (b), where we can see that the lag in $\chi_{st,Eff}(t)$ gets bigger and bigger over time when compared to $\chi_{st}(t)$.

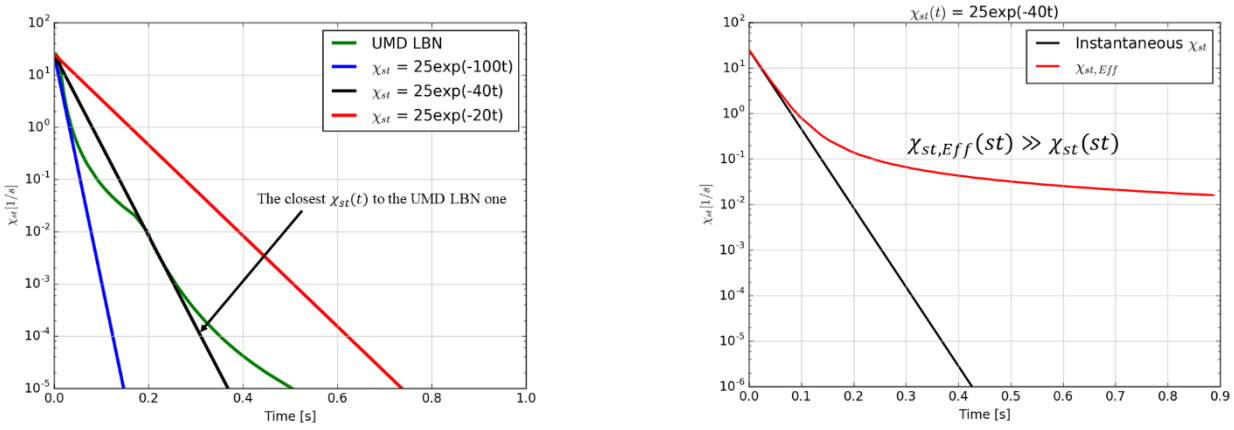


(a) (b)

*Figure 17: (a) Comparison of the stoichiometric scalar dissipation rate over time $\chi_{st}(t)$ for the mathematical formulas and the UMD LBN case; (b) Comparison between the*

*effective and instantaneous scalar dissipation rate for the chosen mathematical formula:*

$$\chi_{st}(t) = 25exp\,(-40t).$$

In the current study, the flame methane-air is considered, so $Z_{st} = 0.055$:

- $C_\varepsilon$ is calculated through the formula (III-19), then $C_\varepsilon \approx 0.0248$.

  •The right plots of Figure 18 and Figure 19 demonstrate radiation time scale tests since $C_{d,2}$ in the formula (III-15) is estimated thanks to these tests, that first identify a time needed for the evolution of an unsteady non-adiabatic flamelet simulation from the adiabatic upper branch to reach the non-adiabatic upper branch of the S-shape curve at a given values of $\chi_{st}$. The process is repeated for different values of $\chi_{st}$. Then, $C_{d,2}$ is estimated by divisions of the time for $\chi_{st}$. Finally, we have $C_{d,2} \approx 0.046$.
- Similar to the identification of $C_{d,2}$, $C_r$ in the formula (III-16) is estimated thanks to flamelet time scale tests, which are presented in the left plots in Figure 18 and Figure 19. The tests are performed for different values of $\chi_{st}$ from the middle branch to the upper branch of the S-shape curve and we have $C_r = 2$.

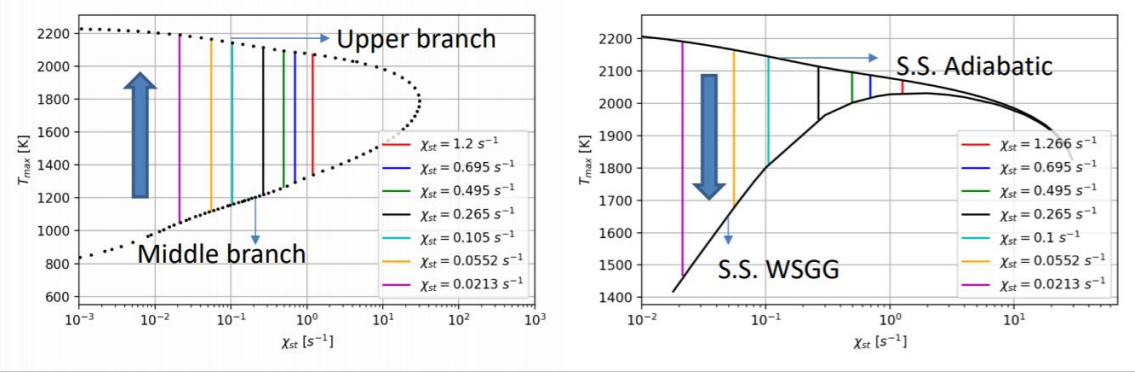


*Figure 18: Flamelet time scale tests (left plot): Ignition process from the middle branch to the upper branch for different values of $\chi_{st}$ in the left plot; Radiation time scale tests (right plot): evolutions at a constant value of $\chi_{st}$ with the WSGG radiation model from the steady state adiabatic upper branch to the steady state upper branch with WSGG.*

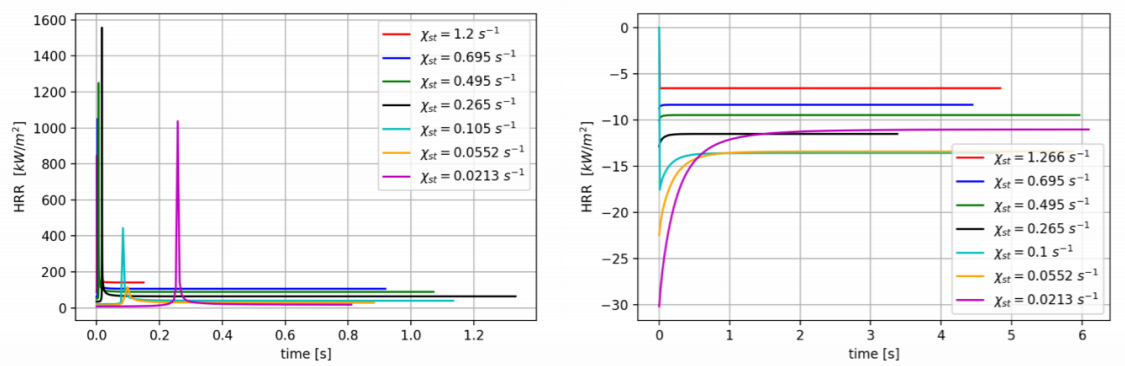


*Figure 19: Flamelet time scale tests (left plot): Time calculated for the integrated heat release rate across the flamelet to reach the middle branch from upper branch; Radiation time scale tests (right plot): time calculated for the integrated HRR in evolutions at a constant value of $\chi_{st}$ with the WSGG radiation model from the steady state adiabatic upper branch to reach the steady state upper branch with WSGG*

Figure 20 presents a comparison between the time characteristics for the case $\chi_{st}(t) = 25exp\ (-40t)$ in log-log plot. The time scale analysis results show that with $\chi_{st,Eff} < 1\ s^{-1}$, the transient flamelets are in the semi-unsteady regime [65], *i.e.*, the condition below is satisfied:

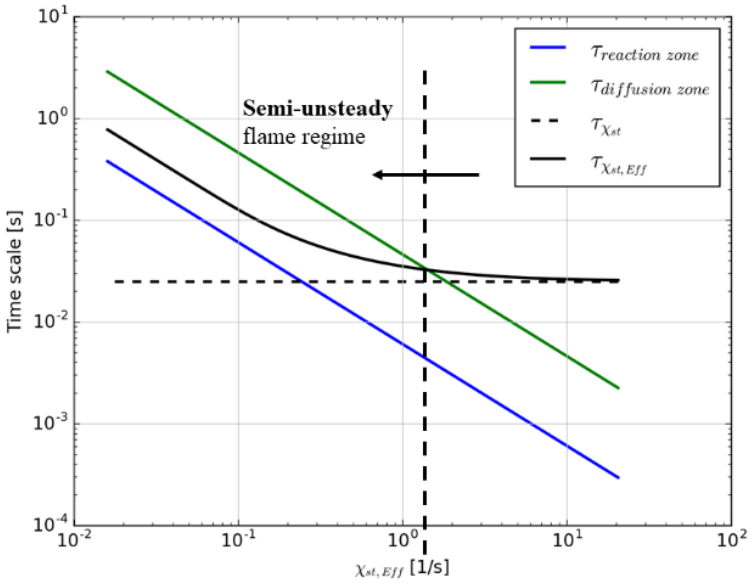


*Figure 20: Comparison between the time characteristics for the case* $\chi_{st}(t) = 25exp\ (-40t)$ *in log-log plot*

$$\tau_{chemistry} < \tau_{reaction\ zone} < \tau_{\chi_{st,Eff}} < \tau_{diffusion\ zone} \quad \text{(III-21)}$$

Figure 21 gives a comparison of the temperature, heat release rate, radiative cooling rate between the unsteady/grey calculated using $\chi_{\mathrm{st,Eff}}(\mathrm{t})$ and the steady/grey case in the place, in which the fire community is interested (the region with low values of flame stretch $\chi_{st,Eff}$). The region of interest stays in the semi-unsteady regime, *i.e.*, the reaction zone of the flamelets adapts almost instantaneously to the convective-diffusive transport or there will be no difference between unsteady and steady solutions in that region [65]. However, our results show some discrepancy when compared with the theory of the semi-unsteady regime by Cuenot *et al.* [65] since there are still slight differences between the unsteady/grey and steady/grey results. Specifically, compared to the steady/grey case, the temperature is still slightly higher and the extinction occurs at smaller value of $\chi_{st}$ in the unsteady/grey case (see Figure 21 (b)). Meanwhile, the heat release rate between two cases does not show any difference in value at high values of flame stretch, but does when the extinction occurs (see Figure 21 (c)). Finally, the radiative cooling rate result (see Figure 21 (d)) is quite consistent with the temperature when there is a slight difference between two cases in value as well as the conditions where the extinction occurs. The discrepancy between our results and the theory

by Cuenot *et al.* can be explained by the radiation heat losses, which is accounted in our study, while not considered in the study be Cuenot *et al.* [65].

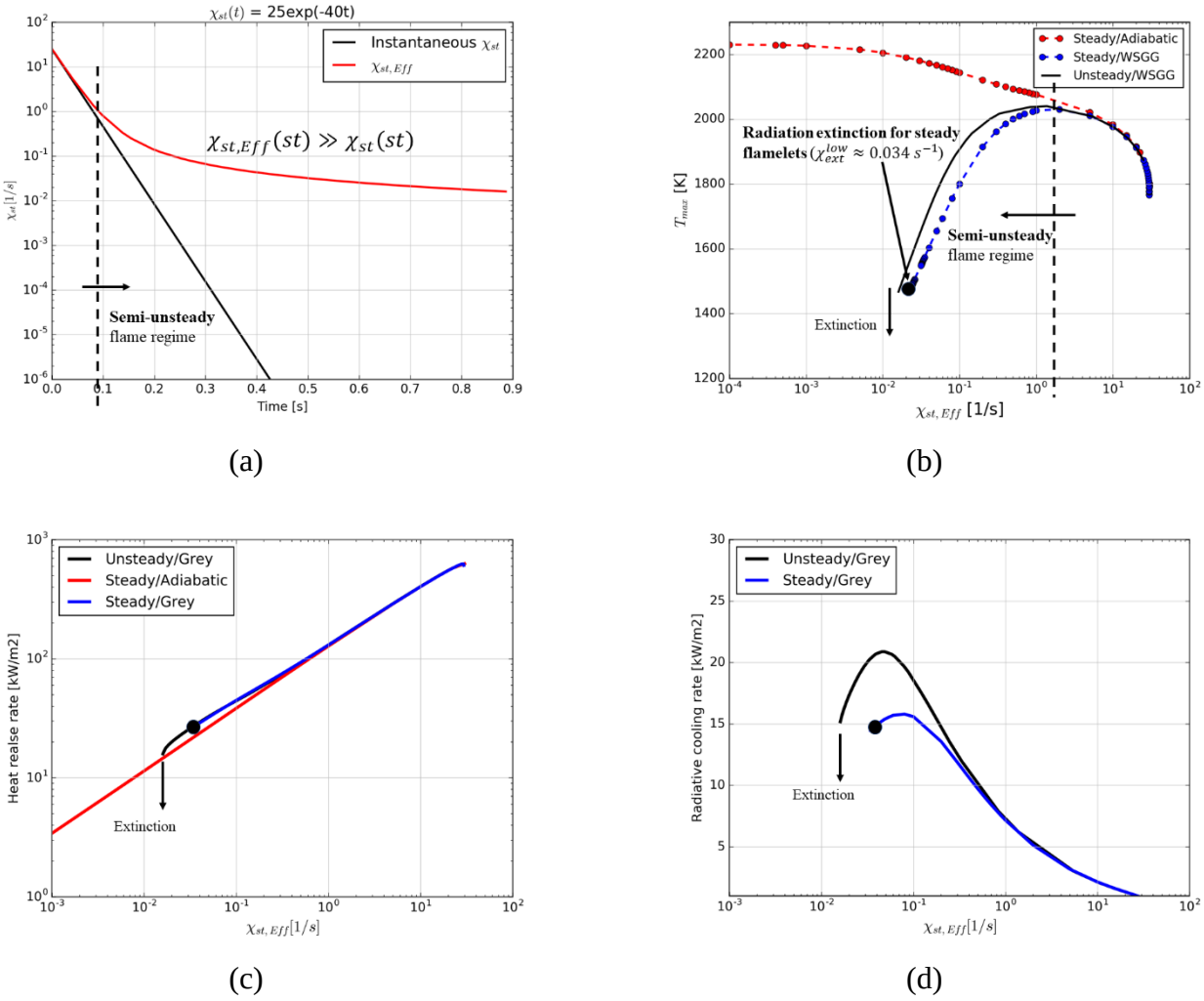


*Figure 21: Comparison of the temperature (b), heat release rate (c), radiative cooling rate (d) between the unsteady/grey calculated using $\chi_{st,Eff}(t)$ and the steady/grey case.*

## III.5 Conclusion

This chapter provides preliminary studies on the laminar, planar, strained counterflow diffusion flame, which is considered as flamelet in the flamelet combustion model. The flamelet combustion model will be described in detail in the next chapter. The basic concepts, notations and governing equations in both physical space and mixture fraction space, which are important to understand how such flows are solved for in combustion codes, are introduced.

The chapter investigates also the sensitivity of the laminar flamelet solutions to modeling choices in radiation model, chemical kinetic mechanism as well as stoichiometric scalar dissipation rate under the steady state assumption to select the baseline modeling choices for the subsequent simulations, and we have:

- Chemical kinetic mechanism sensitivity: we adopt C1-C3 in libOpenSMOKE since C1-C3 is the only choice. For FlameMaster, both GRI v3.0 and UCSD are very good choices. However, we decided to adopt GRI v3.0 in as the computational cost for calculations with GRI v3.0 is slightly cheaper than those calculated with UCSD.
- Radiation model sensitivity: Theoretically, SNB is the best radiation model among the models we can use, but it is computationally too expensive. In contrast, Grey and WSGG are computationally affordable and the performance between these two models is similar. Therefore, we decide to use these two models in the non-adiabatic flamelet calculations.

Finally, interesting and important physical phenomena related to unsteady effects are presented for both constant and time-dependent $\chi_{st}$ cases:

- Constant $\chi_{st}$ over time case: we study on the evolution at different constant values of $\chi_{st}$ with the grey model and find:
  - ✓ The radiation heat losses affect insignificantly the gas temperature and can be ignored at the area of high values of flame stretch, but dominate and have a great impact on the temperature, even they can extinguish the flame at small values of $\chi_{st}$.
  - ✓ The flame response time to radiation of the unsteady calculation depends strongly on the flame stretch.
- Time-dependent $\chi_{st}$ case: we study on the evolution with $\chi_{st}(t) = 25\exp(-40t)$ and the WSGG model and find:
  - ✓ The time scale analysis results show that for $\chi_{st,Eff} < 1\ s^{-1}$, *i.e.*, the region of interest for the fire community, the transient flamelets are in the semi-unsteady regime.

- ✓ In the semi-unsteady regime, our results show some discrepancies when compared with the theory by Ref. [65]. The results can be explained by the radiation heat losses, which is accounted in our study, while not considered in Ref. [65].

# Chapter IV Flamelet combustion modelling

In the present chapter, the principal background of the flamelet combustion modeling for turbulent diffusion flame is presented. First, four different methods are introduced to generate the flamelet libraries based on the basic knowledge about the flamelet provided in Chapter III. Next, the section Chemistry-turbulence interaction introduce the way to export the instantaneous thermo-chemical quantities in the laminar flamelet libraries into the turbulent flame simulations in the Large Eddy Simulation (LES) framework. The turbulent flame Look-Up Table (LUT) is formed and parametrized as a function of $(\tilde{Z}, \widetilde{Z_v}, \tilde{\mathrm{X}}, \tilde{\mathrm{H}})$. The LUT is informed by the values of $(\tilde{Z}, \widetilde{Z_v}, \tilde{\mathrm{X}}, \tilde{\mathrm{H}})$ and provides in return the LES-filtered temperature, $\tilde{T}$, and species mass fractions. The modeling details of $(\tilde{Z}, \widetilde{Z_v}, \tilde{\mathrm{X}}, \tilde{\mathrm{H}})$ are introduced in the last section.

## IV.1 Flamelet library generation methods

Four methods for producing the flamelet library are SLFV1, SLFV2, ULFV1 and ULFV2, which have different input types, parameters as well as ways to function. The laminar flamelet library, which stores thermo-chemical quantities $q^{fl}$ like temperature, mass fraction of species, etc., is generally parameterized by the mixture fraction $Z$, the scalar dissipation rate X and the heat loss parameter H and covers all range of values of these parameters, which can be possibly found in the turbulent line fire. Any thermo-chemical quantities $q^{fl}$ can be written as:

$$q^{fl} = q^{fl}(Z, \mathrm{X}, H) \tag{IV-1}$$

The laminar diffusion flame configuration considered in this chapter is the methane-air flame, which corresponds to the non-premixed turbulent line fire, where the inlet fuel is methane and the co-flow is air.

### IV.1.1 Steady approach

*a Steady Laminar Flamelet Version 1 (SLFV1)*

The flamelet library in SLFV1 is generated by solving the steady flamelet equations (III-13) and (III-14) without the radiation heat loss source term:

$$-\rho\frac{\chi}{2}\frac{\partial^2 Y_k}{\partial Z^2} = \dot{\omega}_k''' \tag{IV-2}$$

$$-\rho\frac{\chi}{2}\left(\frac{\partial^2 T}{\partial Z^2} + \frac{1}{c_p}\frac{\partial c_p}{\partial Z}\frac{\partial T}{\partial Z}\right) = -\frac{1}{c_p}\sum_{k=1}^{n} h_k \dot{\omega}_k''' \tag{IV-3}$$

Instead, the radiation heat loss is treated using the approach reported in [44][66]: enthalpy cut-off method, which removes constantly the sensible enthalpy across the flamelets to get lower temperature. If the same value of the sensible enthalpy is enforced at both the fuel and oxidizer sides, this assumption warrants then the enthalpy deficit $\Delta h$ to be uniform across the flamelet thickness, where the enthalpy defect (or enthalpy deficit) is defined as $\Delta h = (h - h_{ad})$, with $h$ is the total (chemical plus sensible) enthalpy and $h_{ad}$ the value of $h$ under adiabatic conditions, $h_{ad} = (h_O + Z(h_F - h_O))$, where $h_O$ and $h_F$ denote the total enthalpy of the oxidizer and fuel supply streams, respectively. An example of different uniform enthalpy defects $\Delta h$ across the flamelet thickness is given in Figure 22. Since the enthalpy deficit $\Delta h$ is treated as uniform across the flamelet, the flamelet solutions in SLFV1 can be parametrized in terms of three variables, $(Z, \chi_{st}, \Delta h)$:

$$q^{fl} = q^{fl}(Z, \chi_{st}, \Delta h) \tag{IV-4}$$

The flamelet solutions are computed using the solver libOpenSMOKE coupled with the detailed chemical kinetic mechanism developed for C1-C3 combustion chemistry (which has more than a hundred of species and two thousands of reactions and describes the pyrolysis, partial oxidation and combustion of hydrocarbon fuels up to 3 C atoms).

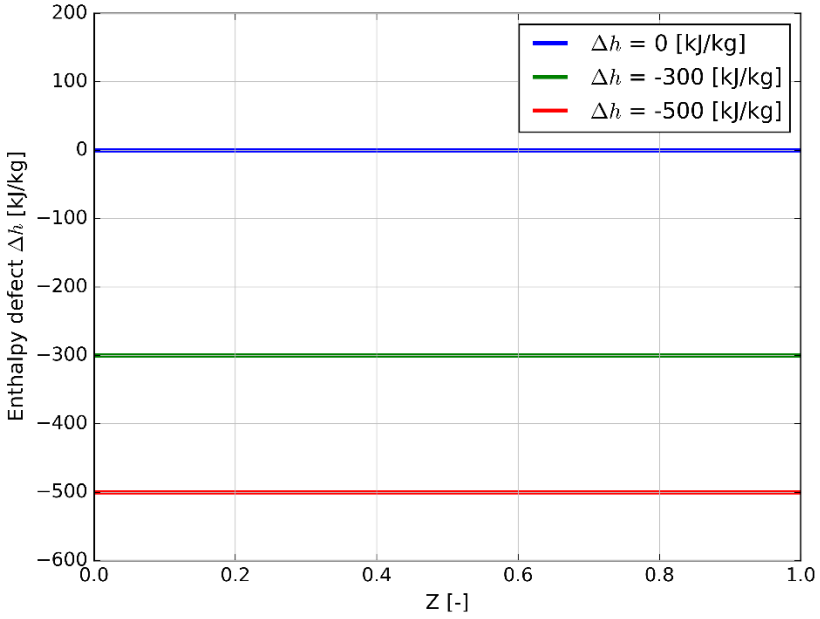


*Figure 22: Three different uniform enthalpy defects Δh across the flamelet thickness.*

Note that the assumption of a uniform distribution of the enthalpy deficit $\Delta h$ is a big approximation. An example of unrealistic temperature profiles for the methane-air flame using this assumption is given in Figure 23. The results show that this assumption leads to values of temperature near the boundaries $Z = 0$ and $Z = 1$ that are below ambient (the ambient temperature is marked by the horizontal dashed line). Figure 24 presents flamelet temperature profiles for different values of $\chi_{st}$ at specific values of $\Delta h$ calculated in libOpenSMOKE. This incorrect prediction near the boundaries is readily corrected in libOpenSMOKE by requiring that the minimum value of temperature is equal to ambient. However, the problem of the incorrect shape of the temperature profile remains (the right plot in Figure 24).

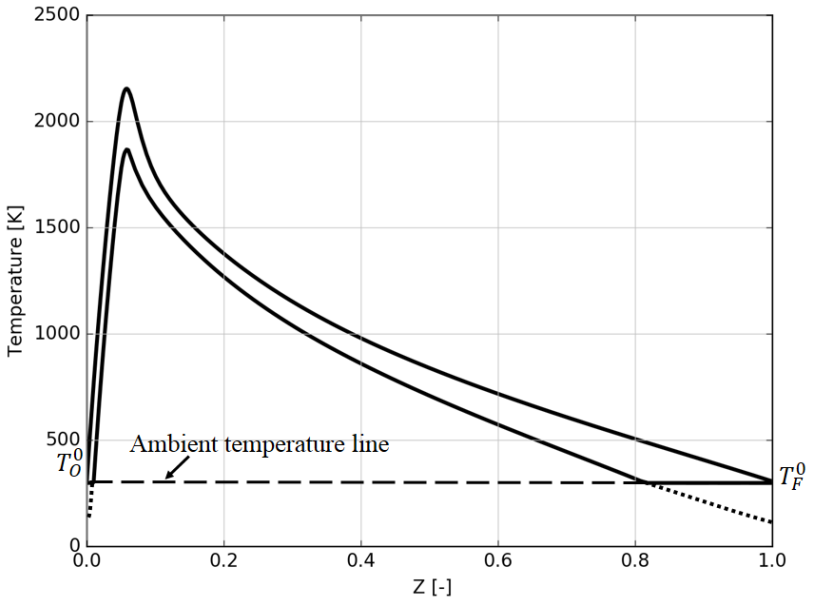


*Figure 23: Comparison of flamelet temperature profiles calculated using libOpenSMOKE for $\chi_{st} = 0.1\ s^{-1}$ and $\Delta h = 0\ kJ/kg$ (upper curve) and $\Delta h = -500\ kJ/kg$ (lower curve).*

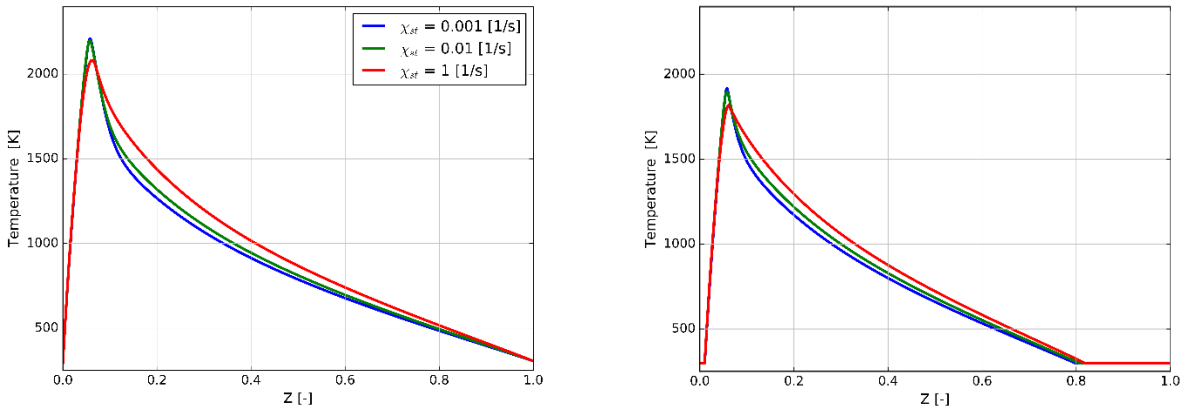


*Figure 24: Comparison of flamelet temperature profiles calculated for different values of $\chi_{st}$ at $\Delta h = 0\ kJ/kg$ (left plot) and at $\Delta h = -500\ kJ/kg$ (right plot).*

In addition, note that the assumption of a uniform distribution of the enthalpy deficit $\Delta h$ corresponds implicitly to an incomplete description of the coupling between non-local radiation phenomena (treated by the CFD solver) and local radiation phenomena (treated by

the flamelet solver). In this description, while CFD-based radiation phenomena are represented at the level of the flamelet solver by $\Delta h$, flamelet-based radiation phenomena are simply ignored at the level of the CFD solver.

In summary, a laminar flamelet library in SLFV1 for the methane-air flame is generated with as many as 10 'shelves', with enthalpy defects $\Delta h = 0, -20, -50, -100, -150, -200, -300, -500, -700, -900$ kJ/kg. Each shelf comprises entries $\chi_{st}$ ranging from near-equilibrium to near-extinction ($10^{-5}$ to 20 $s^{-1}$). Each solution has $120 - 170$ nodes in $Z$ −space. Figure 25 plots the stoichiometric temperature $T_{st}$ and $\Delta h$ over $\chi_{st}$ for all values of $\Delta h$ and the figure gives us an idea how the laminar flamelet library is organized as a function of $\Delta h$, $\chi_{st}$, $Z$.

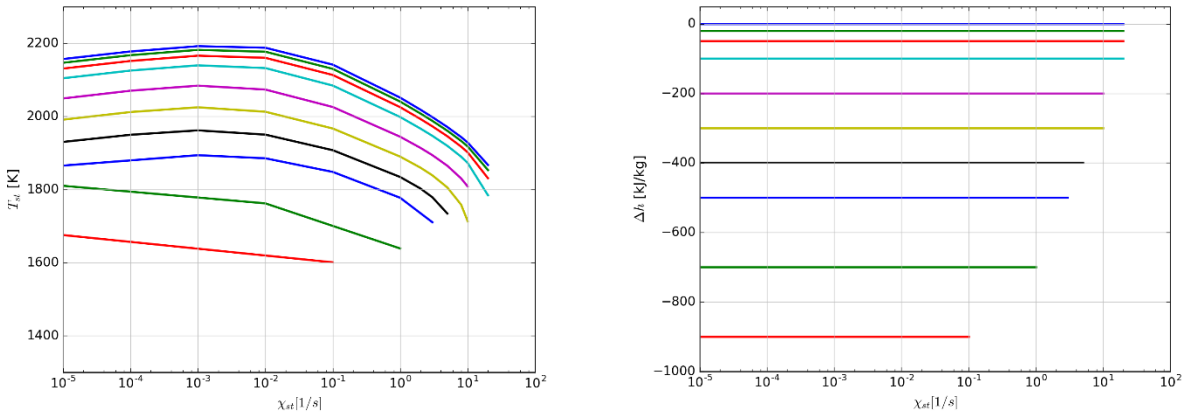


(a) (b)

*Figure 25: Stoichiometric temperature $T_{st}$ (a) and $\Delta h$ (b) over $\chi_{st}$ for all values of $\Delta h$.*

*b Steady Laminar Flamelet Version 2 (SLFV2)*

First, the SLFV1 method with a uniform enthalpy defect presented above has some limitations in the way the radiation heat loss is treated. Second, this method computes the flamelet solutions using the solver libOpenSMOKE, which is not suitable in our desire to develop new models. A new flamelet generation method called SLFV2 using Prescribed Local Radiative Fraction (PLRF) is considered here. In SLFV2, the flamelet solutions are computed using the chemical kinetic mechanism GRI v3.0 and a modified version of FlameMaster in which the steady flamelet equations (III-13), (III-14) are solved with the radiative hat loss term

$\nabla . \dot{q}'' = \chi_{rad}^{l} \times \dot{\omega}_{hs}'''$, where $\dot{\omega}_{hs}'''$ is the heat release rate (per unit volume) due to combustion and $\chi_{rad}^{l}$ is a model coefficient that is treated as uniform across the flamelet and interpreted as a prescribed local radiant fraction (PLRF). An example of the heat release rate and prescribed radiative heat loss rate across the flamelet at a given value of $\chi_{rad}^{l}$ is displayed in Figure 26.

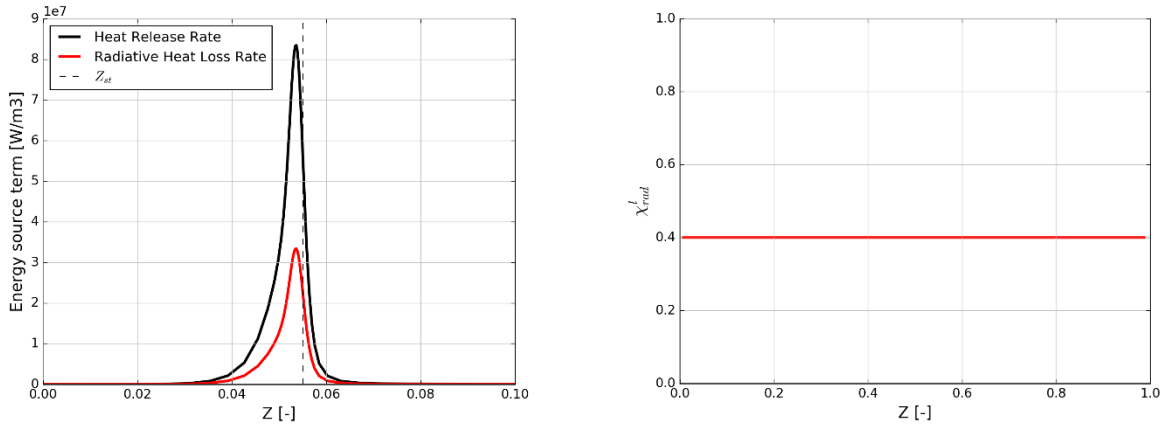


(a) (b)

*Figure 26: Heat release rate and prescribed radiative heat loss rate across the flamelet (a) at constant* $\chi_{rad}^{l} = 0.4$ *over Z (b).*

In SLFV2, similar to SLFV1, the flamelet solutions are described as a function of mixture fraction, $Z$, and flame stretch, $\chi_{st}$. The flamelet solutions are also computed for different levels of heat losses but while in SLFV1, heat losses are represented by a constant value of the enthalpy deficit $\Delta h$, in SLFV2, they are represented by different values of PLRF, $\chi_{rad}^{l}$, which correspond to different profiles of $\Delta h$. Thus, SLFV2 provides realistic temperature profiles, a well-defined profile $\Delta h(Z)$ (as seen in Figure 27) and a description of flame radiant emissions. This is achieved through a simplified semi-empirical treatment of radiation via the PLRF concept. This treatment is quite simple and the more elaborate descriptions of radiation requiring an unsteady flamelet formulation will be reported in section IV.1.2

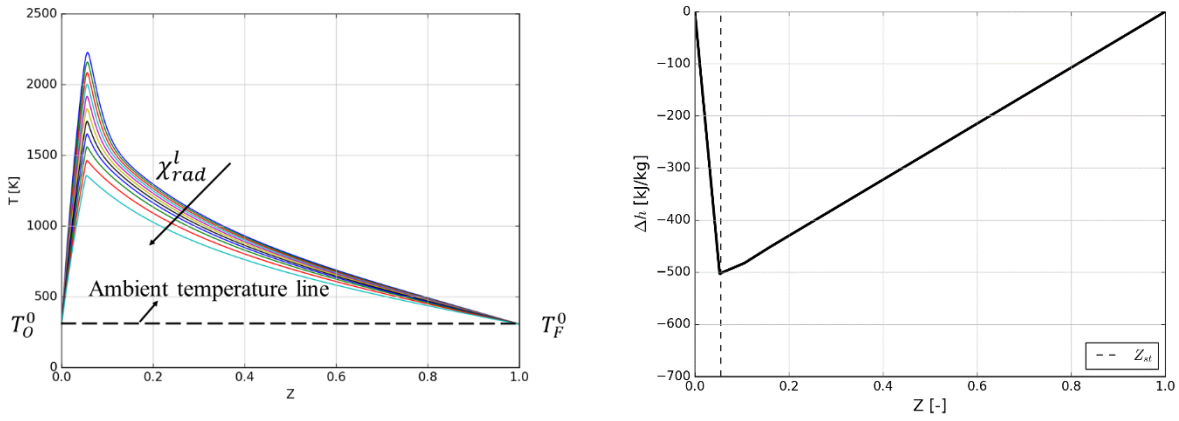


(a) (b)

*Figure 27: (a) Comparison of flamelet temperature profiles calculated using FlameMaster for $\chi_{st} = 0.001\ s^{-1}$ and for different values of $\chi^l_{rad}$ ($0 \leq \chi^l_{rad} \leq 0.5$); (b) Enthalpy deficit profile calculated in PLRF at $\chi_{st} = 0.1\ s^{-1}$ and $\chi^l_{rad} = 0.2$.*

We now turn to the problem of parametrization of the flamelet library in SLFV2. First, because each FlameMaster solution associated with given values of $\chi_{st}$ and $\chi^l_{rad}$ is also associated with a well-defined profile $\Delta h(Z)$, we choose to quantify the magnitude of heat losses in the flamelet solutions by the value taken by the enthalpy deficit at stoichiometry, $\Delta h_{st} = \Delta h(Z_{st})$ (instead of using the value of $\chi^l_{rad}$). However, Figure 28 shows that the flamelet solutions computed for a given value of $\chi^l_{rad}$ do not have a constant value of $\Delta h_{st}$ for different values of $\chi_{st}$ and that makes the flamelet library organization challenging. To overcome this issue, we use a linear interpolation method to obtain flamelet solutions at a same value of $\Delta h_{st}$ for different values of $\chi_{st}$. The solutions obtained using the method is depicted in Figure 29. Thus, any thermochemical properties of the flamelet library in SLFV2 can be written as:

$$q^{fl} = q^{fl}(Z, \chi_{st}, \Delta h_{st}) \tag{IV-5}$$

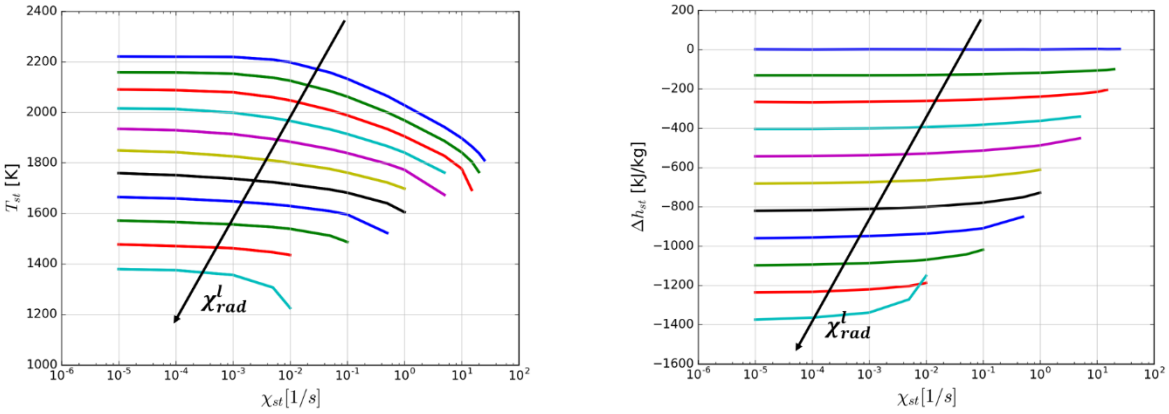


(a) (b)

*Figure 28: Comparison of the stoichiometric temperature $T_{st}$ (a) and the stoichiometric enthalpy deficit $\Delta h_{st}$ (b) calculated using PLRF for different values of $\chi_{st}$ and $\chi^l_{rad}$ ($10^{-5} \leq \chi_{st} \leq \chi_{ext}$, with $\chi_{ext}$ the fast mixing flame extinction limit; $0 \leq \chi^l_{rad} \leq 0.5$).*

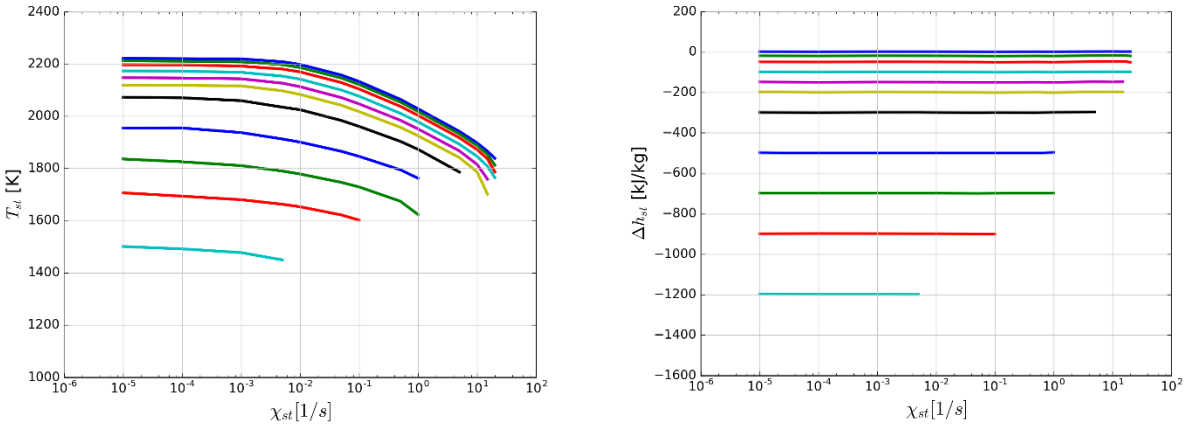


(a) (b)

*Figure 29: The stoichiometric temperature $T_{st}$ (a) and the stoichiometric enthalpy deficit $\Delta h_{st}$ (b) using the linear interpolation method over $\chi_{st}$.*

In summary, in SLFV2, the steady laminar flamelet library is parameterized by $(Z, \chi_{st}, \Delta h_{st})$. The library discretization uses 140 nodes in $Z$-space (ranging from 0 to 1), 13 nodes in $\chi_{st}$-space (ranging from $10^{-5}$ to 20 $s^{-1}$), and 11 nodes in $\Delta h_{st}$-space (ranging from (-1200) kJ/kg to 0).

### IV.1.2 Unsteady approach

Based on the previous works [64][67][68], the steady flamelet approach cannot capture well the radiation effects, the extinction/ignition phenomena, or the pollutant emissions as the unsteady treatment does. Two unsteady flamelet formulations considering radiation effects are introduced in this section: a first formulation called Unsteady Laminar Flamelet Version 1 (ULFV1) with constant $\chi_{st}$ over time and a second formulation called Unsteady Laminar Flamelet Version 2 (ULFV2) with time-dependent $\chi_{st}$. Note that the extinction/ignition phenomena will be studied in future work.

The non-adiabatic unsteady flamelet solutions can be obtained by solving the unsteady flamelet equations (III-8), (III-9) with the radiative heat loss source term $\nabla.\dot{q}''$ calculated through the grey radiation model, in which RTE can be written as:

$$\nabla I.\vec{s} = \kappa I_b - \kappa I \qquad \text{(IV-6)}$$

The absorption coefficient, $\kappa$, is calculated based on the Planck mean absorption coefficients and more details on how to calculate $\kappa$ can be found in section II.5.3. Here, RTE is solved using the discrete ordinates method with $S_8$-approximation [52]. Note that, before solving RTE, the temperature and mass fraction of $CO_2$ and $H_2O$ related to the calculation of $\kappa$ in $Z$-space are needed to transform to physical space.

*a Unsteady Laminar Flamelet Version 1 (ULFV1)*

ULFV1 is first implemented by [64] and has better predictions on the unsteady effect of radiation as well as pollutant emissions. Basically, the unsteady laminar flamelet library generation using ULFV1 includes two following steps: first, steady adiabatic flamelets are generated for different given values of $\chi_{st}$ ranging from $10^{-4}$ to 25 $s^{-1}$ (as showed in Figure 30). Second, unsteady non-adiabatic flamelets are calculated for a given $\chi_{st}$ using the steady adiabatic solution generated in the first step as an initial solution. The unsteady calculation is finished when it reaches the non-adiabatic steady state. The process is repeated for different given values of $\chi_{st}$ covering all the range (as given in Figure 31).

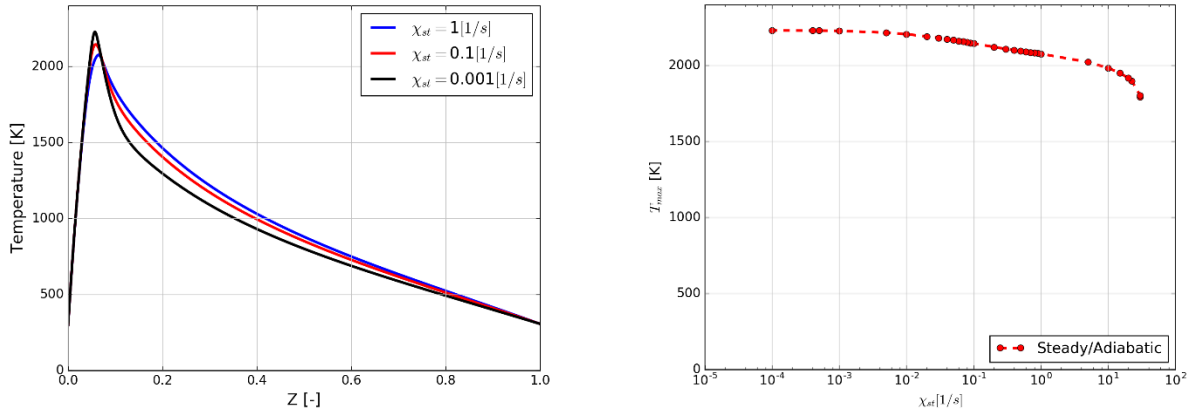


(a) (b)

*Figure 30: (a) Comparison of steady adiabatic flamelet temperature profiles for different value of $\chi_{st}$; (b) The peak temperatures for different values of $\chi_{st}$.*

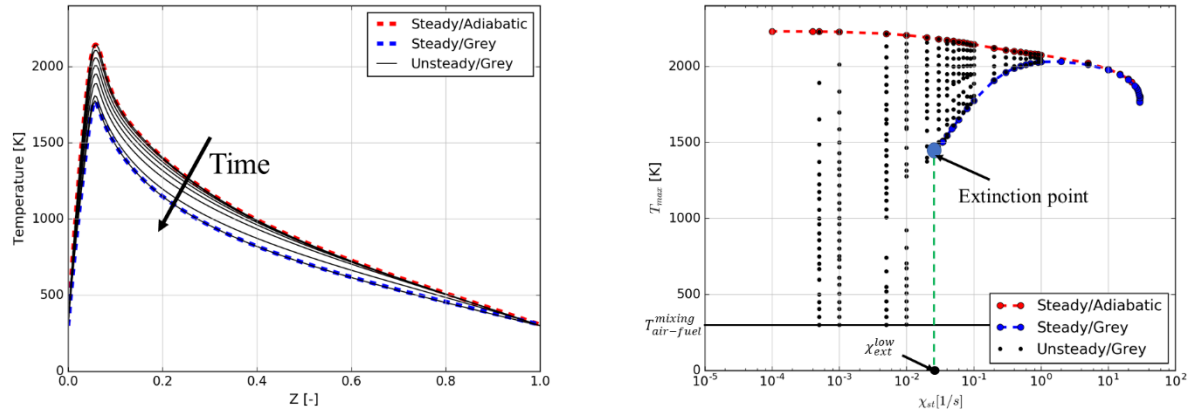


(a) (b)

*Figure 31: (a) The unsteady/grey calculation for $\chi_{st} = 0.1\ s^{-1}$ starts with the steady/adiabatic solution and reaches the steady/grey solution at the end; (b) $T_{st}$-$\chi_{st}$ plot for all unsteady/grey solutions.*

The radiation heat loss has a limited impact on the gas temperature and can be ignored at high values of flame stretch, but dominates and has a great impact on the temperature, even can extinguish the flame at the weak flame stretch area. Figure 31 (b) generated in ULFV1 confirms these points and the lower extinction limit $\chi_{ext}^{low}$ (calculated using the steady/grey condition), which indicates the extinction limit of the flame stretch $\chi_{st}$ due to radiation heat

loss, is approximately 0.034 $s^{-1}$. When we let unsteady calculations long time enough, with $\chi_{st} > \chi_{ext}^{low}$, unsteady/grey calculation will converge to the steady/grey solutions and with $\chi_{st} < \chi_{ext}^{low}$, unsteady/grey calculation will reach the extinction. In addition, when going from high to low values of flame stretch $\chi_{st}$, the flame response time to radiation of the unsteady calculation depends strongly on the flame stretch, *e.g.*, to reach steady/grey point (defined as the point where the maximum temperature no longer changes over time), the unsteady/grey at $\chi_{st} = 0.02\ \mathrm{s}^{-1}$ needs longer time than the case at $\chi_{st} = 0.2\ \mathrm{s}^{-1}$ (around 1.5 second versus 0.4 second) (as seen in Figure 32).

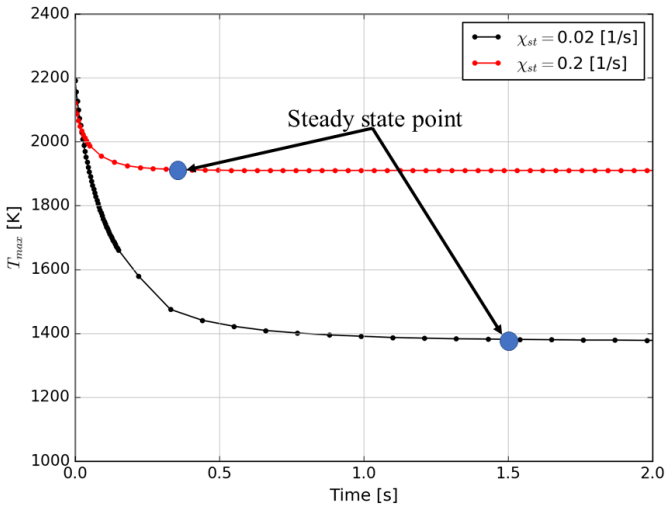


*Figure 32: Peak temperature over time for the unsteady/grey calculation at* $\chi_{st} = 0.02\ s^{-1}$ *and* $\chi_{st} = 0.2\ s^{-1}$.

Now, we focus on the library parameterization. As we know, ULFV1 takes into account radiative heat loss in the physical and natural way by introducing the source term in the energy equation, so it produces a well-defined enthalpy defect profile $\Delta h(Z)$, which is demonstrated as in Figure 33. Like SLFV2, we choose to quantify the magnitude of heat losses in the unsteady flamelet solutions by the value taken by the enthalpy deficit at stoichiometry, $\Delta h_{st} = \Delta h(Z_{st})$. Thus, any thermochemical properties in ULFV1 can be written as:

$$q^{fl} = q^{fl}(Z, \chi_{st}, \Delta h_{st}) \qquad \text{(IV-7)}$$

Since $\chi_{st}$ is constant over time, hence $\chi_{st}$ is equal to $\chi_{st,Eff}$ and we can write:

$$q^{fl} = q^{fl}(Z, \chi_{st}, \Delta h_{st}) = q^{fl}\left(Z, \chi_{st,Eff}, \Delta h_{st}\right) \quad \text{(IV-8)}$$

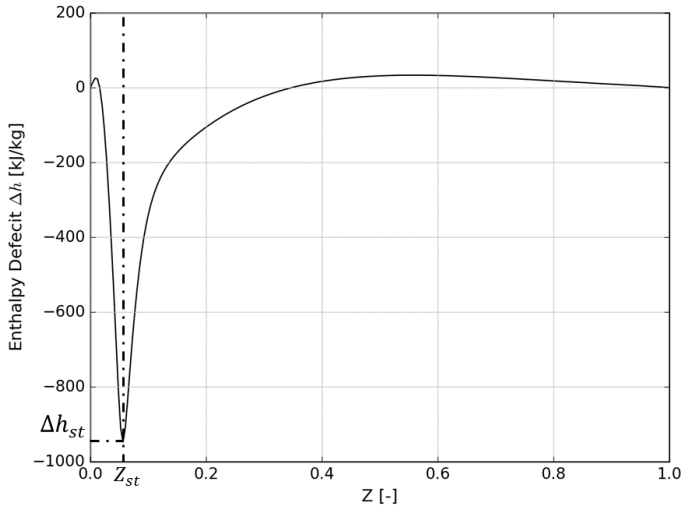


*Figure 33: A well-defined enthalpy defect profile $\Delta h(Z)$ generated using ULFV1 for $\chi_{st} = 0.0005s^{-1}$ at t = 83.33 ms.*

Basically, the good parameterization needs to ensure that at a given value of a set $(\chi_{st}, \Delta h_{st})$, then we will identify only one flamelet $q^{fl}(Z)$. In ULFV1, we detect an issue related to the parameterization step. As demonstrated in Figure 34, for $\chi_{st} < \chi_{ext}^{low}$ (where extinction occurs due to radiative heat loss), the unsteady/grey calculation starts with the steady/adiabatic solution and by the time, the temperature will gradually decrease and stoichiometric enthalpy defect $\Delta h_{st}$ will decrease due to heat loss. However, at some point (we call it *turning point* here), $\Delta h_{st}$ no longer decreases, but increases instead. The reason is that when the temperature is low, the radiative heat loss becomes weaker.Iin addition, the new fresh fuel and air are diffused into the flame region so that will make the total enthalpy higher and increase $\Delta h_{st}$. We have a non-monotonic function $\Delta h_{st}(t)$, so at a given value of $\Delta h_{st}$ we can identify two completely different flamelets that makes $\Delta h_{st}$ no longer a good parameter (see Figure 34). To overcome this issue, all unsteady/grey solutions at the increasing $\Delta h_{st}$ area (the area from the turning point (see Figure 34)), which corresponds to the extinguishing process and low temperature (smaller than 1000 K), will be completely ignored. This assumption does not affect final simulation results of the turbulent line burner with the methane-air flame (where there is no extinction), but resolves the technical difficulty instead. Finally, the unsteady

laminar flamelet library we use for simulations of the turbulent methane-air flame is plotted in Figure 35. When the extinction/re-ignition phenomena is considered, this problem should be addressed by introducing an additional flamelet library parameter typically chosen as a reaction progress variable [67].

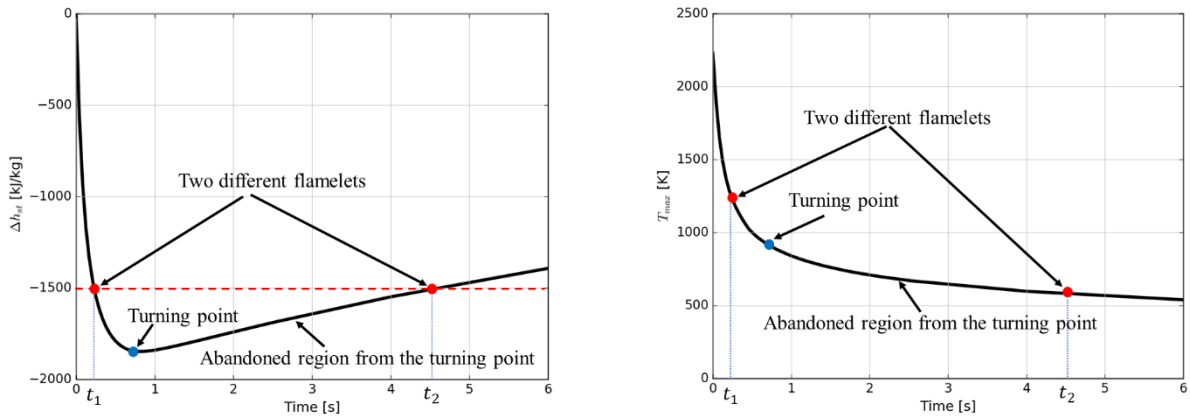


(a) (b)

*Figure 34: Stoichiometric enthalpy defect (a) and peak temperature (b) of the unsteady/grey flamelet solutions over time at* $\chi_{st} = 0.0005s^{-1}$.

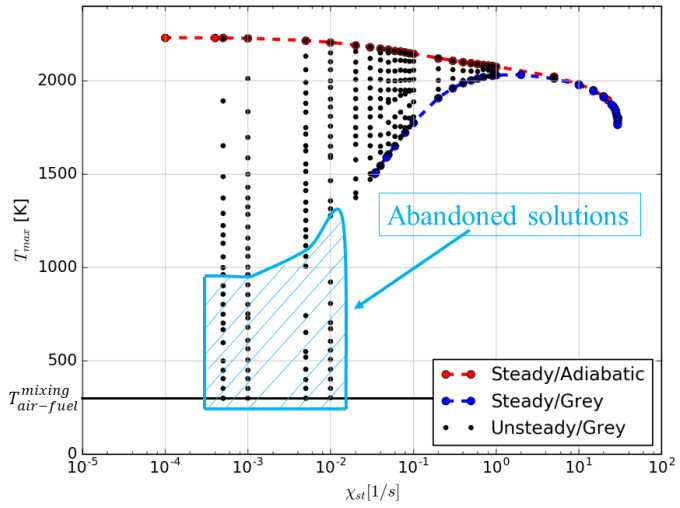


*Figure 35: Abandoned unsteady/grey area in ULFV1.*

In summary, in ULFV1, the unsteady laminar flamelet library is parameterized by $(Z, \chi_{st}, \Delta h_{st})$ (or $(Z, \chi_{st,Eff}, \Delta h_{st})$). The library discretization uses 150 nodes in $Z$-space (ranging from 0 to 1), 24 nodes in $\chi_{st}$-space (or $\chi_{st,Eff}$-space) (ranging from $5 \times 10^{-4}$ to 10 $s^{-1}$), and 14 nodes in $\Delta h_{st}$-space (ranging from (-1500) kJ/kg to 0).

*b Unsteady Laminar Flamelet Version 2 (ULFV2)*

Another unsteady method called ULFV2 is introduced here in order to generate the flamelet library in a more natural and realistic way associated with three-dimensional turbulence flame. In the turbulent line burner diffusion flame, we know that the flame stretch $\chi_{st}$ has high values near the flame base and decays with height. Based on known variables such as flow velocity and distance, we can calculate the flame stretch $\chi_{st}$ as a function of time in the turbulent flame, $\chi_{st}(t)$. Bringing the information related to $\chi_{st}(t)$ from the three-dimensional, turbulent into the one-dimensional, unsteady laminar flame is not only a practical way, but also gives us more insight of the phenomena involved. The following will be a detailed technical description of the laminar flamelet library in ULFV2.

As we know, the unsteady/grey flame calculation in section III.4.2 is a laminar flame, which emits radiation and absorbs its own energy. However, when we consider it as a flamelet in a turbulent, three-dimensional flame, we need to take into account the absorption coming from distant heat sources, *i.e.*, other flamelets. Therefore, in order to generate a flamelet library used for the turbulent flame, we prescribe radiative heat loss fraction of flamelets by introducing the radiative heat loss fraction, $F_{rad}^{l}$, into the flamelet energy equation:

$$\rho \frac{\partial T}{\partial \tau} - \rho \frac{\chi}{2}\left(\frac{\partial^2 T}{\partial Z^2} + \frac{1}{c_p}\frac{\partial c_p}{\partial Z}\frac{\partial T}{\partial Z}\right) = \dot{\omega}_T''' - F_{rad}^{l} \times \frac{\nabla . \dot{q}''}{c_p} \qquad \text{(IV-9)}$$

$F_{rad}^{l}$ covers all possible values ranging from 0 to 1. If $F_{rad}^{l}$ takes 0, it means this flamelet is completely free from radiative heat loss. While if $F_{rad}^{l}$ takes 1, it means other distant heat sources (other flamelets) are neglected. The entire flamelet library is produced computing the unsteady/grey flamelets simulations using $\chi_{st,Eff}(t)$ with $\chi_{st}(t) = 25\exp(-40t)$ (see section III.4.2) for each $F_{rad}^{l}$, which is in the range from 0 to 1 with an interval of 0.1. The result is processed, then presented in Figure 36. Each simulation lasts 900 $s^{-1}$ corresponding to reducing $\chi_{st,Eff}$ from 5 [1/s] to approximately 0.01 [1/s]. For $F_{rad}^{l} = 0$, *i.e.*, at the adiabatic conditions,

the energy is not lost, so the peak temperatures are at the highest values (Figure 36 (a) and (c)) and the stoichiometric enthalpy deficits are zero (Figure 36 (b) and (d)). In contrast, for $F_{rad}^{l} = 0$, *i.e.*, other distant heat sources (other flamelets) are neglected, so the peak temperatures are at the lowest values (Figure 36 (a) and (c)) and the stoichiometric enthalpy deficits are smallest (Figure 36 (b) and (d)).

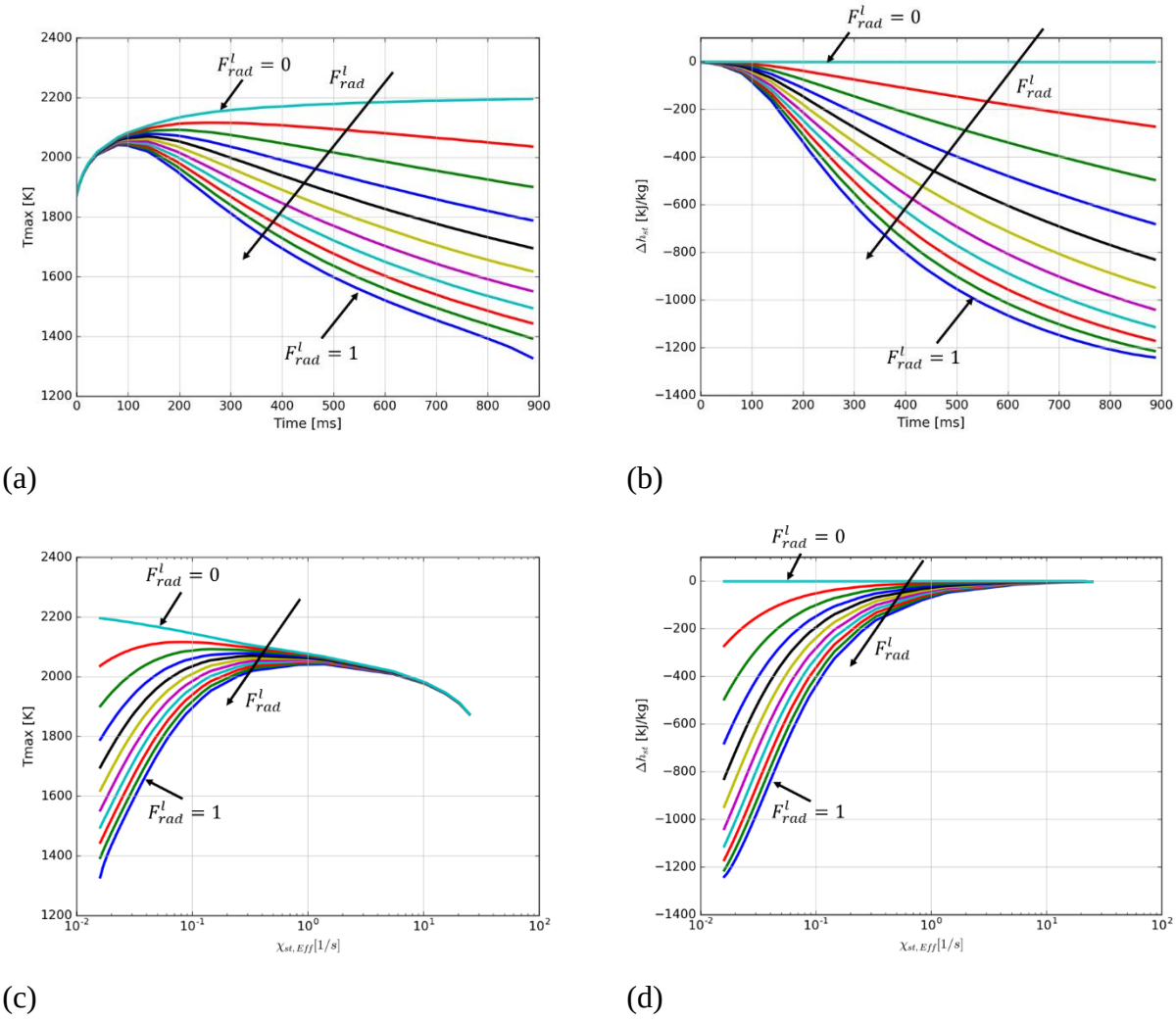


*Figure 36: Comparison of the peak temperature (a), stoichiometric enthalpy deficit (b) as a function of time and temperature (c), stoichiometric enthalpy deficit (d) as a function of* $\chi_{st,Eff}$.

Now we focus on the library parameterization. As we know, ULFV2 takes into account radiative heat loss in a physical way by introducing the source term in the energy equation, so

it produces a well-defined enthalpy defect profile $\Delta h(Z)$. Like ULFV1 and SLFV2, we choose to quantify the magnitude of heat losses in the unsteady flamelet solutions by the value taken by the enthalpy deficit at stoichiometry, $\Delta h_{st} = \Delta h(Z_{st})$(instead of using the value of $F_{rad}^{l}$). Especially, we use $\chi_{st,Eff}$ to quantify the flame stretch, instead of using $\chi_{st}$. Thus, any thermochemical properties in ULFV2 can be written as:

$$q^{fl} = q^{fl}\left(Z, \chi_{st,Eff}, \Delta h_{st}\right) \quad \text{(IV-10)}$$

In summary, in ULFV2, the unsteady laminar flamelet library is parameterized by $\left(Z, \chi_{st,Eff}, \Delta h_{st}\right)$. The library discretization uses 253 nodes in $Z$-space (ranging from 0 to 1), 26 nodes in $\chi_{st,Eff}$-space (ranging from $0.02$ to 15 $s^{-1}$), and 12 nodes in $\Delta h_{st}$-space (ranging from (-1200) kJ/kg to 0).

### IV.1.3 Summary

Four methods (SLFV1, SLFV2, ULFV1 and ULFV2) are introduced in this chapter to produce the flamelet library with:

- Uniform values of enthalpy deficit across the flame in SLFV1.
- Prescribed local radiative heat loss fraction in SLFV2.
- Evolution at different constant values of $\chi_{st}$ with full grey model in ULFV1.
- Evolution with $\chi_{\mathrm{st}}(\mathrm{t}) = 25\exp(-40t)$ and prescribed local radiative heat loss fraction used in modified grey model in ULFV2.

Each method has different inputs, parameters as well as a different way to generate the library and sometimes confuse readers. To have a broader view as well as being clear between the methods, we summarize and choose main information, which is presented in Table 2 below. However, to have a better understanding and more detailed information, readers should consult directly each method, which is specifically documented above.

| | Approach | Flamelet solver | Mechanism | Radiative treatment | Parameters | Resolution & range |
|---|---|---|---|---|---|---|
| Steady Laminar Flamelet Version 1 (SLFV1) | Steady flamelet | libOpenSMOKE | C1-C3 | Uniform values of enthalpy deficit across the flame | $Z, \chi_{st}, \Delta h$ | $Z$: 120-170 nodes & from 0 to 1<br>$\chi_{st}$: 20 nodes & from $10^{-5}$ to 20 $s^{-1}$<br>$\Delta h$: 10 nodes & from -900 to 0 kJ/kg |
| Steady Laminar Flamelet Version 2 (SLFV2) | Steady flamelet | FlameMaster | GRI 3.0 | Prescribed local radiative heat loss fraction | $Z, \chi_{st}, \Delta h_{st}$ | $Z$: 140 nodes & from 0 to 1<br>$\chi_{st}$: 14 nodes & from $10^{-5}$ to 20 $s^{-1}$<br>$\Delta h_{st}$: 11 nodes & from -1200 to 0 kJ/kg |
| Unsteady Laminar Flamelet Version 1 (ULFV1) | Unsteady flamelet | FlameMaster | GRI 3.0 | Evolution at different constant values of $\chi_{st}$ with full grey model | $Z, \chi_{st}, \Delta h_{st}$ | $Z$: 150 nodes & from 0 to 1<br>$\chi_{st}$: 24 nodes & from $5 \times 10^{-4}$ to 10 $s^{-1}$<br>$\Delta h_{st}$: 14 nodes & from -1500 to 0 kJ/kg |
| Unsteady Laminar Flamelet Version 2 (ULFV2) | Unsteady flamelet | FlameMaster | GRI 3.0 | Evolution with $\chi_{st}(t) = 25\exp(-40t)$ and prescribed local radiative heat loss fraction used in modified grey model | $Z, \chi_{st,Eff}, \Delta h_{st}$ | $Z$: 253 nodes & from 0 to 1<br>$\chi_{st,Eff}$: 26 nodes & from 0.02 to 15 $s^{-1}$<br>$\Delta h_{st}$: 12 nodes & from -1200 to 0 kJ/kg |

*Table 2: Summary for the four methods of the flamelet library generation used for turbulent flame simulations in the present study.*

## IV.2 Chemistry-turbulence interaction

Our turbulent fire numerical simulations performed in the Large Eddy Simulation (LES) framework provides LES-filtered (including Favre-filtered and Reynolds-filtered) thermo-chemical quantities, which relate to the local quantities in the laminar flamelet libraries (generated in section IV.1) through the expression following:

$$\tilde{q} = \int_{-\infty}^{+\infty} \int_{0}^{+\infty} \int_{0}^{1} q^{fl}(Z, \mathrm{X}, \mathrm{H}) \tilde{p}(Z, \mathrm{X}, \mathrm{H})\, dZ\, d\mathrm{X}\, d(\mathrm{H}) \tag{IV-11}$$

$$\bar{q} = \bar{\rho} \times \int_{-\infty}^{+\infty} \int_{0}^{+\infty} \int_{0}^{1} \left(\frac{q}{\rho}\right)^{fl} (Z, \mathrm{X}, \mathrm{H}) \tilde{p}(Z, \mathrm{X}, \mathrm{H})\, dZ\, d\mathrm{X}\, d(\mathrm{H}) \tag{IV-12}$$

where $\tilde{}$ and $\bar{}$ are the Favre-filtered and Reynolds-filtered operator respectively, $\bar{\rho}$ is the Reynold-filtered density and H represents the heat loss parameter (H is $\Delta h$ in SLFV1 and $\Delta h_{st}$ in SLFV2, ULFV1 and ULFV2). Similarly, X generally represents the scalar dissipation rate (X is $\chi_{st}$ in SLFV1, SLFV2 and $\chi_{st,Eff}$ in ULFV1, ULFV2). The joint-PDF $\tilde{p}(Z, \mathrm{X}, \mathrm{H})$ is modeled using the presumed PDF approach and its shape is assigned on empirical basis. Many numerical and experimental evidences [47][69] suggested that mixture fraction and scalar dissipation rate are statistically independent. According to the suggestions proposed by Bray and Peters [47], the joint-PDF can be split in the product of three PDF of a single variable:

$$\tilde{p}(Z, \mathrm{X}, \mathrm{H}) = \tilde{p}(Z) \times \tilde{p}(\mathrm{X}) \times \tilde{p}(\mathrm{H}) \tag{IV-13}$$

According to [47], the result of integration with respect to the mixture fraction $\tilde{p}(Z)$ is relatively insensitive to the details of the PDF shape. We introduce in this study two models for $\tilde{p}(Z)$: the $\beta$-PDF and the top-hat PDF, which both need two parameters: $\tilde{Z}$ and $\widetilde{Z_v}$ from the LES-solver and are described in detail below. The scalar dissipation rate PDF $\tilde{p}(\mathrm{X})$ and the heat loss parameter PDF $\tilde{p}(\mathrm{H})$ are assumed to be a Dirac delta function centered on the local mean value of corresponding one (as seen in Figure 37):

$$\tilde{p}(\mathrm{X}) = \delta\left(\mathrm{X} - \tilde{\mathrm{X}}\right) \tag{IV-14}$$

$$\tilde{p}(\mathrm{H}) = \delta(\mathrm{H} - \tilde{\mathrm{H}}) \tag{IV-15}$$

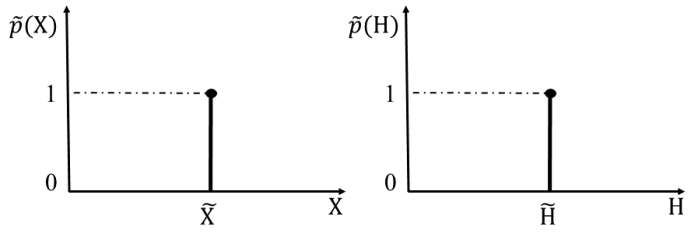


*Figure 37: Representative shapes of the Dirac delta functions, $\tilde{p}(X)$ and $\tilde{p}(H)$.*

where $\tilde{\mathrm{X}}$ and $\tilde{\mathrm{H}}$ are the LES-filtered values for the mean scalar dissipation rate ($\tilde{\mathrm{X}}$ is $\widetilde{\chi_{st}}$ in SLFV1, SLFV2 and $\widetilde{\chi_{st,Eff}}$ in ULFV1, ULFV2) and heat loss parameter ($\tilde{\mathrm{H}}$ is $\widetilde{\Delta h}$ in SLFV1 and $\widetilde{\Delta h_{st}}$ in SLFV2, ULFV1, ULFV2). Combining Eqs. (IV-11), (IV-12) and (IV-13), (IV-14), (IV-15), we can write:

$$\tilde{q} = \int_0^1 q^{fl}\left(Z, \tilde{\mathrm{X}}, \tilde{\mathrm{H}}\right)\tilde{p}(\mathrm{Z})\, dZ \tag{IV-16}$$

$$\bar{q} = \bar{\rho} \times \int_0^1 \left(\frac{q}{\rho}\right)^{fl}\left(Z, \tilde{\mathrm{X}}, \tilde{\mathrm{H}}\right)\tilde{p}(\mathrm{Z})\, dZ \tag{IV-17}$$

An efficient implementation of Eqs. (IV-16), (IV-17) consists in pre-tabulating $\tilde{q}$ and $\bar{q}$ in terms of the LES grid-scale variables, $\tilde{Z}$, $\widetilde{Z_v}$, $\tilde{\mathrm{X}}$ and $\tilde{\mathrm{H}}$. The database formed by post-processed laminar flamelet solutions that are parametrized by $(\tilde{Z}, \widetilde{Z_v}, \tilde{\mathrm{X}}, \tilde{\mathrm{H}})$ is called a turbulent flame look-up table (LUT).

### IV.2.1 $\beta$-PDF

The $\beta$-PDF is the most common approach for modeling the mixture fraction PDF. The $\beta$-PDF is a function of two parameters ($a$ and $b$) and its shape is various as showed in Figure 38. The $\beta$-PDF is described by the following expression:

$$\tilde{p}(\mathrm{Z}) = p_\beta\left(Z; \tilde{Z}, \widetilde{Z_v}\right) = \frac{Z^{a-1}(1-Z)^{b-1}}{\int_0^1 Z^{a-1}\,(1-Z)^{b-1} dZ} \tag{IV-18}$$

where $a$ and $b$ are two non-negative parameters and related to the LES-filtered mixture fraction $\tilde{Z}$ and the sub-grid scale variance of mixture fraction $\widetilde{Z_v}$ with $Z_v = (Z - \tilde{Z})^2$, which are provided by the LES-solver. Then, $a$ and $b$ are computed as follows:

$$a = \tilde{Z} \times \left( \frac{\tilde{Z}(1-\tilde{Z})}{\widetilde{Z_v}} - 1 \right) \tag{IV-19}$$

$$b = (1-\tilde{Z}) \times \left( \frac{\tilde{Z}(1-\tilde{Z})}{\widetilde{Z_v}} - 1 \right) \tag{IV-20}$$

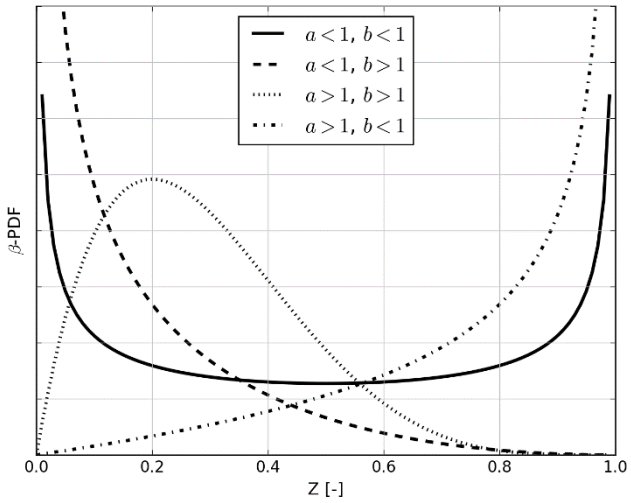


*Figure 38: Representative shapes of the β-PDF as a function of a and b.*

When using the $\beta$-PDF, difficulties found in the numerical integration of the RHS of Eqs. (IV-16), (IV-17) and associated with the possible presence of singularities at $Z = 0$ or $Z = 1$ are overcome by using the method proposed Liu *et al.* in Ref. [70]. The process of implementation Liu's suggestion is complicated, and prone to error. To check our implementation of Liu's suggestion, we realize a test as follows: we know that the temperature profile across the flamelet in Burke-Schumann solutions, which are showed in Figure 39, is given by the following formula:

$$T = \begin{cases} T_O + \left( \dfrac{T_{st} - T_O}{Z_{st}} \right) Z & if\ 0 < Z < Z_{st} \\ \dfrac{Z_{st} T_F - T_{st}}{Z_{st} - 1} + \left( \dfrac{T_{st} - T_F}{Z_{st} - 1} \right) Z & if\ Z_{st} < Z < 1 \end{cases} \tag{IV-21}$$

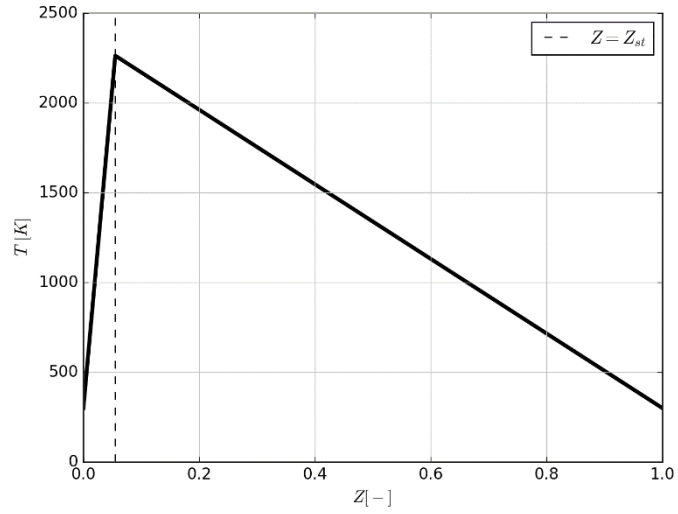


*Figure 39: Temperature profile across the burner in Burke-Schumann's solutions.*

where $Z_{st} = 0.055$, $T_{st} = 2263.3\ K$, $T_F = 306\ K$ and $T_O = 299\ K$. The integration result of Eq. (IV-16) with the instantaneous temperature in Burke-Schumann's solutions could be obtained in two different ways: through an analytical solution (see Ref. [70]) and through Liu's algorithm to implement the $\beta$-PDF integration, which can overcome the singularities issues. Figure 40 and Figure 41 present a comparison of the integration result with the $\beta$-PDF using the analytical method and the Liu's suggestion for different values of Intermittency Factor ($IF$, defined as $\widetilde{Z_v}/[\tilde{Z}(1-\tilde{Z})]$) and the results show that the mean temperature $\tilde{T}$ profiles over $\tilde{Z}$ between the analytical method and Liu's method are exactly the same. Hence, our numerical implementation of Liu's method is verified.

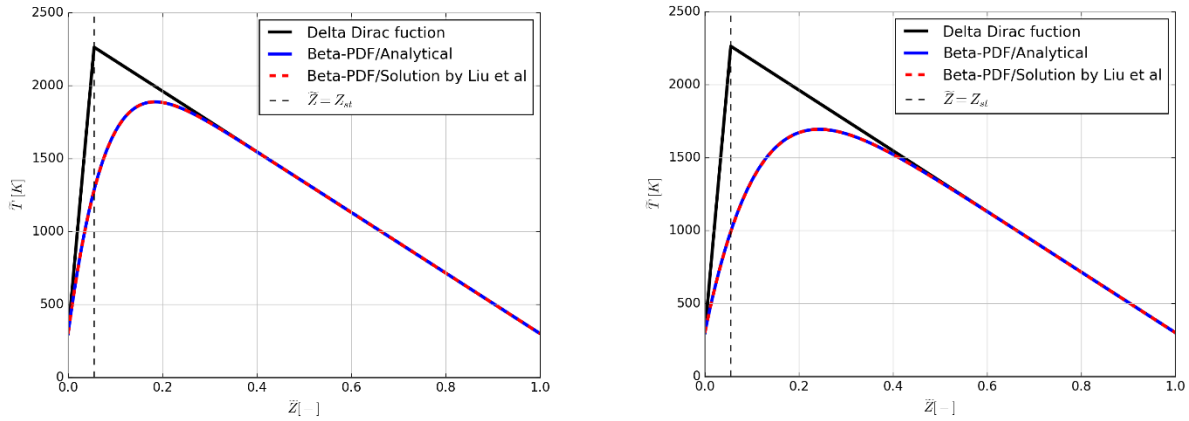


(a) (b)

*Figure 40: Comparison of the integration result with the $\beta$-PDF using the analytical method and the Liu's suggestion for IF = 0.1 (a) and IF = 0.2 (b).*

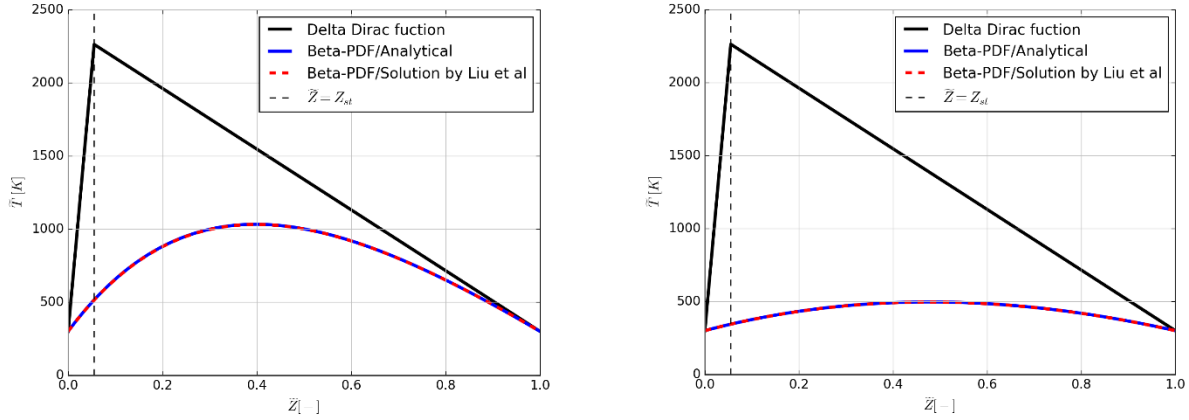


(a) (b)

*Figure 41: Comparison of the integration result with the $\beta$-PDF using the analytical method and the Liu's suggestion for IF = 0.6 (a) and IF = 0.9 (b).*

The integration of the RHS of Eq. (IV-16) for the instantaneous temperature, $T(Z)$, and the $\beta$-PDF is showed in Figure 42 with different values of $IF$. We can see that at a given value of $\tilde{Z}$ around $Z_{st} = 0.055$, the higher the value of $IF$ (or the higher value of $\widetilde{Z_v}$), the lower the LES-filtered $\tilde{T}$. The reason is because when $\widetilde{Z_v}$ is large (or $a$, $b$ are small), the $\beta$-PDF is wider and have more weight to the points near $Z = 0$ or $Z = 1$ (as showed in Figure 38), where the instantaneous temperature, $T(Z)$, stays low.

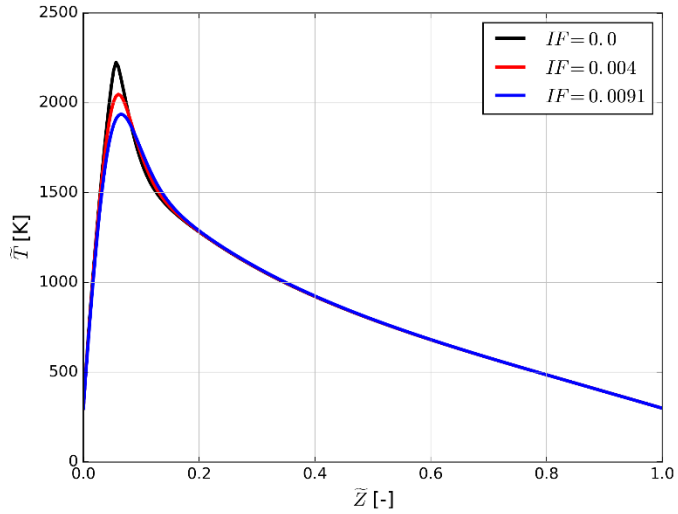


*Figure 42: Comparison of the effect of different values of IF on the LES-filtered temperature $\tilde{T}$ integrated between the instantaneous steady/adiabatic solution, $T(Z)$, at $\chi_{st} = 0.0005$ [1/s] and the $\beta$-PDF.*

### IV.2.2 Top-hat PDF

The second PDF for the mixture fraction, $\tilde{p}(\mathrm{Z})$, adopted in this study is the top-hat PDF model [71], which is a combination of a top-hat function and the Dirac peak at $Z = 0$ or $Z = 1$. The PDF can adopt five different structures that are characterized by distinct ranges of the sub-grid scale variance $\widetilde{Z_v}$ and the LES-filtered mixture fraction, $\tilde{Z}$, as shown in Figure 43:

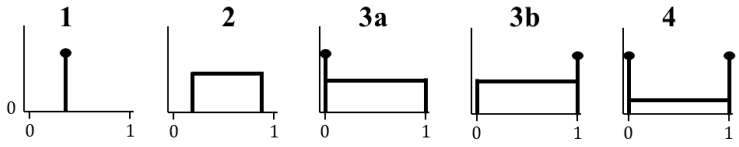


*Figure 43: Graphical representation of the top-hat PDFs for each case. **(1)**: the PDF is a Dirac Delta at $\tilde{Z}$; **(2)**: the PDF is a top hat; **(3a)**: the PDF is a top-hat with a weighted Dirac Delta at $Z = 0$; **(3b)**: the PDF is a top-hat with a weighted Dirac Delta at $Z = 1$; **(4)**: the PDF is a top-hat with a weighted Dirac Delta at $Z = 0$ and $Z = 1$.*

**(1)** For $\widetilde{Z_v} = 0$:

$$\tilde{p}(\mathrm{Z}) = \delta(Z - \tilde{Z}) \tag{IV-22}$$

**(2)** For $0 < \widetilde{Z_v} \leq 1/3 \times min[\tilde{Z}^2, (1-\tilde{Z})^2]$:

$$\tilde{p}(\mathrm{Z}) = \mathrm{T}(Z) \tag{IV-23}$$

**(3a)** For $1/3 \times \tilde{Z}^2 < \widetilde{Z_v} \leq \tilde{Z}\left(2/3 - \tilde{Z}\right)$:

$$\tilde{p}(\mathrm{Z}) = w_0\delta(Z) + \mathrm{T}(Z) \tag{IV-24}$$

**(3a)** For $1/3 \times \left(1-\tilde{Z}\right)^2 < \widetilde{Z_v} \leq (1-\tilde{Z})\left(2/3 - (1-\tilde{Z})\right)$:

$$\tilde{p}(\mathrm{Z}) = \mathrm{T}(Z) + w_1\delta(Z-1) \tag{IV-25}$$

**(4)** For $2/3 \times \tilde{Z} - \tilde{Z}^2 < \widetilde{Z_v} \leq \tilde{Z}(1-\tilde{Z})$:

$$\tilde{p}(\mathrm{Z}) = w_0\delta(Z) + \mathrm{T}(Z) + w_1\delta(Z-1) \tag{IV-26}$$

where $\mathrm{T}(Z)$ is a top-hat function; $w_0$, $w_1$ are model coefficients and can be identified as shown in Table 3.

| | $t_0$ | $w_0$ | $w_1$ | $Z_L$ | $Z_R$ | $l$ |
|---|---|---|---|---|---|---|
| **1** | | | | | | |
| **2** | $\frac{1}{l}$ | | | $\tilde{Z} - \frac{l}{2}$ | $\tilde{Z} + \frac{l}{2}$ | $\sqrt{12\widetilde{Z_v}}$ |
| **3a** | $\frac{1-w_0}{l}$ | $1 - \frac{4\tilde{Z}^2}{3(\widetilde{Z_v} + \tilde{Z}^2)}$ | | 0 | $l$ | $\frac{2\tilde{Z}}{1-w_0}$ |
| **3b** | $\frac{1-w_1}{l}$ | | $1 - \frac{4(1-\tilde{Z})^2}{3(\widetilde{Z_v} + (1-\tilde{Z})^2)}$ | $1-l$ | 1 | $\frac{2(1-\tilde{Z})}{1-w_1}$ |
| **4** | $6(\tilde{Z} - \tilde{Z}^2 - \widetilde{Z_v})$ | $1 - t_0 - w_0$ | $\widetilde{Z_v} - \frac{1}{3}t_0 + \tilde{Z}^2$ | 0 | 1 | |

*Table 3: The coefficients for the top-hat PDF series described in Section IV.2.2*

When using the top-hat PDF, unlike the $\beta$-PDF, we have no difficulty in the numerical integration of the RHS of Eqs. (IV-16), (IV-17) and the computational integration cost is also much cheaper. The integration of the RHS of Eq. (IV-16) for the instantaneous temperature, $T(Z)$, and the top-hat PDF is plotted in Figure 44 with different values of $IF$. The integration

results for the top-hat PDF is quite consistent with the results for $\beta$-PDF: the higher the value of $IF$ (or the higher the value of $\widetilde{Z_v}$), the lower the LES-filtered $\tilde{T}$. The reason is the same that when $\widetilde{Z_v}$ is large (or $a$, $b$ are small), the top-hat PDF has more weight at $Z = 0$ or $Z = 1$ (due to the Dirac delta function) (see Figure 43), where the instantaneous temperature, $T(Z)$, stays low.

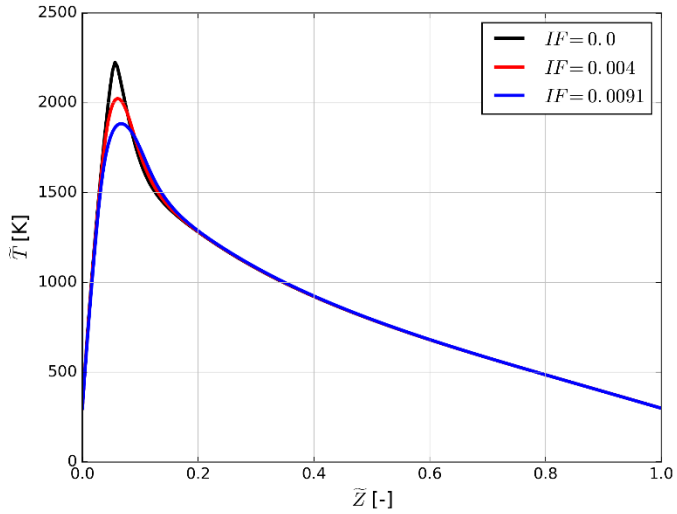


*Figure 44: Comparison of the effect of different values of IF on the LES-filtered temperature $\tilde{T}$ integrated between the instantaneous steady/adiabatic solution, $T(Z)$, at $\chi_{st} = 0.0005$ [1/s] and the top-hat PDF.*

In summary, we use two models for $\tilde{p}(Z)$ in the current study: the $\beta$-PDF and the top-hat PDF, which both need two parameters: $\tilde{Z}$ and $\widetilde{Z_v}$ coming from the LES-solver. Their shape is quite different (see Figure 38 and Figure 43). However, the integration results of the instantaneous quantities in the flamelet library with those PDFs are not too different, an example is found in Figure 45. The results in Figure 45 can confirms that it is insensitive to the choice of $\tilde{p}(Z)$ [47].

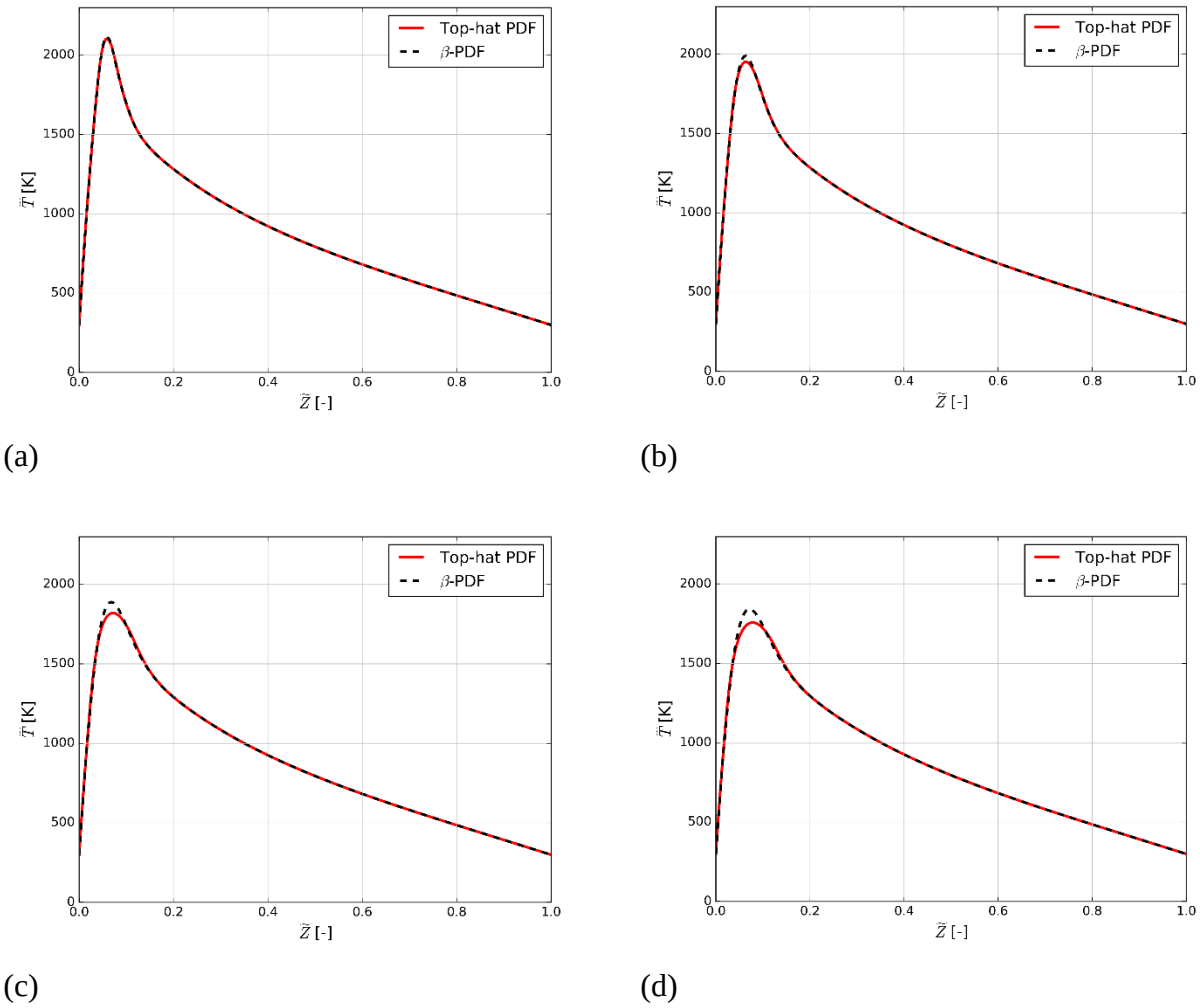


*Figure 45: The LES-filtered $\tilde{T}$ versus the LES-filtered $\tilde{Z}$, which is the result of the integration between the instantaneous steady/adiabatic $T(Z)$ at $\chi_{st} = 0.0005$ [1/s] and $\tilde{p}(Z)$ (the $\beta$-PDF and the top-hat PDF) at $IF = 0.0017$ (a); at $IF = 0.0063$ (b); at $IF = 0.0124$ (c); at $IF = 0.016$ (d).*

## IV.3 Model closures for the parameters in the LES context

As explained above, the turbulent flame look-up table (LUT) generated in section IV.2 taking into account the chemistry-turbulence interaction is parametrized by $(\tilde{Z}, \widetilde{Z_v}, \tilde{X}, \tilde{H})$, which are provided by the LES-solver. In this section, models related to each LES-filtered variable needed for the turbulent LUT are introduced in detail below.

### IV.3.1 LES-filtered mixture fraction $\widetilde{Z}$

Following a standard modeling choice, $\tilde{Z}$ is obtained in the LES solver, FireFOAM, through the solution of a convection/diffusion turbulent transport equation:

$$\frac{\partial}{\partial t}\left(\bar{\rho}\tilde{Z}\right)+\frac{\partial}{\partial x_j}\left(\bar{\rho}\tilde{u}_j\tilde{Z}\right)=\frac{\partial}{\partial x_j}\left(\bar{\rho}\left(\frac{\nu}{Pr}+\frac{\nu_{sgs}}{Pr_{sgs}}\right)\frac{\partial\tilde{Z}}{\partial x_j}\right) \tag{IV-27}$$

where $Pr$ and $Pr_{sgs}$ denote the Prandtl numbers associated with molecular mixing and sub-grid scale turbulent mixing, respectively (we use $Pr_{sgs}=0.5$).

### IV.3.2 Sub-grid scale variance of mixture fraction $\widetilde{Z_v}$

Three modeling options are proposed here for $\widetilde{Z_v}$:

- *Algebraic model 1*:

$$\widetilde{Z_v}=C_v\Delta^2\left|\nabla\tilde{Z}\right|^2 \tag{IV-28}$$

where $\Delta$ is the LES filter size and $C_v$ a model coefficient, $C_v=0.1$ [72].

- *Transport equation*:

$$\begin{aligned}\frac{\partial}{\partial t}\left(\bar{\rho}\widetilde{Z_v}\right)+\frac{\partial}{\partial x_j}\left(\bar{\rho}\tilde{u}_j\widetilde{Z_v}\right)\\ =\frac{\partial}{\partial x_j}\left(\bar{\rho}\left(\frac{\nu}{Pr}+\frac{\nu_{sgs}}{Pr_{sgs}}\right)\frac{\partial\widetilde{Z_v}}{\partial x_j}\right)+2\bar{\rho}\frac{\nu_{sgs}}{Pr_{sgs}}\left(\frac{\partial\tilde{Z}}{\partial x_j}\frac{\partial\tilde{Z}}{\partial x_j}\right)-\bar{\rho}C_Z\frac{Z_v}{\tau_{SGS}}\end{aligned} \tag{IV-29}$$

where $C_Z$ a constant model, $C_Z=2$ and $\tau_{SGS}$ is the sub-grid scale characteristic time scale, $\tau_{SGS}=k_{SGS}/\varepsilon_{\mathrm{SGS}}$. The model is initially developed by Salman Verma when, a PhD student at the Fire Protection Engineering department, University of Maryland.

- *Algebraic model 2:*

In Algebraic model 2, $\widetilde{Z_v}$ is obtained from laminar closure expressions using $(\tilde{Z},\left|\nabla\tilde{Z}\right|)$ and using a formulation that is consistent with the top-hat assumption:

- If $\left|\nabla\tilde{Z}\right| = 0$ or $\tilde{Z} = 0$ or $\tilde{Z} = 1$, then $\widetilde{Z_v} = 0$
- If $\left|\nabla\tilde{Z}\right| \leq min\left(\frac{2\tilde{Z}}{\Delta}, \frac{2(1-\tilde{Z})}{\Delta}\right)$, then $\widetilde{Z_v} = \frac{|\nabla\tilde{Z}|^2\Delta^2}{12}$
- If $\frac{2\tilde{Z}}{\Delta} < \left|\nabla\tilde{Z}\right| \leq \frac{1}{\Delta(2\tilde{Z})}$, then $\widetilde{Z_v} = \frac{2}{3}\tilde{Z}^{3/2}\sqrt{2\left|\nabla\tilde{Z}\right|\Delta - \tilde{Z}^2}$
- If $\frac{2(1-\tilde{Z})}{\Delta} < \left|\nabla\tilde{Z}\right| \leq \frac{1}{\Delta(2(1-\tilde{Z}))}$, then $\widetilde{Z_v} = \frac{2}{3}(1-\tilde{Z})^{3/2}\sqrt{2\left|\nabla\tilde{Z}\right|\Delta - (1-\tilde{Z})^2}$
- Else $\widetilde{Z_v} = 0$

### IV.3.3 Stoichiometric scalar dissipation rate $\tilde{X}$

The general stoichiometric scalar dissipation rate notation, $\tilde{X}$, indicates the instantaneous LES-filtered stoichiometric scalar dissipation rate, $\widetilde{\chi_{st}}$, (which is used for the turbulent LUT's parameterization in SLFV1, SLFV2) or the effective one, $\widetilde{\chi_{st,Eff}}$, (which is used for the turbulent LUT's parameterization in ULFV1, ULFV2). $\widetilde{\chi_{st}}$ can be obtained through an algebraic closure model [73]. Meanwhile, $\widetilde{\chi_{st,Eff}}$ is achieved through a transport equation [65][74]:

$$\widetilde{\chi_{st}} \approx \tilde{\chi} = 2\left(\frac{\nu}{Pr} + \frac{\nu_{sgs}}{Pr_{sgs}}\right)\left|\nabla\tilde{Z}\right|^2 \tag{IV-30}$$

$$\begin{aligned}\frac{\partial}{\partial t}\left(\bar{\rho}\widetilde{\chi_{st,Eff}}\right) + \frac{\partial}{\partial x_j}\left(\bar{\rho}\tilde{u}_j\widetilde{\chi_{st,Eff}}\right) \\ = \frac{\partial}{\partial x_j}\left(\bar{\rho}\left(\frac{\nu}{Pr} + \frac{\nu_{sgs}}{Pr_{sgs}}\right)\frac{\partial\widetilde{\chi_{st,Eff}}}{\partial x_j}\right) + \bar{\rho} \times \frac{2}{C_\varepsilon}\widetilde{\chi_{st,Eff}}\left(\widetilde{\chi_{st}} - \widetilde{\chi_{st,Eff}}\right)\end{aligned} \tag{IV-31}$$

where $C_\varepsilon$ is a constant model and we use $C_\varepsilon = 0.024781$.

### IV.3.4 Heat loss parameter $\tilde{H}$

As discussed above, we do not just use a single variable to parameterize heat loss in all turbulent LUTs. Specifically, we use two: $\widetilde{\Delta h}$ in SLFV1 and $\widetilde{\Delta h_{st}}$ in SLFV2, ULFV1, ULFV2. Based on the standard modeling choice, $\widetilde{\Delta h}$ or more precisely $\tilde{h}$ since $\widetilde{\Delta h} = \left(\tilde{h} - \tilde{h}_{ad}\right) = \left(\tilde{h} - [h_O + \tilde{Z}(h_F - h_O)]\right)$, is obtained through the solution of a convection/diffusion turbulent transport equation:

$$\frac{\partial}{\partial t}(\bar{\rho}\tilde{h}) + \frac{\partial}{\partial x_i}(\bar{\rho}\widetilde{u_i}\tilde{h}) = \frac{\partial}{\partial x_i}\left(\bar{\rho}(\frac{\nu}{Pr} + \frac{\nu_{sgs}}{Pr_{sgs}})\frac{\partial \tilde{h}}{\partial x_i}\right) - \overline{\nabla . \dot{q}''} \quad \text{(IV-32)}$$

where the source term ($-\overline{\nabla . \dot{q}''}$) represents the net radiative power density and is calculated from the solution of the RTE equation in section II.5. In the cases that $\Delta h_{st}$ is used for the heat loss parameterization, Eq. (IV-16) with $q^{fl}$ is $\Delta h$ becomes:

$$\widetilde{\Delta h} = \int_0^1 \Delta h^{fl}(Z, \tilde{\mathrm{X}}, \widetilde{\Delta h_{st}})\tilde{p}(\mathrm{Z})\, dZ \quad \text{(IV-33)}$$

with $\widetilde{\Delta h}$ known from Eq. (IV-32), Eq. (IV-33) can be viewed as an implicit equation for $\widetilde{\Delta h_{st}}$. This equation provides the relationship between $\Delta h_{st} = \widetilde{\Delta h_{st}}$ (since we treat $\tilde{p}(\Delta h_{st})$ as $\tilde{p}(\Delta h_{st}) = \delta(\Delta h_{st} - \widetilde{\Delta h_{st}})$) and $\widetilde{\Delta h}$.

## IV.4 Conclusion

Flamelet models introduced in this chapter differ in the choices made for the flamelet generation, the flamelet parametrization as well as the PDF formulation. Four methods (SLFV1, SLFV2, ULFV1 and ULFV2) are introduced to produce the flamelet library with uniform values of enthalpy deficit across the flame in SLFV1; prescribed local radiative heat loss fraction in SLFV2; evolution at different constant values of $\chi_{st}$ with full grey model in ULFV1 and evolution with $\chi_{\mathrm{st}}(\mathrm{t}) = 25\exp(-40t)$; and prescribed local radiative heat loss fraction used in modified grey model in ULFV2. Each method has different input types, different parameters as well as a different way to produce the flamelet library. The laminar flamelet library, which stores thermo-chemical quantities $q^{fl}$ like temperature, mass fraction of species, etc., is generally parameterized by the mixture fraction $Z$, the scalar dissipation rate X and the heat loss parameter H. The library covers all value range of these parameters, which can be possibly found in the turbulent line fire.

The coupling between non-adiabatic, non-equilibrium chemistry and turbulence is achieved by the statistical description of three parameters: the mixture fraction, the instantaneous scalar dissipation rate and the heat loss parameter. The hypothesis of statistical independence of these three parameters is made. The scalar dissipation rate PDF, $\tilde{p}(\mathrm{X})$, and the heat loss parameter PDF, $\tilde{p}(\mathrm{H})$, are assumed to be Dirac delta functions centered on the

local mean value $\tilde{X}$ and $\tilde{H}$, respectively. The mixture fraction PDF, $\tilde{p}(X)$, is assumed to be the $\beta$-PDF or the top-hat PDF and both PDFs need $\tilde{Z}$ and $\widetilde{Z_v}$ as parameters. $\tilde{q}$ and $\bar{q}$ are then pre-tabulated in terms of the LES grid-scale variables, $\tilde{Z}$, $\widetilde{Z_v}$, $\tilde{X}$ and $\tilde{H}$, and stored in the turbulent flame look-up table (LUT).

The turbulent flame LUT is informed by the values of $(\tilde{Z}, \widetilde{Z_v}, \tilde{X}, \tilde{H})$ and provides in return the LES-filtered temperature, $\tilde{T}$, and species mass fractions (in the current work, $\widetilde{Y_{CH4}}$, $\widetilde{Y_{O2}}$, $\widetilde{Y_{CO2}}$, $\widetilde{Y_{H2O}}$). Different choices are proposed for$(\tilde{Z}, \widetilde{Z_v}, \tilde{X}, \tilde{H})$ modelling and more information can be found in detail in section IV.3. The values of LES-filtered temperature and species mass fractions are linearly interpolated between stored values in the turbulent flame LUT. The LUT discretization uses 120-251 nodes in $\tilde{Z}$-space ranging from 0 to 1, 30 nodes in $\widetilde{Z_v}$-space (more precisely, the discretization in $\widetilde{Z_v}$-space is reformulated in terms of the intermittency factor, $IF = (\widetilde{Z_v}/[\tilde{Z}(1-\tilde{Z})])$, with $IF$ ranging from 0 to 1), 11-20 nodes in $\widetilde{\chi_{st}}$-space ranging from $10^{-6}$ to 20 $s^{-1}$ (or 26 nodes in $\widetilde{\chi_{st,Eff}}$-space ranging from 0.02 to 15 $s^{-1}$), and 10 nodes in $\widetilde{\Delta h}$-space ranging from (-900) kJ/kg to 0 (or 11-14 nodes in $\widetilde{\Delta h_{st}}$-space ranging from (-1500) kJ/kg to 0). Figure 46 presents a flowchart showing the entire workflow in the flamelet combustion models as implemented in FireFOAM.

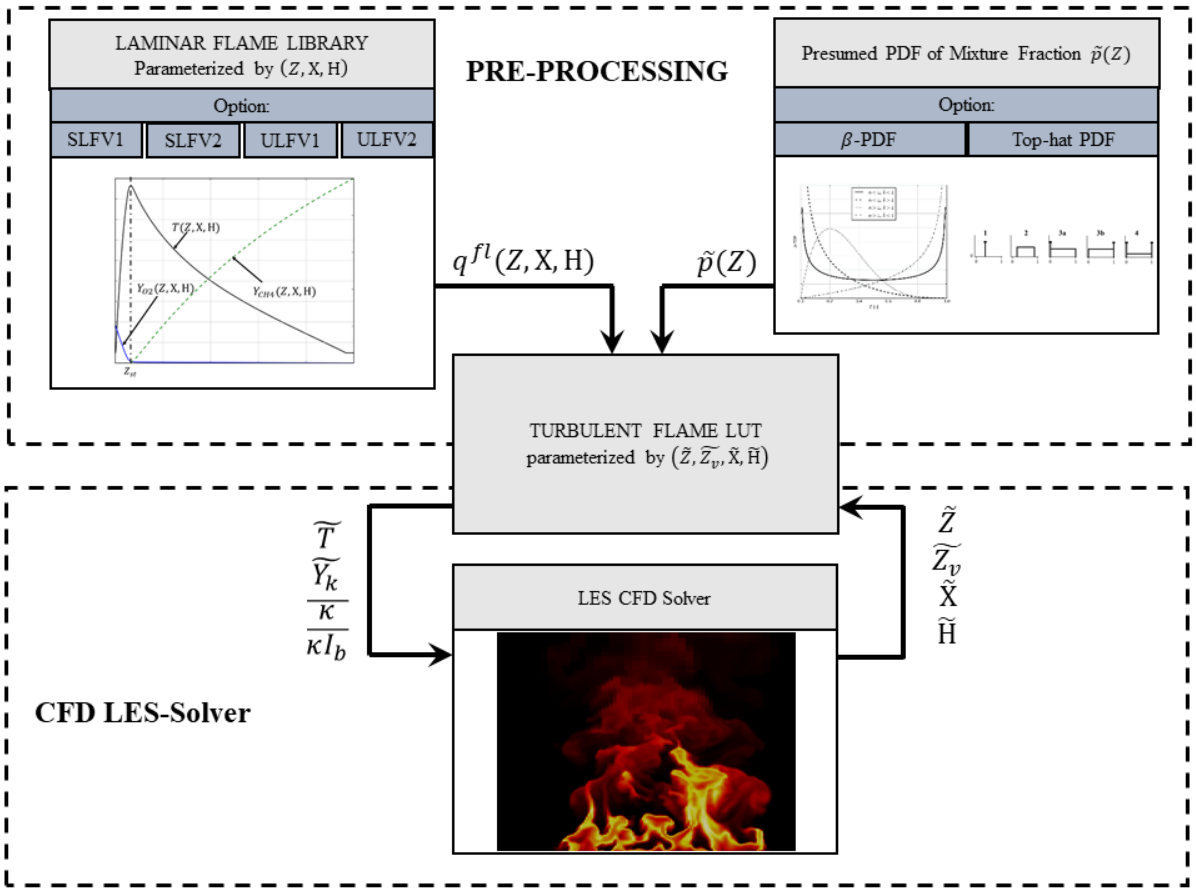


*Figure 46: Flowchart showing the workflow in the flamelet combustion models as implemented in FireFOAM.*

The flamelet model formulations described in this chapter apply to configurations without flame extinction, *i.e.*, to configurations in which the flame dynamics belong to the upper branch of the classical S-curve representing the flame response to stretch [55]. The flamelet model extension of the formulation to cases with flame extinction/ignition phenomena may require a new parameter called progress variable [67] and will be considered in future work.

# Chapter V Results: Turbulent Line Fire for the methane-air flame

The purpose of this chapter is to develop the flamelet combustion model and radiation model for large eddy simulations (LES) of well-controlled laboratory-scale turbulent fires. The development of the combustion model consists of studying:

- The different libraries of flamelet solutions produced using the different methods (SLFV1, SLFV2, ULFV1, ULFV2).
- The different models of the turbulent flame LUT parameters such as the sub-grid scale variance of mixture fraction, the scalar dissipation rate as well as the heat loss parameter.

The radiation model features a description of non-local phenomena through the Radiative Transfer Equation (RTE). Different treatments of coupled combustion and radiation effects at flamelet scale are considered:

- A treatment in which local radiation phenomena are neglected inside the flamelet solver.
- A treatment in which these phenomena are included inside the flamelet solver and also sub-grid scale turbulence-radiation interactions (TRI) are included in the RTE solver.

This modeling framework is incorporated into the LES solver FireFOAM, developed by FM Global. This chapter also presents a study on the sensitivity of the number of outer loops in the PIMPLE algorithm. It is evaluated in simulations of a two-dimensional, plane, buoyancy-driven, methane-fueled turbulent diffusion flame experimentally characterized by measurements of local temperatures and global flame emissive power. The best models and best choice of parameters are determined and going to be used in simulations in the next chapter.

## V.1 Experimental Configuration

The configuration adopted in the present study is the turbulent line burner studied at the University of Maryland [23][31][32]. The configuration corresponds to a buoyant, turbulent, methane-fueled, slot-burner diffusion flame with a controlled co-flow (see Figure 47 and Figure 48). Flames are stabilized above a 5-cm-wide and 50-cm-deep Wolfhard-Parker burner surrounded by a small horizontal plate and an oxidizer co-flow. The co-flow is 50-cm-wide and 75-cm deep. The methane mass flow rate (velocity) is 1 g/s (6 cm/s) and the theoretical heat release rate of the flame is 50 kW. In the present study, the oxidizer co-flow is made of pure air. The mass flow rate (velocity) of the air co-flow is 85 g/s (25 cm/s) or approximately five times the stoichiometric requirement of the methane flow. The flame structure is characterized through measurements of the temporal mean and root-mean-square (rms) gas temperature using 12.7-μm-diameter Type-S (Pt/10%Rh) thermocouples (response time ≈1 ms). The radiation loss from the micro-thermocouples is assumed small and is simply neglected. The flame behavior is also characterized through a measurement of the global radiative loss fraction based on a heat flux transducer located at 1-m distance from the flame combined with time-resolved infrared camera imaging and a multipoint radiation source model [23].

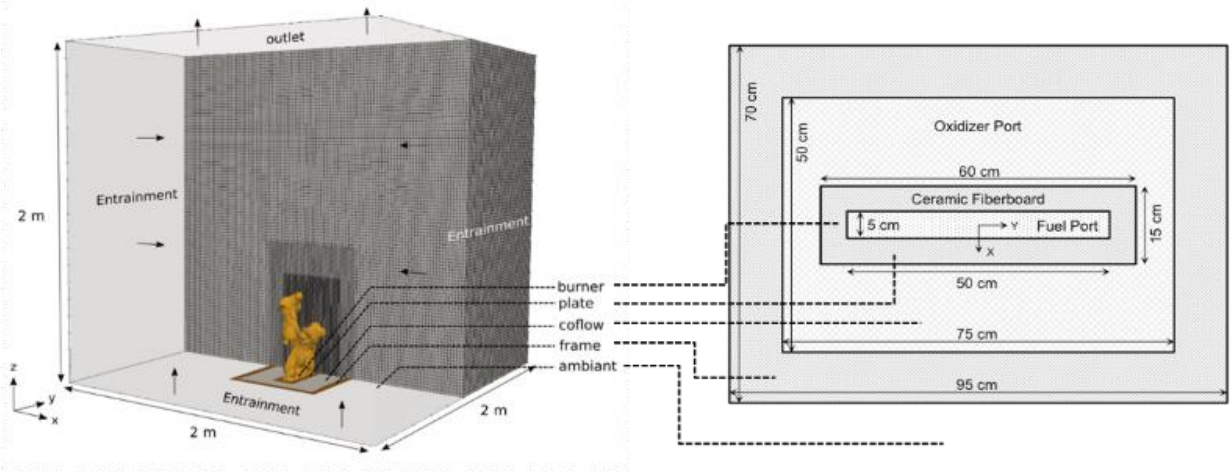


*Figure 47: Computational domain and multi-level mesh refinement. The burner (plate, co-flow) is 5 cm (15 cm, 50 cm) wide in the x-direction and 50 cm (60 cm, 75 cm) long in the y-direction; the flame height is approximately 50 cm.*

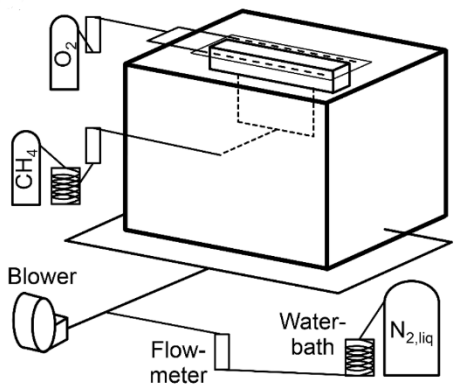


*Figure 48: Diagram of experimental facility.*

## V.2 Numerical Configurations

The computational domain used in this study is 2-m-wide in the cross-stream x-direction, 2-m-long in the spanwise y-direction and 2-m-high in the vertical z-direction. Figure 49 shows the block-structured grid with three levels of resolution. The level-one refinement block (40 × 60 × 60 $cm^3$) contains the flame region and features a uniform grid with cubic cells. The grid cell size is $\Delta x_1 = 4.167$ mm (*i.e.*, 12 grid cells across the burner width). The level-two refinement block (60 × 80 × 80 $cm^3$) features a uniform grid with cubic cells of size equal to $\Delta x_1 = 8.333$ mm. The level-three refinement block covers the far-field air entrainment and plume regions and features a uniform grid with cubic cells of size equal to $\Delta x_1 = 16.667$ mm. The total number of cells is 4.45 million. The present choice of grid resolution comes from past grid convergence tests performed in [22] for EDC/PGRF. This choice is here assumed to still be adequate for the new model variations. Although the most important region, *i.e*, the flame region, stays completely in the level-one refinement of the block-structured grid, the strong cell size gradient at the interface between the blocks still may have some impacts on results. This issue can be overcome using a new grid, which has the same computational domain size (2.0 × 2.0 × 2.0 $m^3$) as the block-structured grid. The new grid showed in Figure 50 has a refinement block (15 × 50 × 30 $cm^3$), which contains almost the flame region and features a uniform grid with cubic cells. The grid cell size is $\Delta x_1 = 5$ mm (*i.e.*, 10 grid cells across the burner width). The outside of the refinement block is stretched in the outward direction from the flame region with the expansion-ratio equal to 4%. The total number of the

new stretched grid is about 4.6 million. The computational cost for two grids is almost unchanged.

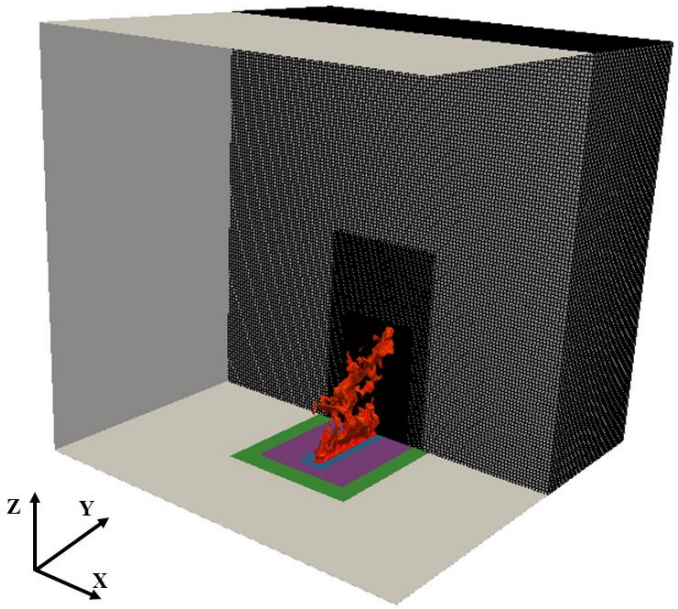


*Figure 49: Computational domain and multi-level mesh refinement.*

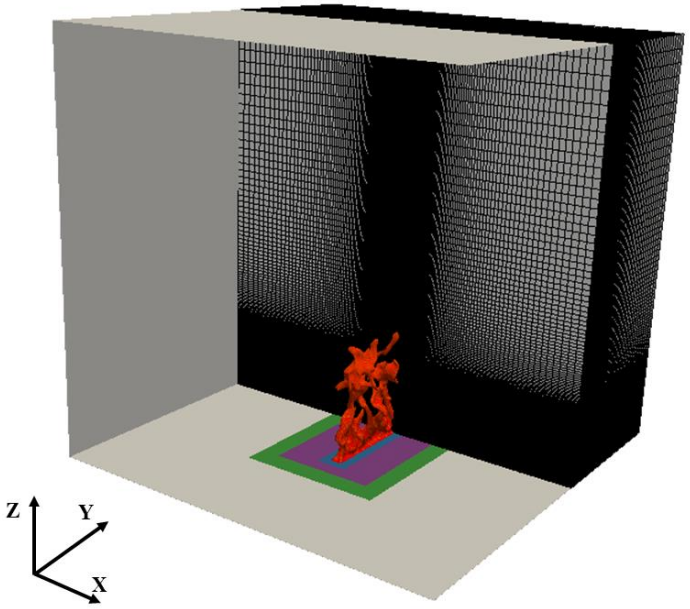


*Figure 50: Computational domain with the stretched mesh.*

The inlet surfaces for fuel and oxidizer (at z = 0) are treated as boundaries with a prescribed mass flow rate. The ceramic fiberboard plate (at z = 0) is treated as a no-slip adiabatic solid wall. The entrainment boundaries (at x = -1 and 1 m and y = 0 and 2 m) and the outlet boundary (at z = 2 m) are treated as boundaries with open flow conditions.

All FireFOAM simulations are performed for a duration of 30 s using the PIMPLE algorithm with 3 outer loops. Turbulent statistics are collected for the final 20 s of each simulation, after the flow and flame become statistically stationary and long enough for the statistics to be converged. The time step is controlled by a classical Courant-Friedrichs-Lewy (CFL) condition and is approximately equal to 0.5 ms. Each simulation is run using approximately 200 processors on a large-scale Linux cluster (made available at the University of Maryland) with the baseline model requiring 25 000 CPU-hours and simulations with the WSGG model requiring 44 000 CPU-hours.

## V.3 Results and Discussion

### V.3.1 SLFV1/Grey vs SLFV1/WSGG

We start this section by looking at the flamelet combustion model using the turbulent flame LUT produced as a result of the integration between the $\beta$-PDF for the mixture fraction and the laminar flamelet library in SLFV1, which is generated using the enthalpy cut-off method. The turbulent flame LUT is parameterized by $(\tilde{Z}, \widetilde{Z_v}, \widetilde{\chi_{st}}, \widetilde{\Delta h})$ provided by the LES-solver in which we adopt the algebraic model 1 for $\widetilde{Z_v}$. The heat loss source term appearing in the transport equation of total enthalpy $\tilde{h}$ is calculated using the grey model without TRI or the WSGG model. Simulated results using the block-structured grid are then evaluated against the baseline EDC/PRFG and the experimental data. Flamelet models differ in the choices made for the flamelet parametrization, the PDF formulation, the models for LES-filtered variables provided for the turbulent LUT, etc. Hence, we summarize choices made in our simulations in the table below. Note that only the methods, or variable, or model that has more than one option are mentioned in the table.

| Simulation name | Laminar flamelet library | $\tilde{p}(Z)$ | $\widetilde{Z_v}$ model | LES-filtered stoichiometric scalar dissipation rate | Radiation model |
|---|---|---|---|---|---|
| **SLFV1/Grey** | SLFV1 parameterized by $(Z, \chi_{st}, \Delta h)$ | $\beta$-PDF | Algebraic model 1 | $\widetilde{\chi_{st}}$ | **Grey** |
| **SLFV1/WSGG** | SLFV1 parameterized by $(Z, \chi_{st}, \Delta h)$ | $\beta$-PDF | Algebraic model 1 | $\widetilde{\chi_{st}}$ | **WSGG** |

*Table 4: Summary for the methods and modelling choices in the current simulations.*

As explained above, unlike the EDC combustion model, we do not solve the transport equation for energy and species in the flamelet combustion models to obtain temperature and species mass fraction, but calculate $(\tilde{Z}, \widetilde{Z_v}, \widetilde{\chi_{st}}, \widetilde{\Delta h})$ and provide these variable to the turbulent flame LUT to get in return the thermo-chemical quantities like $\tilde{T}$ and $\tilde{Y_k}$ ($k$ is $CH_4$, $O_2$, $CO_2$, $H_2O$ in this study), instead. An example of the simulated variables provided for the turbulent LUT and the simulated species mass fraction are presented in Figure 51 and Figure 52, respectively.

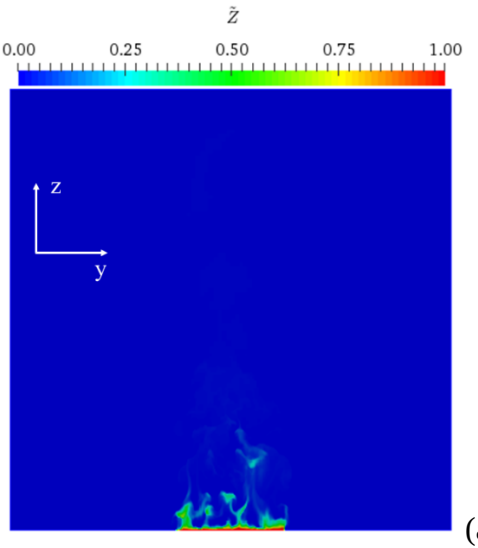


(a)

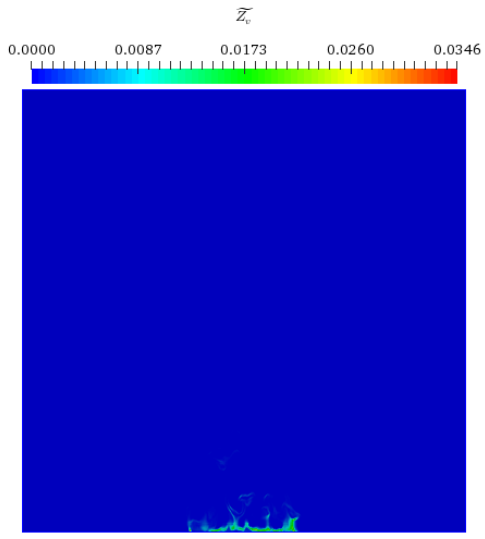


(b)

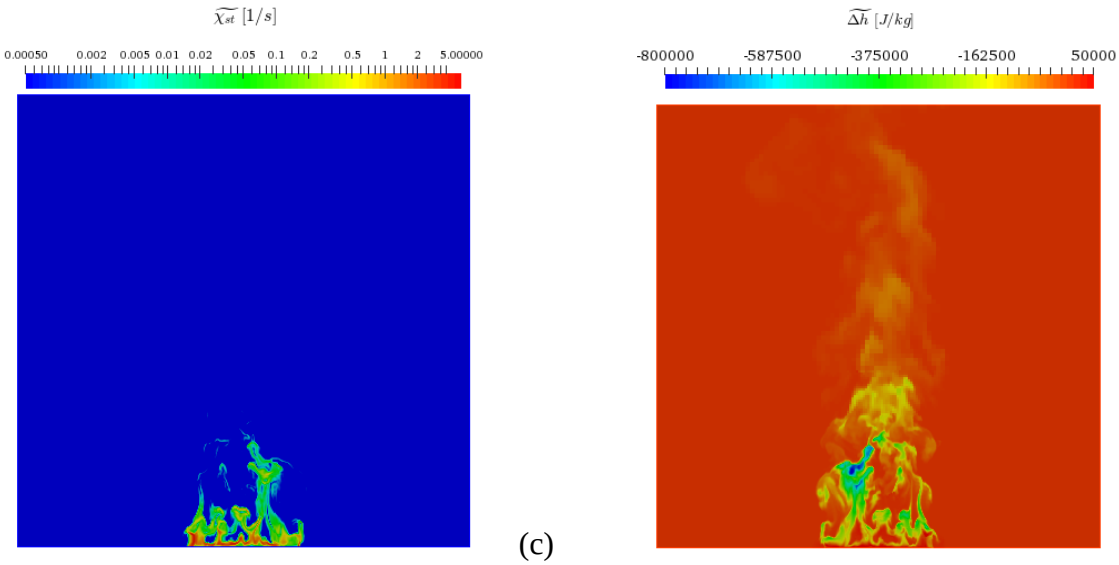


(c) (d)

*Figure 51: Front-view at the center of the burner or at $x = 0$ plane of the simulated variables provided for the turbulent LUT: (a) LES-filtered mixture fraction $\tilde{Z}$; (b) SGS variance of mixture fraction $\widetilde{Z_v}$; (c) LES-filtered stoichiometric scalar dissipation rate $\widetilde{\chi_{st}}$; (d) LES-filtered enthalpy defect $\widetilde{\Delta h}$.*

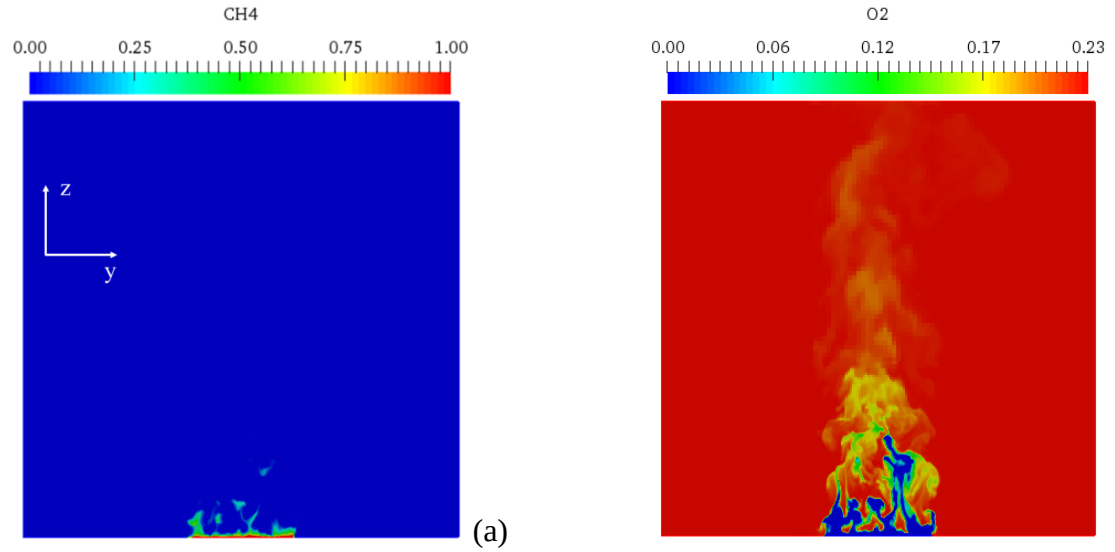


(a) (b)

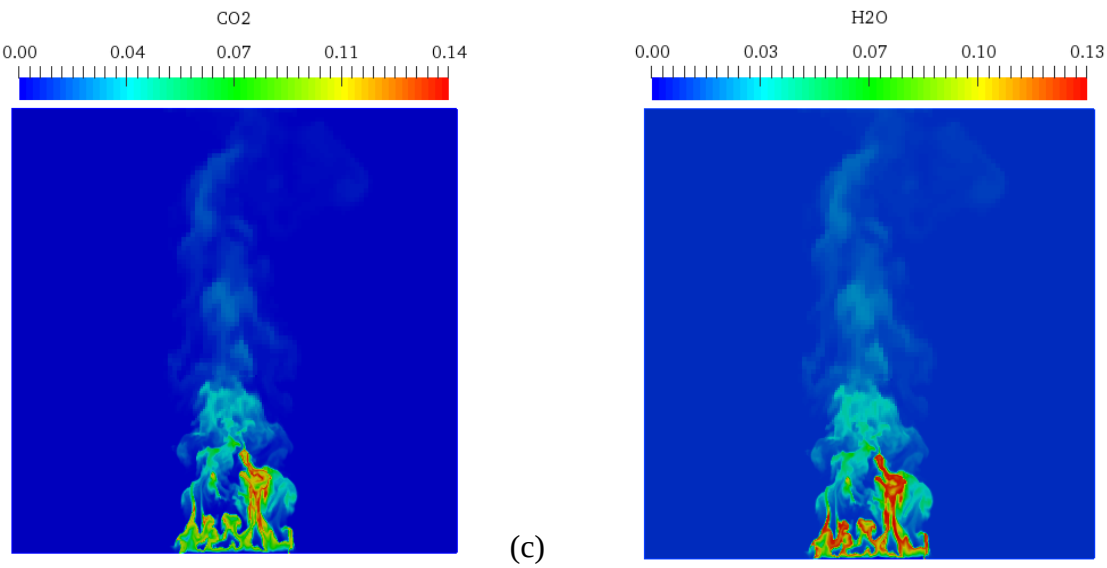


(c) (d)

*Figure 52: Front-view at the center of the burner or at $x = 0$ plane of the simulated species mass fraction: (a) $\widetilde{Y_{CH4}}$; (b) $\widetilde{Y_{O2}}$; (c) $\widetilde{Y_{CO2}}$; (d) $\widetilde{Y_{H2O}}$.*

The assumption made in the EDC and flamelet combustion model are completely different and that leads to different flame behaviors. Figure 53 shows that the flame structure in the flamelet model is much stiffer, *i.e.*, a greater gradient temperature and more fluctuations when compared with those in the EDC model. As a result, the flame brush thickness on Figure 54 (a characteristic measure of the zone where the flame may appear) in the flamelet model is a bit wider than in EDC.

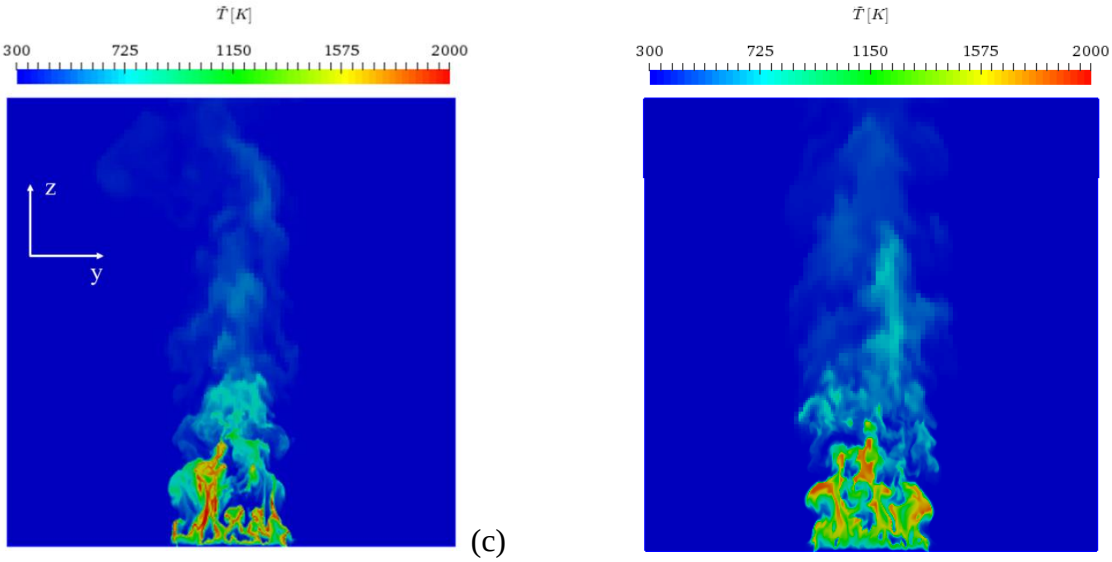


(c) (d)

*Figure 53: Front-view at the center of the burner or at $x = 0$ plane of the instantaneous LES-filtered temperature $\tilde{T}$ for the flamelet combustion model (a) and EDC (b).*

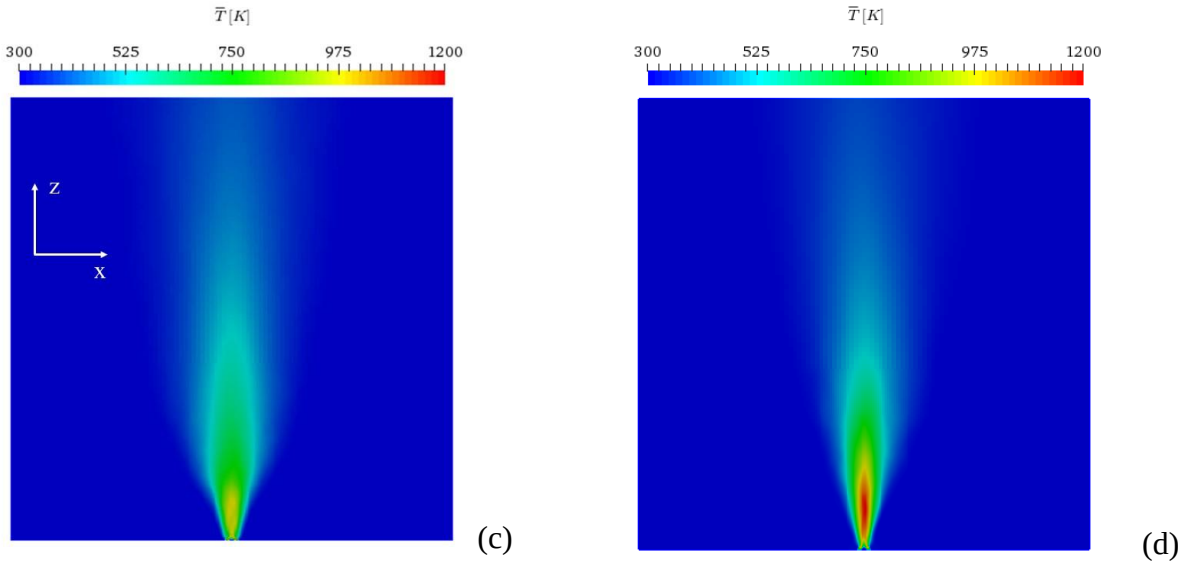


*Figure 54: Side-view at the center of the burner or at $y = 0$ plane of the flame brush thickness (or time-averaged temperature $\bar{T}$) for the flamelet combustion model (a) and EDC (b).*

The simulated flames in both flamelet and EDC models feature the familiar peak and trough structure often observed in buoyancy-driven flames. The mean flame height is equal to 0.5 m with the EDC/PGRF model and 0.4 m with SLFV1/grey and SLFV1/WSGG and. We focus below on gas temperature results and present the spatial variations of the temporal mean and *rms* values, noted $\bar{T}$ and $T_{rms}$, as a function of elevation *z* along the flame centerline at *x* = 0 m (Figure 55), and as a function of cross-stream distance *x* at a fixed elevation, $z = 0.25$ m (Figure 56) and $z = 0.5$ m (Figure 57). $\bar{T}$ and $T_{rms}$ are obtained by post-processing the LES solutions and correspond to the mean value and the amplitude of grid-resolved fluctuations (SGS contributions are assumed small and are not accounted for).

Experimental data in Figure 55 show that: $\bar{T}$ increases rapidly near the flame base, up to a peak value close to 1200 K, and then decreases at elevations larger than 0.3 m. $T_{rms}$ also increases rapidly near the flame base, up to values close to 400 K, and then decreases at elevations larger than 0.5 m. In comparison, numerical results in Figure 55 show that:

EDC/PGRF correctly captures the shape of the *z*-variations of $\bar{T}$ but slightly under-estimates the peak value of $\bar{T}$ (by approximately 100 K); and EDC/PGRF correctly captures the shape of the *z*-variations of $T_{rms}$ in the plume region but does not reproduce these variations in the flame region and over-estimates the peak values of $T_{rms}$ (by approximately 100 K). Furthermore, both SLFV1/grey and SLFV1/WSGG do not correctly capture the shape of the *z*-variations of $\bar{T}$ and $T_{rms}$ and significantly under-estimate (over-estimate) peak values of $\bar{T}$ ($T_{rms}$) by approximately 200 K (by more than 100 K).

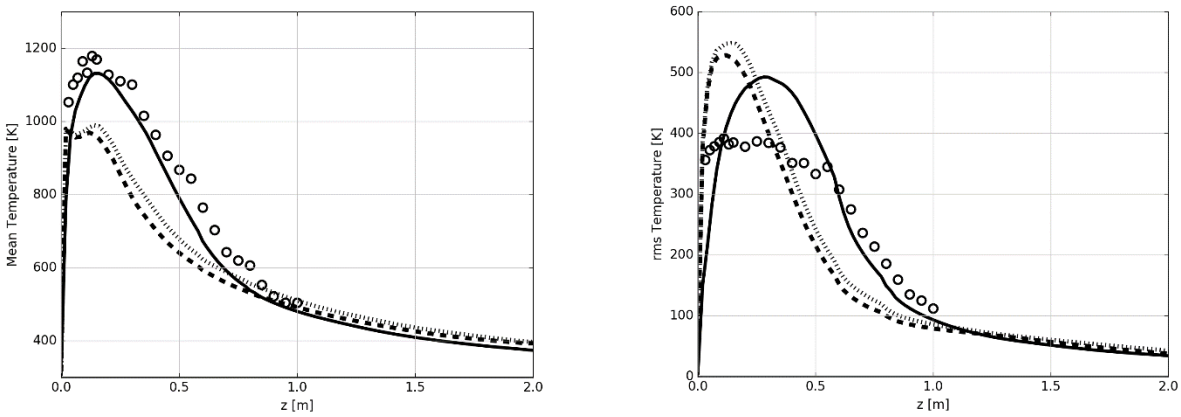


(a) (b)

*Figure 55: LES simulations of the turbulent line burner. Vertical variations of: (a) the mean temperature $\bar{T}$; and (b) the rms temperature $T_{rms}$ along the flame centerline. Comparison between experimental data (symbols) and LES results obtained with EDC/PGRF (solid line), SLFV1/grey (dashed line), SLFV1/WSGG (dotted line).*

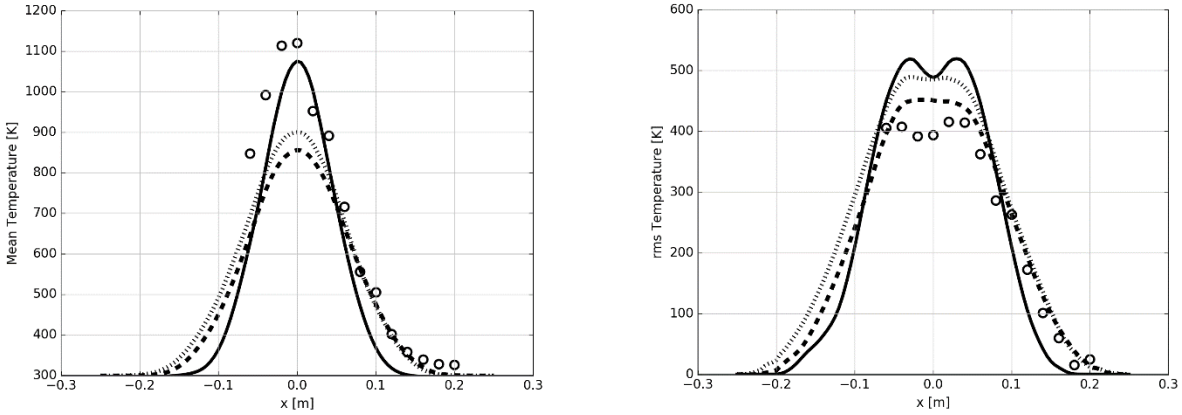


(a) (b)

*Figure 56: Cross-stream variations of: (a) the mean temperature $\bar{T}$ and (b) the rms temperature $T_{rms}$ at $z = 0.25$ m. See caption of Figure 55.*

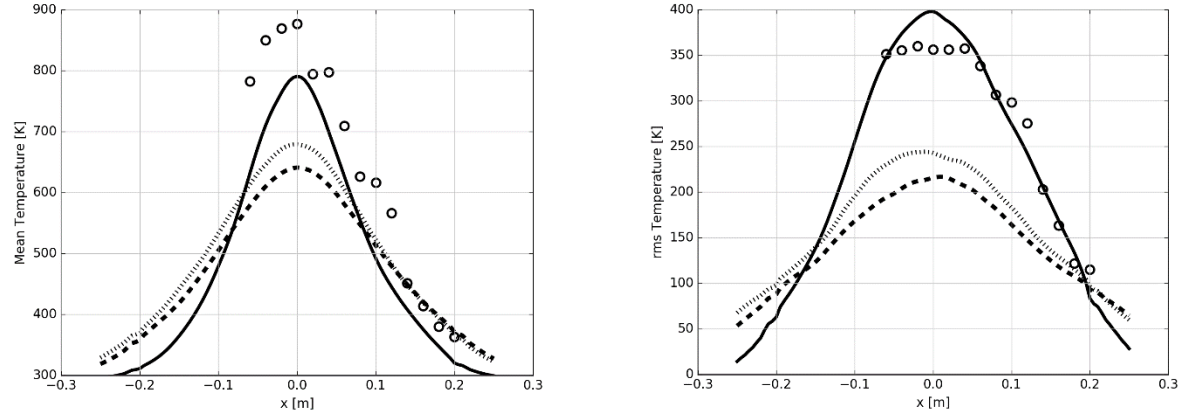


(a) (b)

*Figure 57: Cross-stream variations of: (a) the mean temperature $\bar{T}$ and (b) the rms temperature $T_{rms}$ at $z = 0.5$ m. See caption of Figure 55.*

These results are confirmed in Figure 56 and Figure 57 which show relatively good agreement between experimental data and numerical results for EDC/PGRF but increased discrepancies for SLFV1/grey and SLFV1/WSGG, in particular for the peak value of $\bar{T}$. The decreased accuracy shown in Figure 55, Figure 56 and Figure 57 when going from baseline approximate models in EDC/PGRF to higher-fidelity models in SLFV1/grey and SLFV1/WSGG is somewhat surprising. There are several possibilities that could lead to the

unexpected results. First, SLFV1 has some limitations in the way the heat loss is treated (see section IV.1.1) with the assumption of a uniform distribution of the enthalpy deficit $\Delta h$ over $Z$ and this assumption leads to unrealistic values of temperature near the boundaries $Z = 0$ and $Z = 1$. Second, as discussed in Section IV.2, in the flamelet solutions, grid-resolved temperatures depend on assumptions made in the shape of the sub-grid scale PDF, $\tilde{p}(Z, \chi_{st}, \Delta h)$ (treated as the product of a $\beta$-function times two Dirac $\delta$-functions), and in the estimation of the parameters of the turbulent flame LUT $\left(\tilde{Z}, \widetilde{Z_v}, \widetilde{\chi_{st}}, \widetilde{\Delta h}\right)$. Errors in the assumed PDF shape and/or errors in predictions of the LUT parameters will lead to errors in simulated temperatures.

We do not consider here possible errors in the shape of the PDF and focus instead on the sensitivity of the flamelet solutions on predictions of $\widetilde{Z_v}$, $\widetilde{\chi_{st}}$ and $\widetilde{\Delta h}$ ($\tilde{Z}$ is assumed accurate). We first consider the possibility that the under-estimated values of simulated temperatures are due to over-estimated levels of radiant heat losses. We proceed to calculate the global radiative power by spatially integrating the radiative source term that appears in the $\tilde{h}$-equation (Eq. (IV-32)) over the computational domain, $\dot{Q}_{rad} = \left(\int_V \overline{\nabla . \dot{q}'''} dV\right)$. We find $\dot{Q}_{rad} = 7.6$ kW (time-averaged value) for SLFV1/grey and $\dot{Q}_{rad} = 3.8$ kW (time-averaged value) for SLFV1/WSGG (see Figure 58). After dividing by the global heat release rate (50 kW), these results are found to correspond to $\chi_{rad}^{g} = 15\%$ for SLFV1/grey and $\chi_{rad}^{g} = 7.6\%$ for SLFV1/WSGG. These values are much lower than those used in EDC/PGRF where $\chi_{rad}^{g} = 23\%$ (recall that EDC/PGRF uses an empirically-calibrated radiation model that guarantees the correct global radiative loss fraction). Thus, the low values of simulated temperatures are not explained by excessive values of $\tilde{h}$ and $\chi_{rad}^{g}$. On the contrary, SLFV1/grey and SLFV1/WSGG significantly under-predict radiative emissions (note that because soot radiation is assumed to have a limited impact in methane-air combustion, soot is simply neglected in the present flamelet model. This simplification may account for some of the discrepancies between predicted and measured values of $\chi_{rad}^{g}$ in SLFV1).

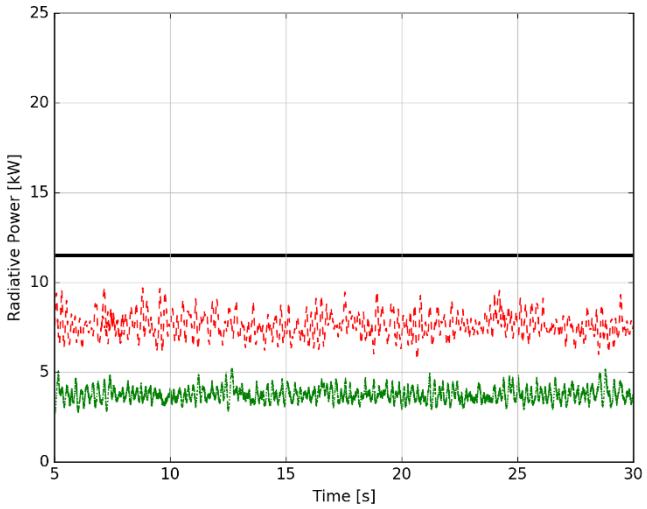


*Figure 58: Global radiative power over time. Comparison between LES results obtained with EDC/PGRF (solid black line), SLFV1/grey (dashed red line), SLFV1/WSGG (dotted green line).*

Next, we consider the possibility that the underestimated values of simulated temperatures are due to errors in predictions of $\widetilde{\chi_{st}}$. We rule out this possibility after checking that values of $\widetilde{\chi_{st}}$ are relatively low (typically less than 5 $s^{-1}$ (see Figure 51 (c))) and that under those conditions, the laminar flame solutions are only weakly sensitive to variations in $\chi_{st}$ (see section III.3.2).

Finally, we consider the possibility that the underestimated values of simulated temperatures are due to over-estimated values of the SGS $Z$-variance, $\widetilde{Z_v}$. We confirm this possibility after checking that values of $\widetilde{Z_v}$ are relatively high: in regions where $\tilde{Z} \approx Z_{st}$, we find that $(\widetilde{Z_v})^{1/2} \geq Z_{st}$ where $Z_{st}$ = 0.055 is the stoichiometric value of mixture fraction. As seen in Figure 59, high values of $\widetilde{Z_v}$ (or high values of intermittency factor $IF$) correspond to a wide $\beta$-PDF in mixture fraction space, which in turn lead to reduced temperatures, in particular for $(Z_{st}/2) \leq \tilde{Z} \leq (2 \times Z_{st})$ (the reduction may be as high as several hundred Ks). Thus, the low values of simulated temperatures can be explained by the large values of $\widetilde{Z_v}$ which are responsible for increasing the effect of statistical filtering associated with the SGS $Z$-PDF. These results suggest that the details of the SGS $Z$-PDF model should be re-examined in order to improve the performance of the flamelet model.

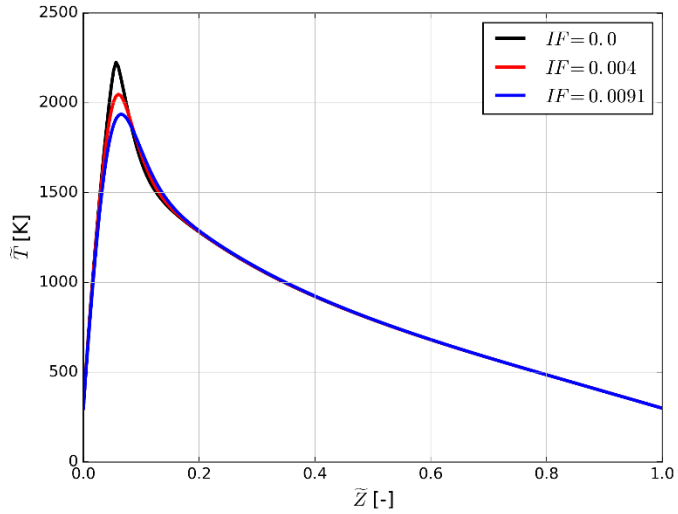


*Figure 59: Comparison the effect of different values of IF on the LES-filtered temperature $\tilde{T}$ integrated between the instantaneous steady/adiabatic solution, $T(Z)$, at $\chi_{st} = 0.0005$ [1/s] and the $\beta$-PDF.*

On a separate but related note, the low values of $\tilde{T}$ result in low values of the radiation emission term $\overline{kI_b}$ (see section II.5), which explains the low values of radiant emissions obtained with SLFV1/grey and SLFLV1/WSGG. These results suggest that the modeling of radiation emission should be re-examined and account for SGS TRI in order to improve the performance of the grey and non-grey models.

### V.3.2 SLFV1/Grey vs SLFV2/Grey

According to the simulated results in section V.3.1, surprising discrepancies for the high-fidelity models (SLFV1/grey and SLFV1/WSGG) when compared to the experimental data are due to several possibilities. One of those possibilities is the limitation in the way the heat loss is treated in SLFV1, which results in a uniform distribution of the enthalpy deficit $\Delta h$ over $Z$ and this assumption leads to unrealistic values of temperature near the boundaries $Z = 0$ and $Z = 1$. In order to overcome the weakness in SLFV1, a more elaborate heat loss treatment is introduced in SLFV2 using a method called Prescribed Local Radiative Fraction (PLRF) (see IV.1.1b), which results in well-defined profiles $\Delta h(Z)$ and $T(Z)$. Simulation for SLFV2/Grey is then performed using the same modeling framework as for SLFV1/Grey (described in section V.3.1), except for the turbulent flame LUT, *i.e.*, SLFV2/Grey (SLFV1/Grey) uses the

turbulent flame LUT generated from the laminar flamelet library in SLFV2 (SLFV1), which is parameterized by $(Z, \chi_{st}, \Delta h_{st})$ ($(Z, \chi_{st}, \Delta h)$) (see Table 5). Then, simulated results in with SLFV1/Grey and SLFV2/Grey are evaluated against the baseline EDC/PRFG and the experimental data.

| Simulation name | Laminar flamelet library | $\tilde{p}(Z)$ | $\widetilde{Z_v}$ model | LES-filtered stoichiometric scalar dissipation rate | Radiation model |
|---|---|---|---|---|---|
| **SLFV1**/Grey | **SLFV1** parameterized by $(Z, \chi_{st}, \boldsymbol{\Delta h})$ | $\beta$-PDF | Algebraic model 1 | $\widetilde{\chi_{st}}$ | Grey |
| **SLFV2**/Grey | **SLFV2** parameterized by $(Z, \chi_{st}, \boldsymbol{\Delta h_{st}})$ | $\beta$-PDF | Algebraic model 1 | $\widetilde{\chi_{st}}$ | Grey |

*Table 5: Summary for the methods and modelling choices in the current simulations.*

As mentioned above, in SLFV2/Grey, we do not use $\widetilde{\Delta h}$ as the heat loss parameter of the turbulent LUT like SLFV1/Grey, but $\widetilde{\Delta h_{st}}$ instead, which is calculated from $\widetilde{\Delta h}$ through the Eq. (IV-33) in section IV.3.4. Figure 60 shows the front-view at the center of the burner of the instantaneous LES-filtered enthalpy defect $\widetilde{\Delta h}$ and the instantaneous LES-filtered stoichiometric enthalpy defect $\widetilde{\Delta h_{st}}$.

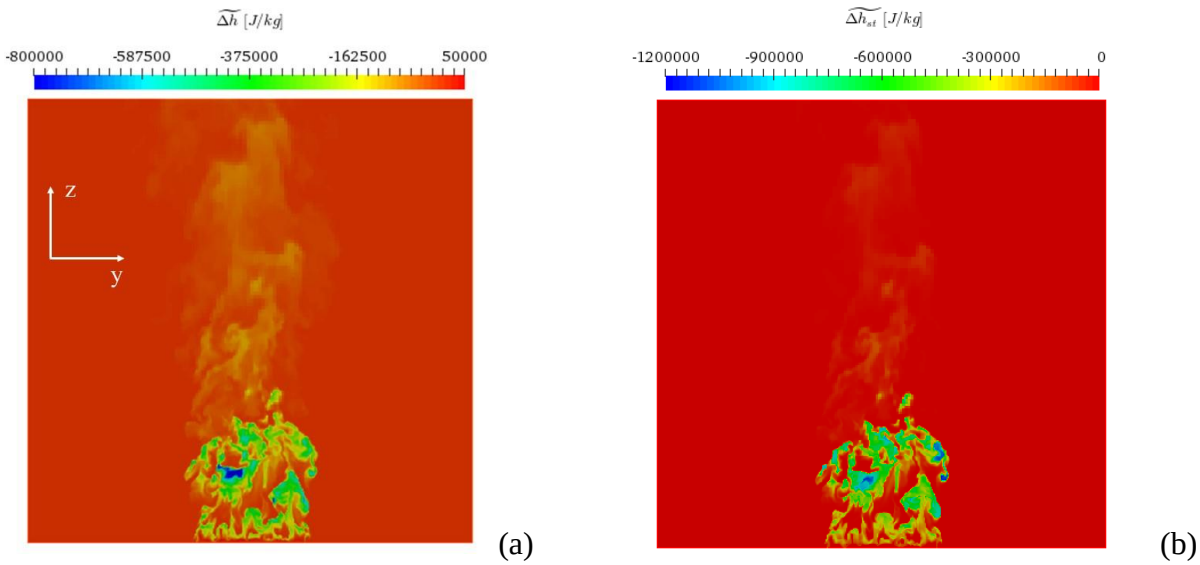


(a) (b)

*Figure 60: Front-view at the center of the burner or at $x = 0$ plane of the instantaneous LES-filtered enthalpy defect $\widetilde{\Delta h}$ (a) and the instantaneous LES-filtered stoichiometric enthalpy defect $\widetilde{\Delta h_{st}}$ (b) in SLFV2/Grey at t = 30 s.*

Now, we focus below on gas temperature results and present the spatial variations of the temporal mean $\bar{T}$ and *rms* values $T_{rms}$ as a function of elevation *z* along the flame centerline at *x* = 0 m (Figure 61), and as a function of cross-stream distance *x* at a fixed elevation, $z = 0.25$ m (Figure 62) and $z = 0.5$ m (Figure 63).

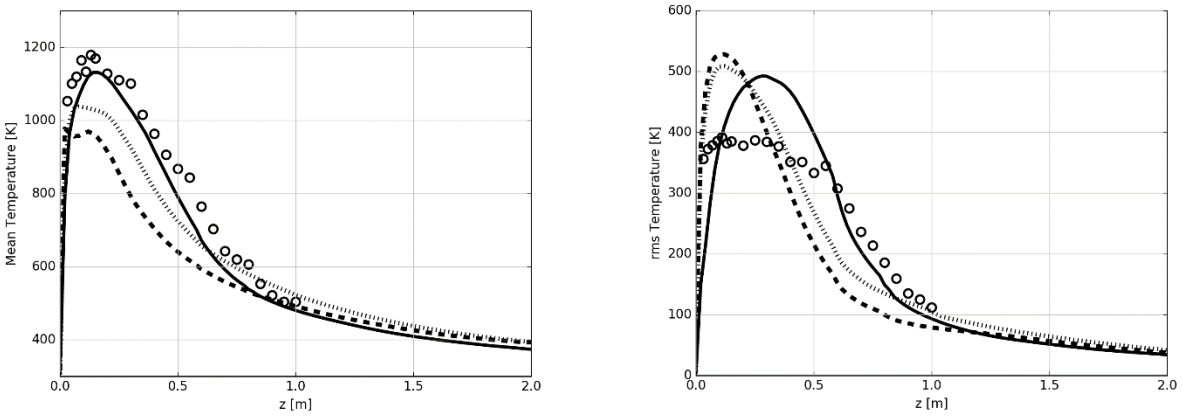


(a) (b)

*Figure 61: LES simulations of the turbulent line burner. Vertical variations of (a) the mean temperature $\bar{T}$ and (b) the rms temperature $T_{rms}$ along the flame centerline. Comparison between experimental data (symbols) and LES results obtained with EDC/PGRF (solid line), SLFV1/grey (dashed line), SLFV2/Grey (dotted line).*

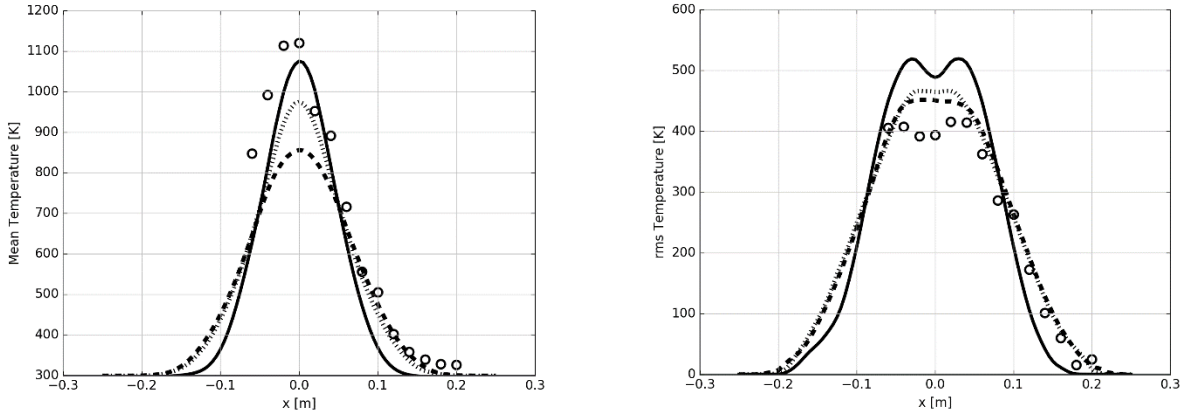


(a) (b)

*Figure 62: Cross-stream variations of (a) the mean temperature $\bar{T}$ and (b) the rms temperature $T_{rms}$ at $z = 0.25$ m. See caption of Figure 61.*

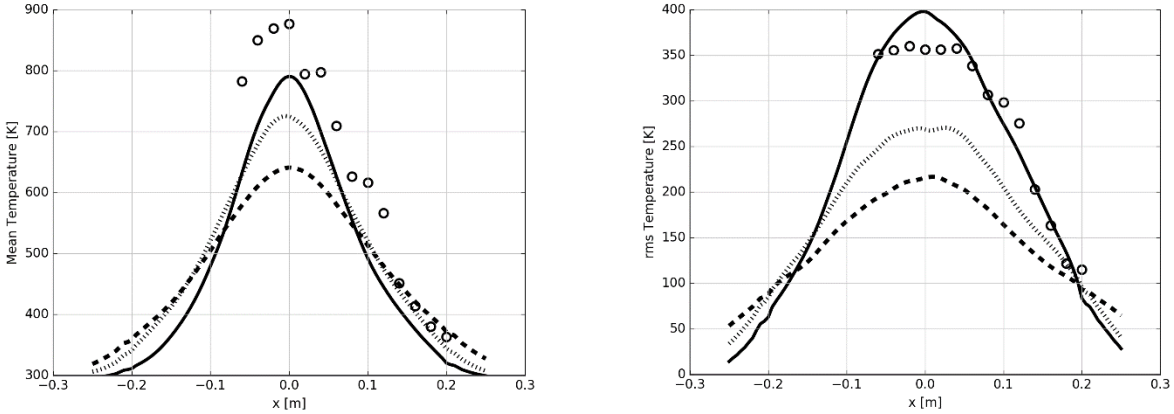


(a) (b)

*Figure 63: Cross-stream variations of (a) the mean temperature $\bar{T}$ and (b) the rms temperature $T_{rms}$ at $z = 0.5$ m. See caption of Figure 61.*

In comparison, numerical results in Figure 61 shows that SLFV2/grey still does not correctly capture the shape of the *z*-variations of $\bar{T}$ and $T_{rms}$, but has a better prediction than SLFV1/Grey in $\bar{T}$ prediction. Specifically, SLFV2/Grey (SLFV1/Grey) under-estimate (significantly under-estimate) peak values of $\bar{T}$ by approximately 140 K (more than 200 K). These results are confirmed in Figure 62 and Figure 63 which also show relatively a slightly better prediction for SLFV2/Grey than SLFV1/Grey. However, these numerical flamelets

models results are still far from the baseline EDC/PGRF and the experimental data. In term of the global radiative power over the computational domain with $\dot{Q}_{rad} = (\int_V \overline{\nabla . \dot{q}'''} dV)$, we find $\dot{Q}_{rad} = 7.6\,\text{kW}$ for SLFV1/Grey and $\dot{Q}_{rad} = 9.8\,\text{kW}$ for SLFV2/Grey, *i.e.*, more radiative heat losses in SLFV2/grey (as seen in Figure 64 and Figure 65). After dividing by the global heat release rate (50 kW), these results are found to correspond to $\chi_{rad}^{g} = 15\%$ for SLFV1/grey and $\chi_{rad}^{g} = 19.6\,\%$ for SLFV2/grey. The value in SLFV2/Grey is closer than in SLFV1/grey to those used in EDC/PGRF where $\chi_{rad}^{g} = 23\%$ (recall that EDC/PGRF uses an empirically-calibrated radiation model that guarantees the correct global radiative loss fraction). The reason is that the higher values of $\tilde{T}$ result in SLFV2/Grey than SLFV1/Grey contribute to a better prediction in the global radiative power. However, the modeling of radiation emission accounting for SGS TRI is not included in SLFV2/Grey and should re-examined in the next section in order to bring simulated value of $\chi_{rad}^{g}$ closer to the experimental value.

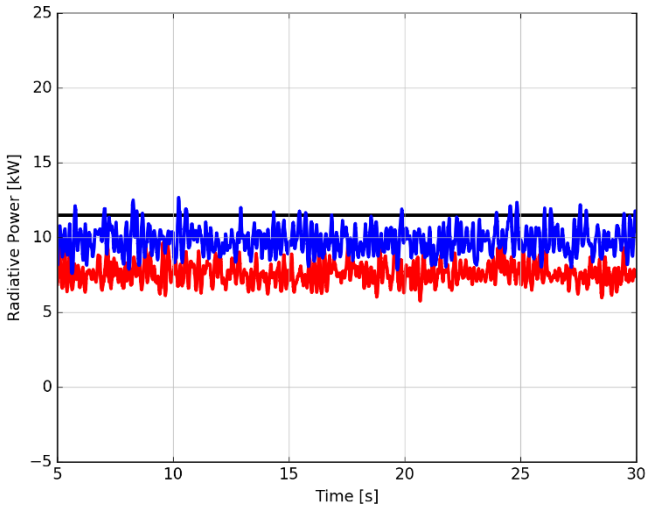


*Figure 64: Global radiative power over time. Comparison between LES results obtained with EDC/PGRF (black line), SLFV1/grey (red line), SLFV2/Grey (blue line).*

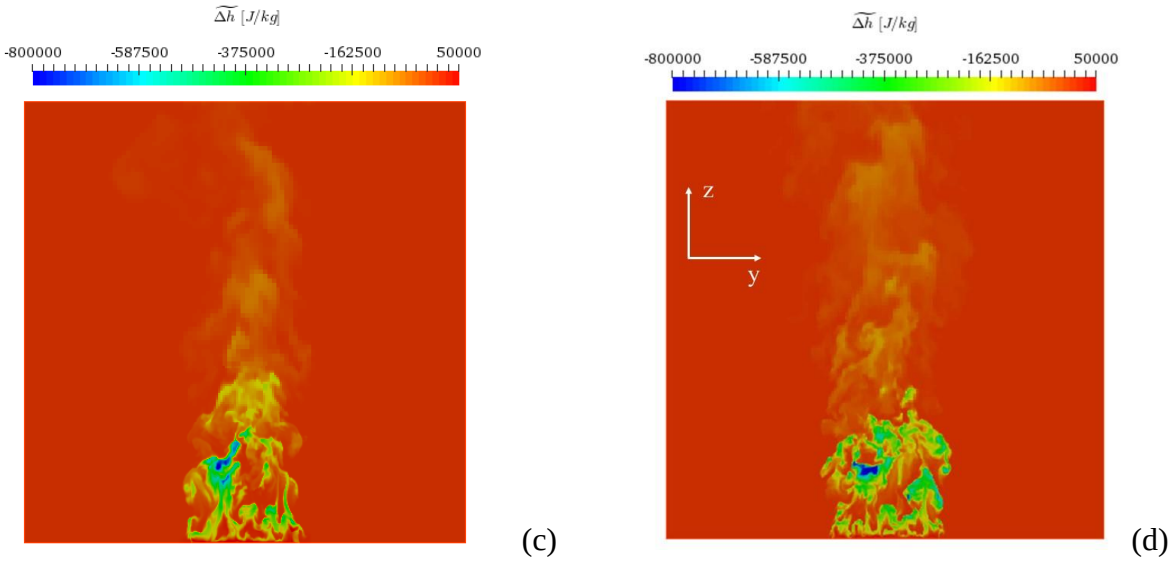


*Figure 65: Front-view at the center of the burner or at $x = 0$ plane of the instantaneous LES-filtered enthalpy defect $\widetilde{\Delta h}$ for SLFV1/Grey (a) and SLFV2/Grey (b).*

### V.3.3 Effects of TRI treatment

So far, the grey radiation model, which we use in SLFV1/Grey and SLFV2/Grey (see sections V.3.1 and V.3.2) to calculate the radiative heat loss term appearing in the $\tilde{h}$-equation, just ignores sub-grid scale turbulence-radiation interactions (TRI) and simply write: $\overline{\kappa I_b} = (\bar{\kappa} \times \sigma \tilde{T}^4/\pi)$, $\overline{\kappa I} = (\bar{\kappa} \times \bar{I})$, and $\bar{\kappa} = p\left(\tilde{x}_{CO2} a_{CO2}(\tilde{T}) + \tilde{x}_{H2O} a_{H2O}(\tilde{T})\right)$ where $\tilde{T}$, $\tilde{x}_{CO2}$ and $\tilde{x}_{H2O}$ are the LES-filtered values of the gas temperature and the mole fractions of carbon dioxide and water vapor, respectively. The grey model underpredicts global radiant emissions, a result that could be explained by the low values of mean temperatures and the absence of a model for SGS turbulence-radiation interactions (TRI). In this section, we investigate two simulations: SLFV2/Grey without TRI and SLFV2/Grey with TRI, denoted SLFV2/ GreyNoTRI and SLFV2/GreyTRI respectively (Table 6). In SLFV2/GreyTRI, we account for sub-grid scale TRI through a flamelet-based description of the emission term and mean absorption coefficient (see Figure 66) that appear in the RTE equation combined with an application of the flamelet-LES coupling expressions presented in section IV.2 and re-written here:

$$\overline{\kappa I_b} = \bar{\rho} \times \left(\widetilde{\frac{\kappa I_b}{\rho}}\right) = \bar{\rho} \times \int_0^1 \left(\frac{\kappa I_b}{\rho}\right)^{fl} \left(Z, \widetilde{\chi_{st}}, \widetilde{\Delta h_{st}}\right) p_\beta\left(Z; \tilde{Z}, \widetilde{Z_v}\right) dZ \quad \text{(V-1)}$$

$$\bar{\kappa} = \bar{\rho} \times \left(\widetilde{\frac{\kappa}{\rho}}\right) = \bar{\rho} \times \int_0^1 \left(\frac{\kappa}{\rho}\right)^{fl} \left(Z, \widetilde{\chi_{st}}, \widetilde{\Delta h_{st}}\right) p_\beta\left(Z; \tilde{Z}, \widetilde{Z_v}\right) dZ \quad \text{(V-2)}$$

Eqs. (V-1) and (V-2) show that in contrast to the model formulation adopted in SLFV2/GreyNoTRI in which the local emissive power of the gas is determined by grid-scale properties (*i.e.*, by $\tilde{T}$, $\widetilde{x_{CO2}}$ and $\widetilde{x_{H2O}}$), in SLFV2/GreyTRI, the local emissive power is determined by the sub-grid scale properties of the flamelets, *i.e.*, by the flamelet temperature and composition, $T^{fl}$, $x_{CO2}^{fl}$ and $x_{H2O}^{fl}$. This treatment is believed to be more accurate and is expected to lead to higher values of global radiant emissions.

| Simulation name | Laminar flamelet library | $\tilde{p}(Z)$ | $\widetilde{Z_v}$ model | LES-filtered stoichiometric scalar dissipation rate | Radiation model |
|---|---|---|---|---|---|
| SLFV2/**GreyNoTRI** | SLFV2 parameterized by $(Z, \chi_{st}, \Delta h_{st})$ | $\beta$-PDF | Algebraic model 1 | $\widetilde{\chi_{st}}$ | Grey |
| SLFV2/**GreyTRI** | SLFV2 parameterized by $(Z, \chi_{st}, \Delta h_{st})$ | $\beta$-PDF | Algebraic model 1 | $\widetilde{\chi_{st}}$ | Grey with **TRI treatment** |

*Table 6: Summary for the methods and modelling choices in the current simulations*

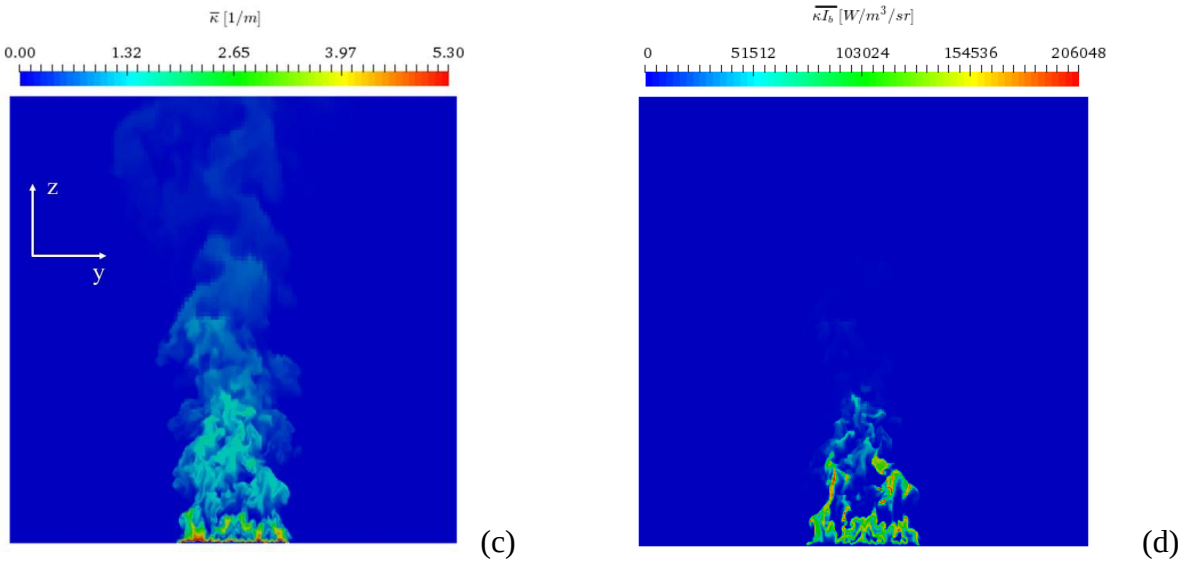


*Figure 66: Front-view at the center of the burner or at $x = 0$ plane of the instantaneous LES-filtered absorption coefficient $\bar{\kappa}$ (a) and the instantaneous LES-filtered directional radiative emission $\overline{\kappa I_b}$ (b) extracted from the turbulent LUT in SLFV2/GreyTRI at t = 30 s.*

Interestingly, the accuracy of predictions in the global radiative power is significantly improved in the case of SLFV2/GreyTRI, we find $\dot{Q}_{rad} = 11.4$ kW and $\chi^g_{rad} = 22.9\%$, in the case of SLFV2/GreyNoTRI and we just have $\dot{Q}_{rad} = 9.8$ kW and $\chi^g_{rad} = 19.6\%$ (see Figure 67). This improved accuracy in SLFV2/GreyTRI can be attributed to the treatment of local radiation effects and turbulence-radiation interactions.

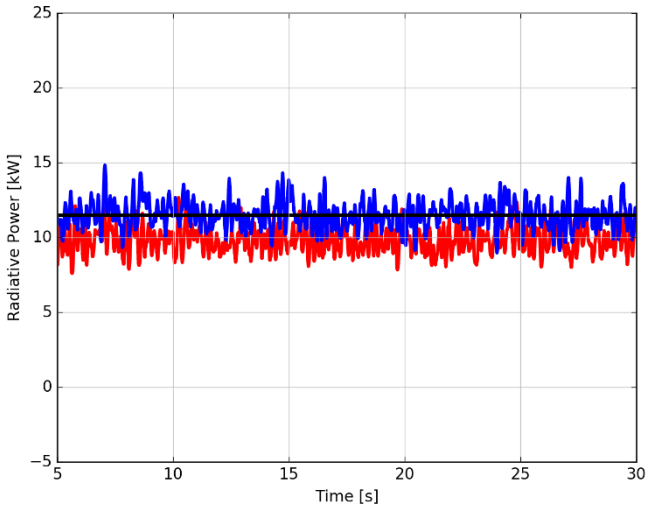


*Figure 67: Global radiative power over time. Comparison between LES results obtained with EDC/PGRF (black line), SLFV2/GreyNoTRI (red line), SLFV2/GreyTRI (blue line).*

The treatment of local radiation effects and turbulence-radiation interactions in SLFV2/GreyTRI improves the performance for the global radiative heat loss prediction by increasing the radiative heat losses, but also makes the temperature lower when compared to those in SLFV2/GreyNoTRI (as presented in Figure 68, Figure 69 and Figure 70). However, comparing to the baseline EDC/PGRF and the experimental data, both flamelet models still significantly under-predict the mean temperatures, a result that could be explained by the large values of the modelled sub-grid scale (SGS) variance of mixture fraction $\widetilde{Z_v}$ controlling presumed SGS $Z$-PDF. These results suggest that the modeling of both the shape of the SGS $Z$-PDF (described as a $\beta$-function) and the SGS $Z$-variance requires additional investigation and will be considered in the next sections.

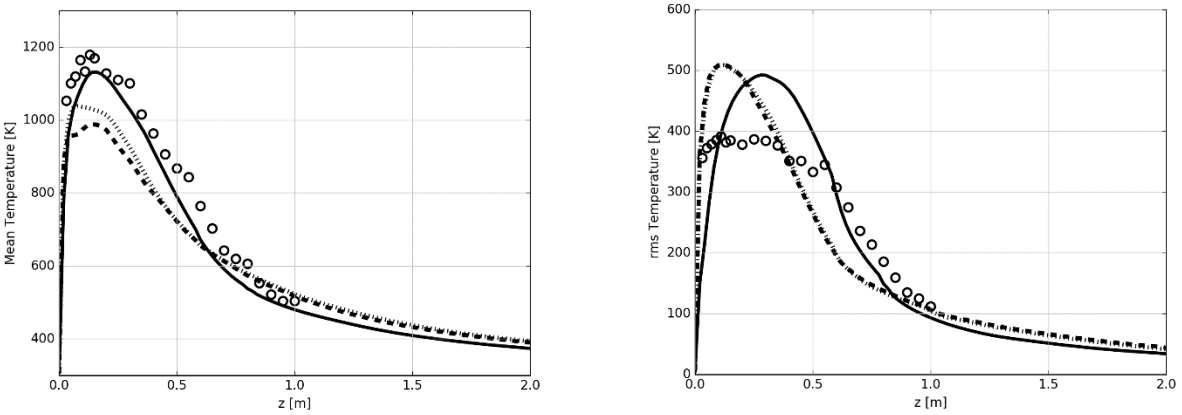


(a) (b)

*Figure 68: LES simulations of the turbulent line burner. Vertical variations of (a) the mean temperature $\bar{T}$ and (b) the rms temperature $T_{rms}$ along the flame centerline. Comparison between experimental data (symbols) and LES results obtained with EDC/PGRF (solid line), SLFV2/GreyTRI (dashed line), SLFV2/GreyNoTRI (dotted line).*

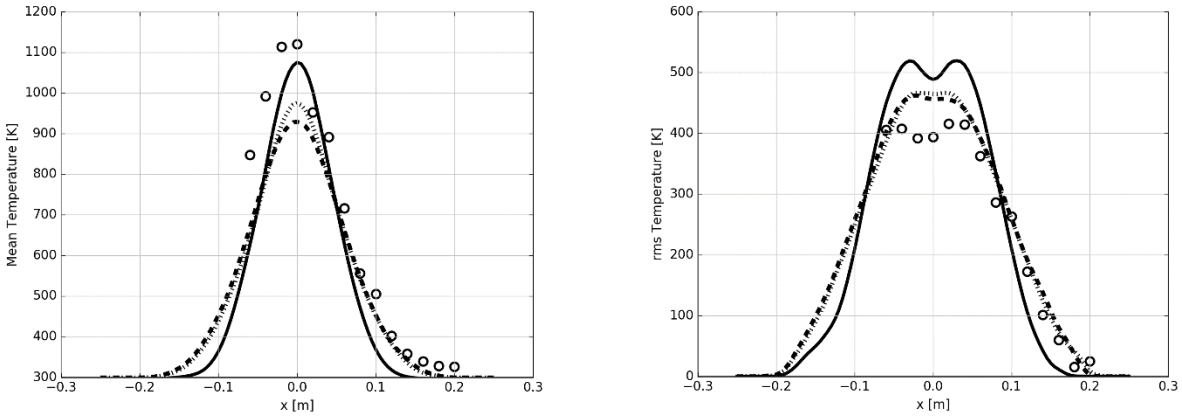


(a) (b)

*Figure 69: Cross-stream variations of (a) the mean temperature $\bar{T}$ and (b) the rms temperature $T_{rms}$ at $z = 0.25\ m$. See caption of Figure 68.*

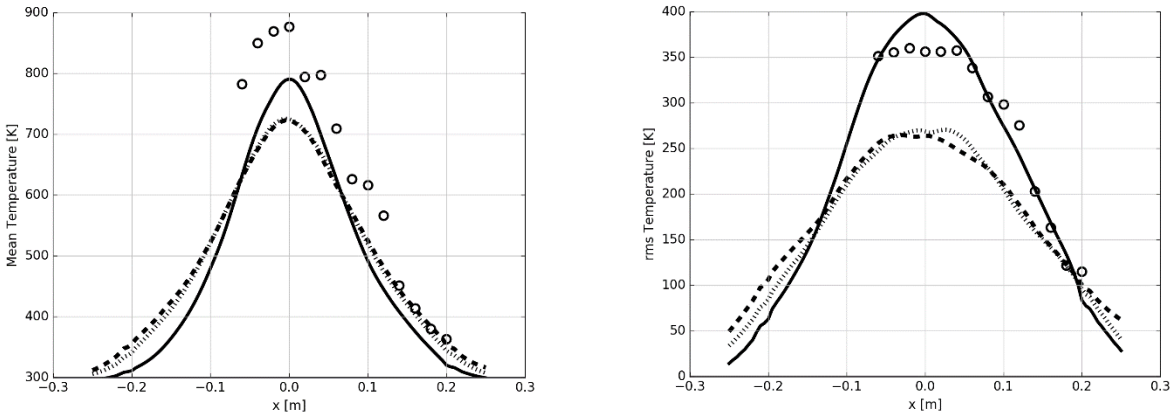


(a) (b)

*Figure 70: Cross-stream variations of (a) the mean temperature $\bar{T}$ and (b) the rms temperature $T_{rms}$ at $z = 0.5$ $m$. See caption of Figure 68.*

### V.3.4 $\widetilde{Z_v}$ models

Error in $\widetilde{Z_v}$'s prediction could be a reason leading to wrong predictions in simulated temperatures in the flamelet models. In this section, we consider performances of three models proposed in section IV.3.2 for $\widetilde{Z_v}$: Algebraic model 1, Algebraic model 2 and Transport equation. Three simulations are performed (Table 7) and its results are evaluated against the baseline EDC/PRFG and the experimental data.

| Simulation name | Laminar flamelet library | $\tilde{p}(Z)$ | $\widetilde{Z_v}$ model | LES-filtered stoichiometric scalar dissipation rate | Radiation model |
|---|---|---|---|---|---|
| **Algebraic model 1** | SLFV2 parameterized by $(Z, \chi_{st}, \Delta h_{st})$ | $\beta$-PDF | **Algebraic model 1** | $\widetilde{\chi_{st}}$ | Grey with TRI treatment |
| **Algebraic model 2** | SLFV2 parameterized by $(Z, \chi_{st}, \Delta h_{st})$ | $\beta$-PDF | **Algebraic model 2** | $\widetilde{\chi_{st}}$ | Grey with TRI treatment |
| **Transport equation** | SLFV2 parameterized by $(Z, \chi_{st}, \Delta h_{st})$ | $\beta$-PDF | **Transport equation** | $\widetilde{\chi_{st}}$ | Grey with TRI treatment |

*Table 7: Summary for the methods and modelling choices in the current simulations*

Figure 71 shows that the instantaneous SGS variance of mixture fraction $\widetilde{Z_v}$ for Algebraic model 1 and Algebraic model 2 are relatively similar with high values near the base and very low values at higher elevations. The fields are quite stiff. In contrast, the $\widetilde{Z_v}$ field in Transport equation has lower values near the base and its structure is quite smooth. Because the thermo-chemical quantities in the turbulent LUT are quite sensitive to $\widetilde{Z_v}$, so the instantaneous LES-filtered temperature $\tilde{T}$ (Figure 72) fields between the cases behave differently. The $\tilde{T}$ fields for both Algebraic model 1 and Algebraic model 2 have higher peak (due to low values of $\widetilde{Z_v}$ at high elevation) and seems to have more fluctuations. the $\widetilde{Z_v}$ field in Transport equation for has lower peak and the $\tilde{T}$ field has less turbulence structure.

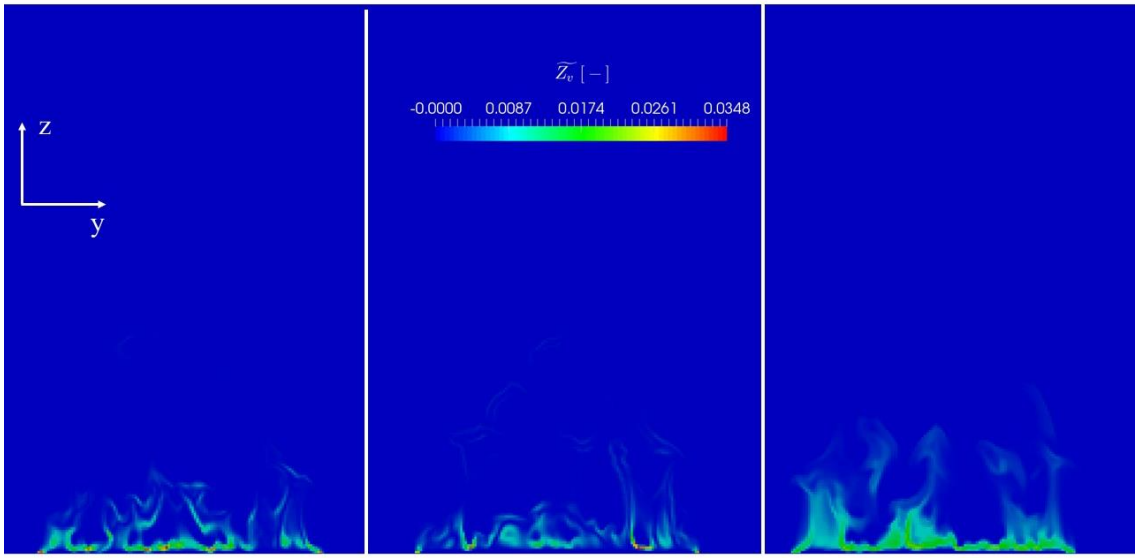


*Figure 71: Front-view at the center of the burner or at $x = 0$ plane of the SGS variance of mixture fraction $\widetilde{Z_v}$ for Algebraic model 1 (left), Algebraic model 2 (center) and Transport equation (right).*

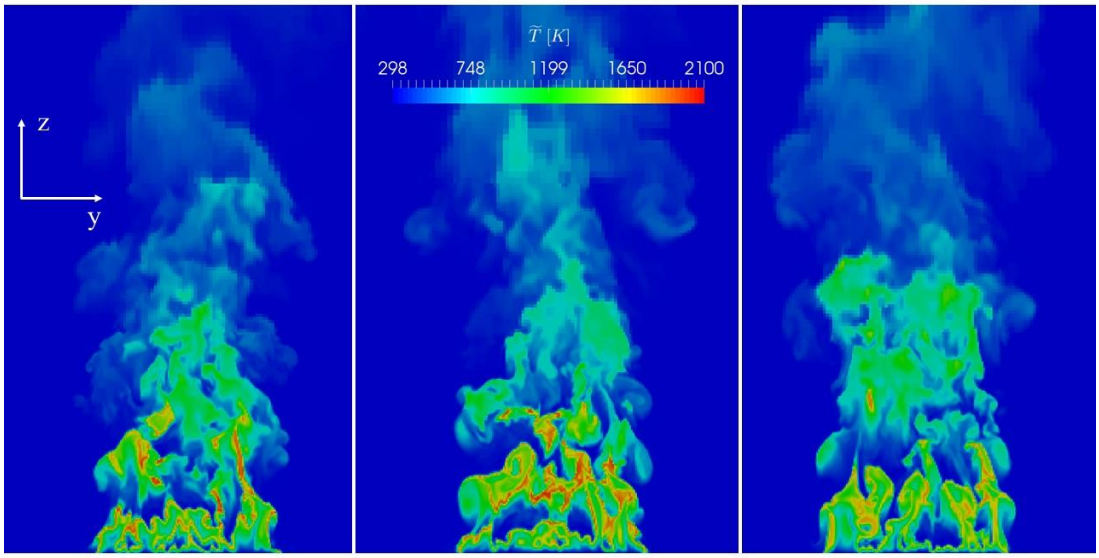


*Figure 72: Front-view at the center of the burner or at $x = 0$ plane of the instantaneous LES-filtered temperature $\tilde{T}$ for Algebraic model 1 (left), Algebraic model 2 (center) and Transport equation (right).*

Figure 73, which introduces vertical variations of the mean SGS variance of mixture fraction $\overline{Z_v}$ along the flame centerline, confirm the points mentioned above when the temporal mean SGS variance of mixture fraction $\overline{Z_v}$ in Transport equation predicts much higher values than those in Algebraic model 1 and Algebraic model 2, which predict quite similarly $\overline{Z_v}$. However, $\overline{Z_v}$ is still bit lower in Algebraic model 2 than in Algebraic model 1.

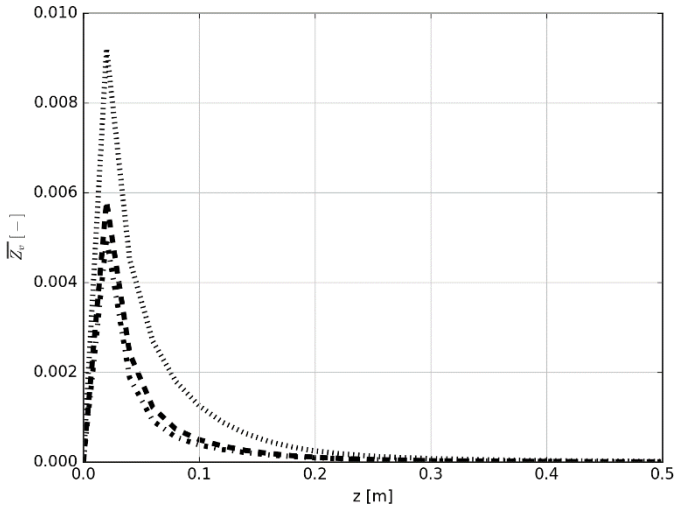


*Figure 73: Vertical variations of the mean SGS variance of mixture fraction $\overline{Z_v}$ along the flame centerline. Comparison between Algebraic model 1(dashed line), Algebraic model 2 (dashed-dotted line), Transport equation (dotted line).*

The simulated results in Figure 74 shows that mean temperature $\bar{T}$ in $\widetilde{Z_v}$ Transport equation case is bit better than those in Algebraic model 1 & 2 due to lower values prediction in the rms temperature $T_{rms}$. The results in the mean temperature and rms temperature for Algebraic model 1 and Algebraic model 2 are similar, but $\bar{T}$ is still bit higher in Algebraic model 2 due to lower prediction values in $\overline{Z_v}$ (see Figure 73 and Figure 74).

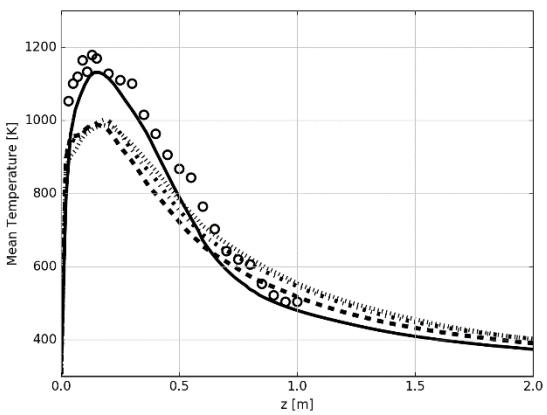


(a)

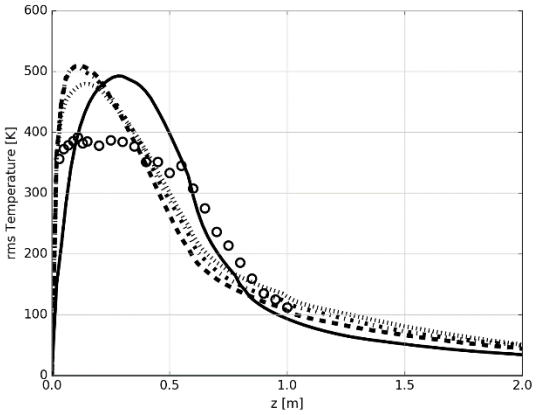


(b)

*Figure 74: LES simulations of the turbulent line burner. Vertical variations of (a) the mean temperature $\bar{T}$ and (b) the rms temperature $T_{rms}$ along the flame centerline. Comparison between experimental data (symbols) and LES results obtained with EDC/PGRF (solid line), the Algebraic model 1(dashed line), the Algebraic model 2 (dashed-dotted line), the Transport equation model (dotted line).*

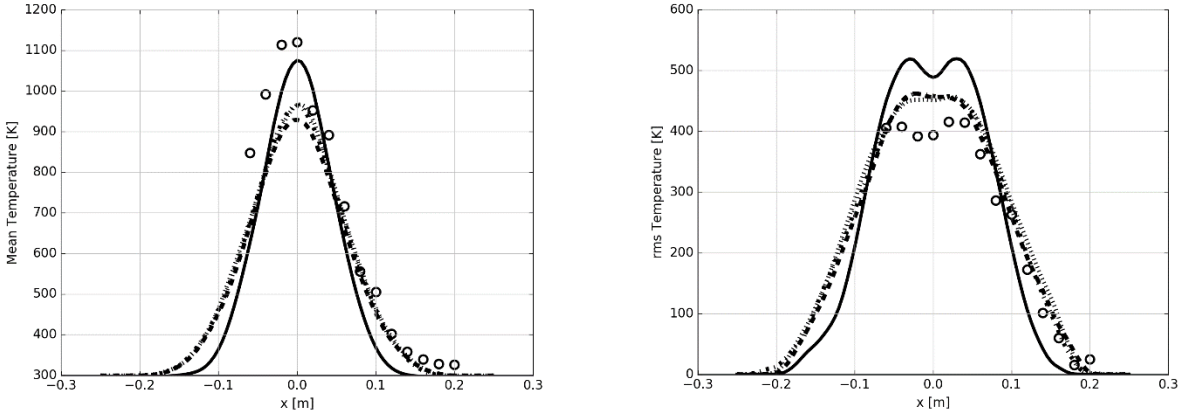


(a) (b)

*Figure 75: Cross-stream variations of (a) the mean temperature $\bar{T}$ and (b) the rms temperature $T_{rms}$ at $z = 0.25\ m$. See caption of Figure 55.*

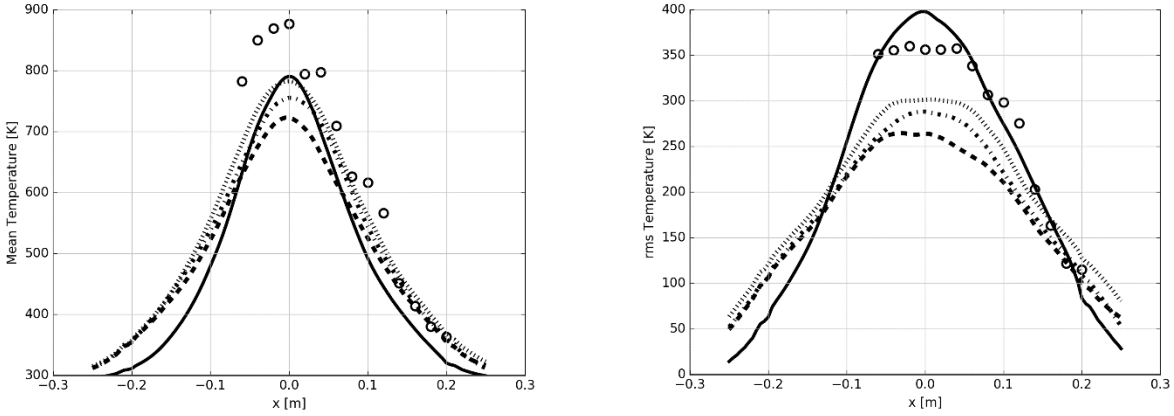


(a) (b)

*Figure 76: Cross-stream variations of (a) the mean temperature $\bar{T}$ and (b) the rms temperature $T_{rms}$ at $z = 0.5\ m$. See caption of Figure 55.*

Now, we turn our attention into the simulated predictions in the global radiative power as seen in Figure 77. Due to higher predicted temperature in Transport equation, we find $\dot{Q}_{rad} = 14.48$ kW, which corresponds to $\chi_{rad}^{g} = 28.96\%$. In Algebraic model 1 and Algebraic model 2, we have $\chi_{rad}^{g} = 22.90\%$ and $\chi_{rad}^{g} = 24.86\%$ respectively. The order of $\chi_{rad}^{g}$ for the cases is consistent with the order of $\bar{T}$.

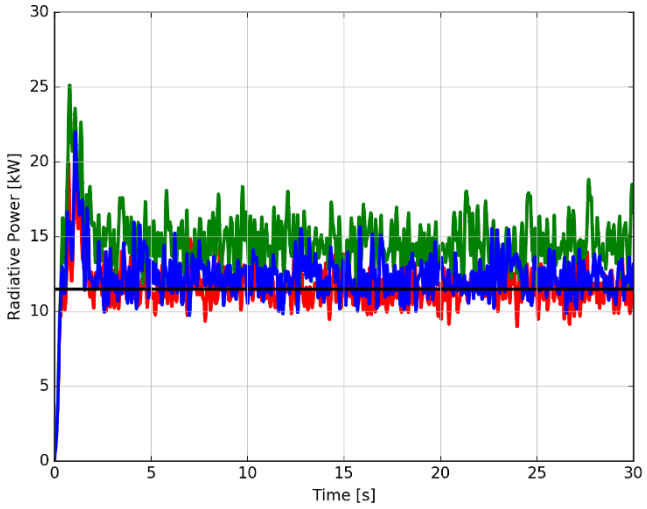


*Figure 77: Global radiative power over time. Comparison between LES results obtained with EDC/PGRF (black line), the Algebraic model 1(red line), the Algebraic model 2 (blue line), the Transport equation model (green line).*

This section shows that the different models for $\widetilde{Z_v}$ can improve the performance in simulated temperature prediction, even the improvement is not big but encouraging. However, one issue coming with the increasing simulated temperature is higher values of $\chi_{rad}^{g}$ (and normally higher than that in the experimental data). This issue can be interpreted as the use of grey assumption in the current radiation model.

### V.3.5 Modeling for the mixture fraction PDF $\widetilde{p}(Z)$: $\beta$-PDF and Top-hat PDF

So far, different studies in the turbulent LUT (SLFV1 vs SLFV2), TRI treatment and $\widetilde{Z_v}$ models can improve slightly the accuracy of predictions in the global radiative power and in the gas temperature. However, this improvement is still not enough when the discrepancy in

temperature between the flamelet models and the experimental data is somehow still large. One possibility could be the reason leading to wrong predictions in simulated temperatures: errors in the assumed $\beta$-PDF shape for the mixture fraction. Another suggestion for $\tilde{p}(Z)$ in this study is the top-hat PDF in which its shape is quite different to those in the $\beta$-PDF (see section IV.2). Two simulations are performed in the SLFV2/Grey's modeling framework (Table 8) and its results are evaluated against the baseline EDC/PRFG and the experimental data.

| Simulation name | Laminar flamelet library | $\tilde{p}(Z)$ | $\widetilde{Z_v}$ model | LES-filtered stoichiometric scalar dissipation rate | Radiation model |
|---|---|---|---|---|---|
| $\boldsymbol{\beta}$-PDF | SLFV2 parameterized by $(Z, \chi_{st}, \Delta h_{st})$ | **$\boldsymbol{\beta}$-PDF** | Transport equation | $\widetilde{\chi_{st}}$ | Grey with TRI treatment |
| **Top-hat** PDF | SLFV2 parameterized by $(Z, \chi_{st}, \Delta h_{st})$ | **Top-hat PDF** | Transport equation | $\widetilde{\chi_{st}}$ | Grey with TRI treatment |

*Table 8: Summary for the methods and modelling choices in current simulations*

The results in both the temperature in Figure 78, Figure 79 and Figure 80 and in the global radiative power in Figure 81 show almost no difference between $\beta$-PDF and Top-hat PDF. These results are quite consistent with previous comparisons between the two cases performed in the pre-processing step (see section IV.2.2). Although the results are not improved, but confirm the point that the result is insensitive to the choice of $\tilde{p}(Z)$ [47].

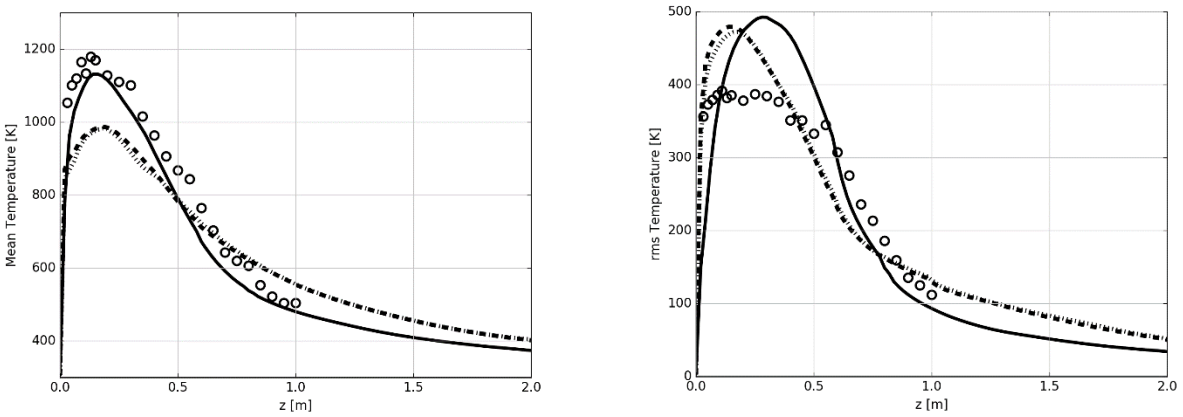


(a) (b)

*Figure 78: LES simulations of the turbulent line burner. Vertical variations of (a) the mean temperature $\bar{T}$ and (b) the rms temperature $T_{rms}$ along the flame centerline. Comparison between experimental data (symbols) and LES results obtained with EDC/PGRF (solid line), $\beta$-PDF (dashed line), Top-hat (dotted line).*

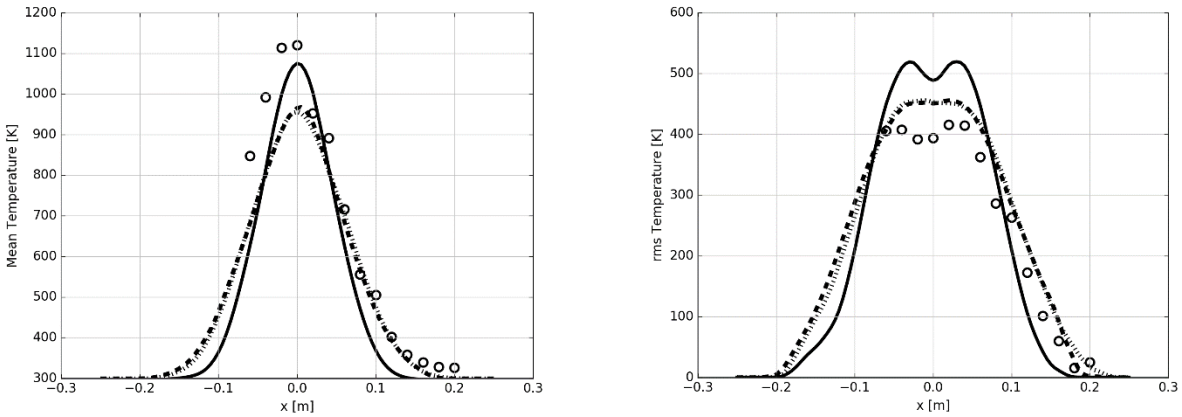


(a) (b)

*Figure 79: Cross-stream variations of (a) the mean temperature $\bar{T}$ and (b) the rms temperature $T_{rms}$ at $z = 0.25\ m$. See caption of Figure 78.*

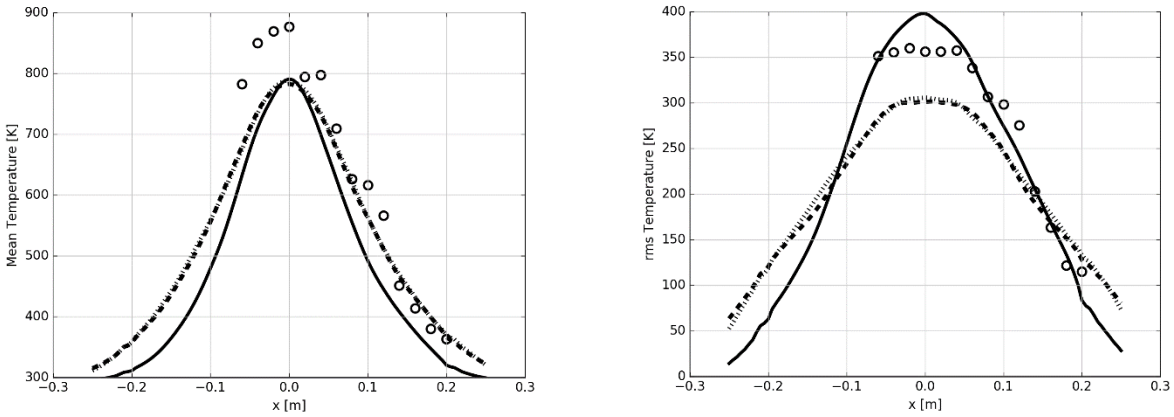


(a) (b)

*Figure 80: Cross-stream variations of (a) the mean temperature $\bar{T}$ and (b) the rms temperature $T_{rms}$ at $z = 0.5\ m$. See caption of Figure 78.*

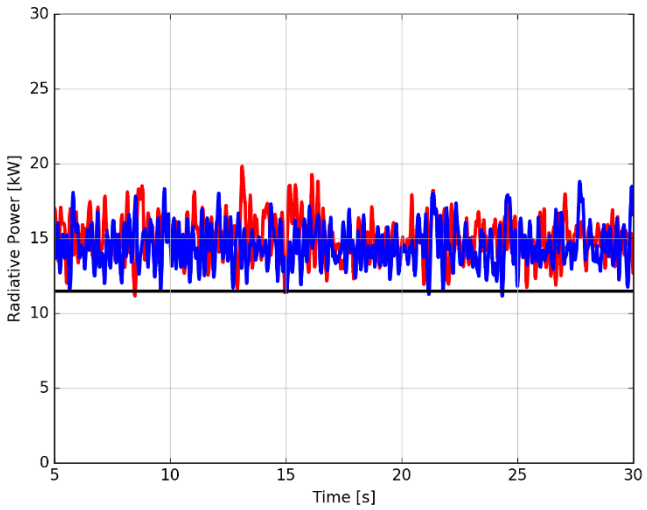


*Figure 81: Global radiative power over time. Comparison between LES results obtained with EDC/PGRF (black line), β-PDF (red line), SLFV2/GreyTRI (blue line).*

### V.3.6 LES-filtered stoichiometric scalar dissipation rate model model

In the previous sections, we used the instantaneous LES-filtered stoichiometric scalar dissipation rate, $\widetilde{\chi_{st}}$ as the flame stretch parameter for looking-up thermo-chemical quantities in the turbulent flame LUT. However, the real flame stretch affecting the flame is not the

instantaneous one, but the effective one, $\widetilde{\chi_{st,Eff}}$ [65][74]. Two simulations are performed and called respectively *the* $\widetilde{\chi_{st}}$ *case* which uses $\widetilde{\chi_{st}}$ as a flame stretch parameter and *the* $\widetilde{\chi_{st,Eff}}$ *case*, which uses $\widetilde{\chi_{st,Eff}}$ as a flame stretch parameter. Its numerical results are then evaluated against the baseline case and the experimental data. The modelling choices for the $\widetilde{\chi_{st}}$ case and the the $\widetilde{\chi_{st,Eff}}$ case are summarized up in Table 9.

| Simulation name | Laminar flamelet library | $\tilde{p}(Z)$ | $\widetilde{Z_v}$ model | LES-filtered stoichiometric scalar dissipation rate | Radiation model |
|---|---|---|---|---|---|
| **The $\widetilde{\chi_{st}}$ case** | ULFV1 parameterized by $(Z, \chi_{st}, \Delta h_{st})$ | $\beta$-PDF | Transport equation | $\widetilde{\chi_{st}}$ | Grey with TRI treatment |
| **The $\widetilde{\chi_{st,Eff}}$ case** | ULFV1 parameterized by $(Z, \chi_{st}, \Delta h_{st})$ | $\beta$-PDF | Transport equation | $\widetilde{\chi_{st,Eff}}$ | Grey with TRI treatment |

*Table 9: Summary for the methods and modelling choices in current simulations.*

Figure 82 shows that the effective $\widetilde{\chi_{st,Eff}}$ field behaves very differently to the instantaneous $\widetilde{\chi_{st}}$ field: the gradient of $\widetilde{\chi_{st,Eff}}$ is smaller than the gradient of $\widetilde{\chi_{st}}$ and at high elevation locations, the $\widetilde{\chi_{st,Eff}}$ field still take finite values while values of $\widetilde{\chi_{st}}$ are close to 0. Figure 83 and Figure 84 compare the temporal mean flame stretch between the $\widetilde{\chi_{st}}$ case and the $\widetilde{\chi_{st,Eff}}$ case. They show that at the location near the flame base (near z = 0 [m]), two fields start to decrease at the initial value around 10 [1/s] and along the center line, $\widetilde{\chi_{st}}$ decays much faster than $\widetilde{\chi_{st,Eff}}$.

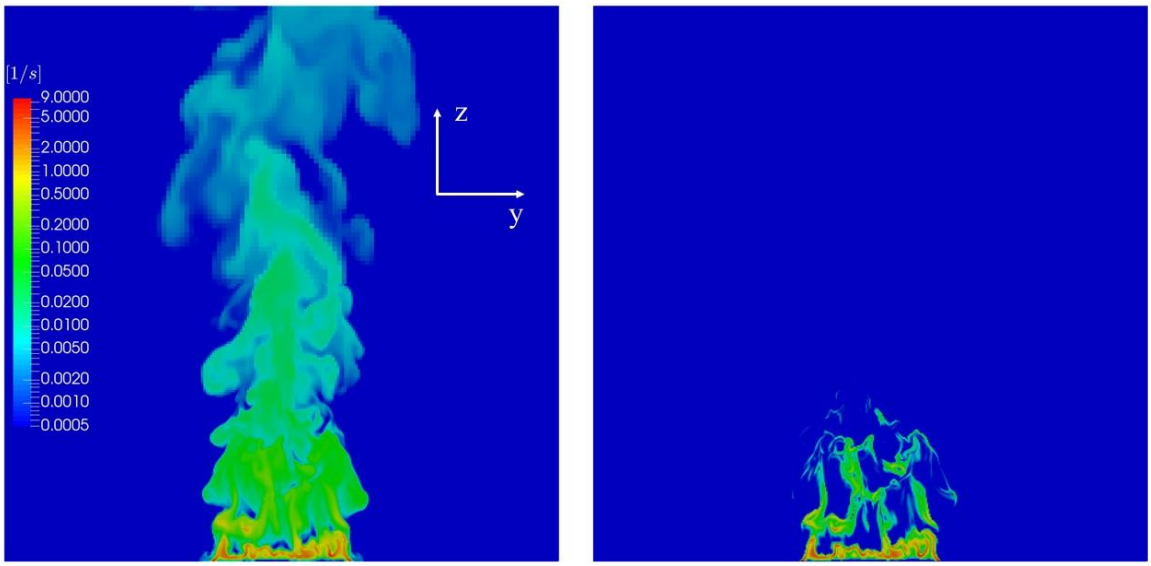


*Figure 82: Front-view at the center of the burner or at $x = 0$ plane for $\widetilde{\chi_{st,Eff}}$ (left) and $\widetilde{\chi_{st}}$ (right).*

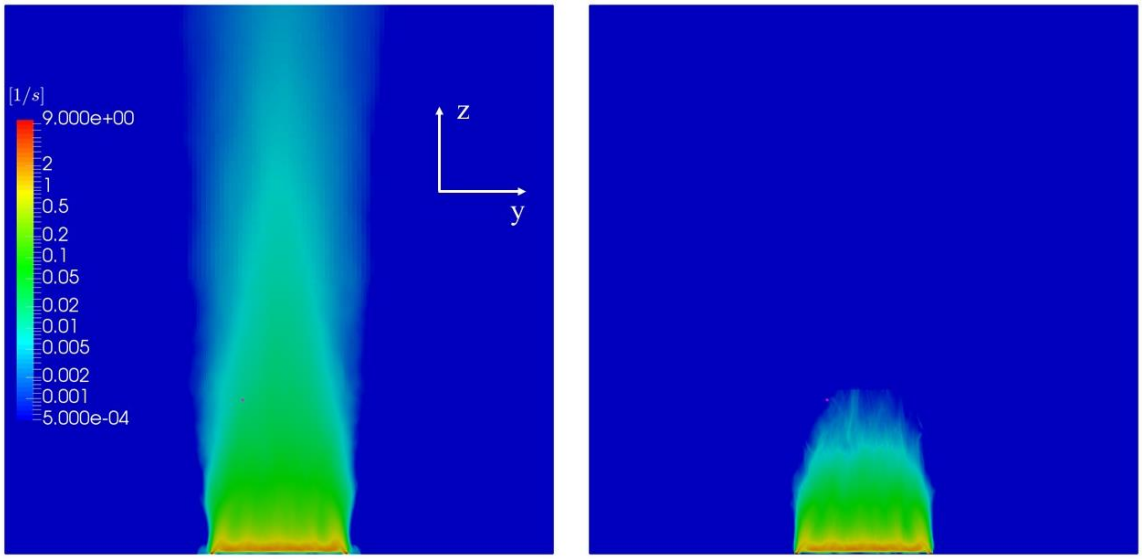


*Figure 83: Front-view at the center of the burner or at $x = 0$ plane for the mean effective stoichiometric scalar dissipation rate, $\overline{\chi_{st,Eff}}$ (left) and the instantaneous one $\overline{\chi_{st}}$ (right).*

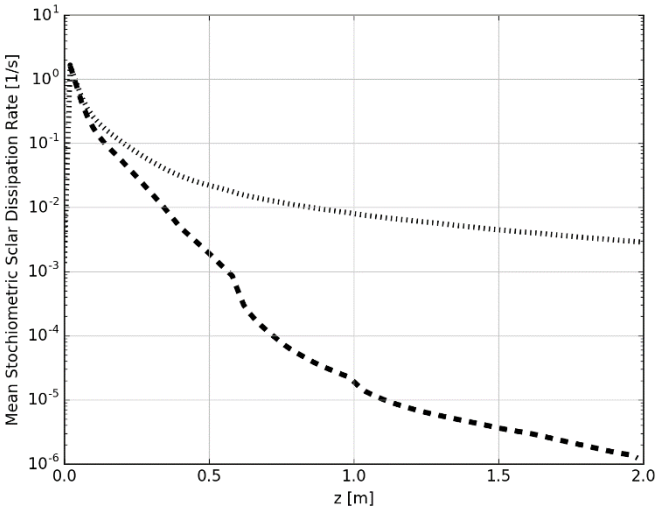


*Figure 84: Vertical variations of the mean stoichiometric scalar dissipation rate along the flame centerline. Comparison between the $\widetilde{\chi_{st}}$ case (dashed line) and the $\widetilde{\chi_{st,Eff}}$ case (dotted line).*

Now, we focus on prediction of the temporal mean $\bar{T}$ and *rms* values $T_{rms}$ between two cases. Figure 85 shows that the peak temperature in two cases is the same and about 150 K lower than the experimental data. Downstream, from the elevation $z = 30$ cm to $z = 100$ cm, $\bar{T}$ in the $\widetilde{\chi_{st}}$ case is quite lower than those in the $\widetilde{\chi_{st,Eff}}$ case (see Figure 85 and Figure 87). The reason for the discrepancy is due to the difference of values in flame stretch predicted between two cases. Higher predicted temperature in the $\widetilde{\chi_{st}}$ case comes along with higher values of the global radiative power ($\chi_{rad}^{g} = 30.83\%$) when comparing with $\chi_{rad}^{g} = 28.14\%$ in the $\widetilde{\chi_{st,Eff}}$ case (see Figure 88).

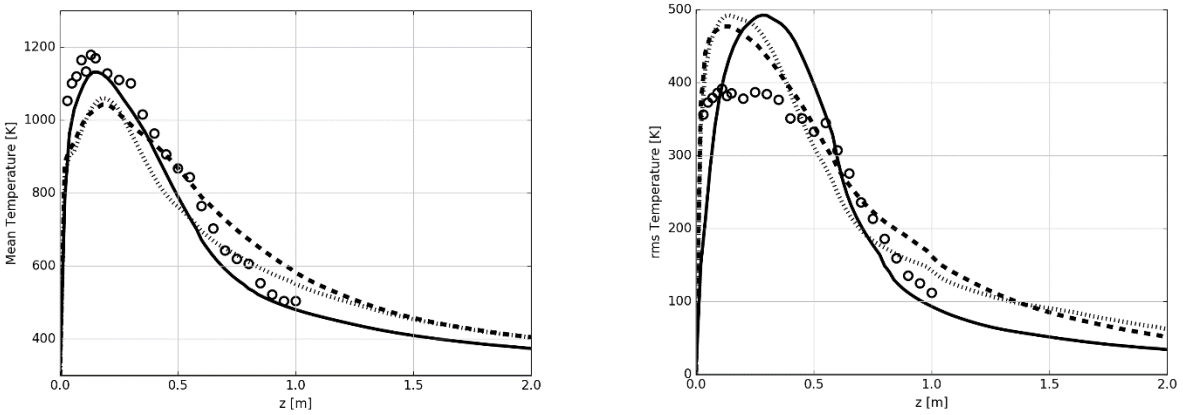


(a) (b)

*Figure 85: LES simulations of the turbulent line burner. Vertical variations of (a) the mean temperature $\bar{T}$ and (b) the rms temperature $T_{rms}$ along the flame centerline. Comparison between experimental data (symbols) and LES results obtained with EDC/PGRF (solid line), the $\widetilde{\chi_{st}}$ case (dashed line), the $\widetilde{\chi_{st,Eff}}$ case (dotted line).*

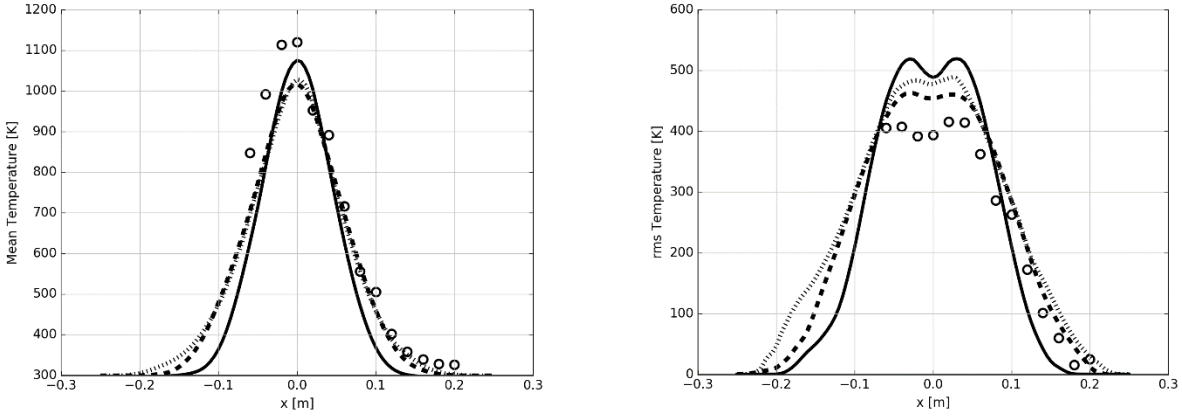


(a) (b)

*Figure 86: Cross-stream variations of (a) the mean temperature $\bar{T}$ and (b) the rms temperature $T_{rms}$ at $z = 0.25$ $m$. See caption of Figure 78.*

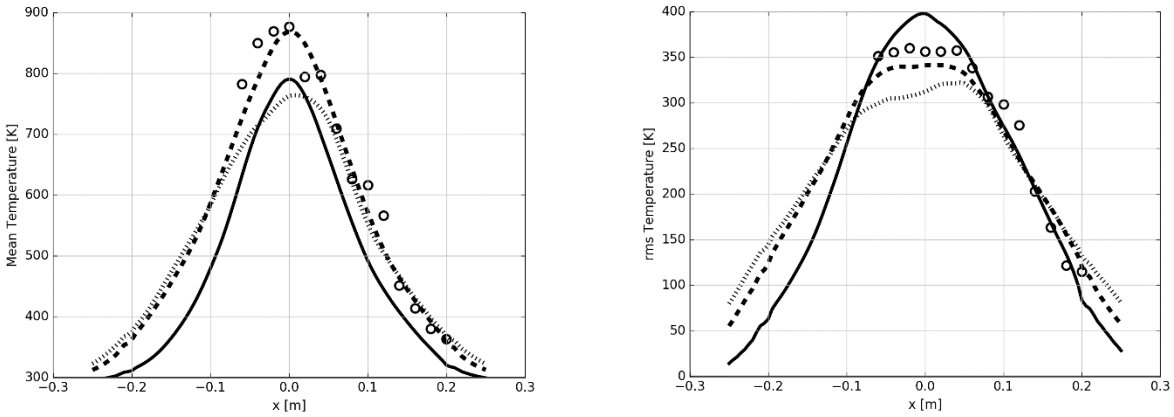


(a) (b)

*Figure 87: Cross-stream variations of (a) the mean temperature $\bar{T}$ and (b) the rms temperature $T_{rms}$ at $z = 0.5\ m$. See caption of Figure 78.*

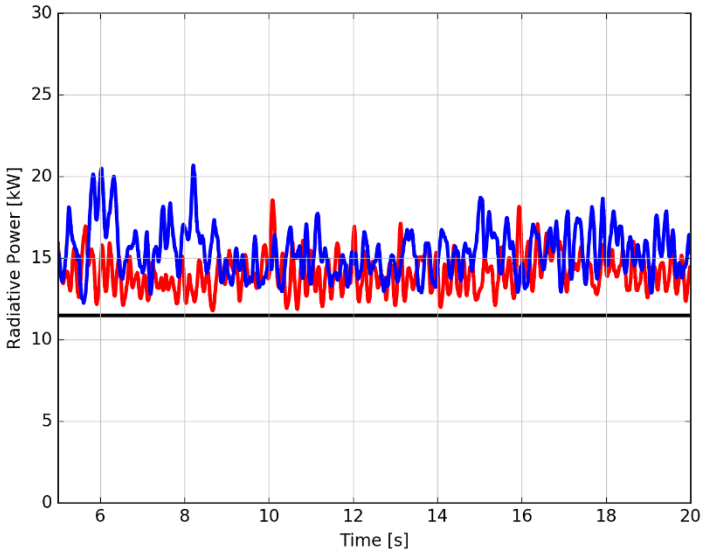


*Figure 88: Global radiative power over time. Comparison between LES results obtained with EDC/PGRF (black line), the $\widetilde{\chi_{st}}$ case (red line) and the $\widetilde{\chi_{st,Eff}}$ case (blue line).*

In the flamelet combustion models, we obtain thermo-chemical quantities of interest like temperature and mass fraction of species not by solving the conservation equations but extracting them from the turbulent flame LUT instead. Hence, the 50-kW flame is not guaranteed. A consistency check for the total heat release rate in the flamelet models to verify

how much heat release rate we have in the flamelet models is performed. We calculate the total heat release rate by spatially integrating the volumetric heat release rate $\overline{\dot{\omega}'''_{h_s}}$, which is extracted from the turbulent flame LUT, $\dot{Q}_{comb} = (\int_V \overline{\dot{\omega}'''_{h_s}} dV)$. We find $\dot{Q}_{comb} = 20.08$ kW for the $\widetilde{\chi_{st}}$ case and $\dot{Q}_{rad} = 40.12$ kW for the $\widetilde{\chi_{st,Eff}}$ case. After dividing by the global heat release rate (50 kW), these results are found to correspond to 40.11 % for the $\widetilde{\chi_{st}}$ case and 80.24 % for the $\widetilde{\chi_{st,Eff}}$ case (as showed in Figure 89 ). The check shows the strong dependence of the heat release rate on the flame stretch. This point is already showed in section III.4.2. Using $\widetilde{\chi_{st,Eff}}$ as the flame stretch parameter brings $\dot{Q}_{rad}$ in the flamelet model much closer to the experimental data than using $\widetilde{\chi_{st}}$. It also proves that for the flame stretch, $\widetilde{\chi_{st,Eff}}$ is a better choice.

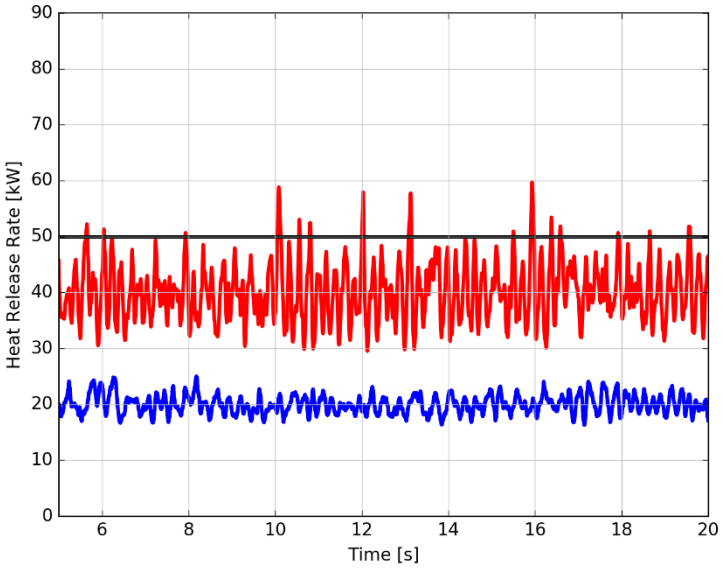


*Figure 89: Global heat release rate over time. Comparison between LES results obtained with EDC/PGRF (black line), the $\widetilde{\chi_{st,Eff}}$ case (red line) and the $\widetilde{\chi_{st}}$ case (blue line).*

### V.3.7 Number of outer loops sensitivity

The study on the sensitivity for the number of outer loops in the PIMPLE algorithm reported by [34] suggests that 3 loops are enough to enforce the mass conservation with a

relative error less than 0.5%. The choice of 3 loops is simply adopted for simulations in the flamelet model. However, simulation using the flamelet model are very unstable with the flame structure is much stiffer, *i.e.*, a greater gradient temperature and more fluctuations when compared to those in EDC (as showed in Figure 53). A new study on the number of outer loops sensitivity in the PIMPLE algorithm for the flamelet model is conducted and aims to provide a suitable choice.

| Simulation name | Laminar flamelet library | $\tilde{p}(Z)$ | $\widetilde{Z_v}$ model | LES-filtered stoichiometric scalar dissipation rate | Radiation model | Number of outer loops in PIMPLE |
|---|---|---|---|---|---|---|
| $\boldsymbol{N=3}$ | ULFV2 parameterized by $(Z, \chi_{st,Eff}, \Delta h_{st})$ | Top-hat PDF | Algebraic model 1 | $\widetilde{\chi_{st,Eff}}$ | Grey with TRI treatment | **3** |
| $\boldsymbol{N=5}$ | ULFV2 parameterized by $(Z, \chi_{st,Eff}, \Delta h_{st})$ | Top-hat PDF | Algebraic model 1 | $\widetilde{\chi_{st,Eff}}$ | Grey with TRI treatment | **5** |
| $\boldsymbol{N=8}$ | ULFV2 parameterized by $(Z, \chi_{st,Eff}, \Delta h_{st})$ | Top-hat PDF | Algebraic model 1 | $\widetilde{\chi_{st,Eff}}$ | Grey with TRI treatment | **8** |
| $\boldsymbol{N=12}$ | ULFV2 parameterized by $(Z, \chi_{st,Eff}, \Delta h_{st})$ | Top-hat PDF | Algebraic model 1 | $\widetilde{\chi_{st,Eff}}$ | Grey with TRI treatment | **12** |

*Table 10: Summary for the methods and modelling choices in current simulations.*

Figure 90, Figure 91 and Figure 92 show that the mean temperature obtained with $N = 3$ is much lower when compared to the experimental data. The results obtained with $N = 5$, $N = 8$ or $N = 12$ show good convergence properties and have a quite good agreement with the measurement (error of 50 K). The simulated results become approximately insensitive to the number of outer loops for $N > 5$, but the mean temperature peak simulated with $N = 8$ seems to be slightly better than the others.

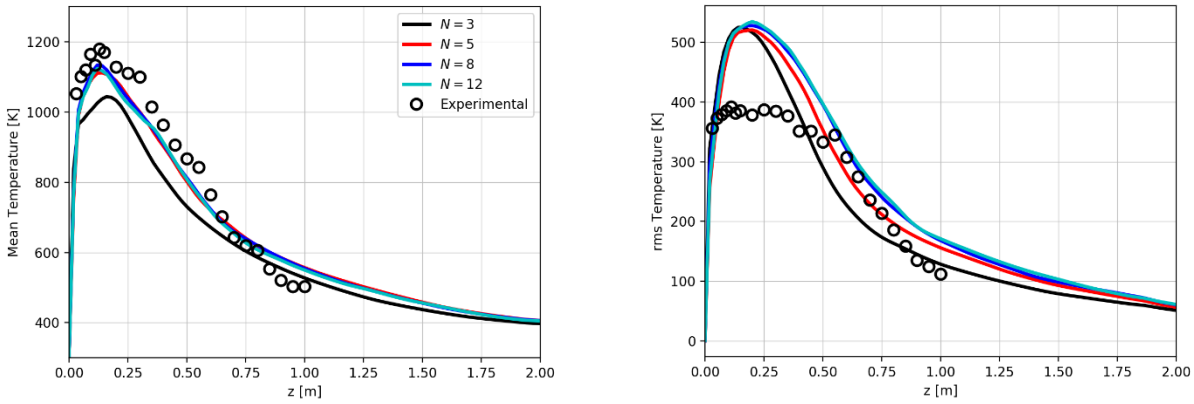


(a) (b)

*Figure 90: LES simulations of the turbulent line burner. Vertical variations of (a) the mean temperature $\overline{T}$ and (b) the rms temperature $T_{rms}$ along the flame centerline. Comparison between experimental data (symbols) and LES results obtained with the number of outer loops N = 3, 5, 8, 12.*

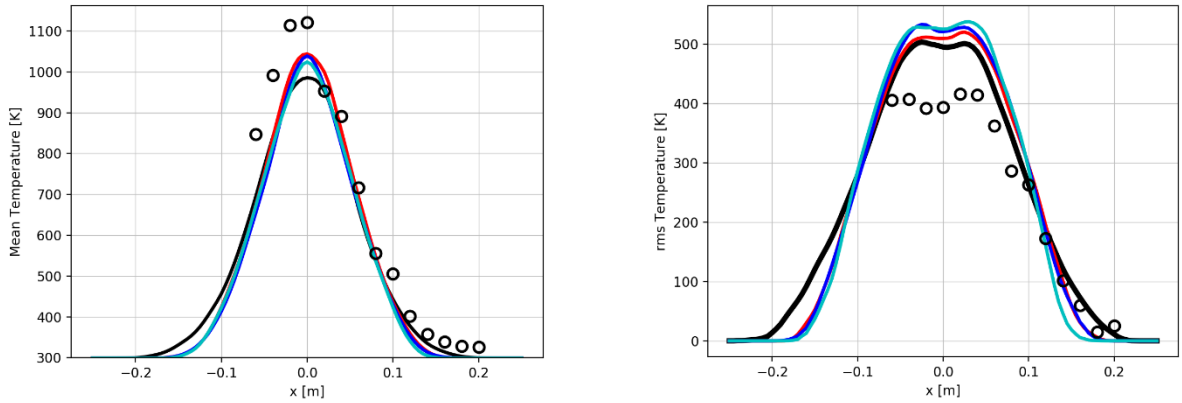


(a) (b)

*Figure 91: Cross-stream variations of (a) the mean temperature $\overline{T}$ and (b) the rms temperature $T_{rms}$ at $z = 0.25\ m$. See caption of Figure 90.*

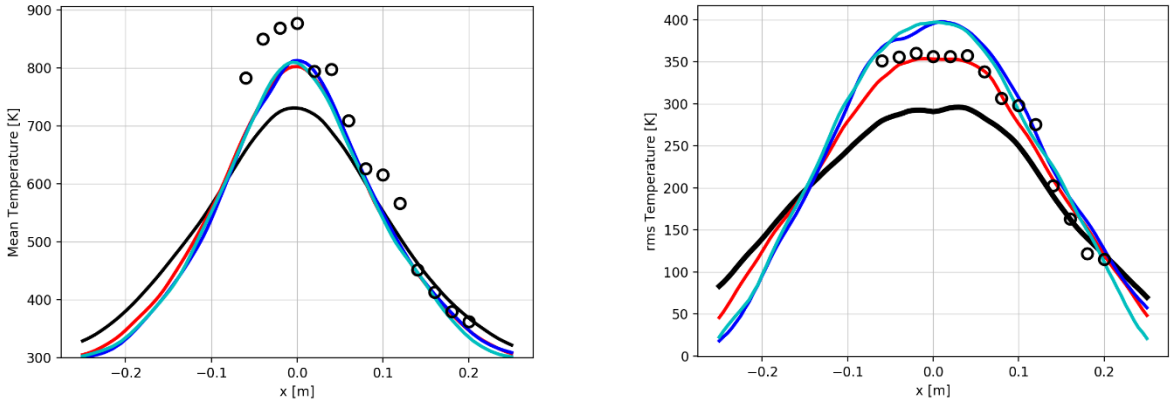


(a) (b)

*Figure 92: Cross-stream variations of (a) the mean temperature $\bar{T}$ and (b) the rms temperature $T_{rms}$ at $z = 0.5$ m. See caption of Figure 90.*

Figure 93 shows the global radiative power over time for different cases $N = 3$, $N = 5$, $N = 8$ and $N = 12$ and respectively, we found the time-averaged of the global radiative heat loss fraction $\chi_{rad}^{g}$ equal to 24.1%, 31.3%, 35.3% and 33.4% ($\chi_{rad}^{g}$ in the experimental data is equal to 23.8 %).

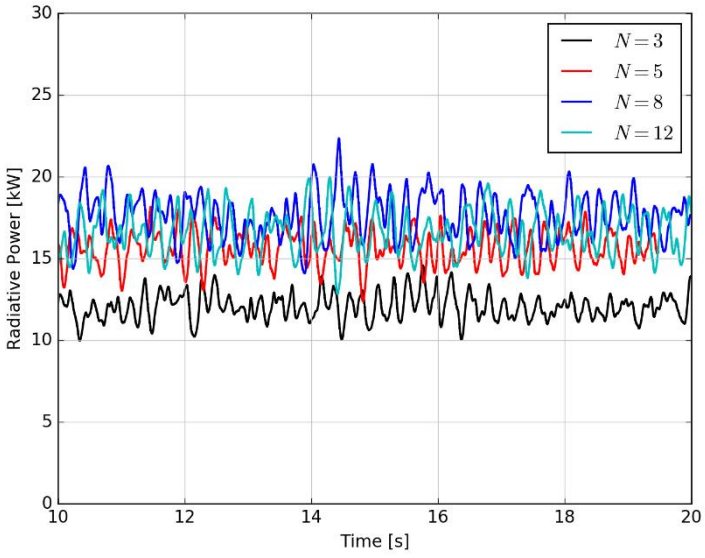


*Figure 93: Global radiative power over time. Comparison between LES results obtained with different number of outer loops N = 3, 5, 8, 12.*

Figure 94 shows the global heat release, which is calculated based on the suggestion in section V.3.6 using the volumetric heat release rate extracted from the turbulent LUT, over time for all cases. We found $\dot{Q}_{comb}$ equal to 33.85 kW, 38.85 kW, 44.87 kW and 42.85 kW for the simulation with $N = 3$, $N = 5$, $N = 8$ and $N = 12$, respectively. The nominal heat release rate of our flame is 50 kW. It means that the performance with $N = 8$ is the best choice. Combining with the analysis on the simulated temperature in the previous paragraph, we decide to choose $N = 8$ for the number of outer loops in the PIMPLE algorithm used in the flamelet model.

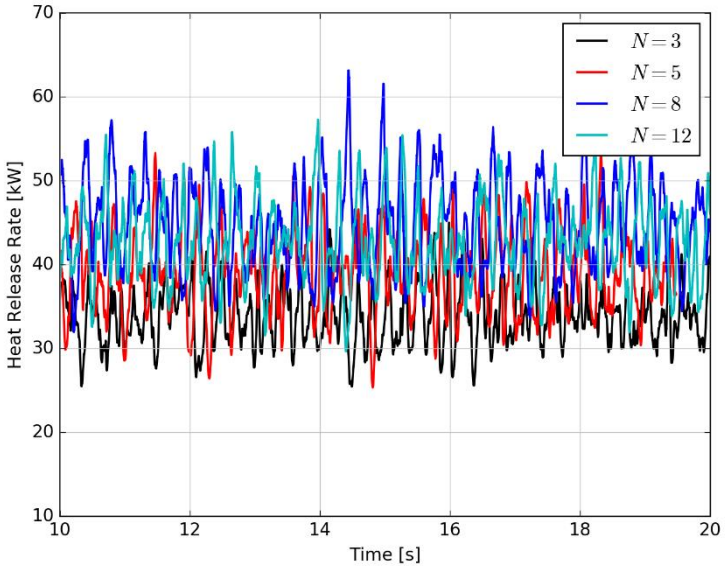


*Figure 94: Global heat release rate over time. Comparison between LES results obtained with different number of outer loops N = 3, 5, 8, 12.*

## V.4 Conclusion

The purpose of the present chapter is to develop the flamelet combustion model and radiation model for large eddy simulations (LES) of well-controlled laboratory-scale turbulent fires. The development of the combustion model consists of studying the different libraries of flamelet solutions produced using the different methods (SLFV1, SLFV2, ULFV1, ULFV2). Studying the different models of the turbulent flame LUT parameters as the sub-grid scale variance of mixture fraction, the scalar dissipation rate as well as the heat loss parameter. The

radiation model features a description of non-local phenomenon through the Radiative Transfer Equation (RTE). Different treatments of coupled combustion and radiation effects at flamelet scale are considered: a treatment in which local radiation phenomena are neglected inside the flamelet solver and a treatment in which these phenomena are included inside the flamelet solver and also sub-grid scale turbulence-radiation interactions (TRI) are included in the RTE solver. This chapter also presents a study on the sensitivity of the number of outer loops in the PIMPLE algorithm.

It is found in SLFV1/grey and SLFV1/WSGG that both cases under-predict significantly the mean temperature $\bar{T}$ when compared to the experimental data, a result is explained by several possibilities:

- Errors in the assumed PDF shape and/or errors in predictions of the LUT parameters, specially the sub-grid scale variance of mixture fraction and the scalar dissipation rate.
- The limitation of the SLFV1 method, which removes constantly the total enthalpy over the mixture fraction when treating with the heat losses to generate the flamelet library.

Plus, the simulated global radiative heat loss fraction in both SLFV1/grey and SLFV1/WSGG is also significantly under-predicted, a result is interpreted as the consequence of the low simulated temperature as well as the absence of the turbulence-radiation interaction (TRI).

The development of the flamelet combustion model is continued and focuses on fixing the limitation in the way the heat losses are treated in SLFV1. SLFV2, which has a more elaborate heat loss treatment using a method called Prescribed Local Radiative Fraction (PLRF), is introduced. Two simulations named SLFV1/Grey and SLFV2/Grey are performed, and their simulated results show that SLFV2/Grey is better in both temperature prediction and global radiative heat loss fraction when compared with SLFV1/Grey. However, the simulated mean temperature $\bar{T}$ (global radiative fraction $\chi_{rad}^{g}$) in SLFV2/Grey is still under-predicted by 100 K (3 %) when compared to the measurements.

The radiation model used in SLFV1/Grey and SLFV2/Grey is the grey model without considering the sub-grid scale turbulence-radiation interactions (TRI). To bring more physics

into the grey radiation model, the sub-grid scale TRI through a flamelet-based description of the emission term and mean absorption coefficient are accounted for. Two simulation named SLFV2/GreyNoTRI (without TRI) and SLFV2/GreyTRI (with TRI) are performed and the results show that the accuracy of predictions in the global radiative power is improved in the case of SLFV2/GreyTRI. We find $\chi_{rad}^{g} = 22.9\%$, in the case of SLFV2/GreyNoTRI. We just have $\chi_{rad}^{g} = 19.6\%$ ($\chi_{rad}^{g} = 23.0\%$ in the experimental data). Note that the simulated mean temperature $\bar{T}$ in all flamelet simulations so far is still low when compared to the measurement, hence, when the prediction of $\bar{T}$ is improved and increased closer to the measurement, $\chi_{rad}^{g}$ will be expected to be higher than the current accurate prediction (22.9%) by the grey model.

One of the possibilities that could lead to wrong predictions in simulated temperatures is errors in the assumed PDF shape and/or errors in predictions of the LUT parameters, specially the sub-grid scale variance of mixture fraction and the scalar dissipation rate. The study in section V.3.4 on the different sub-grid scale variance of mixture fraction $\widetilde{Z_v}$ models shows that the estimated temperature in the Algebraic model 2 and Transport equation cases is slightly better than in Algebraic model 1. Section V.3.5 investigates two PDF models for the mixture fraction $\tilde{p}(Z)$: the $\beta$-PDF and the top-hat PDF and its numerical results shows almost the same results in both temperature and global radiative heat loss fraction, a result proves the point that it is insensitive to the choice of $\tilde{p}(Z)$ [47]. Section V.3.6 studies on the effect of using the effective scalar dissipation rate $\widetilde{\chi_{st,Eff}}$ for replacing the instantaneous one $\widetilde{\chi_{st}}$. The predicted temperature and global radiative heat loss fraction in the $\widetilde{\chi_{st,Eff}}$ case are not better than those in the $\widetilde{\chi_{st}}$ case, but the predicted global heat release rate is (80.24 % for the $\widetilde{\chi_{st,Eff}}$ case and 40.11 % for the $\widetilde{\chi_{st}}$ case when compared to the nominal global heat release rate), a result proves that $\widetilde{\chi_{st,Eff}}$ is a better choice for the flame stretch model.

The last study on the sensitivity for the number of outer loops in the PIMPLE algorithm shows that the simulated results in simulations with $N > 5$ are much better than those obtained with $N = 3$. Detailed analyses on the simulated temperature, global radiative heat loss fraction, global heat release rate help us to choose $N = 8$ as the baseline choice for simulations with the flamelet model.

In conclusion, this chapter focuses on developing combustion and radiation models for LES of well-controlled laboratory-scale fires and it is evaluated in simulations of the methane-fueled turbulent line fire with the co-flow at the air condition. The studies in this chapter determine the best models and choice of parameters, which are going to be selected for simulations in the next chapter.

# Chapter VI Results: Turbulent Line Fire exposed to air-nitrogen co-flow without extinction

The previous chapter focuses on developing combustion and radiation models for LES of well-controlled laboratory-scale fires and it is evaluated in simulations of the methane-fueled turbulent line fire with the co-flow at the air condition. Studies in this chapter are the continuation of the study in previous section and aim to support the development and validation of models used to simulate the response of fires to the activation of suppression systems by gaseous agents.

The modeling framework features the flamelet combustion model and the grey radiation model with TRI, which are developed in Chapter V. The experimental configuration is the turbulent line fire with a controlled co-flow. The co-flow is an air-nitrogen mixture with variable oxygen dilution conditions, in which the conditions leading to full flame extinction is not considered. The flamelet model, which is capable of simulating the full extinction flame, will be developed in future works. Numerical results are evaluated against experimental measurements, which include the mean oxygen mole-fraction at $X_{O2} = 0.18$, the global radiative heat loss fraction and the combustion efficiency.

In the following, the experimental configuration is described in section VI.1. The numerical configurations, which include a description of the laminar flamelet library generation in the flamelet combustion model, are presented in section VI.2. Simulated results in the time-averaged temperature, molar fractions of oxygen, global heat loss fraction, global heat release rate are compared against the experimental data in section VI.3. Finally, conclusions are drawn, and the direction of future works is introduced.

## VI.1 Experimental configuration

The turbulent line burner described in section V.1 corresponds to the baseline unsuppressed flame configuration, *i.e.,* the co-flow is made of pure air. In the present study, the configuration adopted is also the turbulent line burner, but corresponds to suppressed flame configurations, *i.e.,* the air is diluted by nitrogen at the co-flow. The air and nitrogen mass flow

rates are variable while the total mass flow rate is fixed (and equal to 85 g/s). The oxygen mole fraction in the co-flow denoted as $X_{O2}$ varies between 21% and 11%.

An additional small co-flow stream of pure oxygen, called the oxygen anchor, is introduced along the length of the burner to strengthen the base of the flame and oppose liftoff extinction [75] (see Figure 95). The velocity of the oxygen anchor is 1.2 cm/s, corresponding to a mass flow rate of 0.08 g/s, and a nominal anchor-limited total heat release rate of 1 kW or 2% of the size of the unsuppressed flame.

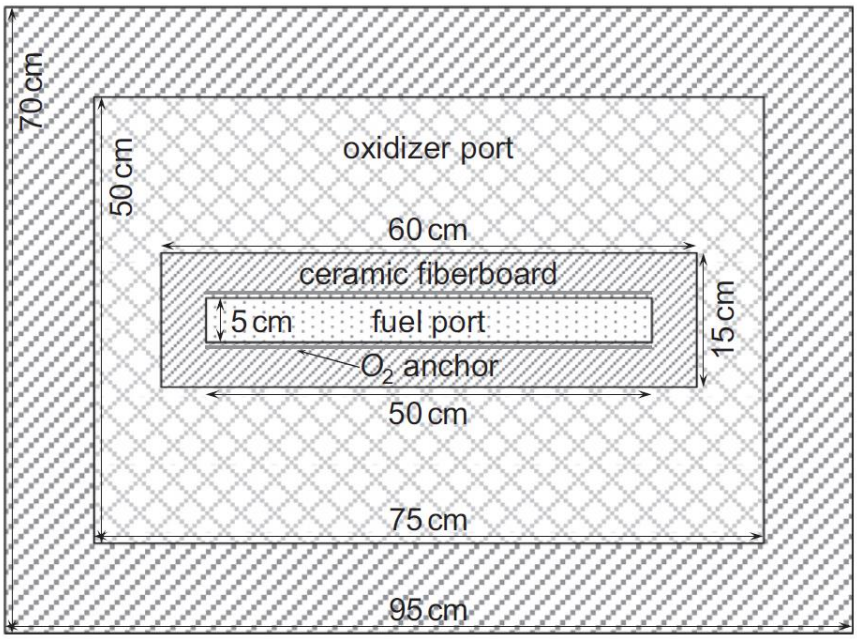


*Figure 95: Top view of the burner/co-flow outlet. Extracted from* [22].

Flame suppression is characterized through a variety of diagnostics including:

- Measurements of the global combustion efficiency using $CO_2$ generation and $O_2$ consumption calorimetry [32].
- Measurements of the global radiative loss fraction using a heat flux transducer combined with time-resolved infrared camera imaging and a multipoint radiation source model [75].
- Measurements of local gas temperature using exposed-junction, 1.0 mm bead-diameter K-type thermocouple probes (uncertainty ± 2 K; response time ~3 s).

- Measurements of local oxygen mole-fraction using a sampling probe connected to a Servomex 540E paramagnetic oxygen-analyzer (uncertainty ± 1250 ppm, response time ~5 s) [75].
- Combustion products for calorimetry measurements are collected in an exhaust duct, where a gas sampling system provides measurement of the mole-fractions of $O_2$, $CO_2$, CO and $H_2O$.

From these measurements, the global heat release rate ($\pm$1.5 kW) is derived via mass conservation analysis (for a detailed description of this measurement, the reader is referred to Ref. [32]). Combustion efficiency ($\pm$3%) is determined by dividing the calorimetry-derived heat release rate by the nominal total heat release rate of the flame (50 kW), defined as the product of the measured fuel mass flow rate times the theoretical heat of combustion. The combustion efficiency is a function of the oxygen mole-fraction in the co-flow. Global flame extinction is observed at $X_{O2,ext} = 12.2\% \pm 0.2\%$.

## VI.2 Numerical configurations

### VI.2.1 Numerical configuration

The test in section V.3.7 suggests that we should use the number of outer loops in the PIMPLE algorithm equal to 8, instead of 3. The over-prediction of the global radiation heat losses in the grey radiation is the reason for motivating us to use the more elaborate model in next steps: the banded Weighted-Sum-of-Grey-Gases (WSGG) model that accounts for spectral variations of radiation properties. The number of outer loops of 8 and WSGG cost computationally expensive and make simulations less practical. To overcome the issue, several solutions are proposed:

- First, the computation domain is reduced from $2 \times 2 \times 2$ m$^3$ and now has only 1.5-m-wide in the cross-stream x-direction, 1.2-m-long the spanwise y-direction and 2-m-high in the vertical z-direction. The grid has almost the same in the refinement block ($15 \times 50 \times 30$ cm$^3$), which contains the flame region and features a uniform grid with cubic cells. The grid cell size is $\Delta x_1 = 5$ mm (*i.e.,* 10 grid cells across the burner width). The outside of the refinement block is stretched in the outward

direction from the flame region with the expansion-ratio equal to 4% (see Figure 96). The total number of cells is reduced from 4.7 million to 2.7 million.

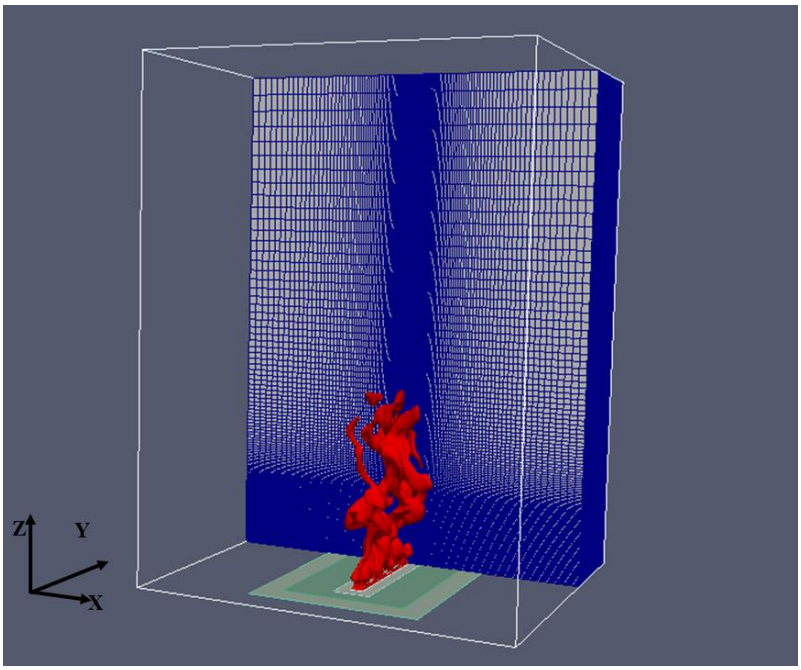


*Figure 96: Reduced computational domain with the stretched mesh.*

- Second, the duration of simulations is reduced from 30 s to 20 s and turbulent statistics are collected for the final 15 s of each simulation after the flow and flame become statistically stationary and long enough for the statistics to be converged.

Some tests studying the effects of the changes of the gird (not shown here) have negligible discrepancies. The computational cost for new simulations after implementing these changes are similar to those with the full size ($2 \times 2 \times 2$ m$^3$) with the number of outer loops of 3.

### VI.2.2 Modeling framework

Modeling choices in the present study, *i.e.*, the flame exposed to the co-flow with decreasing oxygen strength will use the best options so far based on the preliminary studies in Chapter V and they are summarized briefly in Table 11.

| Laminar flamelet library | $\tilde{p}(Z)$ | $\widetilde{Z_v}$ model | Flame stretch | Radiation model | Number of outer loops in PIMPLE |
|---|---|---|---|---|---|
| ULFV1 parameterized by $(Z, \chi_{st,Eff}, \Delta h_{st})$ | Top-hat PDF | Algebraic model 2 | $\widetilde{\chi_{st,Eff}}$ | Grey with the TRI treatment | 8 |

*Table 11: Summary of the modeling choices.*

Numerical simulations in the present study are performed at the mole fraction of oxygen $X_{O2}$ equal to 0.21, 0.18, 0.16, 0.14, 0.13, where the extinction still does not occur. The laminar flamelet libraries used for the different $X_{O2}$ cases are produced using the ULFV1 method. First, the steady adiabatic solutions located at the stable branch of the S-shaped curve for different values of $\chi_{st}$ ranging from $10^{-4}$ [1/s] to the upper extinction limit $\chi_{ext}^{high}$ are generated with only changes in the boundary condition at the oxidizer side for oxygen and nitrogen between all $X_{O2}$ cases (as demonstrated in Figure 97). Figure 98 shows that when decreasing $X_{O2}$, the peak temperature is decreased, and its location tends to move closer toward the boundary at $Z = 0$. The reason is that the stoichiometric mixture fraction $Z_{st}$, which is given by: $Z_{st} = Y_{O2}^0/(\xi Y_{CH4}^0 + Y_{O2}^0)$, where $\xi = 4$ in the methane flame, decreases linearly as a function of $X_{O2}$ (Figure 99).

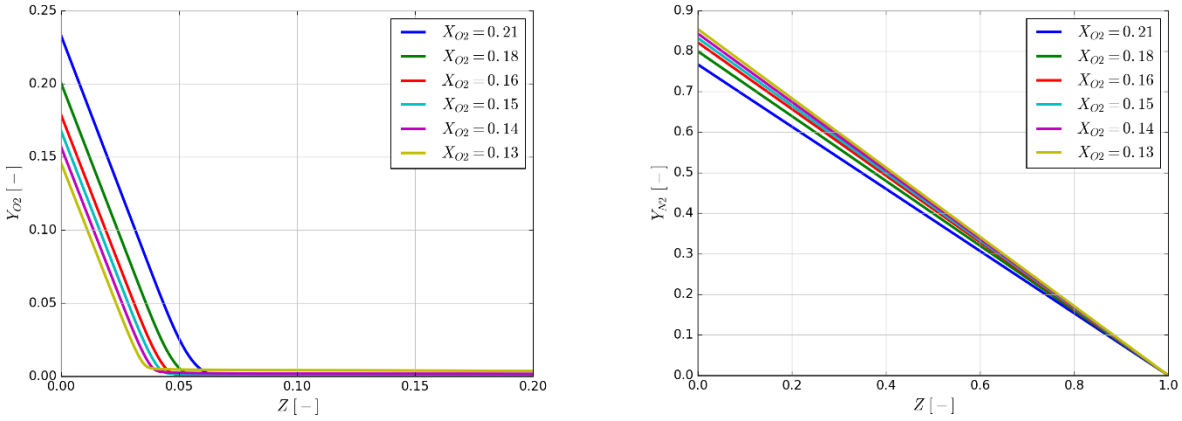


(a) (b)

*Figure 97: Comparison of the mass fraction of oxygen (a) and nitrogen (b) profiles across the flamelet at $\chi_{st} = 0.01$ [1/s] for the different $X_{O2}$ cases.*

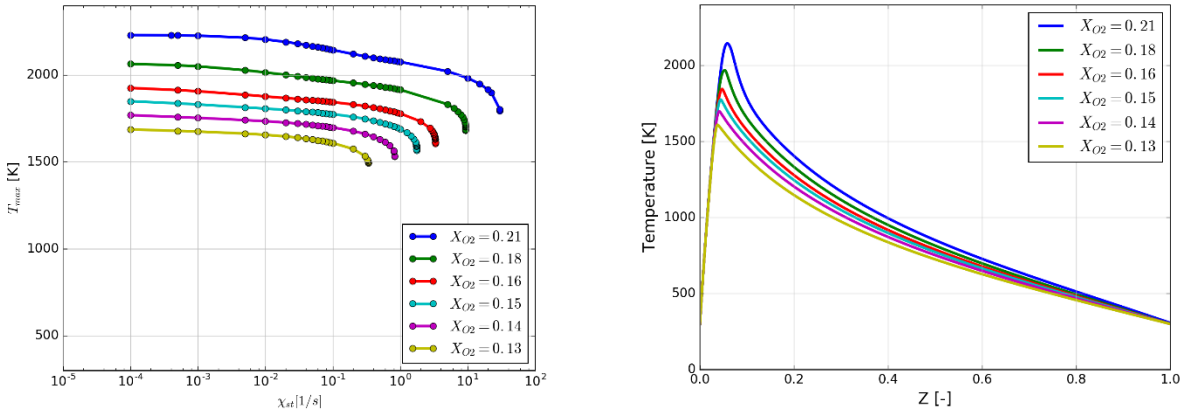


(a) (b)

*Figure 98: (a) Comparison of the peak temperature over $\chi_{st}$ (a) and the temperature profile across the flamelet at $\chi_{st} = 0.1$ [1/s] (b) between all $X_{O2}$ cases at the adiabatic condition.*

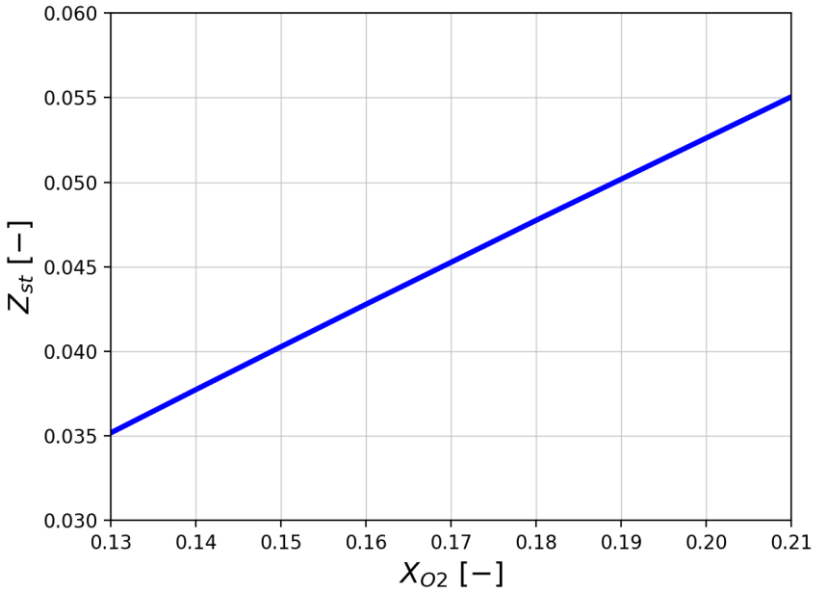


*Figure 99: The stoichiometric mixture fraction $Z_{st}$ as a function of the molar fraction of oxygen $X_{O2}$.*

The steady adiabatic solution then is used as the initial solution for the unsteady flamelet calculations with a given $\chi_{st}$ over time. The process is repeated for different given values of

$\chi_{st}$ covering all the range for each $X_{O2}$. Figure 100 shows the all unsteady flamelet solutions for all $X_{O2}$ cases including the flamelets, which will be used in the flamelet library, and the flamelet, which will be ignored in the flamelet library due to the non-monotonic issues, which is explained in section IV.1.2a

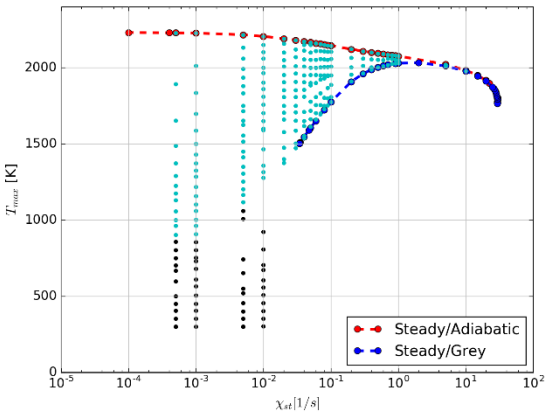


(a)

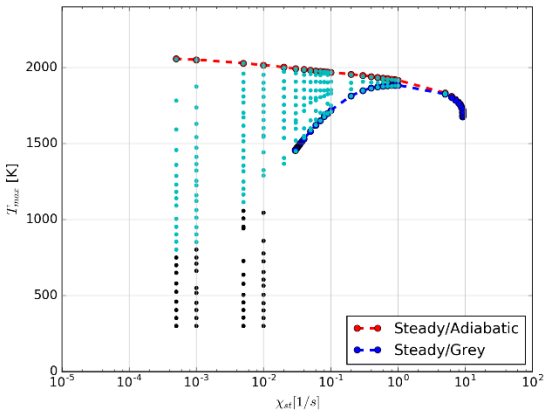


(b)

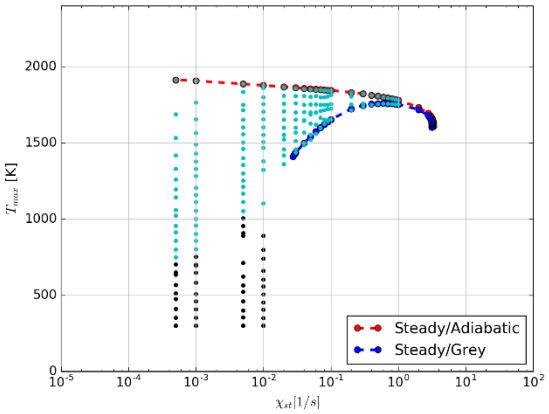


(c)

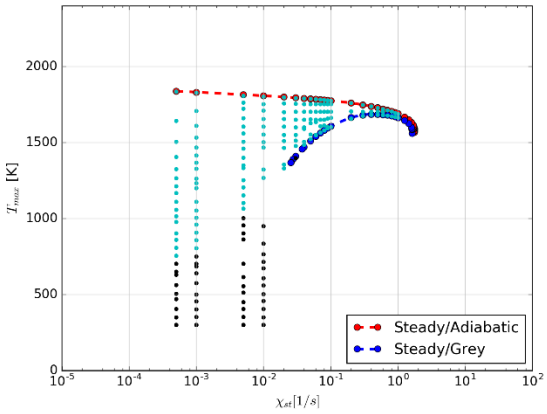


(d)

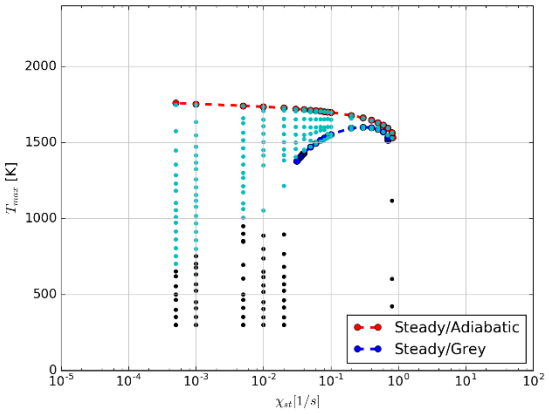


(e)

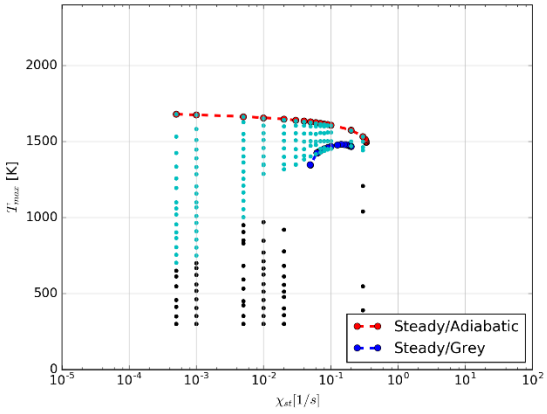


(f)

*Figure 100: Peak temperatures as a function of stoichiometric scalar dissipation rate for all unsteady/grey solutions generated by the ULFV1 method at $X_{O2} = 0.21$ (a), $X_{O2} = 0.18$ (b), $X_{O2} = 0.16$ (c), $X_{O2} = 0.15$ (d), $X_{O2} = 0.14$ (e), $X_{O2} = 0.13$ (f). Cian dots symbols represent unsteady solutions, which will be used in the laminar flamelet library. Meanwhile, black dot symbols are solutions, which are ignored in the laminar flamelet library.*

Some thermochemical quantities of interest in the flamelet library catch our attention in the current study. Figure 101 shows that at the same values of the flamelet library parameters $\chi_{\mathrm{st}}$ and $\Delta h_{st}$, the radiative emission term, which will be extracted and used in the RTE equation in FireFOAM, decreases when $X_{O2}$ is decreased. It implies that the simulated global heat loss fraction $\chi_{rad}^{g}$ for the turbulent line burner is expected to have a decreasing trend when $X_{O2}$ is decreased. Figure 102 shows the magnitude of integrated heat release rate, which is extracted and used in FireFOAM for the flame power check, increases like the square root of $\chi_{st}$ for all $X_{O2}$ cases. However, for a lower value of $X_{O2}$, at a given $\chi_{st}$, the heat release rate is slightly higher.

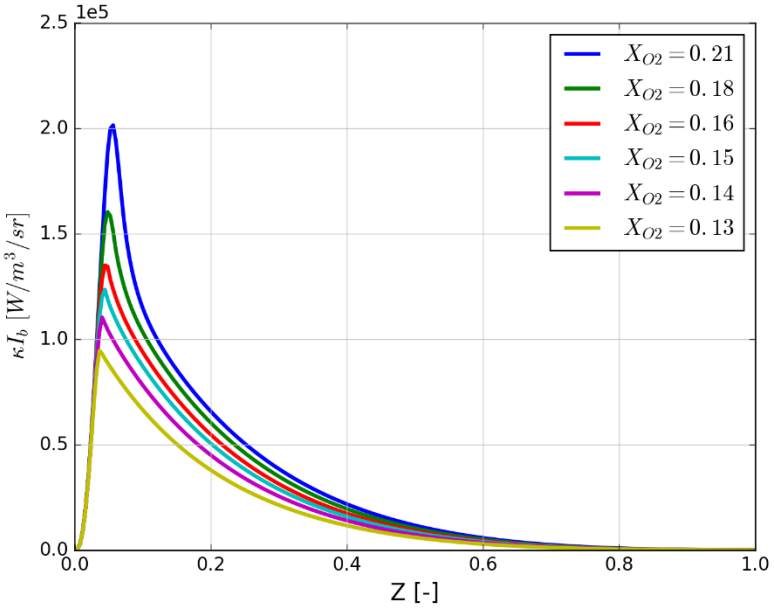


*Figure 101: Comparison of the radiative emission across the flamelet characterized by* $\chi_{st} = 0.1$ *[1/s] and* $\Delta h_{st} = 0$ *[kJ/kg] between* $X_{O2}$ *cases.*

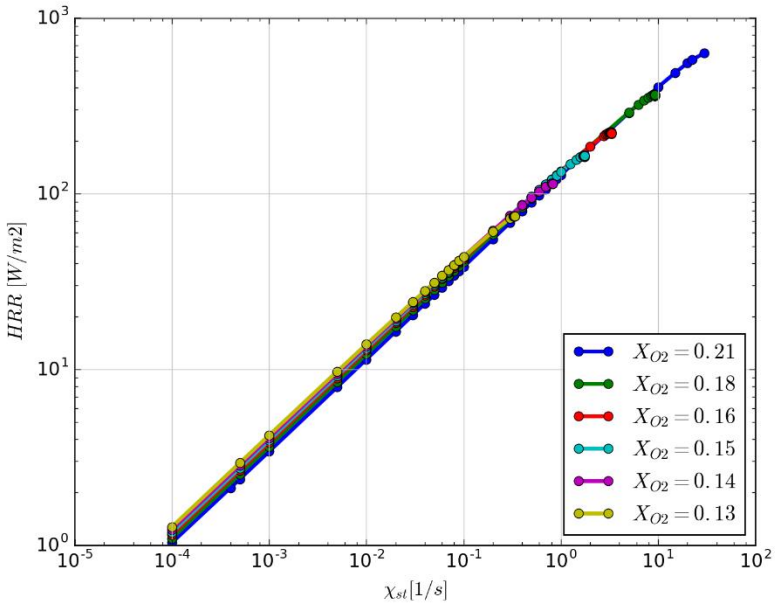


*Figure 102: Comparison of the integrated heat release rate across the flamelet characterized by* $\chi_{st} = 0.1$ *[1/s] and* $\Delta h_{st} = 0$ *[kJ/kg] between* $X_{O2}$ *cases.*

The decreased strength of oxygen of the oxidizer side has a strong impact on the extinction limits. Figure 103 shows that the flame zone, defined as the location between the high extinction limits $\chi_{ext}^{high}$ (which is caused by the aerodynamic strain rate) and the low extinction limit $\chi_{ext}^{low}$ (which caused by the radiation heat loss), narrows down when $X_{O2}$ is decreased. From 0.21 to 0.15 of $X_{O2}$, $\chi_{ext}^{high}$ decreases strongly while $\chi_{ext}^{low}$ is almost unchanged. From 0.15 to 0.13, $\chi_{ext}^{high}$ accelerates the decrease and $\chi_{ext}^{low}$ starts increasing. The results are expected to have no flame zone anymore, *i.e.*, $\chi_{ext}^{high}$ and $\chi_{ext}^{low}$ intersect, when $X_{O2}$ is decreased to lower values than 0.13. At high values of $X_{O2}$ (from 0.21 to 0.16), $\chi_{ext}^{high}$ stays at the locations where radiation heat loss can be neglected, hence $\chi_{ext}^{high}$ can be identified either in the steady/adiabatic calculation or the steady/non-adiabatic calculation. For lower values of $X_{O2}$, (from 0.16 to 0.13), $\chi_{ext}^{high}$ is decreased to lower values, *i.e.*, to flame conditions, where radiation plays an important role and can not be neglected. Hence, $\chi_{ext}^{high}$ is lower in the steady/adiabatic condition than the steady/non-adiabatic condition.

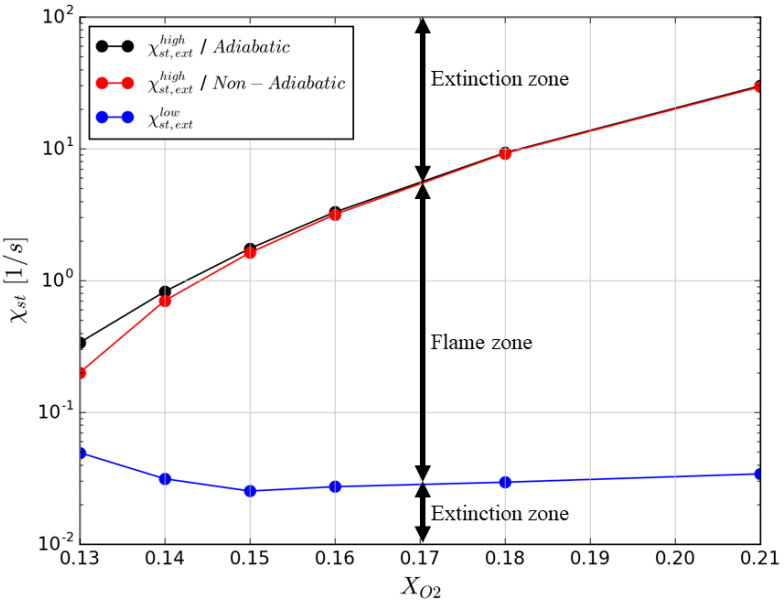


*Figure 103: Peak temperature as a function of stoichiometric scalar dissipation rate for all unsteady/grey solutions.*

## VI.3 Results and discussion

### VI.3.1 Spatial variations of temperature and oxygen mole-fraction

The modeling developments as well as parameter sensitivity studies for the flamelet combustion model in Chapter V are performed with the flame-air condition, *i.e.*, $X_{O2} = 0.21$. The simulated results are evaluated against the baseline EDC/PGRF and the experimental measurements in the mean temperature $\overline{\mathrm{T}}$ and the rms temperature $\mathrm{T_{rms}}$ along the flame centerline (Figure 104), in the cross-stream direction $x$ at the evaluations: $z = 25$ cm (Figure 105), $z = 50$ cm (Figure 106), $z = 75$ cm (Figure 107) and $z = 100$ cm (Figure 108). The numerical results with the flamelet model show a good agreement with the baseline and the experimental data in for the mean temperature $\overline{\mathrm{T}}$. In contrast, the simulated rms temperature $\mathrm{T_{rms}}$ for both the flamelet/grey and the EDC/PGRF are over-predicted by 100 K at the flame region.

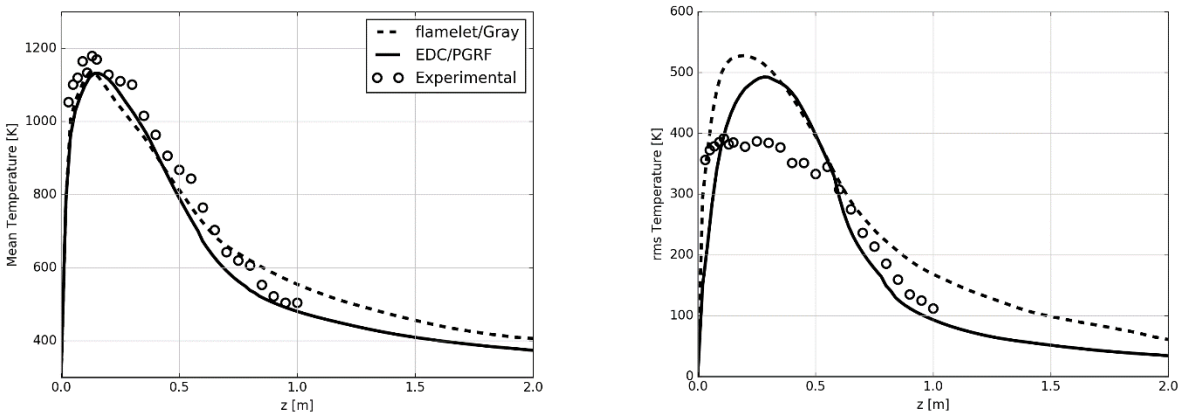


(a) (b)

*Figure 104: LES simulations of the turbulent line burner. Vertical variations of (a) the mean temperature $\overline{T}$ and (b) the rms temperature $T_{rms}$ along the flame centerline at $X_{O2} =$ 0.21.*

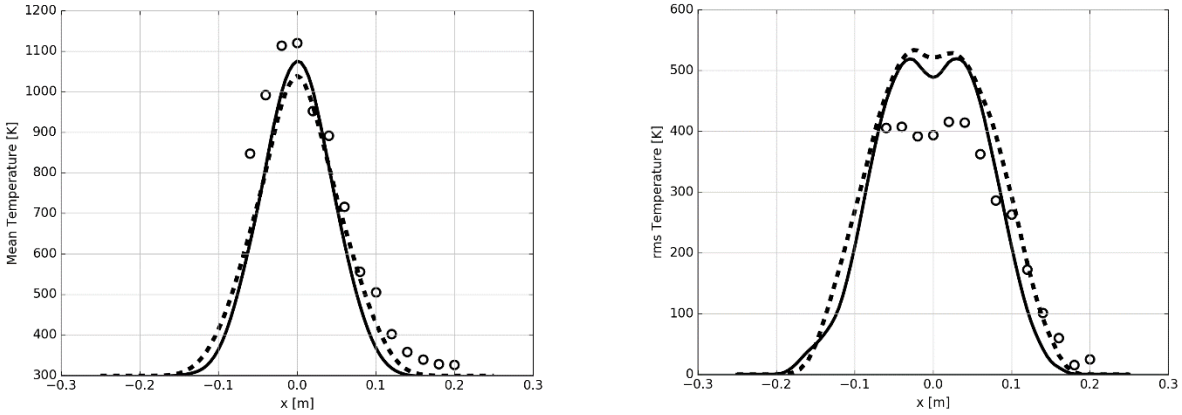


(a) (b)

*Figure 105: Cross-stream variations of (a) the mean temperature $\overline{T}$ and (b) the rms temperature $T_{rms}$ at $z = 0.25\ m$ for $X_{O2} = 0.21$. See the legend of Figure 104.*

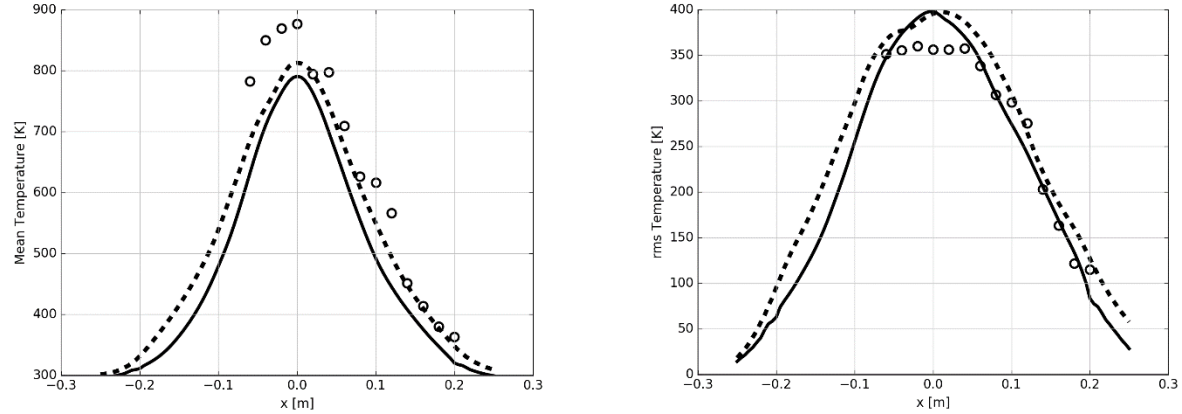


(a) (b)

*Figure 106: Cross-stream variations of (a) the mean temperature $\overline{T}$ and (b) the rms temperature $T_{rms}$ at $z = 0.5\ m$ for $X_{O2} = 0.21$. See the legend of Figure 104.*

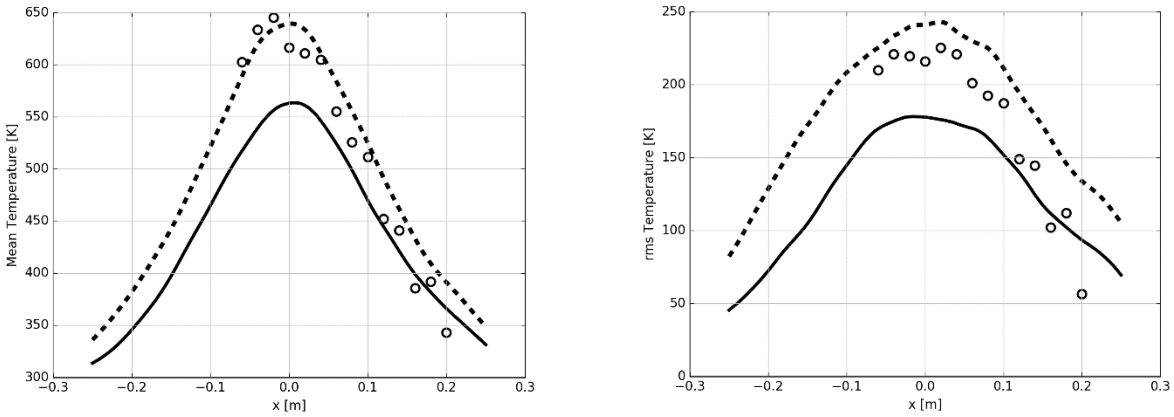


(a) (b)

*Figure 107: Cross-stream variations of (a) the mean temperature $\overline{T}$ and (b) the rms temperature $T_{rms}$ at $z = 0.75\ m$ for $X_{O2} = 0.21$. See the legend of Figure 104.*

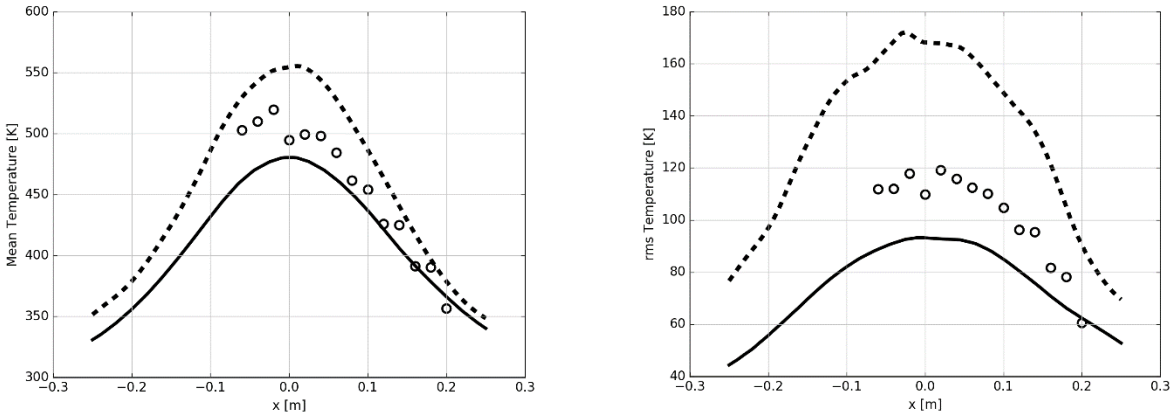


(a) (b)

*Figure 108: Cross-stream variations of (a) the mean temperature $\overline{T}$ and (b) the rms temperature $T_{rms}$ at $z = 1.0\ m$ for $X_{O2} = 0.21$. See the legend of Figure 104.*

The good agreement in the mean temperature with $X_{O2} = 0.21$ suggests that both modeling developments and parameter choices for the flamelet combustion model are at a high accuracy and these modeling choices are simply re-used in simulations for the flame exposed to the co-flow with decreasing oxygen strength.

Now, we turn to a brief description on spatial variations of temperature and oxygen mole-fraction statistics. Except for the $X_{O2} = 0.21$ case, experimental measurements are currently only limited to mean (time-averaged) values (temperature and oxygen mole-fraction), limited to cross-stream profiles at two elevations : z = 0.125 m and z = 0.25 m, and limited to the $X_{O2} = 0.18$ case.

Figure 109 presents a comparison between the simulated and measured mean values of thermocouple temperature and oxygen mole-fraction as a function of the cross-stream distance $x$ at two elevations: $z = 12.5$ cm and $z = 25$ cm. The simulated temperature with both EDC/PGRF and flamelet/grey is slightly under-predicted by less than 10 % when comparing with the experimental measurement. The under-predicted temperature could be due to over-prediction of the radiative heat losses, which will be presented the next section.

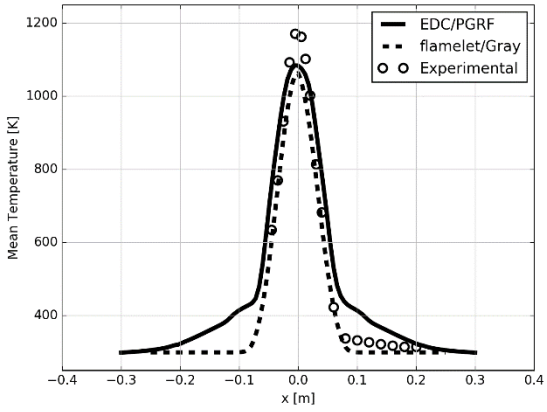


(a)

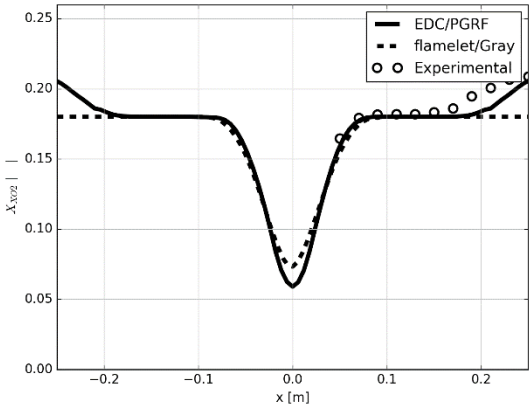


(b)

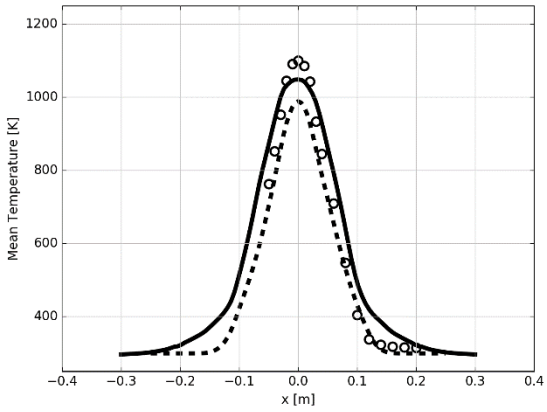


(c)

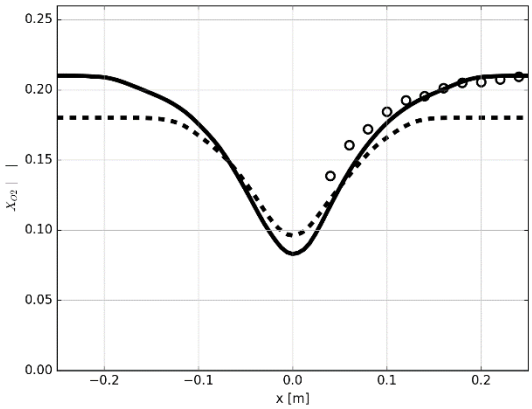


(d)

*Figure 109: Spatial cross-stream variations of simulated (for both the baseline EDC/PGRF and flamelet/grey cases) and measured mean values of temperature and oxygen mole-fraction. Case with diluted air-nitrogen co-flow with $X_{O2} = 0.18$, (a) Mean temperature at z =12.5 cm, (b) Mean oxygen mole-fraction at z = 12.5 cm, (c) Mean temperature at z =25 cm, (d) Mean oxygen mole-fraction at z = 25 cm.*

The simulated oxygen mole-fraction for EDC/PGRF shows good agreement with the experimental data. In contrast, flamelet/grey does not have a good prediction, specially at the locations far away from $x = 0$. The reason for the wrong prediction comes from a restriction of the current flamelet model. We know that the experimental configuration has three streams: Fuel, Co-flow and Air entrainment (Figure 110 (a)) while in the flamelet model, only one mixture fraction is used, hence only the fuel and co-flow streams can be involved. Therefore, we assume that in the numerical configuration for the flamelet model, the air entrainment flow is replaced by the co-flow (see Figure 110 (b)). Figure 109 (b) shows that at $z = 12.5$ cm and for $|x| \geq 0.19$ m, where the co-flow stream with $X_{O2} = 0.18$ and the air entrainment stream with $X_{O2} = 0.21$ mix together, the flamelet model differs to the baseline EDC/PGRF (which does not have the limitation) as well as the measurement. Figure 109 (d) shows that at $z = 25$ cm, where the air entrainment stream and co-flow stream mix basically everywhere, hence the experimental data is much higher than those in flamelet/grey.

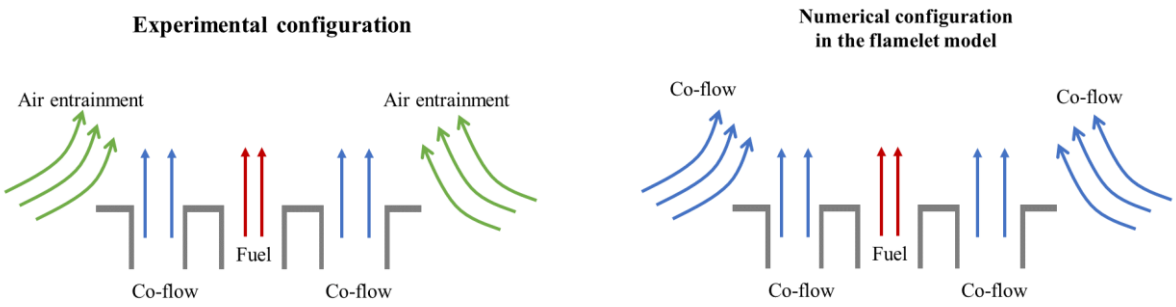


(a) (b)

*Figure 110: Demonstration of three streams in the experimental configuration (a) and two streams in the numerical configuration corresponding to the flamelet model (b).*

### VI.3.2 Flame radiative emissions

The experimental database includes measurements of the global radiative loss fraction $\chi_{rad}^{g}$ using a heat flux gauge (the remote gauge), which is combined with an infrared camera imaging and a radiation source model [23]. It is found in Ref. [23] the global radiative heat loss fraction $\chi_{rad}^{g}$ is not constant throughout a series of experiments and gradually decreases as the flame is exposed to the co-flow with decreasing oxygen strength. In the present study, the description of thermal radiation is treated with the grey radiation model coupled with TRI. Simulations are performed with a duration of 20 s and turbulent statistics are collected for the final 15 s of each simulation for different values of $X_{O2}$ (6 cases: 0.21, 0.18, 0.16, 0.15, 0.14, and 0.13).

Figure 111 and Figure 112 show that the simulated and measured global radiative power $\chi_{rad}^{g}$ decreases gradually as $X_{O2}$ is decreased. While the decreasing trend is well captured in the numerical simulations, flamelet/grey significantly over-predicts $\chi_{rad}^{g}$ when compared to the measurements. The reason could be explained by the usage of the radiation model with the grey assumption. In order to improve the performance of predicting $\chi_{rad}^{g}$, a more elaborate, non-grey model coupled with TRI, which can account for the variation of radiation properties with wavelength, will be considered in future works.

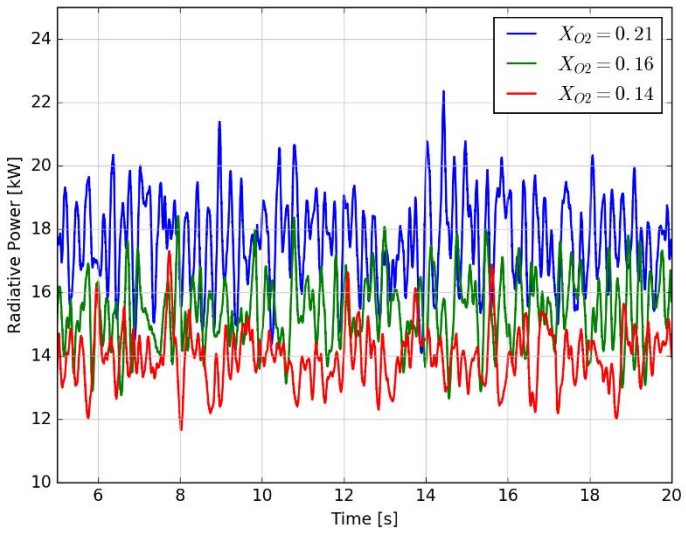


*Figure 111: Global radiative power over time in the flamelet/Grey case for different values of $X_{O2}$.*

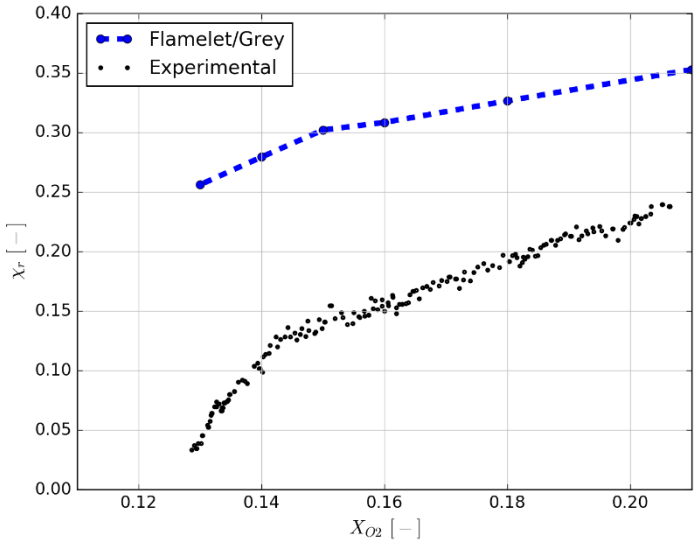


*Figure 112: Comparison of simulated global radiative power against the measurements as a function of oxygen mole-fraction.*

### VI.3.3 Combustion efficiency

Section V.3.6 introduced a method for checking the total energy released in the flamelet model by spatially integrating over the computational domain the volumetric heat release rate $\overline{\dot{\omega}_{h_s}'''}$, which is extracted from the turbulent flame LUT: $\dot{Q}_{comb} = (\int_V \overline{\dot{\omega}_{h_s}'''} dV)$. Since $\overline{\dot{\omega}_{h_s}'''}$ is not used in the energy equation, hence the simulated temperature is not dependent on $\overline{\dot{\omega}_{h_s}'''}$. Therefore, this energy checking method cannot guarantee that that the flamelet-based value of $\dot{Q}_{comb}$ is equal to the experimental 50 kW. Another method, which uses directly relating-temperature quantities to calculate the total energy released in the flamelet model $\dot{Q}_{comb}$, is proposed and calculated as follows:

$$\dot{Q}_{comb} = \int -\overline{\nabla . \dot{q}''} dV + \oint \bar{\rho} \tilde{u}_j \tilde{h}_s dS + \oint \bar{\rho} (\frac{\nu}{Pr} + \frac{\nu_{sgs}}{Pr_{sgs}}) \frac{\partial \tilde{h}_s}{\partial x_j} dS \qquad \text{(VI-1)}$$

where $\tilde{h}_s$ denotes the sensible enthalpy and is obtained through the subtraction of the chemical enthalpy $\tilde{h}_c$ from the total enthalpy $\tilde{h}$ ($\tilde{h}_s = \tilde{h} - \tilde{h}_c$). The R.H.S of the Eq. (VI-1), in which the first, second, third term represents the radiation, convection, diffusion heat transfer respectively, calculates to the total net energy coming out from the computational domain.

Figure 113 (a) shows that for $X_{O2} = 0.21$ diffusion heat transfer's contribution is very small and negligible. The total heat transfer is mainly contributed by the radiation and convection methods, which correspond approximately to 35% and 65% respectively. We found the time-averaged of the total heat transfer rate $\dot{Q}_{comb} = 53.615$ kW and after dividing by the nominal global heat release rate (50 kW), the result is found to correspond to 107.23 % of the nominal global heat release rate. Like for $X_{O2} = 0.21$, we found the similar results for $X_{O2} = 0.18$ with $\dot{Q}_{comb} = 53.84$ kW corresponding to 107.68 % of the nominal global heat release rate.

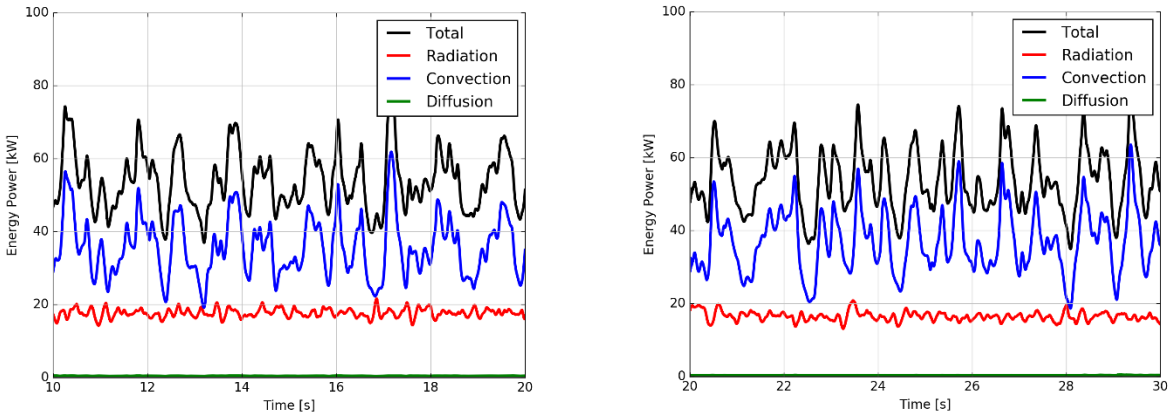


(a) (b)

*Figure 113: Comparison of the heat transfer methods calculating the energy coming out of the numerical domain as a function of time for $X_{O2} = 0.21$ (a) and for $X_{O2} = 0.18$ (b).*

Figure 114 shows the comparison of simulated combustion efficiency against the measurements as a function of $X_{O2}$ with the nominal global heat release rate (50 kW) as a reference. When comparing with the experimental data, we found that the numerical results slightly over-predict the global heat release rate for different values of $X_{O2}$. The simulated global heat release rate is considered as a quite good result since the discrepancy is only about 7%.

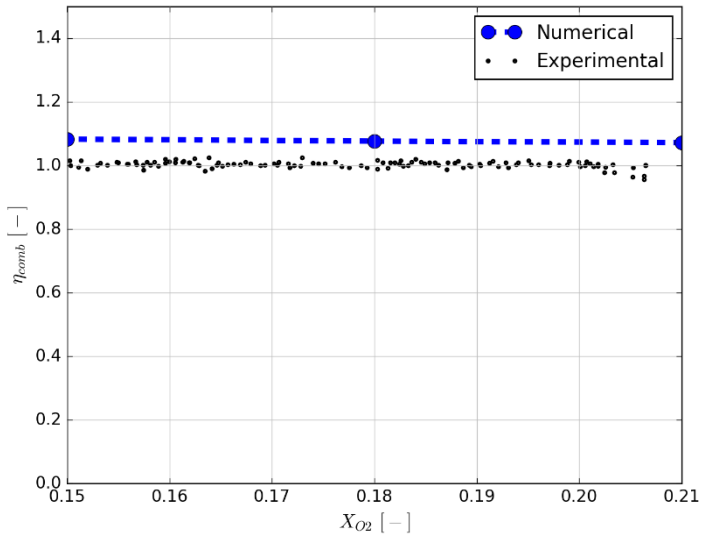


*Figure 114: Comparison of simulated combustion efficiency against the measurements as a function of oxygen mole-fraction.*

## VI.4 Conclusion

The studies in the chapter VI aim to support the development and validation of models used to simulate the response of fires to the activation of suppression systems by gaseous agents. Models and parameters used in the simulations of this chapter are chosen based on the modeling development, parameters sensitivity studies performed in the previous chapter. The modeling framework features the flamelet combustion model and the grey radiation model with TRI. The numerical configuration size is reduced from $2 \times 2 \times 2$ m$^3$ to $1.5 \times 1.2 \times 2$ m$^3$ with the stretched grid type. The experimental configuration is the turbulent line fire with a controlled co-flow. The co-flow is an air-nitrogen mixture with variable oxygen dilution conditions, in which the conditions leading to full flame extinction is not considered. The description of flame extinction and re-ignition events requires an additional laminar flamelet library parameter typically chosen as a reaction progress variable [67]. This extension of the model will be considered in future work.

A series of new numerical simulation for different values of $X_{O2}$ is performed and then evaluated against the experimental measurements. It found that at $X_{O2} = 0.18$, the flamelet model slightly under-predicts the mean temperature (less than 10 %), a result that could be

explained by the over-prediction of radiation heat losses of the grey model. The simulated results of mean oxygen mole-fraction have a big discrepancy when comparing with the measurement, a result that reveals the limitation of the current flamelet model, which allows only two streams (fuel and co-flow) to be involved while the experimental configuration features a third stream, *i.e.*, the air entrainment stream. The comparison between the numerical and experimental methods for the global radiative heat losses $\chi_{rad}^{g}$ are also demonstrated. The numerical results capture well of the decreasing trend of $\chi_{rad}^{g}$ when $X_{O2}$ is decreased, however, significantly over-predict $\chi_{rad}^{g}$ when comparing with the measurements at each $X_{O2}$. The over-prediction of $\chi_{rad}^{g}$ is due to the limitation of the grey model, which neglects the variation effect of radiation properties with wavelength. The simulated combustion efficiency agrees very well with the experimental data with the discrepancy of only 7%.

# Conclusion and future work

The context of this thesis is that CFD modeling applied to fire safety problems has made remarkable progress over the past two decades, but modeling capabilities still remain limited by a number of simplifying assumptions of variable and often unknown accuracy. Combustion models used in simulations of fires generally rely on a global combustion equation and do not include finite rate chemistry. In addition, radiation models used in simulations of fires generally rely on the assumption of a linear relationship between radiative power and heat release rate using a coefficient of proportionality or the global radiant fraction (GRF). These models must rely on the empirical calibration of GRF with fuel type and fire conditions.

Hence, the general objective of this research project is to develop models that account for combustion chemistry, and that calculate (rather than prescribe) radiant emissions. The proposed modeling framework uses the LES approach and is based on a laminar flamelet model and a careful treatment of the coupling between combustion and radiation that differentiates between non-local (*i.e.*, non-flamelet) and local (*i.e.*, flamelet) effects. The model also includes a description of sub-grid scale turbulence-radiation interactions (TRI). This modeling approach is tested against measurements performed in an experiment previously studied at the University of Maryland (UMD) and corresponding to a buoyancy-driven, turbulent line flame with a controlled air-nitrogen co-flow.

The manuscript features six chapters and each chapter is devoted to specific tasks as follows:

- In Chapter I, a brief introduction on fire, principals CFD methods and two solvers of fire modeling, the limitations of the current combustion and radiation models in fire applications are first presented. Then, the plan and objective of this project is introduced.
- In Chapter II, the numerical solver, the general governing equations for flows are introduced, followed by an introduction of the adopted turbulence model, of the baseline combustion model as well as radiation models.
- Chapter III provides some preliminary studies on the laminar, planar, strained counterflow diffusion flame, which is considered as flamelet in the flamelet

combustion model. The basic concepts, notations and governing equations in both physical space and mixture fraction space, which are important to understand how such flows are solved for in combustion codes, are introduced. The chapter investigates also the sensitivity of the laminar flamelet solutions to modeling choices in radiation model, chemical kinetic mechanism as well as stoichiometric scalar dissipation rate under the steady state assumption to select the baseline modeling choices for the subsequent simulations. Finally, interesting and important physical phenomena related to unsteady effects are presented for both constant and time-dependent $\chi_{st}$ cases.

- Chapter IV is devoted to introduce the flamelet combustion model, which differs in choices made for the flamelet library generation, flamelet parametrization, PDF formulation as well as parameter variables used for the turbulent LUT. Four different methods for producing the laminar flamelet library are first proposed. Then, the relation between the instantaneous thermochemical quantities and LES-filtered ones is provided using the presumed PDF approach. The assumption of statistically independent parameters in the joint PDF is made. The scalar dissipation rate PDF $\tilde{p}(\mathrm{X})$, the heat loss parameter PDF $\tilde{p}(\mathrm{H})$ are assumed to be a Dirac delta function; the $\beta$-PDF or the top-hat PDF is adopted for the PDF of mixture fraction $\tilde{p}(Z)$. The turbulent LUT that are parametrized by $(\tilde{Z}, \widetilde{Z_v}, \tilde{\mathrm{X}}, \tilde{\mathrm{H}})$ is pre-tabulated. Finally, the chapter provides various modeling options for $\tilde{Z}$, $\widetilde{Z_v}$, $\tilde{\mathrm{X}}$, and $\tilde{\mathrm{H}}$ in the turbulent LES-solver.
- The purpose of Chapter V is to develop the flamelet combustion model and radiation model for large eddy simulations (LES) of well-controlled laboratory-scale turbulent fires. The development of the combustion model consists of:
  - Studying the different libraries of flamelet solutions produced using four different methods: uniform values of enthalpy deficit across the flame in SLFV1; prescribed local radiative heat loss fraction in SLFV2; evolution at different constant values of $\chi_{st}$ with full grey model in ULFV1 and evolution with $\chi_{\mathrm{st}}(\mathrm{t}) = 25\exp(-40t)$; and prescribed local radiative heat loss fraction used in modified grey model in ULFV2.

- Studying the different models of the turbulent flame LUT parameters such as the sub-grid scale variance of mixture fraction, the scalar dissipation rate as well as the heat loss parameter.

The radiation model features a description of non-local phenomenon through the Radiative Transfer Equation (RTE). Different treatments of coupled combustion and radiation effects at flamelet scale are considered:

- A treatment in which local radiation phenomena are neglected inside the flamelet solver.
- A treatment in which these phenomena are included inside the flamelet solver and also sub-grid scale turbulence-radiation interactions (TRI) are included in the RTE solver.

This modeling framework is incorporated into the LES solver FireFOAM, developed by FM Global. This chapter also presents a study on the sensitivity of the number of outer loops in the PIMPLE algorithm. It is evaluated in simulations of a two-dimensional, plane, buoyancy-driven, turbulent, diffusion methane-air flame experimentally characterized by measurements of local temperatures and global flame emissive power. The best modeling developments and parameters choices are concluded and going to be used in simulations in Chapter VI.

- Chapter V focuses on developing combustion and radiation models for LES of well-controlled laboratory-scale fires and it is evaluated in simulations of the methane-fueled turbulent line fire with the co-flow at the air condition. Studies in Chapter VI are the continuation of the study in Chapter V and aim to support the development and validation of models used to simulate the response of fires to the activation of suppression systems by gaseous agents. The modeling framework features the flamelet combustion model and the grey radiation model with TRI, which are developed in Chapter V. The experimental configuration is the turbulent line fire with a controlled co-flow. The co-flow is an air-nitrogen mixture with variable oxygen dilution conditions, in which the conditions leading to full flame extinction is not considered. The flamelet model, which is capable of simulating flame extinction and re-ignition events, require an additional laminar flamelet library parameter typically chosen as a reaction progress variable. This extension

of the flamelet model will be developed in future work. Numerical results are evaluated against experimental measurements, which include the mean oxygen mole-fraction at $X_{O2} = 0.18$, the global radiative heat loss fraction and the combustion efficiency. Numerical results are found to over-predict the total heat loss fraction, but successfully capture the decreasing trend of the global heat loss fraction when exposing the flame to the co-flow with decreasing oxygen strength. The over-predictions of heat losses can be explained by the limitation of using the grey assumption of the radiation model. We found that at $X_{O2} = 0.18$, the predicted mean oxygen mole-fraction have some discrepancies when comparing with the measurement, a result reveals the limitation of the current flamelet model. Finally, the simulated combustion efficiency agrees very well with the experimental data with the discrepancy of only 7%.

Despite some big progresses in this study on the combustion model development by accounting for combustion chemistry and the radiation model development by calculating (rather than prescribe) radiant emissions, there are still restrictions in the current modeling framework:

- The first restriction is the significant over-prediction of the radiative heat losses by the grey model when compared to the measurement. In order to capture more correctly the global radiative heat loss fraction, the development of a new and more elaborate radiation model with non-grey properties is ongoing (but not shown here) [76] by a member in our research team, Rui Xu, a PhD student at FPE, University of Maryland. The non-grey radiation model in [76] uses the WSGG approach, which is developed by Modest [41]. This approach is often referred to as the banded WSGG model. The WSGG model is implemented in both FlameMaster and FireFOAM: FlameMaster provides a description of local (*i.e.,* flamelet-based) radiation phenomena while FireFOAM provides a description of non-local (*i.e.*, non-flamelet) radiation phenomena.
- The second restriction is that the current flamelet combustion model is limited to the flame configuration without extinction/re-ignition events. The description of these phenomena requires an additional laminar flamelet library parameter

typically chosen as a reaction progress variable [67]; this extension of the model will be considered in future work.

The toxic gases such as unburned hydrocarbons（UHCs）, carbon monoxide（CO) and oxides of nitrogen ($NO_x$）, from combustion processes has gained increasing attention over the past few decades. While carbon monoxide poisoning is the most common cause of fatality in fires, $NO_x$ is regarded as precursor of chemical smog and as contributor to stratospheric ozone depletion. Devising technologies which reduce emissions of such critical species into the atmosphere requires the understanding and control of their formation mechanisms. Using the flamelet model to predict such gases is a very promising direction in future work since the model can provide a complete representation of the generation of intermediate chemical by-products including these toxic gases.

The study in this project is limited to the use of methane in the UMD experiment, which is a weakly sooting fuel, hence, soot is neglected. The extension to cases with more strongly sooting fuels than methane will require soot modeling, which is a particularly challenging problem in turbulent combustion since the study of soot requires strong understanding on the, often small-scale, interactions between turbulence, particle dynamics, and chemistry. In addition, soot can be the principal consideration in radiative transfer, creating a strong two-way coupling between the soot and combustion models. The investigation of soot is left as future work.

The development of the flamelet combustion model and radiation model for large eddy simulations (LES) in this project is limited to laboratory-scale turbulent fires. The development and validation of engineering-level models used in real-world fire safety applications, which need to handle a wide range of interacting physical phenomena and complex geometry in industrial or real scenarios, and without the advantage of an accurate description of the fuel composition and of its combustion chemistry, can be considered in future work.

# Bibliography

[1] V. Novozhilov, “Computational fluid dynamics modeling of compartment fires,” *Prog. Energy Combust. Sci.*, vol. 27, no. 6, pp. 611–666, Jan. 2001.

[2] A. Trouvé and Y. Wang, “Large eddy simulation of compartment fires,” *Int. J. Comut. Fluid Dyn.*, vol. 24, no. 10, pp. 449–466, Dec. 2010.

[3] B. Merci, “Fire Safety Science,” *Proc. Elev. Int. Symp. Int. Assoc. Fire Saf. Sci. 24*, pp. 46–65.

[4] M. K and M. S, “Society of Fire Protection Engineering,” in *SFPE Handbook of Fire Protection Engineering (5th Ed.)*, 2016, pp. 1034–1065.

[5] S. B. Pope, *Turbulent flows*. Cambridge University Press, 2000.

[6] “FDS-SMV.” [Online]. Available: https://pages.nist.gov/fds-smv/. [Accessed: 18-Sep-2019].

[7] FM Global, “FireFOAM.” [Online]. Available: https://github.com/fireFoam-dev. [Accessed: 10-Nov-2018].

[8] “Opencfd ltd. and openfoam.” [Online]. Available: https://www.openfoam.com. [Accessed: 28-May-2019].

[9] Y. Wang, P. Chatterjee, and J. L. de Ris, “Large eddy simulation of fire plumes,” *Proc. Combust. Inst.*, vol. 33, no. 2, pp. 2473–2480, Jan. 2011.

[10] M. Chaos, M. M. Khan, N. Krishnamoorthy, J. L. de Ris, and S. B. Dorofeev, “Evaluation of optimization schemes and determination of solid fuel properties for CFD fire models using bench-scale pyrolysis tests,” *Proc. Combust. Inst.*, vol. 33, no. 2, pp. 2599–2606, Jan. 2011.

[11] Y. Wang, M. Chaos, and S. B. Dorofeev, “Cfd modeling of flame spread over corrugated cardboard panels.,” in *Proceedings of 13 th International Conference on Fire and Materials*, 2013, pp. 437–448.

[12] K. Meredith, J. de Vries, Y. Wang, and Y. Xin, “A comprehensive model for simulating the interaction of water with solid surfaces in fire suppression environments,” *Proc. Combust. Inst.*, vol. 34, no. 2, pp. 2719–2726, Jan. 2013.

[13] K. Meredith, Y. Xin, and J. de Vries, “A Numerical Model for Simulation of Thin-Film Water Transport over Solid Fuel Surfaces,” *Fire Saf. Sci.*, vol. 10, pp. 415–428, 2011.

[14] K. V. Meredith, P. Chatterjee, Y. Wang, and Y. Xin, “Simulating sprinkler based rack storage fire suppression under uniform water application,” in *Proceedings of the 7th International Seminar on Fire and Explosion Hazards (ISFEH7)*, 2013, pp. 511–520.

[15] K. V. Meredith, X. Chatterjee, P. abd Zhou, Y.Wang, and H.-Z. Yu, “Validation of spray water distribution patterns for the k11.2 sprinkler in the presence of a rack storage fire plume generator,” in *3th International Conference and Exhibition on Fire Science and*

*Engineering*, 2013.

[16] P. Chatterjee, J. L. de Ris, Y. Wang, and S. B. Dorofeev, "A model for soot radiation in buoyant diffusion flames," *Proc. Combust. Inst.*, vol. 33, no. 2, pp. 2665–2671, Jan. 2011.

[17] N. Ren, Y. Wang, S. Vilfayeau, and A. Trouvé, "Large eddy simulation of turbulent vertical wall fires supplied with gaseous fuel through porous burners," *Combust. Flame*, vol. 169, pp. 194–208, Jul. 2016.

[18] Z. Hu, Y. Utiskul, J. G. Quintiere, and A. Trouve, "Towards large eddy simulations of flame extinction and carbon monoxide emission in compartment fires," *Proc. Combust. Inst.*, vol. 31, no. 2, pp. 2537–2545, Jan. 2007.

[19] C. L. Beyler, "Flammability limits of premixed and diffusion flames," in *The SFPE Handbook of Fire Protection Engineering (3rd ed)*, 2002.

[20] U. Vaari, J. Floyd, and R. McDermott, "Cfd simulations on extinction of coflow diffusion flames," in *Proc. Eleventh International Symposium, International Association for Fire Safety Science*, 2011, pp. 10:781–793.

[21] A. Y. Snegirev and A. S. Tsoy, "Treatment of local extinction in CFD fire modeling," *Proc. Combust. Inst.*, vol. 35, no. 3, pp. 2519–2526, Jan. 2015.

[22] S. Vilfayeau, J. P. White, P. B. Sunderland, A. W. Marshall, and A. Trouvé, "Large eddy simulation of flame extinction in a turbulent line fire exposed to air-nitrogen co-flow," *Fire Saf. J.*, vol. 86, pp. 16–31, Nov. 2016.

[23] J. P. White, E. D. Link, A. C. Trouvé, P. B. Sunderland, A. W. Marshall, J. A. Sheffel, M. L. Corn, M. B. Colket, M. Chaos, and H.-Z. Yu, "Radiative emissions measurements from a buoyant, turbulent line flame under oxidizer-dilution quenching conditions," *Fire Saf. J.*, vol. 76, pp. 74–84, Aug. 2015.

[24] A. C. Y. Yuen, G. H. Yeoh, V. Timchenko, S. C. P. Cheung, and T. J. Barber, "Importance of detailed chemical kinetics on combustion and soot modelling of ventilated and under-ventilated fires in compartment," *Int. J. Heat Mass Transf.*, vol. 96, pp. 171–188, May 2016.

[25] A. C. Y. Yuen, G. H. Yeoh, V. Timchenko, T. B. Y. Chen, Q. N. Chan, C. Wang, and D. D. Li, "Comparison of detailed soot formation models for sooty and non-sooty flames in an under-ventilated ISO room," *Int. J. Heat Mass Transf.*, vol. 115, pp. 717–729, Dec. 2017.

[26] A. Yu. Snegirev, "Perfectly stirred reactor model to evaluate extinction of diffusion flame," *Combust. Flame*, vol. 162, no. 10, pp. 3622–3631, Oct. 2015.

[27] A. Snegirev, E. Markus, E. Kuznetsov, J. Harris, and T. Wu, "On soot and radiation modeling in buoyant turbulent diffusion flames," *Heat Mass Transf.*, vol. 54, no. 8, pp. 2275–2293, Aug. 2018.

[28] I. Sikic, S. Dembele, and J. Wen, "Non-grey radiative heat transfer modelling in LES-CFD simulated methanol pool fires," *J. Quant. Spectrosc. Radiat. Transf.*, vol. 234, pp.

78–89, Sep. 2019.

[29] J. L. Consalvi, R. Demarco, A. Fuentes, S. Melis, and J. P. Vantelon, “On the modeling of radiative heat transfer in laboratory-scale pool fires,” *Fire Saf. J.*, vol. 60, pp. 73–81, Aug. 2013.

[30] J. L. Consalvi and F. Liu, “Radiative heat transfer in the core of axisymmetric pool fires – I: Evaluation of approximate radiative property models,” *Int. J. Therm. Sci.*, vol. 84, pp. 104–117, Oct. 2014.

[31] J. P. White, “Measurement and Simulation of Suppression Effects in a Buoyant Turbulent Line Fire,” University of Maryland, USA, 2016.

[32] J. P. White, E. D. Link, A. Trouvé, P. B. Sunderland, and A. W. Marshall, “A general calorimetry framework for measurement of combustion efficiency in a suppressed turbulent line fire,” *Fire Saf. J.*, vol. 92, no. February, pp. 164–176, 2017.

[33] “Proceedings of the first workshop organized by the IAFSS Working Group on Measurement and Computation of Fire Phenomena (MaCFP),” *Fire Saf. J.*, vol. 101, pp. 1–17, Oct. 2018.

[34] S. Vilfayeau, “Large Eddy Simulation of fire extinction phenomena,” 2015.

[35] H. Jasak, “Error analysis and estimation for the finite volume method with applications to fluid flows,” *Dep. Mech. Eng.*, vol. PHD, no. June, 1996.

[36] H. G. Weller and G. Tabor, “A tensorial approach to computational continuum mechanics using object-oriented techniques,” *Comput. Phys.*, vol. 12, no. 6, p. 620, 1998.

[37] B. E. Magnussen, “On mathematical modelling of turbulent combustion with special emphasis on soot formation and combustion,” in *16th symposium (International) on Combustion*, 1976, pp. 719–729.

[38] C. Fureby, G. Tabor, H. G. Weller, and A. D. Gosman, “A comparative study of subgrid scale models in homogeneous isotropic turbulence,” *Phys. Fluids*, vol. 9, no. 5, p. 1416, Sep. 1998.

[39] R. Viskanta and M. P. Mengüç, “Radiation heat transfer in combustion systems,” *Prog. Energy Combust. Sci.*, vol. 13, no. 2, pp. 97–160, Jan. 1987.

[40] “Radiation sub-models, TNF Workshop.” [Online]. Available: http://public.ca.sandia.gov/TNF/radiation.html. [Accessed: 10-Nov-2018].

[41] M. F. Modest, “The Weighted-Sum-of-Gray-Gases Model for Arbitrary Solution Methods in Radiative Transfer,” *J. Heat Transfer*, vol. 113, no. 3, p. 650, Aug. 1991.

[42] E. R. G. Eckert, “Radiative transfer, H. C. Hottel and A. F. Sarofim, McGraw-Hill Book Company, New York, 1967. 52 pages,” *AIChE J.*, vol. 15, no. 5, pp. 794–796, Sep. 1969.

[43] R. Johansson, B. Leckner, K. Andersson, and F. Johnsson, “Account for variations in the H2O to CO2 molar ratio when modelling gaseous radiative heat transfer with the weighted-sum-of-grey-gases model,” *Combust. Flame*, vol. 158, no. 5, pp. 893–901,

2011.

[44] P. Giordano and D. Lentini, “Combustion-radiation-turbulence interaction modeling in absorbing/emitting nonpremixed flames,” *Combust. Sci. Technol.*, vol. 2202, no. July, 2017.

[45] T. Poinsot and D. Veynante, *Theoretical and numerical combustion*. Edwards, 2005.

[46] H. Pitsch and N. Peters, “A Consistent Flamelet Formulation for Non-Premixed Combustion Considering Differential Diffusion Effects,” *Combust. Flame*, vol. 114, no. 1–2, pp. 26–40, Jul. 1998.

[47] N. Peters, “Laminar diffusion flamelet models in non-premixed turbulent combustion,” *Prog. Energy Combust. Sci.*, vol. 10, no. 3, pp. 319–339, 1984.

[48] J. S. Kim and F. A. Williams, “Structures of flow and mixture-fraction fields for counterflow diffusion flames with small stoichiometric mixture fractions,” *SIAM J. Appl. Math.*, vol. 53, no. 6, pp. 1551–1566, 1993.

[49] H. Pitsch, M. Chen, and N. Peters, “Unsteady flamelet modeling of turbulent hydrogen-air diffusion flames,” in *Symposium (international) on combustion*, 1998, vol. 27, no. 1, pp. 1057–1064.

[50] F. Cassol, R. Brittes, F. H. R. França, and O. A. Ezekoye, “Application of the weighted-sum-of-gray-gases model for media composed of arbitrary concentrations of H2O, CO2 and soot,” *Int. J. Heat Mass Transf.*, vol. 79, pp. 796–806, 2014.

[51] H. Pitsch, “FlameMaster, an open source C++ program package for 0D combustion and 1D laminar flame calculations.” [Online]. Available: https://itv.rwth-aachen.de/index.php. [Accessed: 18-Dec-2018].

[52] K. D. Lathrop and B. G. Carlson, “Discrete ordinates angular quadrature of the neutron transport equation,” Los Alamos, NM (United States), Sep. 1964.

[53] A. Cuoci, A. Frassoldati, T. Faravelli, and E. Ranzi, “Kinetic modeling of soot formation in turbulent nonpremixed flames,” *Environ. Eng. Sci.*, vol. 25, no. 10, pp. 1407–1422, 2008.

[54] A. Cuoci, A. Frassoldati, T. Faravelli, and E. Ranzi, “Formation of soot and nitrogen oxides in unsteady counterflow diffusion flames,” *Combust. Flame*, vol. 156, no. 10, pp. 2010–2022, Oct. 2009.

[55] N. Peters, *Turbulent Combustion*. Cambridge: Cambridge University Press, 2000.

[56] E. Ranzi, A. Frassoldati, R. Grana, A. Cuoci, T. Faravelli, A. P. Kelley, and C. K. Law, “Hierarchical and comparative kinetic modeling of laminar flame speeds of hydrocarbon and oxygenated fuels,” *Prog. Energy Combust. Sci.*, vol. 38, no. 4, pp. 468–501, Aug. 2012.

[57] F. Mauss, N. Peters, B. Rogg, and F. A. Williams, “Reduced Kinetic Mechanisms for Premixed Hydrogen Flames,” in *Lecture Notes in Physics Monographs*, 1993, pp. 29–43.

[58] "Chemical Mechanism: Combustion Research Group at UC San Diego." [Online]. Available: https://web.eng.ucsd.edu/mae/groups/combustion/mechanism.html. [Accessed: 28-Jul-2019].

[59] G. Smith, D. Golden, M. Frenklach, B. Eiteener, M. Goldenberg, C. Bowman, R. Hanson, W. Gardiner, V. Lissianski, and Z. Qin, "GRI-Mech Home Page." [Online]. Available: http://combustion.berkeley.edu/gri-mech/. [Accessed: 11-Jun-2019].

[60] V. M. Le, A. Marchand, S. Verma, J. White, A. Marshall, T. Rogaume, F. Richard, J. Luche, and A. Trouvé, "Simulations of a Turbulent Line Fire with a Steady Flamelet Combustion Model and Non-Gray Gas Radiation Models," *J. Phys. Conf. Ser.*, vol. 1107, no. 4, p. 042009, Nov. 2018.

[61] V. M. Le, A. Marchand, S. Verma, R. Xu, J. White, A. Marshall, T. Rogaume, F. Richard, J. Luche, and A. Trouvé, "Simulations of a turbulent line fire with a steady flamelet combustion model coupled with models for non-local and local gas radiation effects," *Fire Saf. J.*, vol. 106, pp. 105–113, Jun. 2019.

[62] A. Soufiani and J. Taine, "High temperature gas radiative property parameters of statistical narrow-band model for H2O, CO2 and CO, and correlated-K model for H2O and CO2," *Int. J. Heat Mass Transf.*, vol. 40, no. 4, pp. 987–991, Mar. 1997.

[63] H. Pitsch and M. Ihme, "An Unsteady/Flamelet Progress Variable Method for LES of Nonpremixed Turbulent Combustion," in *43rd AIAA Aerospace Sciences Meeting and Exhibit*, 2005.

[64] M. Ihme and H. Pitsch, "Modeling of radiation and nitric oxide formation in turbulent nonpremixed flames using a flamelet/progress variable formulation," *Phys. Fluids*, vol. 20, no. 5, p. 055110, May 2008.

[65] B. Cuenot, F. Egolfopoulos, and T. Poinsot, "An unsteady laminar flamelet model for non-premixed combustion," *Combust. Theory Model.*, vol. 4, no. 1, pp. 77–97, Mar. 2000.

[66] B. Marracino and D. Lentini, "Radiation Modelling in Non-Luminous Nonpremixed Turbulent Flames Radiation Modelling in Non-Luminous Nonpremixed Turbulent Flames," *Combust. Sci. Technol.*, vol. 128, no. July, pp. 23–48, 1997.

[67] M. Ihme and Y. C. See, "Prediction of autoignition in a lifted methane/air flame using an unsteady flamelet/progress variable model," *Combust. Flame*, vol. 157, no. 10, pp. 1850–1862, Oct. 2010.

[68] M. E. Mueller and H. Pitsch, "LES model for sooting turbulent nonpremixed flames," *Combust. Flame*, vol. 159, no. 6, pp. 2166–2180, Jun. 2012.

[69] R. W. Bilger, "The structure of turbulent nonpremixed flames," *Symp. Combust.*, vol. 22, no. 1, pp. 475–488, Jan. 1989.

[70] F. Liu, H. Guo, G. J. Smallwood, Ö. L. Gülder, and M. D. Matovic, "A robust and accurate algorithm of the β-pdf integration and its application to turbulent methane–air diffusion combustion in a gas turbine combustor simulator," *Int. J. Therm. Sci.*, vol. 41, no. 8, pp. 763–772, 2002.

[71] T. Ma, O. T. Stein, N. Chakraborty, and A. M. Kempf, “A posteriori testing of algebraic flame surface density models for LES,” *Combust. Theory Model.*, vol. 17, no. 3, pp. 431–482, 2017.

[72] N. Branley and W. P. Jones, “Large Eddy simulation of a turbulent non-premixed flame,” *Combust. Flame*, vol. 127, no. 1–2, pp. 1914–1934, Oct. 2001.

[73] C. D. Pierce and P. Moin, “A dynamic model for sub-grid scale variance and dissipation rate of a conserved scalar,” *Phys. Fluids*, vol. 10, no. 12, p. 3041, Nov. 1998.

[74] D. C. Haworth, M. C. Drake, S. B. Pope, and R. J. Blint, “The importance of time-dependent flame structures in stretched laminar flamelet models for turbulent jet diffusion flames,” *Symp. Combust.*, vol. 22, no. 1, pp. 589–597, Jan. 1989.

[75] F. S. L. H. Liu and E. C. C. J. Mccartney, “Development of an Analytical β-Function PDF Integration Algorithm for Simulation of Non-premixed Turbulent Combustion,” *Flow, Turbul. Combust.*, vol. 83, no. 2, pp. 205–226, 2009.

[76] R. Xu, V. M. Le, A. Marchand, S. Verma, T. Rogaume, F. Richard, J. Luche, and A. Trouvé, “Simulations of the Coupling between Combustion and Radiation in a Turbulent Line Fire Using an Unsteady Flamelet Model,” in *submited in International Association for Fire Safty Science (IAFSS 2020)*, 2020.